Study of the variability of planktonic ecosystems and biogeochemical cycles in the Levantine basin by 3D coupled hydrodynamic-biogeochemical modeling

Joelle Habib

To cite this version:

Joelle Habib. Study of the variability of planktonic ecosystems and biogeochemical cycles in the Levantine basin by 3D coupled hydrodynamic-biogeochemical modeling. Ocean, Atmosphere. Université Paul Sabatier - Toulouse III, 2023. English. NNT : 2023TOU30030 . tel-04213252

HAL Id: tel-04213252
https://theses.hal.science/tel-04213252

Submitted on 21 Sep 2023

THÈSE

En vue de l'obtention du

DOCTORAT DE L'UNIVERSITÉ DE TOULOUSE

Délivré par : *l'Université Toulouse 3 Paul Sabatier (UT3 Paul Sabatier)*

Présentée et soutenue le *12/01/2023* **par :**
Joelle HABIB

Étude de la variabilité des écosystèmes planctoniques et des cycles biogéochimiques dans le bassin Levantin: modélisation 3D couplée hydrodynamique-biogéochimique

---

JURY

Isabelle Dadou	LEGOS	Présidente du Jury
Thierry MOUTIN	MIO	Rapporteur
Bruno ZAKARDJIAN	MIO	Rapporteur
Marilaure GRÉGOIRE	FOCUS	Rapportrice
Abed el Rahman Hassoun	GEOMAR/NCMS	Examinateur
Claude ESTOURNEL	LEGOS	Directrice de thèse
Milad FAKHRI	NCMS	Co-directeur de thèse
Caroline ULSES	LEGOS	Co-encadrante de thèse

École doctorale et spécialité :
SDU2E : Océan, Atmosphère, Climat
Unité de Recherche :
LEGOS (UMR 5566)
Directeur(s) de Thèse :
Claude Estournel et *Milad Fakhri*
Rapporteurs :
Marilaure Grégoire, *Thierry Moutin* et *Bruno Zakardjian*

Résumé — La Méditerranée est une mer oligotrophe dont l'hydrodynamique et la biogéochimie sont en partie forcées par des formations d'eau denses. Les Eaux Intermédiaires Levantines, formées principalement dans le Gyre de Rhodes, un gyre cyclonique persistant dans l'est de la Méditerranée, jouent un rôle clé dans la circulation thermohaline de l'ensemble des bassins est et ouest. Ce travail de thèse, réalisé dans le cadre du projet PERLE (Pelagic Ecosystem Response to deep water formation in the Levant Experiment), vise à étudier la variabilité des cycles biogéochimiques et de l'écosystème pélagique dans le Bassin Levantin sur une période pluriannuelle à l'aide d'une approche de modélisation haute résolution 3D couplée.

Pour cela, un modèle 3D couplé hydrodynamique-biogéochimique, SYMPHONIE-Eco3M-S, a été mis en place au niveau de la mer Méditerranée et pour la période entre 2011-2020. Il a été calibré et évalué à l'aide d'observations de campagnes, de satellites et de flotteurs BGC-Argo. L'évaluation du modèle montre qu'il reproduit raisonnablement bien les principales variabilités spatiales et temporelles observées.

En se basant sur le modèle couplé, nous avons d'abord étudié la dynamique du carbone organique dans le Gyre de Rhodes. À l'échelle annuelle, le Gyre de Rhodes agit comme un écosystème autotrophe et est une source de carbone organique pour les zones environnantes. La rigueur de l'hiver influence fortement le fonctionnement de l'écosystème phytoplanctonique et la variabilité de la dynamique du carbone organique de la zone : les années caractérisées par une forte perte de chaleur à la surface de la mer et un mélange profond montrent dans la couche supérieure une intensification de l'apport en nutriments des couches plus profondes, de la croissance du phytoplancton et des exportations de carbone organique vers des profondeurs intermédiaires et la zone environnante du Bassin Levantin.

Ensuite, le modèle couplé a été utilisé pour quantifier la contribution des flux air-mer, des processus biologiques et des flux d'échange avec les mers voisines dans la variabilité de la dynamique de l'oxygène dissous dans le Bassin Levantin, et, à une échelle inférieure, le gyre de Rhodes. La Mer Levantine agit comme un puits d'oxygène pour l'atmosphère, avec des taux d'absorption maximaux dans le Gyre de Rhodes pendant l'hiver. La couche supérieure du Bassin Levantin s'est avérée être une source d'oxygène pour la couche intermédiaire et la mer Égée.

Mots clés : Mer Méditerranée, Bassin Levantin, oxygène dissous, carbone organique, zone de convection, LIW, modélisation

Abstract — The Mediterranean is an oligotrophic sea where hydrodynamics and biogeochemistry are driven in part by dense water formations. Levantine Intermediate Water (LIW), formed mostly in the Rhodes Gyre, a persistent cyclonic circulation in the eastern Mediterranean Sea, plays a key role in the thermohaline circulation of the entire eastern and western basins. This PhD thesis work, carried out as part of the PERLE (Pelagic Ecosystem Response to deep water formation in the Levant Experiment) project, aims to study the variability of the biogeochemical cycles and pelagic ecosystem in the Levantine Basin, and in particular in response to the LIW formation, over a multi-annual period, using a high-resolution coupled modeling approach.

For that purpose, a 3D coupled hydrodynamic-biogeochemical model, SYMPHONIE-Eco3M-S, was implemented over the Mediterranean Sea and the period from 2011 to 2020. It was calibrated and assessed using cruises, satellite, and BGC-Argo float observations. The assessment of the model shows that it reproduces reasonably well the main spatial and temporal variability observed.

Based on the coupled model, first we investigate organic carbon dynamics in the Rhodes Gyre. On an annual scale, the Rhodes Gyre acts as an autotrophic ecosystem and a source of organic carbon for the surrounding areas. Winter severity markedly influences the phytoplankton ecosystem functioning and organic carbon variability of the area: years characterized by strong heat loss at the sea surface and deep mixing show in the upper layer enhanced nutrient supply, phytoplankton growth and exports of organic carbon towards intermediate depths and the surrounding Levantine Basin.

Second, the coupled model was used to quantify the contribution of air-sea flux, biological processes, and exchange fluxes with the neighboring seas in the variability of the dissolved oxygen dynamics in the Levantine Basin, and at a lower scale, the Rhodes Gyre. The Levantine acts as an oxygen sink for the atmosphere, with maximum rates of uptake in the Rhodes Gyre during winter. The upper layer of the Levantine Basin was found to be a source of oxygen for the intermediate layer and the Aegean Sea.

Keywords:organic carbon, dissolved oxygen, dense water formation, LIW, modeling, Mediterranean Sea, Levantine Basin

Remerciement

Je tiens tout d'abord à remercier mes directeurs de thèse: Claude Estournel, Caroline Ulses et Milad Fakhri pour le soutien qu'ils m'ont accordé durant l'encadrement de cette thèse. Claude, merci de m'avoir fait confiance pour cette thèse au tout début, merci de m'avoir permis de réaliser la campagne PERLE, merci pour ta connaissance sans faille des processus physiques et enfin merci pour tes précieux conseils, ton orientention et ton encouragement tout au long de ce travail! Merci pour ta sympathie et tes super commentaires rigolots! Merci de ta présence durant tout, et de me faire partie de ta famille!

Cette thèse n'aurait bien sûr pas été possible sans le soutien de ma co-directrice de thèse, Caroline Ulses. C'est avec toi que j'ai appris tout! Merci de m'avoir passionnée pour la modélisation, tes idées lumineuses, pour les améliorations qui n'en finissent plus d'amèliorer. Merci pour ta patience lorsque je comprenais pas et je répétais la question plusieurs fois. Merci pour avoir été présente et enthousiaste à chaque étape! Merci pour tout ces documents que tu as dû remplir et ces guerres que tu as dû entamer (toi et claude) pour que j'aie le financement et que je puisse finir!

Je remercie aussi mon co-directeur de thèse, Milad Fakhri, qui même a distance a su m'orienter et me conseiller dans ce travail de recherche! Merci pour ton soutien lors de mes séjours au Liban, Merci de m'avoir accompagnée durant mon master et mon doctorat, et ta confiance en moi.

Je remercie la directrice de l'école doctorale, Geneviève Soucail, Laurent Mortier et le laboratoire LEGOS pour votre contribution durant la période non financée, c'est grâce à vous que les quelques mois de fin de thèse se sont déroulés dans des conditions optimales. Je vous suis reconnaissante! Une thèse au LEGOS ne serait pas non plus possible sans les membres de l'équipe redoutable du GESSEC? Merci Brigitte et Agathe! Merci pour votre disponibilité, votre soutien! Brigitte Merci pour les astuces, ta bonne humeur quotidienne et pour les papotages dans les couloirs.

Cette thèse est le fruit de nombreuses collaborations intra et inter laboratoires. Tout d'abord, merci à Patrick Marsaleix pour ton aide dévouée lors de la mise en place du modèle et les heures passées sur le calcul du bilan. Merci aussi à Thomas, pour ton aide précieuse tout au long du travail de modélisation. Également, je tiens à remercier l'ensemble des personnes, marins et scientifiques, ainsi que la team PERLE qui ont contribué à l'obtention des données utilisées dans ces travaux de thèse. Merci aussi à Thibaut Wagener, Julien Juanno et Arthur Capet, merci d'avoir accepté de me suivre dans mon comité de thèse et pour les échanges enrichissants et pertinents que nous avons pu avoir à cette occasion.

J'exprime ma vive gratitude à Marilaure Grégoire, Thierry Moutin et Bruno Zakardjian qui ont accepté d'évaluer mes travaux de recherche. Je remercie également les membres du jury, Isabelle Dadou et Abed el Rahman Hassoun, pour l'honneur qu'ils me font de prendre part à cette soutenance. Votre implication dans l'aboutissement de ces travaux m'honore. Merci

pour le temps passé à la relecture critique du manuscrit et l'ensemble de vos remarques constructives.

Je tiens à remercier aussi mes amis de cantine: Méredith, Inés, Benjamin, Renaut, Samira, Jérémy, Camille, Boris, Thibault, Zahra, ainsi que ma collègue de bureau: Alexandra. Merci Alexandra pour ces années de rires (beaucoup), pour le chaos de nos bureaux, pour les thés, cafés et tisannes et les goûters surprises. Tu vas me manquer le plus! Merci aussi à Victorien pour ses commentaires bizarres et ses danses génantes. Paul, merci, soirée lisbonne? I would also like to thank my best friend: Maria, who forced me to be her friend and to practise my english. I am so lucky to have shared this journey with you, together in the lab. Thank you for believing in me always! See you soon in Greece or anywhere!

Je tiens à remercier aussi mes potes à vie! À ma copine d'école, Elena, merci pour tes podcasts qui m'ont divertis pas mal de temps durant ces 3 années! Merci Georges pour ton humour, ton support, les fous rires, nos concerts dans ta voiture et les randonnées! Ta présence a rendu la vie un peu plus supportable!

Merci à ma famille Française: Pierre, Sylvie et Romain. Pierre tu es parmi les plus belles rencontres que j'ai pu faire au cours de cette thèse, je ne peux pas mettre les mots dessus, merci pour tout.

Même à distance, je tiens à remercier ma famille, cette fois Libanaise, mon père, mon oncle et mes deux soeurs Carine et Christelle qui m'accompagnent bien au-delà de cette expérience. Bien que pour la plupart du temps, vous ne comprenez pas ce que je fais ou je dis, merci pour votre soutien durant cette aventure! Merci Carine de m'avoir supportée lorsque je rageais seule pour rien (tu sais quand), pour me pourigater partout avec tes moules et ton strogonof! tu es la meilleure! Merci Christelle pour ces longues discussions en larmes (toi, la plupart du temps) concernant ton rapport de Master, franchement tu m'as mis plus de pression que la thèse! Je vous aime fort mes petites!

Merci aussi à ma famille au delà, ma mère et ma grand mère! Merci maman pour tout ces appels en larmes, tout tes je t'aime, tu as mangé et tu me manques... Tu me manques! J'aurai bien aimé que tu sois là! Grand mère, Je suis là aujourd'hui grâce à toi. Téta, C'est toi qui m'a élevée et qui étais là pour moi toujours! Tu es et tu resteras mon tout!

Finalement, Merci Ronan! Tu sais déjà !

Contents

List of Figures

List of Tables

Acronyms

AW	*Atlantic Water*
MW	*Mediterranean Water*
DW	*Deep Water*
LIW	*Levantine Intermediate Water*
LSW	*Levantine Surface Water*
WMDW	*Western Mediterranean Deep Water*
EMDW	*Eastern Mediterranean Deep Water*
EMT	*Eastern Mediterranean Transient*
POEM	*Physical Oceanography of the Eastern Mediterranean*
RG	*Rhodes Gyre*
AMC	*Asia Minor Current*
CC	*Cilician Current*
LEC	*Libyo-Egyptian Current*
MMJ	*Mid-Mediterranean jet*
IE	*Ierapetra Eddy*
EE	*Egyptian Eddies*
MME	*Mersa-Matruh Eddy*
ShE	*Shikmona Eddy*
CE	*Cyprus Eddy*
LTE	*Latakia Eddy*
DCM	*Deep Chlorophyll Maximum*
Chl	*Chlorophyll*
DOC	*Dissolved Organic Carbon*
POC	*Particulate Organic Carbon*
NPP	*Net Primary Production*

NCP	*Net community Production*
PP	*Primary Production*
DIC	*Dissolved Inorganic Carbon*
OML	*Oxygen Minimum Layer*
SOM	*Subsurface Oxygen Maximum*

General Introduction

General context

Owing to its morphology and geographical position, the Mediterranean Sea is a unique ocean basin. It is defined as a “miniature global ocean” (Bethoux et al., 1999) due to the processes of dense water formation (Lascaratos et al., 1999), and its thermohaline circulation. Its small size associated with short renewal times of the water masses induces a fast response to climate change (Somot et al., 2006) and to continental inputs for example on nutrient concentrations.

Because of these similarities with the global ocean, the Mediterranean has become a major area of scientific interest since the 60s. Dense water formation similar to the one observed in the Labrador Sea and Greenland (Marshall and Schott, 1999) was at the origin of the MEDOC program focused on the Gulf of Lion.In the eastern Mediterranean, the formation of dense water and the study of the general circulation were at the origin of the international program POEM (Malanotte-rizzoli et al., 1988). Later, the quantification of these physical processes and their impact on biogeochemical processes and balances focused the respective interest of the HyMeX (Drobinski et al., 2014) and MerMex (The MerMex Group, 2011) programs of the international meta-program MISTRALS and led to large-scale observation campaigns (Estournel et al., 2016; Conan et al., 2018).

The Mediterranean basin is also considered as a hotspot of climate change (The MerMex Group, 2011). It is one of the most vulnerable marine ecosystems to human activity pressure and is acutely sensitive to environmental change (Williams, 1998). Climate model projections predict a decrease in the rainfall rate, the drying of continental surfaces, an increase in evaporation over the sea and its warming during the twenty-first century with strong modifications of water formation, thermohaline circulation, and ocean climate evolution (Somot et al., 2006; Giorgi and Lionello, 2008; Diffenbaugh and Scherer, 2011).

Because of its socio-economic importance (Randone et al., 2017), the Mediterranean sea undergoes high anthropogenic pressure given the large inflow of tourism: it covers 1/3 of tourism globally, in addition to being a highly populated area (512 million people UNEP, 2020). These pressures are problematic for this ecosystem, therefore, it is important to understand and try to anticipate the pressure-induced changes of this sea in order to propose effective solutions.

Lastly, the Mediterranean possesses a high ecosystem diversity confined in a very small area representing 0.7 % of the global ocean. It gathers the most dynamic mechanisms of the global ocean, as well as trophic regimes ranging from "bloom" to strict oligotrophic regions (D’Ortenzio and Ribera d’Alcalà, 2009). Its study can thus provide a better understanding of the biogeochemical functioning of a wide variety of ocean regions. The atmospheric and hydrodynamic conditions associated with it generate highly variable physical and biogeochemical characteristics, and this at various spatial and temporal scales. The Mediterranean Sea also represents an ideal framework for modeling, since it makes it possible to model the whole basin at high resolution at reasonable computing costs.

Scientific context and questions

Previous studies highlighted the unique feature of the Eastern Mediterranean as a "laboratory basin" of contrasting ecosystems (Malanotte-Rizzoli and Eremeev, 1999) from extreme eutrophic (Northern Adriatic) to extreme oligotrophic (Levantine Basin) and from ecosystems driven by rivers inputs (Northern Adriatic) to ecosystems driven by wind forcing and dense water formation processes (Levantine Basin). The ultra-oligotrophic Levantine Basin possesses a primary production rate corresponding to half of the Sargasso Sea (Krom et al., 2003). Nutrient concentrations in its deep water are the lowest of all the oceans even though this basin has considerable atmospheric and riverine nutrient inputs. Low nutrient concentrations result from a combination of the anti-estuarine circulation and the relatively young age of the water masses. The N:P ratio in the deep waters (28:1) of this basin is also atypical, approximately twice the Redfield ratio (16:1, Krom et al., 1991). These unusual properties make it an ideal natural laboratory to examine the nutrient cycles and processes related to carbon uptake in the ocean.

This PhD work focuses on the Levantine Sea, one of the major basins in the Eastern Mediterranean and the seat of the Levantine Intermediate Water (LIW) formation. Studies have shown the crucial role of LIW in the Mediterranean deep water formation for the eastern and western basins (Skliris and Lascaratos, 2004). This water is mainly formed in the Rhodes Gyre during winter (Lascaratos et al., 1993), with a formation rate close to the Atlantic inflow at the Gibraltar Strait.

Most of our knowledge about the LIW derives from the POEM Group observation efforts conducted during the 80's and 90's. The observational project depicted the eastern Mediterranean circulation (Özsoy et al., 1989, 1993; Robinson et al., 1991; The POEM group, 1992; Robinson and Golnaraghi, 1993b; Malanotte-Rizzoli et al., 1997). Nevertheless, many questions remained after POEM and required further investigations. Observational and modeling gaps still exist, in particular on the LIW formation and dispersion and their role in the biogeochemical cycles of the Levantine Basin.

Here, we will develop some of the main open scientific questions regarding the LIW dynamics:
First, **the LIW formation areas**. Other formation areas have also been proposed i.e. the Antalya Basin (Sur et al., 1993; Kubin et al., 2019; Fach et al., 2021), the Cyprus Eddy (Moutin and Prieur, 2012). Even though the Rhodes Gyre seems to play a main part in the LIW formation, the Levantine Basin lacks an advanced description of the LIW formation in coastal and offshore areas.
The factors driving the LIW formation, such as the reversal of the circulation in the North Ionian Gyre modifying the LIW physical properties, might have consequences on biogeochemical processes (Ozer et al., 2016, 2022).
The limited comprehension of the LIW dynamic suggests gaps in the biogeochemical cycles of the Levantine Basin as well. Some of those gaps concern:
The oligotrophic feature of the Levantine Basin is presumably due to the position of the LIW and its residence time (Crispi et al., 2001; Moutin and Prieur, 2012). As a matter of fact, the LIW collects sinking organic matter from the surface biological production and

flows to the west prevailing the deep nutrient stock in the Eastern Basin.
The unusual stochiometric ratio compared to other oceanic provinces characterizes the Eastern Basin (Ribera d'Alcalà et al., 2003; Krom et al., 2005). The induced biological effects however are partially understood. The LIW might shape the distribution of nutrients along the water column, i.e, the position of the nutricline was suggested to follow the west-east gradient of oligotrophy (Pujo-Pay et al., 2011) with the top of the phosphacline coinciding with the top of the LIW layer (Van Cappellen et al., 2014).
The trophic regime in the Levantine Basin. This basin is composed of two regimes: the intermittent bloom regime for the Rhodes Gyre and the no bloom regime for the surrounding area. The Rhodes Gyre is characterized by a primary production significantly higher than in the surrounding region of the Levantine basin (D'Ortenzio et al., 2003). The increase in chlorophyll is linked to the vertical mixing associated with dense water formation (Yilmaz et al., 1994; Ediger and Yilmaz, 1996). Its high primary production makes it an important study area for the carbon cycle. Yet, Mayot et al. (2016) detected an alternating occurrence between the intermittent, and the no bloom regimes in the Rhodes Gyre. This occurrence has not been explained, highlighting the need to understand the underlying mechanisms and to evaluate whether future climatic changes will promote the oligotrophy of the entire basin.
Finally, **the study of the prokaryotic and eukaryotic diversity** in the eastern basin are scarce, very little is known about the regulation of the biogeochemical cycles by these communities. In addition, the nature and the fate of the produced dissolved organic carbon (DOC) in the euphotic layer in the eastern Mediterranean are still poorly characterized. In fact, Santinelli et al. (2015) reported a DOC removal in the LIW core due to the remineralisation and export of semi labile DOC during the LIW path from the Levantine Basin to the Sicily Channel.

Although the Levantine Basin plays a crucial role in the Mediterranean Sea, it is still tremendously undersampled and is limited in modelling studies. This thesis work takes place within the context of the PERLE (Pelagic ecosystem response to dense water formation in the Levant experiment) project of the MERMEX-MISTRALS program. This project aims to better understand the formation and the spreading of the LIW and its influence on nutrient distribution and the pelagic ecosystem through intensive field work activity. The work done within this thesis covered an additional goal of the project which is the improvement of the modelling performance by implementing a biogeochemical model coupled to hydrodynamics and validating it with the collected data, modelling that will then be used to complete the observation derived knowledges on the hydrodynamics and biogeochemistry, and to predict future possible changes.

Objectives and organization of this manuscript

Within the context of the above issues, the focus of my thesis is to study the impact of LIW formation on the variability of the planktonic ecosystem and the biogeochemical cycles in the Levantine Basin, based on regional 3D coupled physical-biogeochemical models.

This focus has been partitioned into four research objectives:

1. The first objective was to implement the coupled physical-biogeochemical models in the Levantine Basin. Attention was given to the initialization of the nutrients, dissolved oxygen, and chlorophyll in this basin, in addition to the different regions of the Mediterranean Sea.
2. The second objective was a detailed validation of the biogeochemical model.
3. The third objective was to determine the impact of dense water formation on the annual cycle of nutrients, and the planktonic ecosystem. We quantify the organic carbon budget in the Rhodes Gyre, the most productive region in the Levantine Basin.
4. Finally, the last objective was to estimate the dissolved oxygen budget in the Levantine Basin and analyze the impact of the LIW formation on it.

This manuscript is composed of six chapters:

→ Chapter 1 details the knowledge needed to address the results presented in this thesis. It reviews the general hydrodynamic and biogeochemical characteristics of the Mediterranean Sea, it also covers the state of art of the modeling emphasizing on the Levantine Basin.

→ Chapter 2 describes the coupled hydrodynamic-biogeochemical models SYMPHONIE-Eco3M-S and the data sets used to assess the latter.

→ Chapter 3 is dedicated to the evaluation of the model performance by comparing it against several observational data sets i.e. ocean color, float and cruise data.

→ Chapter 4 is based on a submitted article covering the modeling of the organic carbon variation in the Rhodes Gyre, major site of intermediate water formation. We analyze the seasonal and interannual variability of nutrients and the planktonic ecosystem. The various processes contributing to the organic carbon budget are also analyzed.

→ Chapter 5 studies the seasonal and interannual variabilities of the dissolved oxygen cycle in the Levantine Basin and its exchanges with the neighbouring basins in the surface and intermediate layers and between them.

→ Finally, Chapter 6 summarizes the main results found during this thesis and presents the perspectives.

The Appendix is composed of details of the comparisons between model outputs and observations in order to validate the biogeochemical model. It also presents the parameters of the biogeochemical model and its initialization.

Introduction générale

Contexte général

De par sa morphologie et sa position géographique, la mer Méditerranée est un bassin océanique unique. Ce bassin est défini comme un « océan global miniature » (Bethoux et al., 1999) en raison des processus de formation d'eau dense (Lascaratos et al., 1999), de la circulation thermohaline, de l'influence des apports continentaux sur les nutriments et de sa réponse rapide au changement climatique (Somot et al., 2006).

Du fait de ces similitudes avec l'océan mondial, la Méditerranée est devenue une zone d'intérêt scientifique majeur depuis les années 60. La formation d'eau dense semblable à celle observée dans la mer du Labrador et le Groenland (Marshall and Schott, 1999) est à l'origine du programme MEDOC axé sur le Golfe du Lion.En Méditerranée orientale, la formation de l'eau dense (EMDW, LIW) et l'étude de la circulation générale ont été à l'origine du programme POEM (Malanotte-rizzoli et al., 1988). Plus tard, la quantification de ces processus physiques et leur impact sur les processus et les équilibres biogéochimiques ont focalisé l'intérêt respectif des programmes HyMeX (Drobinski et al., 2014) et MerMex (The MerMex Group, 2011) du méta-programme international MISTRALS et ont conduit à des campagnes d'observation à grande échelle (Estournel et al., 2016; Conan et al., 2018).

La mer Méditerranée est également considérée comme un “hotspot” du changement climatique (The MerMex Group, 2011). C'est l'un des écosystèmes marins les plus vulnérables à l'activité humaine et ce dernier est extrêmement sensible aux changements environnementaux (Williams, 1998). Les projections des modèles climatiques ont prédit une diminution des précipitations, l'assèchement des surfaces continentales et une augmentation de l'évaporation en mer ainsi que de son réchauffement au cours du 21ème siècle avec des modifications des formations des masses d'eau, de la circulation thermohaline méditerranéenne et du climat de la mer (Somot et al., 2006; Giorgi and Lionello, 2008; Diffenbaugh and Scherer, 2011).

En raison de son importance socio-économique (Randone et al., 2017), la mer Méditerranée subit une forte pression anthropique compte tenu de l'afflux important de tourisme, qui couvre 1/3 du tourisme mondial, en plus d'être une zone très peuplée (512 millions de personnes (UNEP, 2020)). Ces pressions sont problématiques pour les écosystèmes, il est donc important de comprendre et d'essayer d'anticiper les changements induits afin de proposer des solutions efficaces.

Enfin, la Méditerranée possède une biodiversité d'écosystèmes marins représentant 0.7 % de l'océan mondial, confinés dans une très petite zone. Elle rassemble la plupart des mécanismes dynamiques de l'océan global, ainsi que des régimes trophiques allant du régime de “bloom” à celui de l'oligotrophie ,“no bloom” (D'Ortenzio and Ribera d'Alcalà, 2009). Son étude peut ainsi permettre de mieux comprendre le fonctionnement biogéochimique d'une large variété de régions océaniques. Les conditions atmosphériques et hydrodynamiques qui lui sont associées génèrent des caractéristiques physiques et biogéochimiques très variables, et ce à des échelles spatiales et temporelles variées. La mer Méditerranée représente également un cadre idéal pour la modélisation, puisqu'elle permet de modéliser l'ensemble du bassin à haute résolution, à un coût de calcul raisonnable.

Les enjeux scientifiques

Des études antérieures ont mis en évidence la caractéristique unique de la Méditerranée orientale en tant que «bassin laboratoire» d'écosystèmes contrastés (Malanotte-Rizzoli and Eremeev, 1999) depuis l'extrême eutrophie (Nord Adriatique) à l'extrême oligotrophie (bassin Levantin), et allant des systèmes dominés par les apports fluviaux (Nord Adriatique) aux systèmes forcés par le vent et les formations d'eau dense (bassin Levantin). Ce bassin ultra-oligotrophe possède une production primaire correspondant à la moitié de celle de la mer des Sargasses (Krom et al., 2003). Les concentrations de nutriments dans ses eaux profondes sont les plus basses mesurées dans le fond des océans, même si ce bassin reçoit des apports de nutriments atmosphériques et fluviaux. Les faibles concentrations de nutriments résultent de la combinaison d'une circulation anti-estuarienne et de l'âge relativement jeune des masses d'eau. Le rapport N:P dans les eaux profondes (28:1) de ce bassin est également atypique, environ le double du rapport de Redfield (16:1, Krom et al., 1991). Ces propriétés inhabituelles en font un laboratoire naturel idéal pour examiner les cycles des nutriments et les processus liés à l'absorption du carbone dans l'océan.

Cette thèse se concentre sur le bassin Levantine l'un des principaux bassins de la Méditerranée orientale et le siège de la zone de formation des Eaux Levantines Intermédiaires (LIW pour Levantine Intermediate Water). Des études ont montré le rôle crucial de la LIW dans la formation des eaux profondes méditerranéennes pour les bassins est et ouest (Skliris and Lascaratos, 2004). Cette eau se forme principalement dans le Gyre de Rhodes pendant l'hiver (Lascaratos et al., 1993), avec un taux de formation proche du flux d'eau Atlantique entrant au détroit de Gibraltar.

La plupart de nos connaissances sur la LIW proviennent des observations du groupe POEM dans les années 80-90. Le projet d'observation a tenté de représenter la circulation de la Méditerranée orientale (Özsoy et al., 1989, 1993; Robinson et al., 1991; The POEM group, 1992; Robinson and Golnaraghi, 1993b; Malanotte-Rizzoli et al., 1997). Néanmoins, de nombreuses questions demeurent après POEM et nécessitent des études plus approfondies. Des lacunes d'observation et de modélisation existent encore sur la formation et la dispersion des LIW et sur leur rôle dans les cycles biogéochimiques du bassin Levantin.

Nous posons ici les principales questions scientifiques concernant la dynamique de la LIW:
Tout d'abord, **les zones de formation LIW**: on suppose généralement que la LIW se forme dans le Gyre de Rhodes (Lascaratos et al., 1993) contrôlé par le préconditionnement de ce gyre cyclonique (Nittis and Lascaratos, 1998). Toutefois, d'autres zones de formation ont également été proposées comme le bassin d'Antalya (Sur et al., 1993; Kubin et al., 2019; Fach et al., 2021) et le tourbillon de Chypre (Moutin and Prieur, 2012). Même si le Gyre de Rhodes semble jouer un rôle primordial dans la formation de la LIW, une étude complète de la formation des LIW dans les zones côtières et du large manque encore.
D'autre part, **les facteurs à l'origine de la formation de la LIW**, tels que la variabilité interannuelle des flux air-mer ou l'inversion de la circulation dans le gyre nord-Ionien modifiant les propriétés physiques de la LIW, pourraient avoir des conséquences sur les processus biogéochimiques (Ozer et al., 2016, 2022). La compréhension limitée de la dynamique de la

LIW suggère également des lacunes dans la compréhension des cycles biogéochimiques du bassin Levantin.

Au titre de ces lacunes:

La caractéristique oligotrophe du bassin levantin. Elle est vraisemblablement due à la présence de la LIW et à son temps de séjour (Crispi et al., 2001; Moutin and Prieur, 2012). En fait, la LIW recueille la matière organique provenant de la production biologique de surface et le transporte vers l'ouest aux dépens du stock profond de nutriments dans le bassin oriental.

Le rapport stoechiométrique inhabituel par rapport aux autres provinces océaniques caractérise le bassin oriental (Ribera d'Alcalà et al., 2003; Krom et al., 2005) induisant des effets biologiques partiellement compris. La LIW pourrait façonner la distribution des nutriments le long de la colonne d'eau, par exemple, la position de la nutricline suit le gradient ouest-est d'oligotrophie (Pujo-Pay et al., 2011) avec la partie supérieur de la phosphacline coïncidant avec celle de la couche LIW (Van Cappellen et al., 2014). L'évolution des caractéristiques hydrodynamiques et biogéochimiques de la LIW le long de son chemin vers l'Atlantique influencent également la distribution des nutriments.

Le régime trophique dans le bassin levantin. Ce bassin est composé d'un régime de bloom (croissance phytoplanctonique rapide en surface après la période de mélange hivernal) intermittent au niveau du Gyre de Rhodes et d'un régime "no bloom" (croissance phytoplanctonique continue et modérée pendant la période de mélange hivernal) pour la zone environnante. Le Gyre de Rhodes se caractérise par une production primaire nettement plus importante que dans la zone environnante du bassin Levantin (D'Ortenzio et al., 2003). L'augmentation de la chlorophylle est supposée être liée au mélange vertical associé à la formation d'eau dense (Yilmaz et al., 1994; Ediger and Yilmaz, 1996). Sa production primaire élevée en fait une zone de grand intérêt pour l'étude du cycle du carbone. Cependant, Mayot et al. (2016) ont détecté une occurrence alternée entre les régimes intermittent, de bloom et de no bloom dans le Gyre de Rhodes. Cette alternance n'a pas été expliquée, soulignant la nécessité de comprendre les mécanismes sous-jacents et d'évaluer si les futurs changements climatiques favoriseront l'oligotrophie du bassin.

Enfin, **les études de la diversité procaryote et eucaryote dans le bassin oriental** dans le bassin oriental sont rares, on en sait très peu sur la régulation des cycles biogéochimiques par ces communautés. De plus, la nature et le devenir du carbone organique dissous (DOC pour Dissolved Organic Carbon) produit dans la couche euphotique en Méditerranée orientale sont encore mal caractérisés. En fait, Santinelli et al. (2015) a signalé une élimination du DOC dans la LIW en raison de la reminéralisation et de l'exportation de DOC semi-labile au cours du trajet de la LIW du bassin Levantin au Détroit de Sicile.

Bien que le bassin levantin joue un rôle crucial dans la mer Méditerranée, il est encore extrêmement sous-échantillonné et limitée en études de modélisation. Ce travail de thèse s'inscrit dans le cadre du projet PERLE (Réponse de l'écosystème pélagique à la formation d'eau dense dans l'expérience du Levant) du programme MERMEX-MISTRALS. Ce projet vise à mieux comprendre la formation et la dispersion de le LIW et leur influence sur la distribution des nutriments et l'écosystème pélagique grâce à un travail de terrain intensif. Le travail effectué dans le cadre de cette thèse a couvert un objectif supplémentaire du projet qui est l'amélioration des performances de la modèlisation à travers l'implémentant d'un modèle biogéochimique couplé à un modèle hydrodynamique et en le validant avec les données collectées.

Objectifs et structure du manuscrit

Dans le cadre des questions ci-dessus, l'objectif de ma thèse est d'étudier l'impact de la formation de la LIW sur la variabilité de l'écosystème planctonique et des cycles biogéochimiques dans le bassin Levantin, en se basant sur un modèle régional 3D physique couplé à la biogéochimie.
Cet axe a été divisé en quatre objectifs de recherche :

1. Le premier objectif est de mettre en œuvre le modèle couplé dans le bassin Levantin. L'attention a été portée sur l'initialisation des nutriments, de l'oxygène dissous et de la chlorophylle dans ce bassin, en plus des différentes régions de la mer Méditerranée: les bassins ouest et est communiquent en effet par le détroit de Sicile et s'influencent mutuellement.
2. Le deuxième objectif est une validation détaillée du modèle biogéochimique.
3. Le troisième objectif est d'étudier l'impact des formations d'eau dense sur le cycle annuel des nutriments et l'écosystème planctonique. Nous quantifions le bilan de carbone organique dans le Gyre de Rhodes, la région la plus productive du bassin Levantin, d'un point de vue biologique.
4. Enfin, le dernier objectif est d'analyser l'impact de la formation de LIW sur le bilan d'oxygène dissous dans le bassin levantin.

Ce manuscrit est composé de six chapitres :

- → Le chapitre 1 détaille les connaissances nécessaires pour aborder les résultats présentés dans cette thèse. Il apporte une revue des caractéristiques hydrodynamiques et biogéochimiques générales de la mer Méditerranée, il couvre également l'état de l'art de la modélisation en mettant l'accent sur le bassin Levantin.
- → Le chapitre 2 décrit les modèles couplés hydrodynamique - biogéochimique Symphonie - Eco3M-s et les jeux de données utilisés pour valider ces derniers.
- → Le chapitre 3 est consacré à l'évaluation des performances des modèles en le comparant à plusieurs ensembles de données d'observation: les images satellites, les flotteurs et les campagnes en mer.
- → Le chapitre 4 est basé sur un article soumis portant sur la modélisation de la dynamique du carbone organique dans le Gyre de Rhodes, site majeur de formation de la LIW. Nous y analysons la variabilité saisonnière et interannuelle des nutriments et de l'écosystème planctonique. Les différents processus contribuant au budget de carbone sont également analysés.

→ Le chapitre 5 étudie la variabilité saisonnière et interannuelle du cycle de l'oxygène dans le bassin levantin, ses échanges avec les bassins voisins dans les couches superficielle et intermédiaire.

→ Enfin, le chapitre 6 résume les principaux résultats trouvés au cours de cette thèse et présente les perspectives.

L'annexe est composée de comparaisons détaillées entre les sorties du modèle et les observations afin d'évaluer le modèle biogéochimique. Il présente également les paramètres du modèle biogéochimique et son initialisation.

Chapter 1

The Mediterranean Sea

Contents

1.1 Hydrodynamic of the Mediterranean Sea

1.1.1 The Mediterranean Sea

1.1.1.1 General overview

The Mediterranean is a marginal sea composed of two sub-basins: the western and the eastern connected together by the Sicily Strait. It also communicates with the Atlantic Ocean via the strait of Gibraltar. The Sicily Strait plays a major role in the hydrological and biological distinctions between these two sub-basins. Both of these straits are shallow, the Sicily Strait is approximately 400 m depth and the Gibraltar Strait is about 300 m depth at the Camarinal Sill.

1.1.1.2 Circulation

The semi-enclosed Mediterranean Sea is identified as an evaporation basin, where the high evaporation rate exceeds the river's runoffs and precipitation. It loses up to 0.6 m of water per year at the sea surface that is compensated by river discharge and net water inflow from the Atlantic Ocean through the Gibraltar Strait, as well as from the Black Sea through the Dardanelles Strait (Sanchez-Gomez et al., 2011). Along its course and following the evaporation episodes, the Atlantic Water (AW) loses heat and gains salinity. Therefore, its physical characteristics are modified and it gradually becomes part of the *Mediterranean Water* (MW). Warm, less salty water (compared to the MW) is transformed into cold, salty, and then dense water in different places of the basin. First of all, the Levantine Intermediate Water is formed in the east of the basin. This water mass constitutes an important part of the outflow in Gibraltar which is also an important source of the warming at mid-depth observed in the past fifty years in the North Atlantic (Potter and Lozier, 2004). This type of circulation, with a surface inflow in the surface and an export of waters at depth, is qualified as anti-estuarine (Hecht et al., 1988; Menna et al., 2012). It forms the zonal thermohaline circulation cell of the Mediterranean that connects the two basins.

Figure 1.1 shows the general circulation with the primary open circulation cell dominating the basin from the west to the east and the two secondary closed cells. The primary cell is open to the Atlantic Ocean and thus is controlled by the inflow and the outflow in the Gibraltar strait. It transforms Atlantic less saline, cold water (compared to the Mediterranean water) into more saline and warm water, the LIW. The secondary cells within the Mediterranean basin where *Western Mediterranean Deep Water* (WMDW) and *Eastern Mediterranean Deep Water* (EMDW) are formed, are oriented from the north to the south. During the *Eastern Mediterranean Transient* (EMT) at the end of the 80s, the secondary closed cell shifted from the Adriatic to the Aegean, where the Eastern Mediterranean deep water was formed for a few years.

The surface circulation is also a branch of two internal meridional cells of deep circulation, "the Mediterranean Conveyor Belts" managed by the deep water formation in the eastern and the western basins (Fusco et al., 2003). The latter is generated in the Gulf of Lion and the former in the southern Adriatic Sea (Roether and Schlitzer, 1991) or in the Aegean Sea

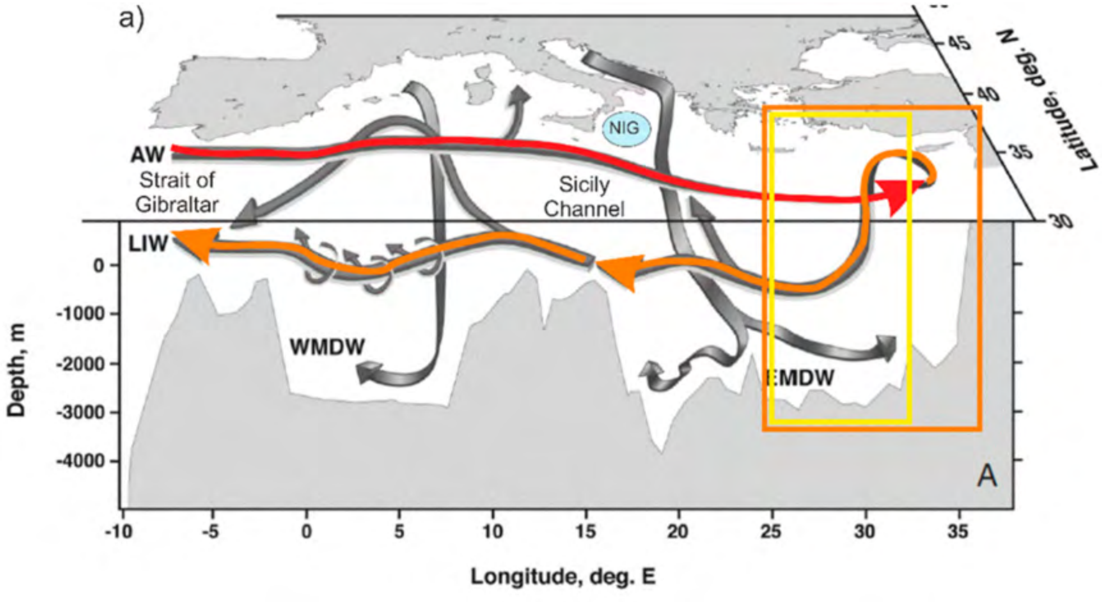

Figure 1.1: The thermohaline circulation in the Mediterranean Sea (Kubin et al., 2019).

(Lascaratos et al., 1999).

1.1.2 The eastern Mediterranean

1.1.2.1 Localisation and topography

Located on the eastern side of the Sicily Strait, the Eastern Mediterranean is composed of 4 discernible sub-basins (Fig. 1.2). The Adriatic and the Ionian are connected through the strait of Otranto which has a vertical extent of 800 m. The Aegean and Ionian seas communicate through different shallow straits west of the Cretan arc, notably the Antikythira and the Kythira straits. The Ionian Sea is divided into two sub-basins: the south Ionian and the north Ionian. This division is due to the presence of a series of seamounts extending from the southeast of Sicily to the Libyan coast. The eastern limits are occupied by the Levantine Basin. It is the second-largest basin of the eastern Mediterranean. The Levantine Basin is surrounded by the Middle East coast in the east, in the north by the Minor Asian coast, and in the south by the African continent (Fig. 1.9). This basin possesses a volume of 7.5 x 10^5 km^3 and a 4300 m maximum depth, the mean depth is between 2000 – 3000 m (Akpinar et al., 2016). It is divided into 5 sub-basins: the Rhodes basin which is the deepest basin reaching 4000 m depth including part of the Hellenic Trench, the Antalya basin (2500 m), the Cilicia basin (1000 m), the Lattakian basin (1500 m) and the Herodotus abyssal plain with a 3500 m depth in the southwestern part of the basin. As for other bathymetric elements present, we can cite the Anaximander seamounts between Rhodes and Antalya, and the Eratosthenes seamount south of Cyprus (or Cyprus). Straits between the islands forming the East Cretan Arc (Rhodes, Karpathos, Kasos, and Crete) bind the Levantine Basin with the Aegean Basin. The Aegean Basin is connected to the Black Sea by the Dardanelles Strait, the Marmara Sea, and the Bosphorus Strait (Özsoy et al., 1989, 1991, 1993) and to the Levantine Basin through the eastern straits of Crete.

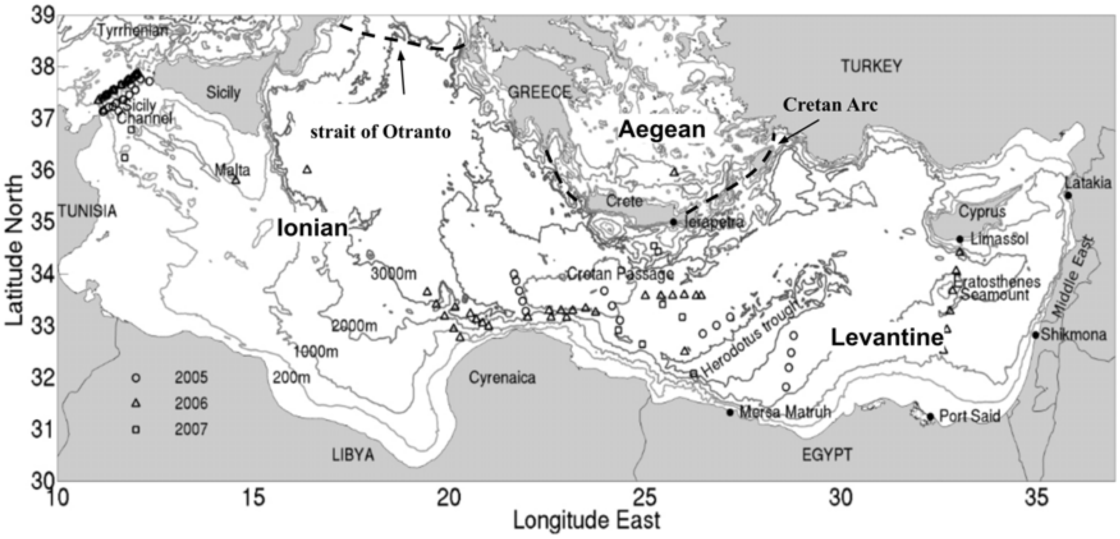

Figure 1.2: Topography and geography of the Eastern Mediterranean (Gerin et al., 2009).

1.1.2.2 Wind patterns

The eastern basin is surrounded by chains of mountains, their configuration has a significant effect on the wind patterns. The reliefs (for example Mount Taurus in Turkey (3920 m); Mount Lebanon in Lebanon (3090 m)) favor the creation of regional winds and consequently influence the precipitation and the temperature regime in the basin (Somot, 2005). Among the regional winds created in response to these constraints (Fig. 1.3) from the north, the Bora blowing from the Alps on the Adriatic and the Etesians (also called Meltemi) in the Aegean sub-basin. Several regional winds blow from Africa: the Sirocco blowing from the Sahara, the Chlouk also called Khamsin from Egypt and the Ghibli from Libya. The Etesians are annual recurring summer winds usually dry and rather cool blowing over large parts of Greece, the Aegean Sea, and the eastern Mediterranean. The Khamsin wind is a dry, dusty, and hot desert wind, generally southerly or southeasterly. They occur in spring and are preceded by a heat wave. The Khamsin and the Ghibli winds are extensions of the Sirocco wind (Reiter, 1975).

1.1.2.3 The basin circulation

The eastern Mediterranean Sea circulation is complex because of the different places of water mass formation (compared to the western basin), the topography (presence of straits and numerous islands), and forcings (the regional winds). The thermohaline circulation is composed of two cells linked to the intermediate/deep water formation in the Levantine and the Adriatic, respectively (Fig. 1.4A). The sub-basin scale is characterized by the presence of permanent and semi-permanent gyres related to the wind curl and bounded by jets and meandering currents following the continental slope (Fig. 1.4B). These currents seasonally produce mesoscale meanders, especially along the African coast.

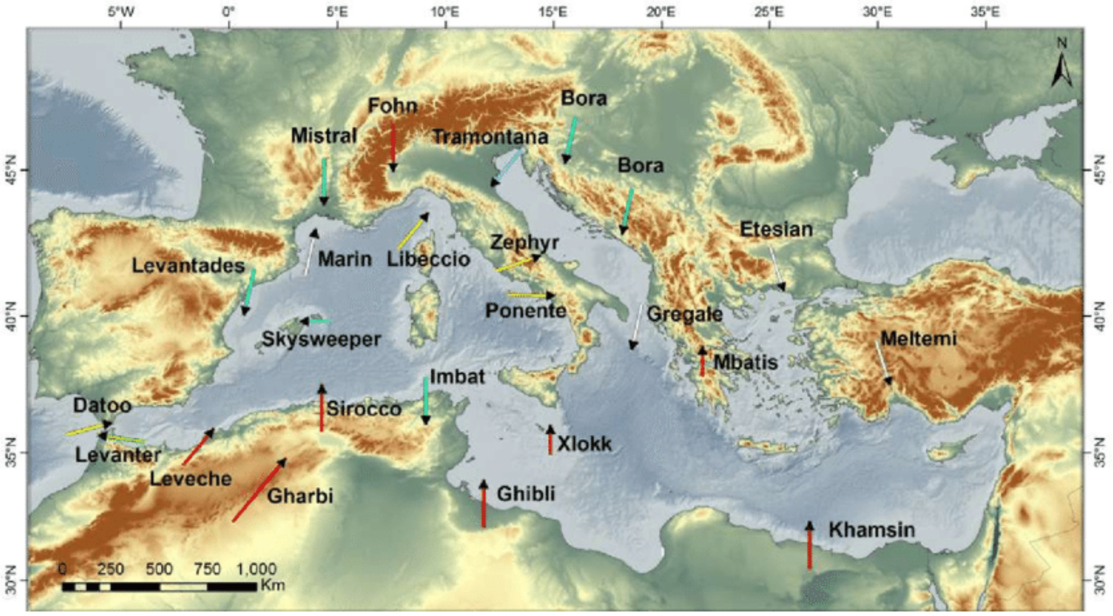

Figure 1.3: Local Mediterranean winds extracted from Boero et al. (2016)

The surface Circulation

Different controversial descriptions were elaborated to delineate the general circulation in the eastern basin. The first description of the circulation was conducted in 1912, in which Nielsen (1912) presented the circulation in the eastern basin as cyclonic along the coast of the basin controlled by the Coriolis force. This current enters the Levantine Basin along Libya through the passage of Crete and then follows the African coast, it then moves to the north and runs west along Asia Minor and Greece passing through the Aegean Sea to descend into the Ionian Basin and flowing into the Adriatic.

Multiple studies were conducted between 1960-1975 on this circulation (Wüst, 1961; Ovchinnikov, 1966; Lacombe, 1972). Ovchinnikov (1966) presented a new eastern circulation with different gyres. Entering the eastern basin, the Atlantic Water contributes to the formation of two gyres in the Ionian basin, an anticyclonic gyre in the south and a cyclonic one in the north. A large cyclonic gyre occupies the area between the islands of Crete, Cyprus, and Rhodes: the Rhodes Gyre. Two additional gyres in the Levantine Basin were mentioned for the first time, a permanent anticyclone in the Mersa-Matruh area (MMA) and a cyclone in the Shikmona area.

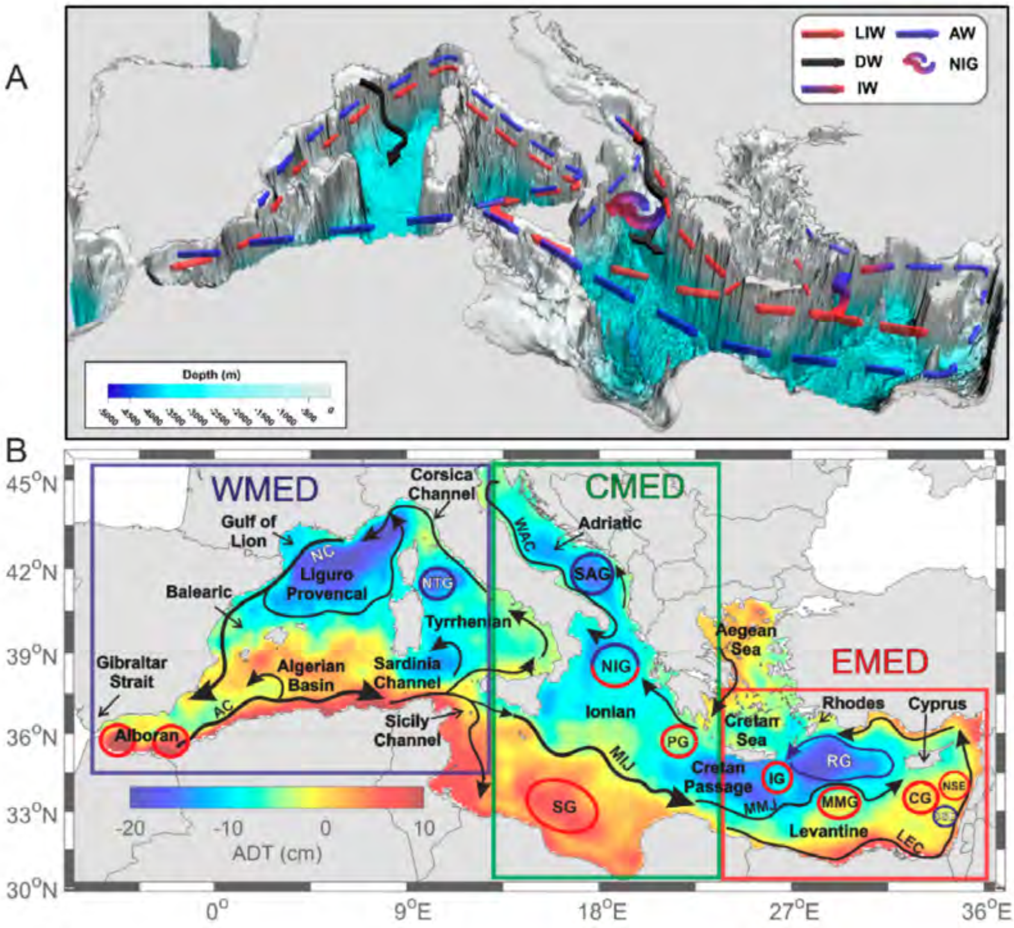

Figure 1.4: (A) The thermohaline circulation in the Mediterranean Sea (Intermediate and deep water formation are only present), (B) a schematic representation of the main currents and circulation structures in red and blue; geographical extension of the three main sub-basins (WMED, CMED, and EMED). Acronyms: AW, Atlantic Water; LIW, Levantine Intermediate Water; DW, dense water; IW, Intermediate Water; NIG, Northern Ionian Gyre; AC, Algerian Current; NC, Northern Current; NTG, Northern Tyrrhenian Gyre; SG, Sidra Gyre; MIJ, Mid-Ionian-Jet; SAG, Southern Adriatic Gyre; WAC, Western Adriatic Current; PG, Pelops Gyre; MMJ, Mid-Mediterranean Jet; LEC, Libyo-Egyptian Current; IG, Ierapetra Gyre;RG, Rhodes Gyre; MMG, Mersa-Matruh Gyre; CG, Cyprus Gyre; SSE, South Shikmona Eddy; and NSE, North Shikmona Eddy (Menna et al., 2022)

The circulation studies of the eastern basin were limited and dispersed in time until the *Physical Oceanography of the Eastern Mediterranean* (POEM) program was carried out where stations were surveyed regularly between 1985 and 1987. These observations supported the idea of a general circulation controlled by a “sub-basin scale gyre connected by jets” (Robinson et al., 1991; The POEM group, 1992; Robinson and Golnaraghi, 1993a). They differentiated three permanent gyres: the Cretan Gyre, the West Cyprus Gyre, and the Rhodes Gyre and jets contributing to this circulation: the Atlantic Ionian Stream (AIS), the Mid Ionian Jet (MIJ), the Mid Mediterranean Jet (MMJ), and the Asia Minor Current AMC. The Atlantic

Water entering the Ionian basin forms the MIJ and then continues towards the Levantine Basin forming the MMJ without interacting with the south part of the basin, it moves from the southwest to the northeast to meet the AMC north. The southern Levantine is an anticyclonic high-pressure region with a current flowing from the northeast to the southwest. The described circulation is shown in Fig. 1.5a.

Later on, a description of the eastern circulation based on sea surface temperature images (Hamad et al., 2005, 2006) was suggested (Fig. 1.5b). The eastern basin possesses a cyclonic along-slope circulation with the western basin being a transitional basin for the Atlantic Water. This current is stable except along the libyo-egyptian slope where energetic anticyclonic eddies are formed. These eddies are trapped in the Herodotus Trough. When they separate they release AW rejoining the along slope current Millot and Taupier-Letage (2005). The instabilities continue from the Nile up to the Middle East, with small eddies formation. This might be the result of shallower topography along this region. The surface water then continues its cyclonic course with the Asia Minor Current following the Turkish coast. This current then is divided into two veins: a northwestern vein and a southwestern vein. The first one circulates along the Turkish coast and enters the Aegean Sea. It separates into two sub veins, the first enters the northern Aegean whereas the second: the southern Aegean where it plays an important role in the formation of the deep and Intermediate Aegean water. The northern sub-vein mixes with the Black Sea outflow. Then the modified AW leaves the Aegean through the West Cretan Arc. The southwestern vein moves along the Arc up to Crete, it is associated with the formation of Levantine Intermediate Water in winter. This vein forms the northern branch of the cyclonic eastern gyre.

Following Millot and Taupier-Letage (2005), the southwestern vein never leaves the Levantine Basin during summer, this means that most of the Atlantic Water retreat from the Levantine Basin through the Aegean Sea via the west arc of Crete. On the contrary, in summer, Estournel et al. (2021) found a westward current that breaks away from the eastern gyre and skirts Crete to the south. In the Levantine Basin, the surface AW becomes Levantine Surface Water (LSW) by gaining heat and salt and moves then into the Ionian either via the Aegean or by skirting Crete to the south. It bifurcates into two veins, one moves into the Adriatic sea and contributes to the formation of the Adriatic Deep Water in the southern part or North Adriatic dense water in the northern part, whereas the remainder moves west towards Sicily Strait.

The along-slope cyclonic current found by Millot and Taupier-Letage (2005) was confirmed by Menna et al. (2012) and Estournel et al. (2021) whereas the presence of the Mid Mediterranean Jet of Robinson and Golnaraghi (1993a)(see Fig 1.5a) was also validated by Poulain et al. (2012); Menna et al. (2012); Mauri et al. (2019) and Menna et al. (2020). It should be noted that Millot and Taupier-Letage (2005)did not distinguish the Mid Mediterranean Jet, they characterized it as being a northern projection of the anticyclonic eddies caused by the instabilities of the Libyo-Egyptian current via a paddle-wheel effect.

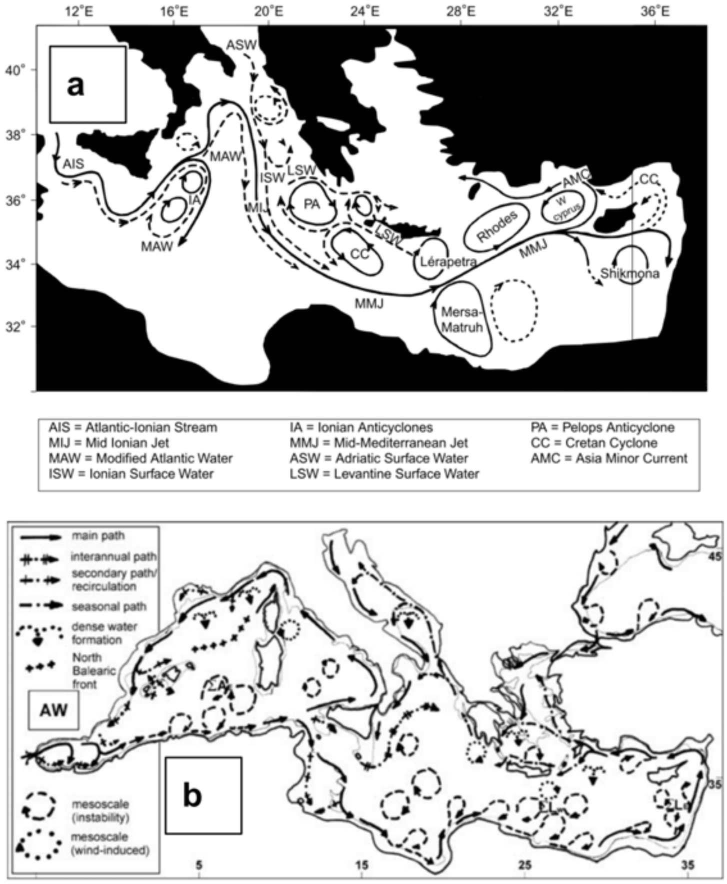

Figure 1.5: Schematic of the surface circulation in the eastern basin extracted from (a) Robinson et al. (2001) based on Robinson and Golnaraghi (1993a), and (b) Millot and Taupier-Letage (2005).

The intermediate circulation

Several areas and processes have been hypothesized for the formation of the LIW (developed in the following sections). The LIW is one of the saltiest and warmest waters in the Mediterranean Sea produced in high volume (Millot and Taupier-Letage, 2005). The circulation of intermediate water resembles what was presented earlier for surface water with some differences. The intermediate water moves cyclonically in the eastern basin, the differences lie in the north of the basin and in the Aegean Sea. The penetration of LIW is almost limited to the southern part of the Aegean because of the complex topography between the southern and the northern Aegean Sea. Part of the Levantine Intermediate Water passes through the sills in the south Aegean where it mixes with the surface water during winter and contributes to the formation of the Aegean Deep Water. The Levantine Intermediate Water does not flow in its integrality through the sills of the Cretan Arc because of the tight openings. Part of the LIW then flows westward along the southern slope of Crete. It is then eventually dragged by the Ierapetra and the Pelops anticyclones and then flows along the northeast coast of the Ionian and then towards the southern Adriatic where it mixes with surface water to contribute to the formation of dense water in winter.

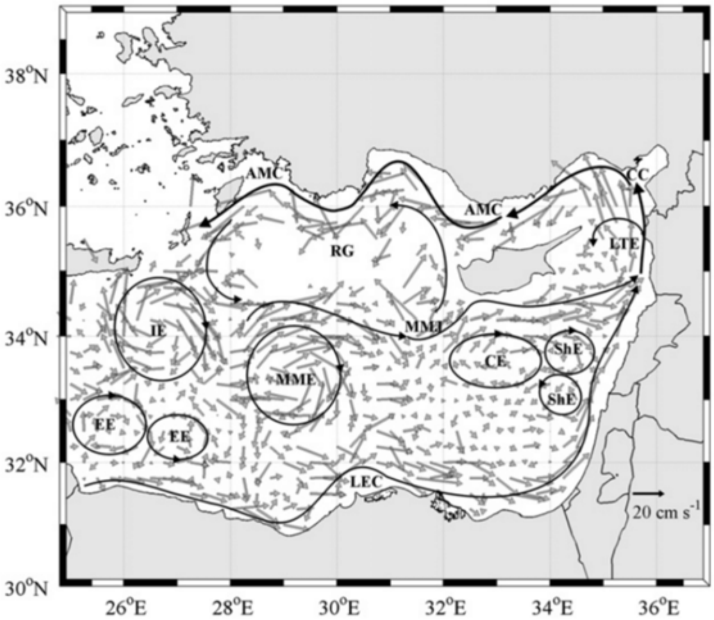

Figure 1.6: Main currents, Eddies and Gyre in the Levantine Basin. The gray arrows represent the Pseudo-Eulerian mean velocity field for the period 1992–2010 (Menna et al., 2012) AMC: Asia Minor Current, CC: Cilician Current, LEC: Libyo-Egyptian Current, MMJ: Mid-Mediterranean jet, IE: Ierapetra Eddy, EE: Egyptian eddies, MME: Mersa-Matruh Eddy ShE: Shikmona Eddy, CE: Cyprus Eddy, LTE: Latakia Eddy,RG: Rhodes Gyre.

The deep circulation

The main water masses involved in the deep circulation are the Aegean Deep Water (AeDW) and the Adriatic Deep Water (AdDW), together they form the Eastern Mediterranean Deep Water. The Aegean sea possesses both saltier and warmer surface and intermediate waters than the Adriatic which explains why AeDW is saltier and warmer compared to the AdDW. These two water masses are found in deep depressions in the Aegean (for AeDW) and the southern Adriatic (for AdDW) before outflowing to the different basins of the Eastern Mediterranean Sea. They flow into the northern Levantine, the northern Cretan, and the northern Ionian (Millot and Taupier-Letage, 2005). They cascade along the slope and follow a cyclonic path in the deep eastern basin.

The circulation characteristics at different scales

The Levantine Basin is controlled by the interaction of large-scale currents (the Libyo-Egyptian Current, the Asia Minor Current), a cyclonic gyre (the Rhodes Gyre), and numerous more or less permanent mesoscale structures: the Ierapetra, Anaximander, Antalya, Mersa Matruh, Cyprus, and Shikmona eddies... (Fig. 1.6). The main gyre in the Levantine Basin is the cyclonic Rhodes Gyre.

The Rhodes Gyre is a cyclonic gyre that dominates the area between Crete and Cyprus (Anati, 1984; Özsoy et al., 1993). With a 300 km of diameter, it is located in the southeast of Rhodes. On its outer limits, various anticyclonic eddies are present. This gyre is delimited in the north by the Asia Minor Current according to Theocharis et al. (1993). On the other hand,Robinson et al. (1991) mentioned the gyre being delineated by the Mediterranean Mid Jet. The Rhodes Gyre is driven by various factors: the bathymetry of the Rhodes basin (4200 m), and the surface heat fluxes (Sur et al., 1993). This gyre defines the formation zone of the LIW. During winter, the water present in the center of the gyre loses heat and thus becomes cold. This results in an increase in its density. The water mass then descends layers, with the same density, towards the periphery of the gyre. Cooling and upwelling episodes in this gyre lead to convective overturning and therefore the formation of dense water (Lascaratos et al., 1993).

1.1.2.4 The circulation variability

The interannual and internal variability

An essential key point for the interannual variability of the surface and intermediate waters circulation is the reversal of the circulation of the North Ionian Gyre (NIG), also defined as the Adriatic-Ionian Bimodal Oscillating system – BiOS thoroughly described in Gačić et al. (2010, 2011). The gyre alternates between a cyclonic and an anticyclonic circulation and was mentioned in various studies (Civitarese et al., 2010; Theocharis et al., 2014; Ozer et al., 2016). When the NIG is in a cyclonic period (Fig 1.7b) the modified AW moves from the south Ionian towards the Levantine Basin whereas high salinity LIW is injected into the south Adriatic which might favor the formation of the Adriatic Deep Water (Gačić et al., 2010, 2011). In periods of anticyclonic NIG (Fig 1.7a), the AW is advected in the northern Ionian and the Adriatic, at the expense of the Levantine Basin, limiting the formation of the AdDW. This explains the increase in the salinity of the Surface and Intermediate Levantine waters (Gačić et al., 2011). Ozer et al. (2016)found that the BiOS mechanism has a direct impact on the concentration of chlorophyll and the nutrients available in the eastern basin. Therefore, the circulation presents different schematizations depending on the direction of the NIG. In addition, the Eastern Mediterranean is characterized by an interannual variability due to the wind and the surface heat flux (Pinardi et al., 1997) and related to mesoscale variability. For example, the LIW formed in the Rhodes gyre and its peripheries can be limited by the presence of three lobes of southern anticyclones in the Levantine Basin (Malanotte-Rizzoli et al., 1999; Kress et al., 2003).

Seasonal circulation of surface water

The circulation in the surface layer possesses a high seasonal variability in the Levantine Basin (Estournel et al., 2021) as illustrated in Figure 1.8. The general circulation in the basin is cyclonic along-slope, unstable during summer (Hamad et al., 2006)favoring the presence of anticyclonic eddies in the south, and more intense and stable during winter. Another difference lies in the extreme east of the basin, where the current flows near the shores of the Middle East during summer whereas, during winter, it flows above the 1000 m isobath. The water exiting the basin flows towards the Aegean during winter through the eastern straits: Rhodes and Karpathos straits as was mentioned by Millot and Taupier-Letage (2005); Hamad et al. (2006); Estournel et al. (2021) while in the summer, the water exits along the southern slope of Crete.

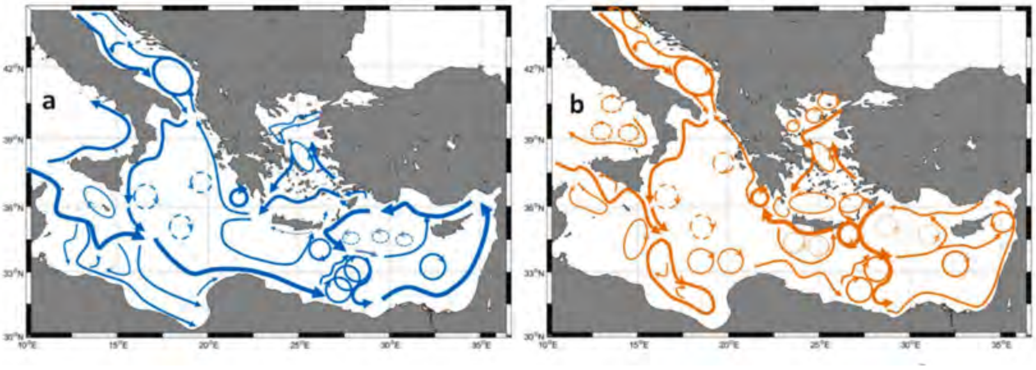

Figure 1.8: Seasonal simulated circulation of the surface water (a) for winter, (b) summer (Estournel et al., 2021)

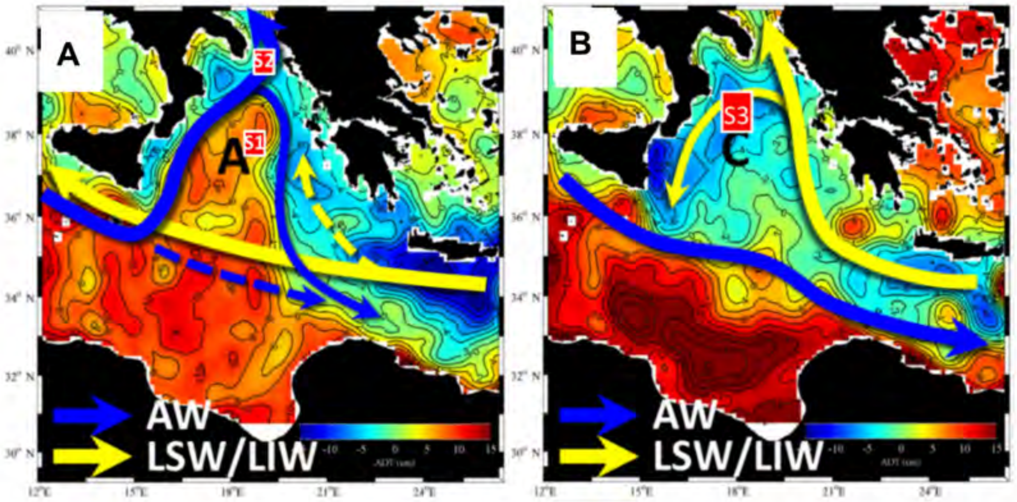

Figure 1.7: Schematic representation of the north Ionian gyre upper-layer circulation during anticyclonic (a) and cyclonic (b) regimes (Menna et al., 2018). AW, LSW and LIW refer to Atlantic Water, Levantine Surface Water, and Levantine Intermediate Water, respectively

Seasonal circulation of the Levantine Intermediate Water

The literature did not mention the seasonality of the circulation of the LIW, except Estournel et al. (2021) based on modeling. Those authors show that during winter the intermediate current is cyclonic and along-slope in the Levantine Basin, similar to the surface circulation. The Rhodes Gyre ensures the dispersion of the Intermediate water. During summer, the cyclonic circulation is broken and there is an inversion in the Middle East circulation, the anticyclonic circulation occupying the southeast, redistributes the intermediate water southwards. The intermediate water exits the basin as was described for the surface water.

1.1.3 The Levantine Basin

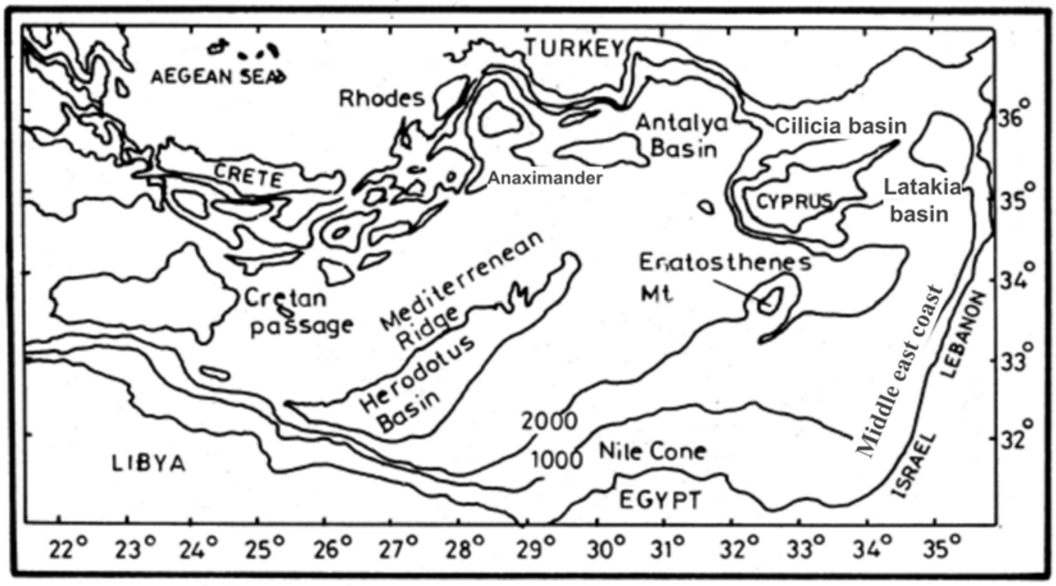

Figure 1.9: Topography and geography of the Levantine Basin (Özsoy et al., 1989)

1.1.3.1 The water masses

Hydrological studies showed the existence of 3 permanent water masses in the Levantine Basin: the Levantine Surface Water (LSW), the Levantine Intermediate Water (LIW), and the Eastern Mediterranean Deep Water (EMDW). Nevertheless, multiple studies divided the surface waters into two different water masses with different characteristics: the LSW and the Atlantic Water (AW). The different characteristics of each of the water masses (Fig. 1.10) in the Levantine Basin are as follows:

(i) LSW:
These waters form the shallow summer mixed layer. They are easily distinguished by their high temperature (> 25°C) and maximum salinity (> 39) induced by the strong warming and evaporation taking place in this basin. They occupy the first 30's m. Their density is lower than 27.5 kg m^{-3} (Manca et al., 2004).

(ii) AW:
Located under the LSW, Atlantic Waters are identified by salinities lower than 39 in the Levantine Basin. They correspond to the layer located between 40 and 100 m during the stratified period.

(iii) LIW:
The LIW is generally between 100 and 400 m in the eastern basin with a core at 200 m in the Levantine, easily discernible by its maximum salinity between 39 and 39.2. Its potential temperature is between 15 and 17 °C for the density it varies between 28.85 and 29.0 kg m^{-3} in the Levantine Basin (Ozer et al., 2016). For example, Cardin et al. (2015) found a maximum salinity of 39.24 in 2011 analyzing the Meteor Campaign and CTD

(Conductivity, Temperature, and Depth) data. As for Kress et al. (2003), the core of the LIW was determined with a maximum salinity of 39.07 and a potential temperature range between 15 and 16.5 °C. When moving to the west, salinity and temperature of LIW decrease because of its mixing with the AW in the surface, and deep waters in the deep. The LIW is identifiable all over the Mediterranean Sea with its maximum salinity. While flowing westward, it loses its physical characteristics gradually due to its dilution with other water masses. Flowing out of the Sicily Strait, it possesses a maximum temperature of 14.86 °C and a salinity of 38.9 (Schroeder et al., 2017). It then flows into the Tyrrhenian Basin, reaching the northwestern Mediterranean. Margirier et al. (2020) reported an LIW temperature of 13.2°C and 38.52 for the salinity in the Gulf of Lions during 2009 - 2013. This Mediterranean water is the main component of the outflow at Gibraltar.

(iv) Transitional Mediterranean Water:
This water is located between the LIW and the *Deep Water* (DW) with intermediary features. It corresponds to deep water present before the Eastern Mediterranean Transient (EMT) which was replaced by the dense Aegean outflow produced during the EMT (early 90s), and uplifted to layers of about 300–1800 m in depth (Velaoras et al., 2015).

(v) EMDW
This water mass is at equilibrium at depths that are higher than 1000 m. Before the EMT, it was characterized by high density (> 29.15 kg m^{-3}), low salinity (38.7), and temperature (13.5 °C). The Adriatic basin was the main source of this water (Wüst, 1961; Sur et al., 1993; Malanotte-Rizzoli et al., 1997). During the EMT, the thermohaline properties in the eastern Mediterranean were modified by the formation of very dense water in the Aegean (T=13.9–14.1 °C, and S=38.78–38.86). Malanotte-Rizzoli et al. (2003) mentioned the presence of an additional water mass: the Levantine deep water (LDW), this water is formed in the Rhodes region and is denser than the LIW, it is located between the LIW and the DW. It is identified by its temperature of around 13.7 -14 °C, the salinity of S=38.7, and density of 29.15 kg m^{-3}.

1.1.3.2 The formation of the Levantine Intermediate Water

LIW formation areas

Different formation regions have been proposed since the beginning of the 20th century for the Levantine Intermediate Waters. At first, Nielsen (1912) identified the Rhodes Gyre as a potential source of LIW. Thereafter, Lacombe (1972) pointed out that the region between Cyprus and Rhodes has perfect formation conditions. Wüst (1961) proposed a formation region between both the Aegean and the north of the Levantine Basin near Rhodes. Ovchinnikov (1984) conducted a study about the water mass characteristics of the Levantine Basin during two winters and proposed the Rhodes Gyre as the main formation region of the LIW. However, others suggested different formation zones: in the Antalya basin (Sur et al., 1993; Kubin et al., 2019; Fach et al., 2021), in the southern parts of the Levantine Basin (Lascaratos et al., 1993) in the northeastern Levantine between the coast of Turkey and Cyprus (Fach et al., 2021) or even other zones or in all the Levantine Basin (The POEM group, 1992).

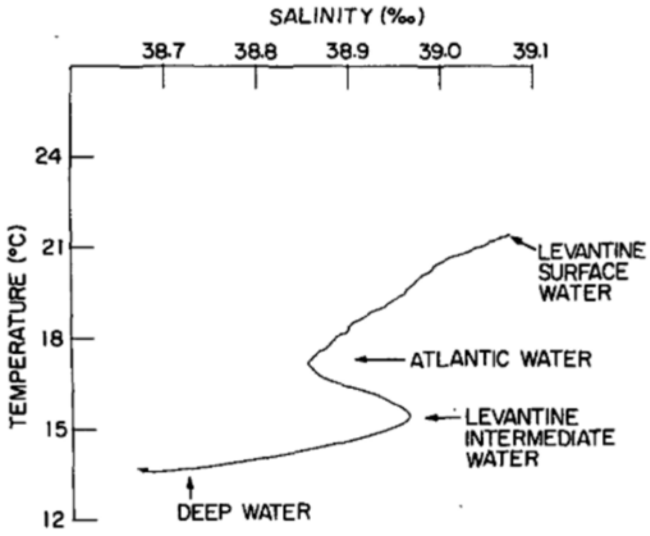

Figure 1.10: T-S diagram showing the different water masses in the Levantine Sea (Hecht et al., 1988)

Levantine Intermediate Water formation

During summer, the surface layer is formed of LSW and AW. Ovchinnikov (1984) connected the formation of the LIW with a cold and dense water dome at the center of the cyclonic Rhodes Gyre acting as a preconditioning. In early November, the water column starts to lose stability. Cooling and evaporation increase the density of the surface layer which leads to the mixing and the sinking of this water mass to intermediate depths during February – March in the northern basin (Hecht et al., 1988; Özsoy et al., 1989; Sur et al., 1993; Nittis and Lascaratos, 1998; Lascaratos et al., 1999). After its formation, this water spreads throughout the whole eastern basin (Estournel et al., 2021)and then heads towards the western basin.
The amount of LIW formed and their characteristics depend on the amount of heat loss every winter. Mild winters reduce the amount of LIW formed while during severe winters, large amounts of denser water are formed in the center and around the gyre (Nittis and Lascaratos, 1998). The formation time scale of the LIW is related to two factors: the mean season forcing and the extreme heat loss events. The mean season forcing limits the LIW formation to 1–2 months between February and March. The time scale of the extreme short events is a few days, such events are important for LIW formation especially if they take place when the stratification is weak at the end of the heat loss period (Nittis and Lascaratos, 1998).

1.1.4 Conclusion

Although many observational campaigns and various studies have been conducted to better understand the circulation and variability of the eastern basin, it is clear that many questions remain. The formation of the Levantine Intermediate Water is variable from year to year, at a decadal scale and probably on a long-term basis and its properties also vary in space in the Levantine Basin. If there is no longer any doubt that the densest water is formed in the Rhodes Gyre, one can wonder about the lighter water that is formed at other sites such as the Turkish coast. What happens to these water masses? Are they permanently buried? Are they ventilated again in the following years and then do they participate in the preconditioning? Concerning the temporal variability, what is the contribution of the different mechanisms (climatic variability or trend, internal variability of the Mediterranean of BIOS type)? Studies based on recent data (e.g. Ozer et al., 2022; Taillandier et al., 2022) provide insight that should be pursued in future years.

1.2 The biogeochemistry of the Mediterranean Sea

The Mediterranean is an oligotrophic sea with a strong N/P ratio and low phytoplankton production. In addition, its geographical position close to the Sahara Desert, and the fact that it is a semi-enclosed sea make it sensitive to external nutrient inputs. In this section, we will briefly present the particularities of the western and eastern basins of the Mediterranean.

1.2.1 Oligotrophy

An oligotrophic sea is a sea containing low nutrient contents and which consequently has low primary production. Uitz et al. (2012) estimated the average primary production (PP) in the Mediterranean Sea to 0.19 gC m^{-2} d^{-1}. Water is considered oligotrophic when its primary production is inferior to 0.3-0.4 gC m^{-2} d^{-1} (Longhurst et al., 1995). The oligotrophy varies between the basins, it increases going from the west to the east (Krom et al., 1991; Bosc et al., 2004), with the highest *Primary Production* (PP) in the western Mediterranean and Alboran Sea (0.29 gC m^{-2} d^{-1}) and the lowest in the southern eastern basin (0.16 gC m^{-2} d^{-1}), the Levantine Basin being defined as an ultra-oligotrophic basin.

Factors endorsing this oligotrophy

Regardless of the multiple sources of nutrients (from rivers and abundant atmospheric deposition), distinctive factors endorse their dilution and exhaustion (Berman et al., 1984) in the euphotic layer: (1) the anti-estuarine circulation; (2) low freshwater inputs from rivers especially in the southern part of the basin; (3) a narrow continental shelf with limited nutrient recycling at the benthic–pelagic interface (Wüst, 1961).

The main reason for this nutrient exhaustion is linked to the anti estuarine circulation (Fig. 2.1). The AW entering through the strait of Gibraltar (0.8 10^6 m^3 s^{-1}; Huertas et al., 2009, 2012) flows toward the east. On the contrary, the LIW flows westward through the strait of Sicily reaching the Gibraltar strait and returning to the Atlantic Ocean. The nutrients contained in the AW water mass are consumed by the marine organisms, all along its journey to the eastern Mediterranean (Crispi et al., 2001). Part of the nutrients are consumed as soon as they pass through the western basin along the Algerian coast (Crise et al., 1999). After their consumption, the nutrients are transformed into organic matter and exported toward the intermediate and the deep layers where they are remineralized by bacteria. LIW progressively gains nutrients as they progress toward the west. At the strait of Gibraltar, the intermediate waters leave the Mediterranean forming the Mediterranean Outflow Water (MOW), enriching the Atlantic at about 1000 m depth. The amount of nutrients flowing in the surface layer (with concentrations of 0.05 - 0.20 µM for phosphate, 1 - 4 µM for dissolved inorganic nitrate and ∼ 1.2 µM for silicate, (Coste et al., 1988)) to the Mediterranean is weaker than the amount flowing out in the bottom layer (0.25 - 0.5 µM for phosphate, 6 µM for dissolved inorganic nitrogen and 6.5 µM for silicate, (Coste et al., 1988)). The net nutrient exchanges at Gibraltar conduct to a loss of 50 % of silicate and 10 % of dissolved inorganic nitrogen and dissolved inorganic phosphorus of the Mediterranean outflow (Coste et al., 1988).

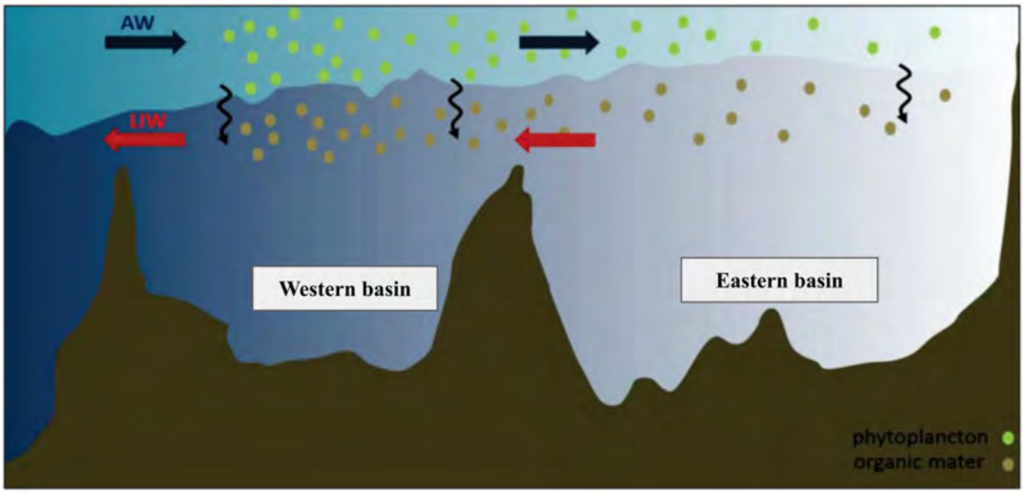

Figure 1.11: Conceptual representation of the anti-estuarine circulation in the Mediterranean (Pasqueron and Dynamique, 2016)

1.2.2 Nutrient distribution

The Mediterranean is marked by a decrease in the surface nutrients concentration (nitrates and phosphates) following a west-east gradient, accompanied by a deepening of the nitracline and the phosphacline (Moutin and Raimbault, 2002; Pujo-Pay et al., 2011). Nitrate, phosphate, and silicate concentrations in the surface water rarely exceed 0.5, 0.05 et 1.5 µM (Ribera d'Alcalà et al., 2003). Apart from the Rhodes Gyre possessing intermediate to deep winter mixing and a moderate nutrient injection, the Levantine basin possesses low concentrations of nitrate and phosphate (Lazzari et al., 2016) amounting to 1 and less than 0.05 µM for the nitrate and phosphate, respectively, in the surface layer (Kress et al., 2014). The average concentrations in deep waters are respectively 8-10 µM for the nitrate and 0.35-0.45 µM for the phosphate in the western basin and 4-6 µM and 0.14-0.2 µM in the eastern basin (Fig 2.2, Bethoux et al., 1998; Ribera d'Alcalà et al., 2003; Manca et al., 2004; Pujo-Pay et al., 2011). The nitracline and phosphacline in the eastern basin are located at 80 m and more than 100 m, respectively, whereas they are located at 40 and 60 m, respectively, in the western basin (Pujo-Pay et al., 2011). Similar to the Mediterranean Sea, the Levantine Basin also has a nutrient gradient from the west to the east (Pujo-Pay et al., 2011). This oligotrophic gradient is characterized by the decrease of the nitrate and phosphate concentrations in the surface and along the water column, in addition to the deepening of the nutricline in its most eastern parts (Moutin and Raimbault, 2002; Pujo-Pay et al., 2011).

1.2.2.1 The N:P ratio in the Mediterranean Sea

Another characteristic of the Mediterranean Sea is the high nitrate to phosphate (N:P) ratio measured in the deep layers (Krom et al., 1991) which is between 22:1 and 30:1 (Bethoux et al., 2002, 2005) higher than the Redfield ratio (RR) for the Global Ocean 16:1 (Redfield, 1934). The nutrients measured in the deeper layers are the result of biological processes (remineralization), Redfield based this ratio on the consumption and use of the nutrients by marine organisms. However, in the Mediterranean Sea, there is an excess of N compared to P with a ratio increasing in the east of the Mediterranean up to 27-29 (Fig 1.12, Krom et al., 1991; Kress and Herut, 2001; Kress et al., 2003; Ribera d'Alcalà et al., 2003; Krom et al., 2004). This phosphate deficit might be due to external contributions (low phosphate in atmospheric and riverine inputs) (The MerMex Group, 2011), or the high fixation rate of nitrogen (N_2) leading to the accumulation of nitrogen in deep waters or the adsorption of phosphates or iron-rich particles from atmospheric deposition leading to the exhaustion of the phosphate (Krom et al., 1991).

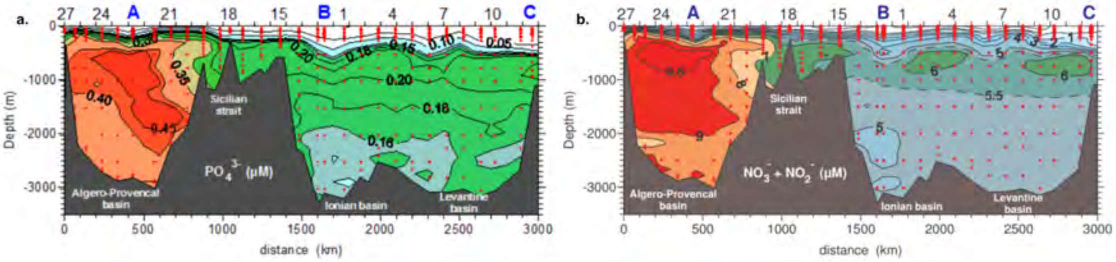

Figure 1.12: Vertical sections of (a) phosphate ($PO4^{3-}$) (b) nitrate + nitrite ($NO3^{-}$ $+NO2^{-}$) along the BOUM transect for the whole water column (Pujo-Pay et al., 2011)

Bethoux et al. (1992, 1998) reviewed the nutrient inputs to the Mediterranean and found that the excess of N cannot be explained by external inputs such as Gibraltar, rivers, or atmospheric deposition. The excess of N can only be explained by internal processes in the sea. Several hypotheses have been elaborated: (1) strong nitrogen fixation in the Mediterranean by diazotrophs (Bethoux and Copin-Montégut, 1986), (2) phosphate leaching through its adsorption on particles from the Sahara (Krom et al., 1991). Due to the negligible P adsorption rates on the Sahara dust, the second hypothesis has been ruled out (Ridame et al., 2003). The vast majority of observations revealed a negligible nitrogen fixation in the basin (Yogev et al., 2011). These studies highlight the limited knowledge of the mechanisms controlling nitrogen fixation in the Mediterranean Sea.

Impact of the high N:P ratio

Studies in the Mediterranean Sea advance a limitation in phosphate or a co-limitation in nitrate and phosphate. This limitation reflecting the low availability of nutrients impacts the phytoplankton regime. The primary production has been found to be limited by phosphate during spring (Diaz et al., 2001) and summer (Thingstad and Rassoulzadegan, 1995) in the

Gulf of Lion as well as in the eastern basin (Krom et al., 2004). A co-limitation of phosphate and nitrates in the Levantine Basin was also shown by other studies (Zohary et al., 2005; Krom et al., 2005). Because phosphate is only available in its inorganic form or through the remineralization of organic matter, its limitation impacts the biogeochemical processes in the Mediterranean Sea leading to strong competition and organism adaptation. The P limitation also affects its recycling time, phosphate renewal times of around 1 hour have already been observed, during periods of limitation (Thingstad and Rassoulzadegan, 1995). Under such conditions, phosphorus in the dissolved organic matter is quickly remineralized leading to an accumulation of N and C in the organic matter (Thingstad et al., 1997; Pujo-Pay et al., 2011; Santinelli et al., 2013) or only C in case of a co limitation.

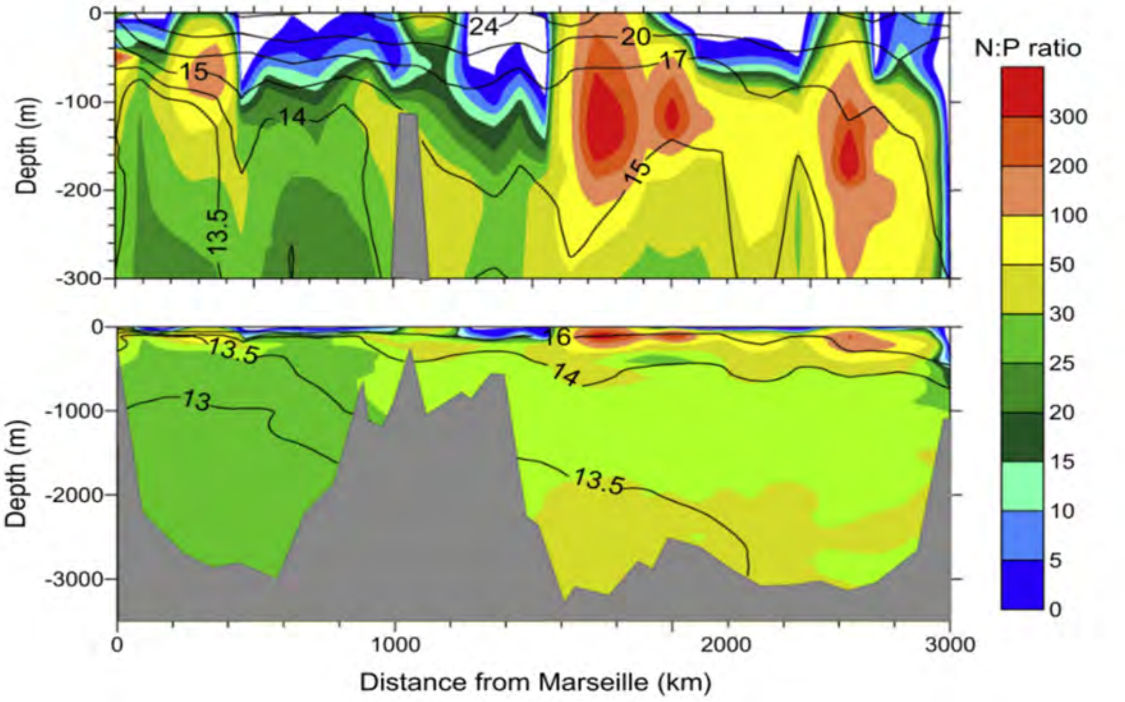

Figure 1.13: Vertical distribution of the NO3:PO4 ratio and temperature (black line,°C) during the BOUM cruise in the 0–300-m layer and 0-3000 m (The MerMex Group, 2011) Black lines represent the temperature (°C).

1.2.3 Nutrients

1.2.3.1 Influence of physical processes on the nutrients distribution

Exchanges at the Gibraltar Strait

The strait of Gibraltar is the main source of external water and nutrients in the Mediterranean Sea therefore its inputs are a major driver of the nutrient budget in the western and eastern basin (Bethoux et al., 2002; Huertas et al., 2012). The inflow of Atlantic Water is 4 to 5% greater than the outflow of the Mediterranean water (Bryden et al., 1994). The net exchange at Gibraltar represents a loss in nutrients and dissolved inorganic matter. The exchange rate

Table 1.1: Average inflow and outflow of biogeochemical variables at the Gibraltar Strait

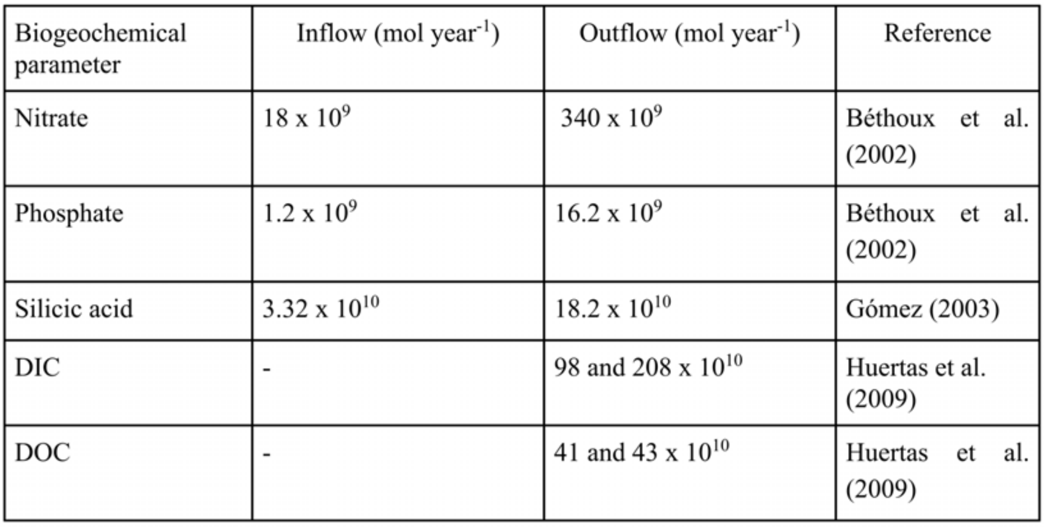

Biogeochemical parameter	Inflow (mol year^{-1})	Outflow (mol year^{-1})	Reference
Nitrate	18 x 10^{9}	340 x 10^{9}	Béthoux et al. (2002)
Phosphate	1.2 x 10^{9}	16.2 x 10^{9}	Béthoux et al. (2002)
Silicic acid	3.32 x 10^{10}	18.2 x 10^{10}	Gómez (2003)
DIC	-	98 and 208 x 10^{10}	Huertas et al. (2009)
DOC	-	41 and 43 x 10^{10}	Huertas et al. (2009)

at the strait for the different biogeochemical parameters is described in table 1.1. Negative flux means that the net flow is directed toward the Atlantic.

Table 1.1 confirms the results advanced by Crise et al. (1999) and previously discussed in this chapter. The estuarine circulation drives nutrient rich AW flowing into the Strait of Gibraltar eastwards in the surface layer. Nutrients are consumed by phytoplankton during its path and are transformed into detritus. The downward flux of detritus reduces the total amount of nutrients reaching the Eastern Mediterranean. The LIW on the other hand, moves towards the west, and its nutrient content increases because of the mineralization of incoming detritus and mixing with the deep waters, this explains the high nutrient outflow towards the Atlantic.

Influence of the circulation and the exchange at Gibraltar on the eastern basin

Even though the eastern basin is surrounded by lands with nutrient discharges, the main nitrogen and phosphorus inputs are attributed to the high volume of Atlantic Waters headed to the eastern basin. According to Powley et al. (2016a), 77 % of the P input of the western surface water passes through the Sicily Strait and contributes to 37 % of the eastern basin's new production. Béthoux et al. (2002) found a P and N flux to the western basin of 7.2 and 170 x 10^9 mol yr^{-1} respectively at the Sicily strait while Schroeder et al. (2020) estimated an export of 4.1 and 92 x 10^9 mol yr^{-1} of P and N respectively for the Sicily Strait. The eastern inflow to the eastern basin is 2.2 and 16 x 10^9 mol yr^{-1} for P and N respectively (Krom et al., 2004).

Influence of dense water formation

Regions of dense water formation and cyclonic circulation - North West Mediterranean (Medoc group, 1970), the Rhodes Gyre (Lascaratos et al., 1993) and the southern Adriatic (Roether and Schlitzer, 1991) - generate mixed layers ($>$ 200 m) and upwelling (preconditioning) allowing access to large amounts of nutrients sustaining phytoplankton blooms whereas the mixed layers in the other regions with seasonal moderate cycles typical of subtropical regions, allow only a moderate supply of nutrients to the surface layer. The phytoplankton biomass is generally low in these regions which are classified as no bloom regions in the classification of D'Ortenzio and Ribera d'Alcalà (2009). Estimates of the net inputs of nitrogen and phosphorus in the surface layer have already been reported in the north-western deep convection area by Kessouri et al. (2017), they estimated vertical physical inputs of 6.3474 and 3.640 x10^9 mol year^{-1} for N and P respectively.

1.2.4 External nutrient inputs

River inflows

Rivers are a large supply of fresh water and a source of nutrients for the Mediterranean Sea (Fig. 1.14). The river's nutrient input supports 2 % of primary production (Ludwig et al., 2009). The river inflow of fresh water and nutrients is influenced by climate change and anthropogenic factors (Ludwig et al., 2009, 2010). A 20 % decrease in riverine water inputs was observed between 1960 and 2000 (Ludwig et al., 2009), mainly due to anthropogenic activities (construction of dams, water withdrawal for agriculture . . .), and, to a lesser extent, the variability of climate (e.g. decrease in precipitation (Struglia et al., 2004)). Regarding nutrients, nitrate, and phosphate inputs increased until 1995 with the use of fertilizers in crops. According to Ludwig et al. (2009), the amount of nitrates increased by more than 5 times, from 1.6x10^{10} mol year $^{-1}$ to 7.7x10^{10} mol year^{-1} between 1963 and 1998. Phosphate input reached 0.33 x10^{10} mol year^{-1} due to the phosphate contained in the wastewater. However, since then, it has declined to about the levels of the early 1970s (0.07 x10^{10} mol year^{-1}) because of the ban of P in detergents and upgrades in the wastewater treatment system (Ludwig et al., 2009). The construction of dams on rivers, more precisely the Nile river, had also an impact on the fluvial supply of silicic acid.

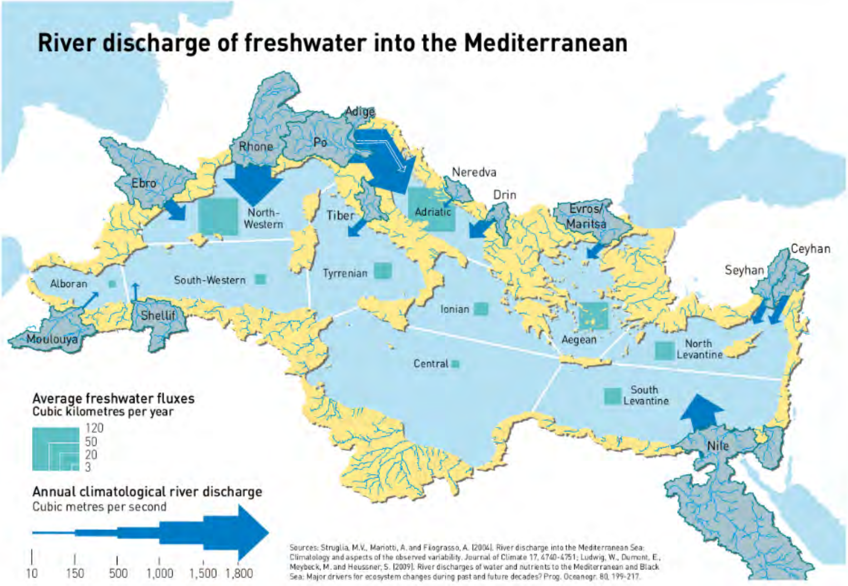

Sources: Struglia, M.V., Mariotti, A. and Filograsso, A. (2004). River discharge into the Mediterranean Sea: Climatology and aspects of the observed variability. Journal of Climate 17, 4740-4751; Ludwig, W., Dumont, E., Meybeck, M. and Heussner, S. (2009). River discharges of water and nutrients to the Mediterranean and Black Sea: Major drivers for ecosystem changes during past and future decades? Prog. Oceanogr. 80, 199-217.

Figure 1.14: Major river basins draining into the Mediterranean based on Struglia et al. (2004) for data from 1973 to 1984 and Ludwig et al. (2009) based on modeling and observational data (1960-2006).

Atmospheric inputs

The proximity of the coasts, the presence of desertic surfaces to the south, and the urbanization and industrialization favor the atmospheric inputs which contribute to the biogeochemical cycles of nutrients. Duce et al. (2008) and Mahowald et al. (2008) estimated atmospheric deposition on the Mediterranean Sea to 67 Tg N yr^{-1} and 1.39 Tg P yr^{-1}, respectively. Atmospheric deposits are estimated to be of the same order of magnitude as riverine inputs and would contribute respectively to 61 % and 28 % of the total balance of N (nitrate + ammonium) and P in the eastern basin (Krom et al., 2004). The contribution of atmospheric deposition in the Mediterranean varies geographically. The atmospheric deposition of inorganic nitrogen ranges from 18.1 to 47.7 mmol m^{-2} yr^{-1}, with higher values in the eastern basin than in the western. As for the dissolved inorganic phosphate, the flux ranges from 0.243 to 0.608 mmol m^{-2} yr^{-1} with no visible difference between the basins (Markaki et al., 2010). Moreover, there is an excess of N compared to P in atmospheric deposits, the DIN: DIP ratio is around 60 in the west and 100 in the eastern basin (Markaki et al., 2010).

During winter and spring, when nutrient and coastal supply are maximum, atmospheric deposition has less impact on nutrients budget than during summer when the surface is virtually depleted in nutrients (Richon et al., 2017). The nitrate deposition triggers a 20–30 % increase in carbon export at 100 m in the eastern coastal areas (Richon et al., 2017). Aerosol depositions fertilize the basin and lead to increases in surface primary production, chlorophyll production, plankton concentration, and also carbon export from the surface. Christodoulaki et al. (2013) found that primary production is enhanced up to 30 % in the eastern Mediterranean because of atmospheric deposition of inorganic N and P.

Atmospheric inputs can be attributed to dry or humid deposition. Humid deposition represents the rainfall contribution. It is therefore of short duration. On the other hand, dry deposition is a slow and continuous process as the nutrients contained in the atmosphere fall due to gravity. The type of deposition varies geographically: for example, in the northwestern Mediterranean, the deposition is of the wet form (Loÿe-Pilot et al., 1990; Bergametti et al., 1992). Details of wet and dry deposition in the western and eastern Mediterranean Sea can be found in Table **??**. Dry deposition accounts for 20 % of total deposition in the majority of Mediterranean areas (Violaki et al., 2018), the atmospheric deposition of the total phosphate was estimated to enhance new production by 38 % in the eastern Mediterranean, while it could increase to 14 % in the north-western Mediterranean during oligotrophic periods (Violaki et al., 2018). The total nitrate deposition (DON) contributes up to 20-30 % of the new production in the eastern basin (Violaki et al., 2010).

Even though these inputs are sources of nutrients to the Mediterranean Sea, their bioavailability will depend on various parameters: (1) the deposition process and/or the transformations undergone by the particles in the atmosphere, (2) the properties of the water in which the deposition takes place: Mendez (2010) found that the Mediterranean waters dissolve the iron contained in Saharan dust better than Pacific waters.

The impact of the atmospheric deposition on the plankton ecosystem depends on the period of the year: phytoplankton has different responses when the concentration of nutrients is already high during winter or during summer when stratification favors the oligotrophy of the system. During the summer period, and because of the stratification, nutrient concentrations are extremely low, and the main source of nutrients in the surface is atmospheric deposits (Migon et al., 2002; Ridame and Guieu, 2002).

1.2.5 Phytoplankton

Satellite images highlight the oligotrophic nature of the Mediterranean Basin and its intensification going to the east (Fig. 1.15). The mean chlorophyll concentration varies from 0.4 mg m^{-3} in the west basin to 0.05 mg m^{-3} in the east (Bosc et al., 2004). The *Chlorophyll* (Chl) follows the same seasonal cycle around almost the whole basin, which generally presents a maximum surface chlorophyll concentration during winter and a minimum during summer. In the northwestern basin high Chl peaks are observed in winter or early spring (Bosc et al., 2004). A *Deep Chlorophyll Maximum* (DCM) is present during the stratification period (Sauzède et al., 2015) over the entire basin (Barbieux et al., 2019). This DCM deepens from the west ($\sim$ 70 m) to east ($\sim$ 120 m, Moutin and Raimbault, 2002; Mignot et al., 2011). This is also true for primary production (Uitz et al., 2012).

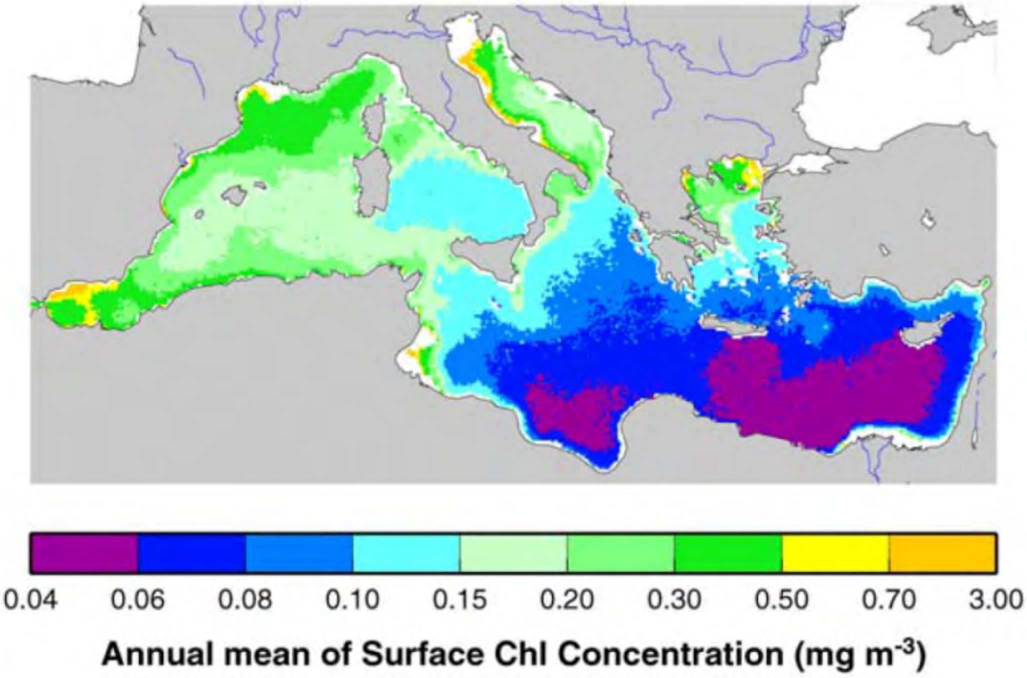

Figure 1.15: Annual mean of surface chlorophyll concentration in the Mediterranean Sea from September 1997 to December 2001 (Bosc et al., 2004)

The Mediterranean Sea is characterized by a dynamic trophic phytoplankton ecosystem, which can evolve rapidly, depending on the seasons and regions (Siokou-Frangou et al., 2010). As a matter of fact, spring bloom waters in the South Aegean Sea are dominated by micro-phytoplankton while the Levantine and Ionian waters have a mixed composition of micro and nano phytoplankton more abundant than in the Aegean waters (Varkitzi et al., 2020). The northwestern Mediterranean at the DYFAMED station is dominated mostly year-round by nano-phytoplankton, yet, during January-February micro phytoplankton contribute most to the phytoplankton biomass (Marty et al., 2002). Vidussi et al. (2001) showed variability of phytoplankton communities in the same mesoscale feature, the Rhodes Gyre. In the core of the gyre, the plankton community was dominated by micro and nanophytoplankton classes while at the border of the gyre, nano, and pico prevailed over micro-phytoplankton during the mixing period (December-February).

D'Ortenzio and Ribera d'Alcalà (2009) used the seasonality of the surface chlorophyll concentration to identify the different trophic regimes of the Mediterranean. They applied the clustering method (k-means cluster analysis) to climatological Chl-a satellite normalized cycles for each available pixel. The main cycles of phytoplankton biomass (Fig. 1.16) and their geographical distribution are then easily identified with 4 main regimes:

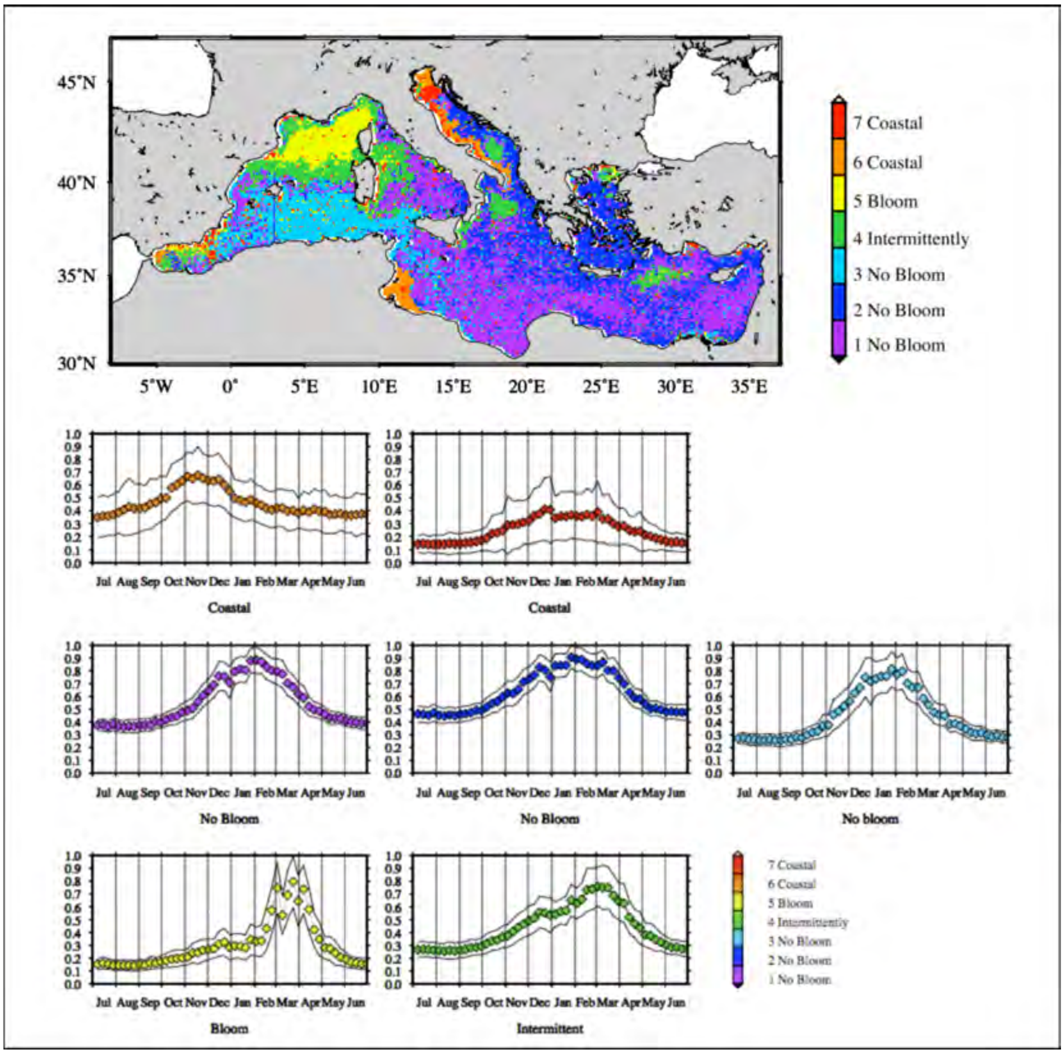

Figure 1.16: Biogeochemical classification of the Mediterranean Basin derived from the analysis of SeaWiFS surface chlorophyll satellite data (D'Ortenzio and Ribera d'Alcalà, 2009).

1. The bloom regime (yellow in Fig. 1.16) occupies areas of deep water formation (mostly, the Gulf of Lion), as well as their periphery, with a strong renewal of nutrients in the euphotic layer in winter. The mixing for this regime is intense and deep enough to induce light limitation of primary production, allow the accumulation of nutrients, and support a strong spring increase in biomass at the re-stratification of the water column (Bosc et al., 2004; D'Ortenzio and Ribera d'Alcalà, 2009; Lavigne et al., 2013).

2. The intermittent regime (in green) concerns regions with cyclonic circulations like the Rhodes Gyre, the south Adriatic, the north Ionian and the north Tyrrhenian.

3. The no-bloom regime occupies almost all of the eastern Mediterranean and south of the western Mediterranean. The seasonal cycle of chlorophyll presents a maximum in winter when the mixed layer can be thick enough to reach nutriclines under the euphotic layer and shallow enough to allow photosynthesis.

4. Coastal areas / continental shelves (red) influenced by river inputs and winter mixing.

Even though satellite images contribute to the understanding of the spatiotemporal variations of the Chl-a, it has been shown that optical anomalies can occur with the presence of Saharan dust or coccoliths in the Mediterranean (Claustre et al., 2002) leading to a 40% overestimation of chlorophyll concentration by the algorithms (O'Reilly and Maritorena, 2000). This bias is more important for regions where Chl doesn't exceed 0.4 mg m^{-3} (Volpe et al., 2007) which led to developing more regional algorithms for the basin (D'Ortenzio et al., 2002; Bosc et al., 2004; Volpe et al., 2007).

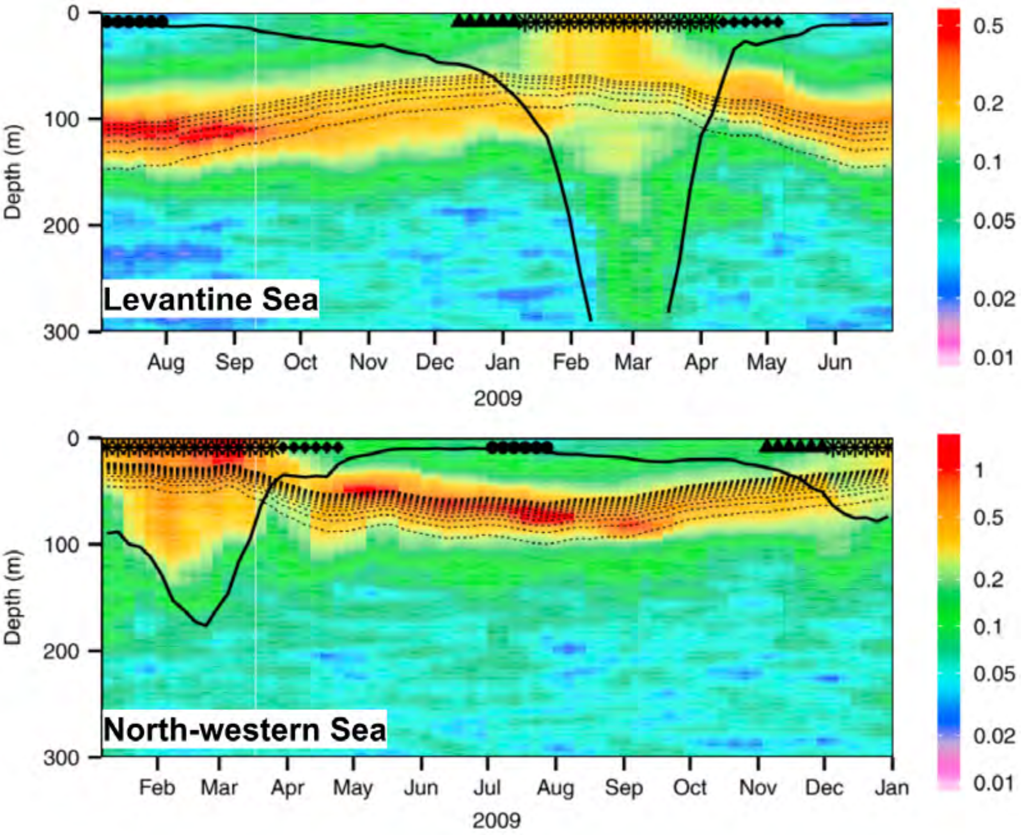

Figure 1.17: Time series of the 0–300 m vertical distribution of Chl for the Levantine and the North-western Sea (Mignot et al., 2014). The solid black line is the mixed layer depth (MLD), the stars represent the profiles during the mixing period.

The Levantine, the Ionian, and the southwestern Mediterranean present the same seasonal evolution of the vertical distribution of chl along the water column, with lower values in the Eastern Basin (Fig. 1.17). The chlorophyll concentration is higher from the surface to the base of the pycnocline from December to March, while the rest of the year is characterized by the presence of a DCM (Lavigne et al., 2015). The western basin displays a shifting in its cycle, DCM occurs from May to October. All regions are characterized by a deepening of the DCM from May to July and a shallowing from August to September. While the increase in the surface chl concentration is the result of the nutrient injection and photo-acclimation, the

DCM might be due to the contrasted gradient of two essential resources in a stratified water column: nutrients supplied from depths and light supplied from the surface (Mignot et al., 2014).

1.2.6 Oxygen dynamic

Oxygen affects the cycle of key elements in the sea: carbon, nitrogen, and many others. It is fundamental for biogeochemical processes like mineralization and is required for the sustainability of marine life at the surface and in the deep sea. The oxygen's concentration and distribution are closely related to different physical and biological processes: atmospheric exchange, mixing, and advection, as well as respiration and photosynthetic production, depending on the water layer. The different processes controlling the oxygen distribution are as follow: in the surface layer, the ocean-atmosphere interface allows oxygen enrichment or release. In addition, this euphotic layer is dominated by photosynthetic activities due to the presence of light: photosynthetic processes generally surpass respiration, thus increasing oxygen concentration in parallel to the consumption of nutrients. Throughout the water column, oxygen is consumed for respiration processes and the decomposition of organic matter (Kress et al., 2003). For regions deeper than 1500 m, oxygen concentration increases again because of the decline of its consumption by bacteria (refractory form) and the intrusion of oxygen-rich waters from the convection zones.

Even though there is a major gap of information concerning oxygen distribution, oxygen presents a similar vertical distribution all across the basin. The Mediterranean Sea is a well-oxygenated sea, with high concentrations in the surface water, slowly decreasing in the LIW to reach the oxygen minimum layer's (OML) whose depth depends on the basin (west /east, Fig 2.7). The minimum oxygen concentration in the intermediate layer is 170-180 µmol kg^{-1} because of frequent and intense ventilation (Roether and Schlitzer, 1991). Below the OML, the concentration increases towards the bottom (Picotti et al., 2014). A survey in the western basin attributed this increase to recently formed deep waters (Schroeder et al., 2006). The oxygen concentration in the surface layer depicts a seasonal variability, with a surface maximum in winter and a *Subsurface Oxygen Maximum* (SOM) for the rest of the seasons, prominent in summer (Di Biagio et al., 2022). The surface oxygen follows the cycle of oxygen saturation. In winter, with mixing and air and sea interactions, the surface layer is undersaturated in oxygen and thus absorbs atmospheric oxygen. Production is concentrated in the surface leading to important surface oxygen concentrations. However, during spring, this layer is oversaturated in oxygen and loses oxygen to the atmosphere (Kress and Herut, 2001). The oxygen increase in the subsurface follows biological and physical processes such as the deepening of the phytoplankton growth for spring and summer.

Prior to the change in deep water masses in the eastern Mediterranean (EMT), dissolved oxygen was uniformly distributed below 1000 m depth in the eastern basin (except Ionian) (Schlitzer et al., 1991). The established origin of deep water was the Adriatic Sea. This pattern changed after the beginning of the Eastern Mediterranean Transient (EMT). The deep Adriatic water was pushed to the surface by the younger more oxygenated Deep Aegean Water (Lascaratos et al., 1999). These changes are responsible for the current vertical oxygen distribution.

Although oxygen follows the same vertical distribution in the Mediterranean basin, its concen-

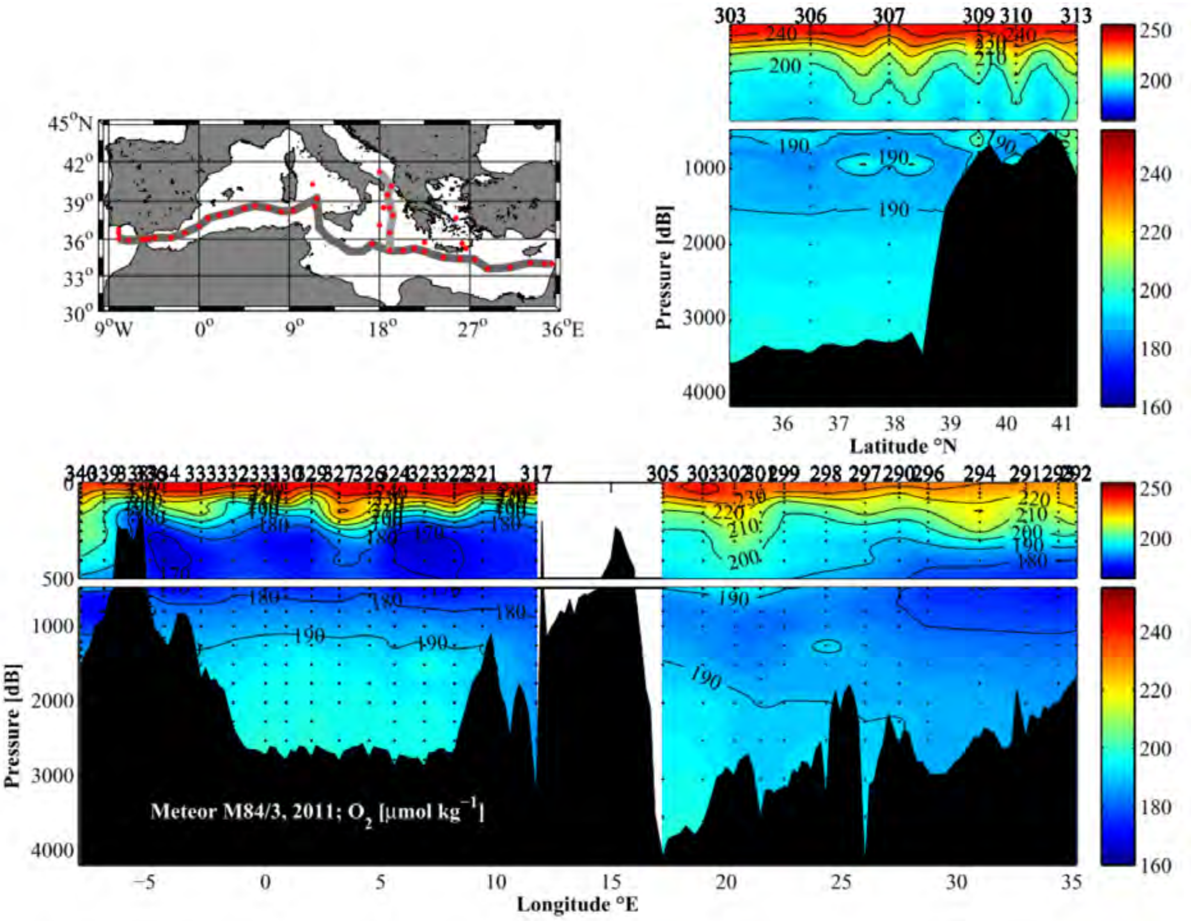

Figure 1.18: Sections of dissolved oxygen (µmol kg^{-1}) in the Mediterranean Sea from the Meteor cruise M84/3 in April 2011. The top-right panel is a meridional section from the Adriatic Sea to the Ionian Sea (light gray line on the map) and the lower panel is the zonal section from the strait of Gibraltar to the coast of Lebanon in the eastern Mediterranean Sea (Tanhua et al., 2013)

tration varies for the different sub-basins. A subsurface oxygen maximum is slightly higher in the western basin than in the eastern (Fig. 1.19). It is estimated to be between 235 and 255 µmol kg^{-1} with the lower values in the Levantine Sea (Kress and Herut, 2001) and higher values in the Northwestern Mediterranean (Copin-Montegut and Begovic, 2002) and the southern Adriatic Sea (Manca et al., 2004). The SOM is located at shallow depths in the western basin (20-40 m, Copin-Montegut and Begovic, 2002 and Di Biagio et al., 2022) and deeper in the eastern basin (between 50 -100m, Kress and Herut, 2001). The oxygen subsurface increase is the result of high phytoplanktonic productivity (Manca et al., 2004) and the low potential temperature (Mavropoulou et al., 2020). Di Biagio et al. (2022) identified the downward transport as the main driver for the SOM concentration and depth. The low potential temperature in the western basin favors the increase of oxygen in the surface layer (Fig. 1.19). In the western basin, the oxygen minimum is located at depths between 400 - 600 m (in the LIW) while in the eastern basin, it is located between 600 and 1200 m. It occupies the area between the LIW and the deep waters namely the Transitional Mediterranean Water (Nittis et al., 2006). The LIW is more oxygenated in the eastern basin (197-210 μmol kg^{-1}, Mavropoulou et al., 2020) than in the western basin (160-180 μmol kg^{-1}, Coppola et al., 2018).

The ventilation of the Mediterranean Sea is fast compared to the Global Ocean showing a large temporal variability (Schneider et al., 2014). However, although the eastern basin is subject to fast water formations, it is slowly ventilated between 1200 - 2000 m. The dense water renewal in the western basin is estimated to 40 years faster than in the eastern (70 - 150 years) (Roether et al., 1996). In addition, the eastern basin possesses a peculiar morphology limiting the oxygenation of the deeper layers, and the more stratified water column in the east resulting in slower mixing (Tanhua et al., 2013). Thus, oxygen concentrations in deeper layers for the east and west basin differ, with concentration higher in the western basin until 3000 m (195-205 μmol kg^{-1} vs. 171-184 μmol kg^{-1}).

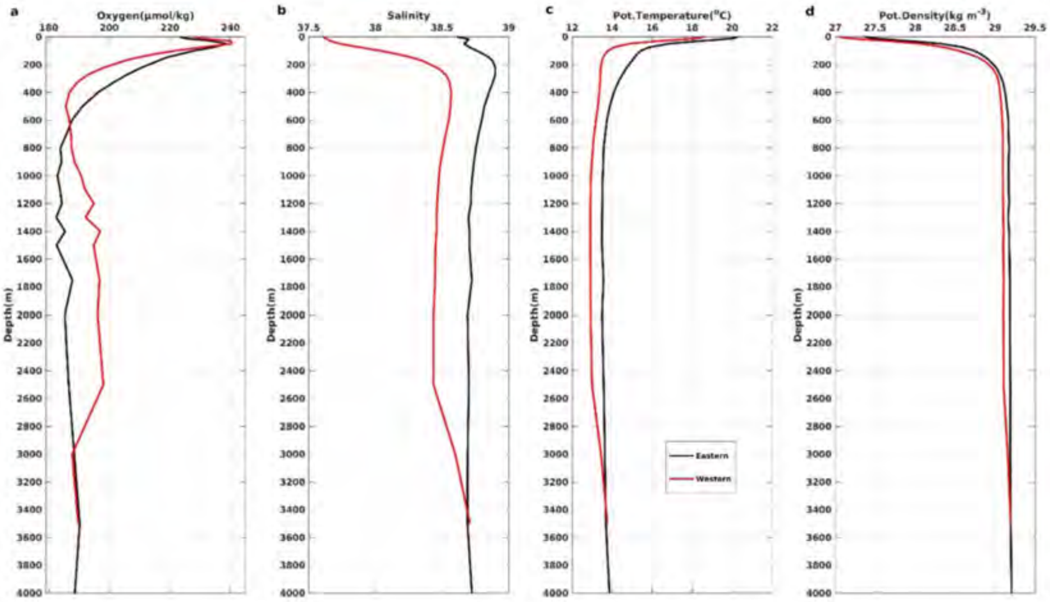

Figure 1.19: Climatological profiles of dissolved oxygen, salinity, potential temperature and potential density anomaly (sigma-theta) for the Eastern (black line) and the Western Mediterranean (red line) Sea (Mavropoulou et al., 2020)

1.2.7 Organic carbon dynamics

Biological processes i.e. photosynthesis and respiration impact the carbon system and control its concentration and its forms. The biological pump transforms inorganic carbon into *Particulate Organic Carbon* (POC). This carbon is either remineralized in these waters by bacterial activity or exported to the deep sea in a particulate or dissolved form where it will be remineralized but at slower rates. The efficiency of the biological pump depends on the ratio of carbon exported to the deep sea and the carbon produced by primary production (Ducklow et al., 2001).

Net Primary Production (NPP)

Previous studies documented the amount of organic carbon produced in the photic layer during the stratification period and were based on satellite, in situ observations, and modeling estimates in the Mediterranean Sea. Algorithms have been developed to estimate primary production from satellite observations of Chl-a (Antoine et al., 1996)). It should be noted that the net primary production is the difference between the total rate of organic carbon production by phytoplankton, also known as growth primary production (GPP), and their respiration. Bosc et al. (2004) estimated the *Net Primary Production* (NPP) at 163 ± 7 gC m^{-2} yr^{-1} in the western basin and 121 ± 5 gC m^{-2} yr^{-1} in the eastern basin. Uitz et al. (2012) re estimated the NPP and found values lower than what was previously found by Bosc et al. (2004), the NPP values in the west and east basins are 79 gC m^{-2} yr^{-1} and 61 gC m^{-2} yr^{-1} respectively. Lazzari et al. (2012) using modeled climatological maps also showed that the net primary production has a west-east gradient, with higher NPP values in the western sub-basin (131 ± 6 gC m^{-2} yr^{-1}) and lower values are found in the eastern basin (76 ± 5 gC m^{-2} yr^{-1}). Even though higher integrated primary production was observed in the western basin, dense water formation regions in the east also showed enhanced NPP compared to the oligotrophic eastern basin. Napolitano et al. (2000) estimated the modeled primary production at 97 ± 5 gC m^{-2} yr^{-1} in the Rhodes Gyre. The deep water formation area in the Southern Adriatic NPP ranges between 140-160 gC m^{-2} yr^{-1} (Bosc et al., 2004). The zonal trophic gradient of primary production reflects a sink of particulate carbon at a 2-fold higher carbon export rate in the western sub-basins than that of the eastern sub-basins. The *Net community Production* (NCP), the difference between primary production and community respiration, tends to follow the same trend as the net primary production. Studies reported higher NCP in the western basin compared to the east, 155 and 83 mmol O2 m^{-2} d^{-1} respectively during summer (Regaudie-De-Gioux et al., 2009), with higher respiration rates in the west. During late spring, planktonic ecosystems tend to become heterotrophic when respiration was dominant compared to production.

Export of organic carbon

Biological cycling of the dissolved and particulate organic carbon in the euphotic zone of the Mediterranean Sea varies regionally and seasonally between regions with higher production and increased carbon export to regions with lower production and particle export reduced by remineralization (Thingstad and Rassoulzadegan, 1995; Speicher et al., 2006). Based on satellite-deduced chlorophyll data, the maximum primary production was found between winter and spring in the Mediterranean while the lowest was during the stratification period when the nutrient supply is limited (Bosc et al., 2004). Dissolved organic carbon in the Mediterranean Sea ranges between 57 - 68 µM in the surface layer (Santinelli et al., 2010). Its concentrations are high at the end of summer when stratification and regenerated production dominate.

The main drivers of particulate organic carbon POC and *Dissolved Organic Carbon* (DOC) export are the dense water formation and the convective turn of the water column. Kessouri et al. (2018) showed that in the deep water formation area of the northwestern Mediterranean Sea, the export of DOC and POC at 150 m was 6 times higher during convection periods than during the rest of the year. This was also detected in the Ligurian Sea, Avril (2002) estimated a DOC export of 12 gC m^{-2} yr^{-1} through the 100 m interface at the Dyfamed station, with 91 % of the export resulted from winter mixing. Gogou et al. (2014) found an increase in OC export during enhanced primary production. Boldrin et al. (2002) reported an increase in the inorganic nutrient supply during convection leading to enhancement of primary production and thus organic export in the southern Adriatic Sea in early spring, POC export flux amounts for 3.3 g C m^{-2} yr^{-1} at 150 m, representing 9 % of primary production. Santinelli et al. (2013) also estimated the DOC export by winter mixing and reported a net export of 3.2 and 15.4 g C m^{-2} yr^{-1} in the southern Tyrrhenian and Adriatic Seas, respectively.

The west–east decrease in phytoplankton biomass in the Mediterranean Sea is well reflected in the POC and DOC export, with approximately one order of magnitude lower POC fluxes recorded in the EMED because of the more occurrent episodic fertilization events (convective mixing) in the Western Basin (Gogou et al., 2014). POC export below the euphotic layer has been estimated to represent between 1.2 and 12.5 % of the daily integrated NPP in the Mediterranean varying between 3.5 to 44.2 g C m^{-2} d^{-1} (Moutin and Raimbault, 2002). These estimates are close to those obtained by Gogou et al. (2014), with 11.4 and 10.8 % for the Gulf of Lion and the Ionian Sea respectively. They found, respectively, a POC export of 23.3 and 15.7 g C m^{-2} yr^{-1} for the sites derived at 100 m depth. A modeling study (Guyennon et al., 2015) also highlighted a difference in the POC flux at 100 m between the eastern and the western basin (9.8 vs 2.4 g C m^{-2} yr^{-1}). In the Western Mediterranean, deep winter mixing causes a surge of nutrient upwelling that support large phytoplankton growth and triggers high and episodic export production of POC to the deep sea floor. While in the Eastern Basin, because of shallow winter mixing, the water is dominated by small phytoplankton groups and microbial food web favoring the remineralization of carbon and very low export to the deeper layers (Gogou et al., 2014). The difference between basins can also be found below 2000 m depth, the fraction of primary production exported averaged 0.61 % and 0.31 % in the Western Mediterranean and the Eastern Mediterranean respectively.

1.2.8 The carbonate system in the Mediterranean Sea

The dynamics of the carbonate system in the Mediterranean are influenced by the exchanges with the Atlantic Ocean, the Black Sea, and the Red Sea, and the contributions from the continent. The latter can be caused by anthropogenic discharges due to human activities, atmospheric inputs, or natural leaching and erosion of the soil.

The oceanographic cruises that took place in the Mediterranean Sea have made it possible to characterize the Mediterranean carbonate system via discrete measurements of Total Alkalinity (AT), Total Carbon (CT), and pH. They highlighted the singularity of the Mediterranean carbonate system. The Mediterranean Sea is an evaporation basin which means high concentrations of salt are present, and because the AT variations depend on the salinity, the waters of the Mediterranean basin have higher AT values than most of the waters of the globe. The total alkalinity in the Mediterranean basin varies between 2500 - 2650 µmol kg^{-1} (e.g. Álvarez et al., 2014; Hassoun et al. 2015b) with a higher AT mean concentration in the eastern basin than in the western basin. Conversely, CT, ranging between 2200 (Gemayel et al., 2015) and 2340 µmol kg^{-1} (Álvarez et al., 2014), shows higher concentrations in the western basin. The weak CT in the oriental Mediterranean can be explained by the increased oligotrophy of this region (Pujo-Pay et al., 2011): the very low productivity of the eastern basin tends to attenuate the CT vertical gradient. Since productivity is greater in the western sub-basin, the CT content of the surface waters decreases. Upon their arrival to the oriental basin, the heating of the water favors a loss of CO_2 by air-sea exchange, which will accentuate those lower CT values in that region. Due to the contrast in AT and CT between the east and west of the basin, the eastern waters are less acidified than those of the western basin (Hassoun et al., 2015a). Wimart-Rousseau et al. (2021) also showed significant ocean acidification and a decrease in the oceanic surface pH in the eastern Mediterranean. D'Ortenzio et al. (2008) showed that the total Mediterranean sea plays the role of a sink of atmospheric CO_2, with a western basin mainly "sink" and an eastern basin mainly "source" of CO_2. Due to the strong temperature dependency of pCO_2, there is a permanent west-east gradient with maximum values of $pCO_2 \sim 500$ µatm during the summer season in the Ionian and Levantine seas (Álvarez et al., 2014), and minimum values of around 250 µatm observed in the Alboran Sea.

1.3 The state of the art of the coupled hydrodynamic biogeochemical models in the Mediterranean Sea

1.3.1 State of art of the coupled hydrodynamic biogeochemical models

The first biogeochemical model used for the whole Mediterranean Sea was implemented by Sarmiento and Herbert (1988). This model, corresponding to a box model, was developed to determine if conditions of anoxia could be encountered in the eastern Mediterranean in the future. The authors found that the limited nutrients control the level of oxygen present in the deep waters and that the open-sea eastern basin will never reach the anoxic state unless there is a reversion in the flow direction of the eastern Mediterranean, with AW entering through intermediate layers while LIW flowing out through the surface layer.

The need to add more compartments to the biogeochemical models, compared to the NPZD models, was identified, for example, to improve the description of the groups of phyto- and zooplankton, to include silicon and phosphorus and to add the microbial loop. The models have moved towards multi-nutrient model types and multi-functional groups favoring a realistic representation of the process (Baklouti et al., 2006).

Modeling of the Mediterranean Sea

The first coupled hydrodynamic–biogeochemistry models for the entire Mediterranean Sea were developed and described by Crise et al. (1998, 1999) and Crispi et al. (2001). The model was coupled to an NDP (nitrates, detritus, and phytoplankton) model. The main hypothesis of the study was that the anti-estuarine circulation is not enough to explain the oligotrophy of the region.

Allen et al. (2002) used a one-dimensional coupled approach model to simulate the primary and bacterial production along the west–east trophic gradient of the Mediterranean Sea. They ascertained the physical and biogeochemical factors, found by the previously mentioned 3D studies, that determine regional variations in production between the different basins. The same results were also advanced by Crispi et al. (2002) who used a three dimension model including a microbial loop.

More recently, Lazzari et al. (2012) used the more sophisticated biogeochemical model MED-BFM (Biogeochemical Flux Model) coupled to the hydrodynamic model OPA-MED16 to study the chlorophyll and the primary production. MED-BFM is a multi-nutrient, multi-functional model with 9 planktonic groups (Vichi et al., 2007). It presents a co-limitation of nitrate and phosphate. The authors showed the spatial and temporal variability of primary production and chlorophyll concentrations in the basin. They also showed that atmospheric deposition and river inputs boost the net primary production (NPP) by 5 %. MED-BFM was also used by Lazzari et al. (2013) and Lazzari et al. (2016). The former investigated the future evolution of organic carbon stock and flows. Their model shows an increase by 5 % of the primary production, resulting from the increase in temperature, counterbalanced by an increase in community respiration. The MED-BFM was also used more recently by Cossarini et al. (2021). They observed a basin-wide surface deoxygenation and an increase in alkalinity at the surface as a consequence of the temperature and salinity increase over the last 20 years. Macías et al. (2014b) studied the maximum subsurface chlorophyll with the 3D hydrodynamic model GETM coupled with the biogeochemical model MedERGOM. This biogeochemical model incorporates three macro-nutrients, three phytoplankton classes, one zooplankton variable, detritus, dissolved oxygen, and a sediment compartment. The authors showed that the deep chlorophyll maximum contributes to 60 and 63 % of the integrated primary production in western and eastern basins, respectively.

Kalaroni et al. (2020) also implemented a 3D hydrodynamic-biogeochemical model, based on POM (Princeton Ocean Model) and ERSEM (European Regional Seas Ecosystem Model), in the Mediterranean Sea. The authors assessed its accuracy in representing the main biogeochemical components and seasonal dynamics of the Mediterranean planktonic system.

Guyennon et al. (2015) estimated the organic carbon stock and exports in all of the Mediterranean Basin, through a modeling approach based on a coupled model over 14 years. The model combined a hydrodynamic simulation NEMO – MED 12 and the biogeochemical model Eco3M-MED. They found that export in the eastern basin is high despite the low production compared to the western basin (60 % of the organic carbon is exported in the east), dissolved organic carbon (DOC) is the dominant form of the total organic carbon export. They also showed high spatial variability between DOC and POC in the basins and a temporal uncoupling of their export. NEMO-MED12 and PISCES were also coupled to model the effects of the atmospheric and dust deposition of nitrogen and phosphorus on the Mediterranean's biogeochemistry by Richon et al. (2018). Pagès et al. (2020b) using a coupled physical-biogeochemical 3D model (NEMO-MED12/Eco3M-Med), showed the impact of the variations in river input during the last decades on the biogeochemical cycle of phosphorus and carbon, particularly in the Eastern Mediterranean Basin.

High-resolution future projections of the physical and biogeochemical state of the Mediterranean Basin have also been developed. These analyses showed the Mediterranean as a prone region to climate change with the increasing temperature trend. Pagès et al. (2020a) suggested an enhancement in the oligotrophic status of the sea and a 14 % decrease in the primary production over the basin. They also estimated a reduction of 38 % of large phytoplankton abundance in the eastern basin and a further limitation in nitrate in the surface. Reale et al. (2022) also reported changes in nutrient content and net primary production, however, they emphasized the decrease in the oxygen concentration in the surface and intermediate layers of the Mediterranean due to the temperature increase in the water column and the strengthening of community respiration. In their projection, the atmospheric CO2 absorption rises in the surface leading to an increase in inorganic carbon concentration and in the acidification of the basin. This study is in agreement with the findings of Solidoro et al. (2022), who found an increment in the *Dissolved Inorganic Carbon* (DIC) pool in the basin.

Other modeling studies were also implemented on a regional scale, to study the influence of upwellings, deep water convection, and the dense water formation in the NW Mediterranean (Pinazo et al., 1996; Tusseau et al., 1997; Lévy et al., 1998; Raick et al., 2005; Herrmann et al., 2008, 2013; Ulses et al., 2016; Kessouri et al., 2018) and other regions: the Alboran Sea (Macías et al., 2014a), the Adriatic Sea (Zavatarelli et al., 2000; Polimene et al., 2007), Aegean and Levantine Sea (Mattia et al., 2013).

Modeling of the Levantine Basin

A small number of modeling studies have focused on the Levantine basin. A 1D coupled hydrodynamic - biogeochemical modeling has been carried out in the Rhodes Gyre (Napolitano et al., 2000). The authors estimated the primary production in the Rhodes Gyre and described its seasonal variability. The strength of the atmospheric cooling influences the intensity of vertical mixing in winter months and thus primary production. Reduced cooling led to a shallower mixed layer and lower vertical mixing and hence a weaker nutrient supply. The hydrodynamic variability of the Rhodes and the Ierapetra gyres was also assessed by Marullo et al. (2003) from the pre-conditioning to the spreading of the Levantine Intermediate Waters over the period 1994-1995. They studied the hydrodynamic variability of Rhodes and Ierapetra gyres.

The biogeochemical dynamic of the eastern basin in the 1990s was also studied by Mattia et al. (2013). They used the coupled NEMO - BFM models to describe the simulated changes in the dynamics of the physical and biogeochemical features in the eastern Mediterranean during the EMT episode. Petihakis et al. (2009), using the BFM model, were able to reproduce the variability of chlorophyll, from the eutrophic to extremely oligotrophic areas of the eastern basin and they also emphasized on the influence of vertical mixing on the primary production rates.

Lastly, Van Cappellen et al. (2014) and Powley et al. (2014) implemented a mass balance model to simulate the P and N cycles during the period 1950–2000. Powley et al. (2014) used this model and found that one-third of the P supplied was exported to the Western Mediterranean Sea through the LIW outflow, while another third was exported to the EMDW. These mechanisms favored the limitation of P by drawing it away from the primary producers.

1.4 Conclusion

3D numerical studies of the planktonic pelagic ecosystem in the Mediterranean have highlighted the essential role of physical processes in the evolution of pelagic plankton in the Mediterranean. However, the review of the current coupled hydrodynamic-biogeochemical studies presented for the Mediterranean basin indicates the small number of attempts to study the variability of the biogeochemical cycles in the LIW formation basin: the Levantine basin. We propose here to develop a tool to investigate the biogeochemical cycles in this region, and more specifically the Rhodes Gyre, where the LIW, flowing in and influencing hydrodynamics and biogeochemistry of the whole Mediterranean, is mostly formed.

Chapter 2

The numerical tools and observations

Contents

In this chapter, we will be presenting the 3D hydrodynamic-biogeochemical coupled models used in this Ph.D. thesis. First, the hydrodynamic and biogeochemical models will be described, then a presentation of the chosen study area will be given. Finally, a list of the available observational data which have been used for model validation is provided.

2.1 The coupled hydrodynamic - biogeochemical model

2.1.1 The hydrodynamic model

To simulate the evolution of the hydrodynamics conditions in the basin, a 3D primitive equation ocean model, SYMPHONIE, with a free surface was used. The SYMPHONIE model has been primarily used to describe the response to wind forcing and the dynamics of the Rhone plume (Estournel et al., 1997, 2001; Marsaleix et al., 1998), the coastal circulation in the Gulf of Lion (Estournel et al., 2003; Petrenko et al., 2008), the coastal dense water formation (Estournel et al., 2005; Ulses et al., 2008), the open sea convection (Herrmann et al., 2008; Estournel et al., 2016; Ulses et al., 2016), the shelf-slope exchanges in the Gulf of Lion (Mikolajczak et al., 2020) and the circulation in the Eastern Mediterranean (Estournel et al., 2021). The model is described in detail in Marsaleix et al. (2006, 2008); Estournel et al. (2016) and Damien et al. (2017). It calculates primitive equations for momentum, physical tracers, sea level, and turbulent closure variables on an Arakawa type C grid using numerical finite difference methods. The model parameterizes the effects of the sub-mesh turbulence with either the scheme of Gaspar et al. (1990) or the K-epsilon scheme.

2.1.2 Implementation of the hydrodynamical model

The domain of the model engulfs the Mediterranean Sea as well as the Marmara Sea and reaches 8° west of the gulf of Cadiz (Estournel et al., 2021). The horizontal grid is characterized by a resolution that varies between 2.3 and 4.5 km north–south and west–east for a better representation of the mesoscale processes and with the increase of the Rossby deformation radius. As for the Gibraltar Strait, a narrowing was conducted with a 1.3 km grid for a better representation of the exchange area between the Mediterranean and the Atlantic Ocean. The bathymetry of the model is based on the GEBCO database. The vertical grid has 60 levels with closer levels ranging near the surface. A vanishing quasi sigma (VQS) vertical coordinate concept (Dukhovskoy et al., 2009) was used for a better representation of the bathymetry, as well as the reduction of the errors associated with the sigma, coordinates (Siddorn and Furner, 2013; Graham et al., 2018).

Daily analyses of the configuration PSY2V4R2 based on the NEMO ocean model at a resolution of 1/12° over the Atlantic and the Mediterranean operated by the Mercator – Ocean International operational system are used for the initialization of the model (Lellouche et al., 2013). They are also used for the forcing of the western lateral boundaries. Based on Estournel et al. (2016), observations covering all the Mediterranean were used for the stratification debiasing of the initial state for a better representation of the mesoscale characteristics.

The exchanges between the Black Sea and the Marmara Sea are controlled by the net flow of water through the Bosphorus Strait. Based on Unlulata et al. (1990), the flow is defined at 300 km^3 $year^{-1}$ to which was added a seasonal cycle described in Tugrul et al. (2002). The

Marmara Sea is characterized by a two-layer structure. A relaxation was imposed toward a temperature of 14.5°C and a salinity of 38.6 for depths greater than 22 m with a relaxation time of 20 days.

Other than the open boundary conditions, the hydrodynamic model is forced using 2 external forcing types: the river discharges and the atmospheric fluxes. The atmospheric forcing is calculated through a bulk formula using the hourly operational forecasts of ECMWF at 1/8° horizontal resolution. The spatial resolution of air-sea forcing seems enough resolved to depict the general circulation of the Mediterranean Sea, in particular cyclonic and anticyclonic gyres, and the water formation controlling the intermediate and deep circulation.

The solar flux penetration in the surface layer was parameterized based on satellite observations. Paulson and Simpson (1386) divided the solar flux into two bands, the first band is absorbed over the first tens of centimeters while the other is over the first tens of meters. The deeper attenuation extinction concerning the 42% of the solar flux was calculated based on the monthly averages of the OLCI Diffuse Attenuation Coefficient at 490 nm (product Copernicus Marine Service: OCEANCOLOUR_MED_OPTICS_L4_NRT_OBSERVATIONS_009_039) over a period of 3 years followed by the interpolation of the data over our model's grid. The water transparency increases going from the west to the east and decreases in coastal areas. The attenuation values of the depth used for the exponential attenuation law were adjusted between 10 and 30 m based on temperature profile comparisons in the Levantine Basin and the Gulf of Lion.

A total of 142 rivers are considered in the model: 136 in the Mediterranean and 6 in the Gulf of Cadiz. Rivers with few data like the ones located on the Spanish and the Tyrrhenian coasts as well as Algeria and Tunisia were assigned a constant discharge value according to the literature, in contrast with 10 French rivers plus Ebro, Arno, and Po rivers with daily discharge measurements set. Rivers discharge on the Greek and Turkish coasts are based on the seasonal climatology of Poulos et al. (1997). As for the rivers of the Levantine Basin, the same procedure was used, except for the Nile River where the discharge value was set to 475 $m^3\ s^{-1}$, this value being estimated by Nixon (2003) following the Aswan damming. To properly reconstruct the dense water formation on the eastern Adriatic coast, 26 rivers completed the Po so that the average annual flux over 2012-2019 (north of 40°N) is 137 m^3 $year^{-1}$.

An additional forcing to the simulation is applied by tides with 9 tidal waves: M2, M2, S2, K2, K1, O1, P1, Q1, M4. At the Atlantic open boundaries, the harmonic analysis of FES2014 (Lyard et al., 2021), and the tidal generating potential mentioned in Pairaud et al. (2008) were used.The time step is 208 s. The hydrodynamic model ran from April 2011 to April 2021. Mean daily outputs were stored every day.

2.1.3 The biogeochemical model

Eco3M-S is a biogeochemical multi-nutrient and multi-plankton functional type model, representing the dynamics of the pelagic plankton ecosystem. It follows the temporal evolution of 36 state variables previously described by Herrmann (2008); Auger et al. (2011); Kessouri et al. (2015) and Ulses et al. (2021). The model was previously used to study the pelagic ecosystem in the Rhone river plume (Auger et al., 2011), the dynamics of nutrients and particulate organic carbon in the Gulf of Lion shelf (Many et al., 2021), and the biogeochemical processes in the NW Mediterranean deep convection area (Herrmann et al., 2013; Auger et al., 2014; Ulses et al., 2016; Kessouri et al., 2017, 2018; Ulses et al., 2021). It describes the biogeochemical cycles of the following biogenic variables: carbon (C), nitrogen (N), phosphorus (P), silicium (Si), dissolved oxygen (O2), and chlorophyll (Chl). The model is constituted of 8 compartments, every compartment being expressed based on the elements constituting it: **Dissolved Inorganic Matter** (DIM) or **nutrients** (v), nitrate NO3 (N), ammonium NH_4^+ (N), phosphate PO_4- (P), and silicate H_3SiO_4 (Si), **dissolved oxygen**, **phytoplankton** represented by three size classes (micro, nano, picophytoplankton), **zooplankton** (C) formed of three size classes (nano, micro, mesozooplankton), **bacteria** (C), **Particulate Organic Matter** (POM), divided into two groups based on their sinking velocity(we will refer to small and large POM in the following), and **Dissolved Organic Matter** (DOM) under the form of N, P and C.

The internal composition (ratios of the elements composing the organisms) of phytoplankton in the model is variable The representation of phytoplankton follows the model of Eco3m developed by Baklouti et al. (2006) on one hand. On the other hand, zooplankton and bacteria formed of nitrogen and phosphorus have constant (N:C) and (P:C) ratios in the model meaning their composition depends on the internal carbon concentration. Their representation is based on the model of Anderson and Pondaven (2003).

A summary diagram of the food web structure of the model and the interactions between the compartments is represented in Fig. 2.1. In the following sections, the biogeochemical processes involved in the functioning of the different planktonic groups are detailed for each group as well as a summary of the interactions and the processes equations. Detailed model description can be found in Appendix A.

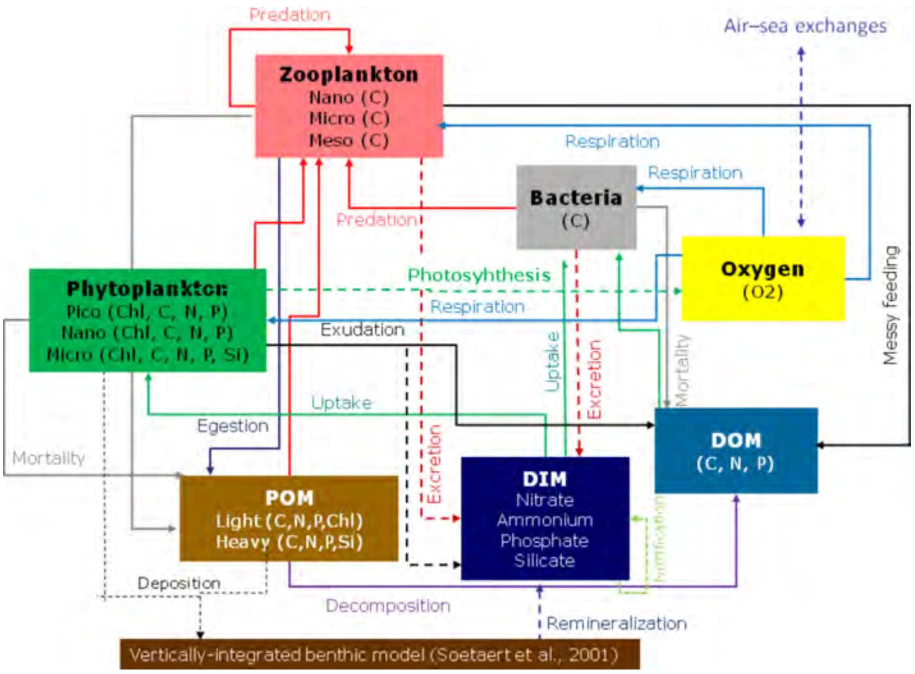

Figure 2.1: Schematics of the biogeochemical model Eco3M-S

2.1.3.1 Phytoplankton

Based on their size, phytoplankton is divided into 3 groups, from the largest to the smallest: microphytoplankton, $XPhy_3$ ($>$ 20µm, X=[C,N,P,Si,Chl]), mainly formed of diatoms followed by nanophytoplankton, $XPhy_2$ (2- 20 µm, X=[C,N,P,Chl]), mainly formed of cryptophytes and chromophytes (dinoflagellates) and picophytoplankton, $XPhy_1$ ($<$ 2µm, X=[C,N,P,Chl]), represented by the Synechococcus. The 3 phytoplanktons are all composed of chlorophyll, carbon, nitrogen and phosphorus. In addition, micro-phytoplankton is also composed of silicium. The micro-phytoplankton group possesses a sinking rate contrary to the other groups. The dynamics of the phytoplankton compartment is controlled by the following processes: gross primary production, synthesis of chlorophyll, uptake of nutrients, respiration, exudation of dissolved organic matter following the absorption of nutrients, exudation of dissolved organic carbon, respiration related to the nutrients uptake, natural mortality and grazing. During photosynthesis, phytoplankton transform dissolved inorganic carbon into organic carbon. The fixation of the carbon is dependent on the availability of nutrients. The other components forming the phytoplankton such as N, P, Si, come from the nutrients uptake. In case of excess of one of the elements compared to the carbon, exudation of the excess nutrient takes place in the organic form of the element. As for the synthesis of the chlorophyll, it is driven by the absorption of the nitrogen and a maximum ratio between chlorophyll and nitrogen, and light availability. The natural mortality of phytoplankton contributes to the formation of detritus. The equations below represent the rate of change of the carbon (C), nitrogen (N), phosphorus (P) and silicium (Si) (only for micro-phytoplankton) concentrations in phytoplankton. Index i refers to the phytoplankton group. *GPP* stands for gross primary production, *RespPhy* for phytoplankton respiration, *Exu* for exudation, *MortPhy* for phytoplankton mortality, *Graz* for zooplankton grazing, *UptPhy* for nutrient uptake and *SynthChl* for production of chlorophyll.

$$\frac{dCPhy_i}{dt} = GPP_i - RespPhy_i - Exu_{i,C} - MortPhy_{i,C} - \sum_{j=1}^{3} Graz_{j,CPhy_i} \tag{2.1}$$

$$\frac{dNPhy_i}{dt} = \sum_{j=1}^{2} UptPhy_{i,Nut_j} - Exu_{i,N} - MortPhy_{i,N} - \sum_{j=1}^{3} Graz_{j,NPhy_i} \tag{2.2}$$

X=P,Si

$$\frac{dXPhy_i}{dt} = UptPhy_{i,XO_4} - Exu_{i,X} - MortPhy_{i,X} - \sum_{j=1}^{3} Graz_{j,XPhy_i} \tag{2.3}$$

$$\frac{dChlPhy_i}{dt} = SynthChl_i - MortPhy_{i,Chl} - \sum_{j=3}^{3} Graz_{j,ChlPhy_i} \tag{2.4}$$

2.1.3.2 Zooplankton

The zooplankton description is based on the model of Anderson and Pondaven (2003), adapted by Raick et al. (2005) in the Ligurian Sea. Zooplankton is divided into 3 size based classes: nano-zooplankton [$<$ 20µm] represented by small ciliates and bacterivorous flagellates, micro-zooplankton [20µm $<$ diameter$<$ 200µm] composed of ciliates and flagellates and meso-zooplankton [> 200µm] represented by the copepods. The main processes driving the dynamics of the zooplankton biomass are predation, excretion, sloppy feeding, egestion, respiration, mortality, and grazing. Zooplankton feeds on phytoplankton, bacteria, detritus, and zooplankton. After the feeding of zooplankton, a part of the prey is not ingested: this process is called messy feeding, sustaining the dissolved organic matter pool. Another part of preys is discarded as detritus during egestion, producing fast and slow sinking fecal pellets. Chlorophyll and silicium are entirely discarded because they are not accounted for in the composition of the zooplankton. The constant internal composition is maintained by the excretion of inorganic dissolved matter and determines the zooplankton growth. The mortality of zooplankton contributes to the production of fast and slow sinking particles. The equation below gives the rate of change of the carbon concentration in class i of zooplankton. *GrowthZoo* represents growth, *Graz* grazing of the 3 classes (index j) on the class i, *RespZoo* the respiration, *MortZoo* the natural mortality for classes 1 and 2, and *PredZoo* is the mortality and predation of the largest class by the higher trophic levels not represented in the model.

$$\frac{dCZoo_i}{dt} = GrowthZoo_{i,C} - \sum_{j=1}^{3} Graz_{j,CZoo_i} - Respzoo_i^{add} - (\delta_{i,1}+\delta_{i,2}) MortZoo_{i,C} - \delta_{i,3} PredZoo_{3,C} \tag{2.5}$$

Growth results from the balance between grazing on the different prey and losses by egestion and messy feeding.

$$GrowthZoo_{i,C} = K_{c,Zoo_i}.(Graz_{i,C_{prey}} - Eges_{i,C} - MessyFeeding_{i,C}) \tag{2.6}$$

2.1.3.3 Bacteria

Similarly, as for zooplankton, bacteria have a constant internal composition. The description of bacteria is also based on the model of Anderson and Pondaven (2003). While this latter was modified to take into consideration the potential limitation of dissolved organic carbon, nitrogen, or phosphorus. Uptake of DOM, respiration, excretion of nutrients, grazing, and mortality are the processes driving the dynamics of the bacteria compartment. Bacteria feed on the dissolved organic matter primarily. However, when DON or DOP are unavailable they can compete with phytoplankton on inorganic nitrogen (ammonium) and/or phosphate to maintain their internal N:P ratio. Their main role is the remineralization of dissolved organic matter. Excretion, respiration, and nutrient uptake help to maintain their constant stoichiometry. Their mortality feeds the DOM pool. The equation below represents the rate of change of the carbon concentration of bacteria. *GrowthBac* is bacteria growth, *MortBac* is mortality and *Graz* grazing by the class j of zooplankton.

$$\frac{dCBac_i}{dt} = GrowthBac - \sum_{j=1}^{3} Graz_{j,CBac} - MortBac_C \tag{2.7}$$

2.1.3.4 Particulate organic matter (POM)

It is divided into two main groups based on their sinking velocity: slow and fast sinking particles, referred also as small and large POM. These particles come from dead phytoplankton and zooplankton as well as the egestion of zooplankton. They are consumed by zooplankton and remineralized into inorganic matter. Particulate organic carbon, nitrogen, and phosphorus discarded during egestion contribute to small particles. The egestion of silicium produces small and large particles. The equations below represent the rate of change of the different elements' concentration in the light detritus (DetL) and heavy detritus (DetH). Phytoplankton mortality and zooplankton egestion feed only the small particles. Zooplankton mortality feeds both particle types.
X ϵ [C, N, P]

$$\begin{aligned}\frac{dXDet_L}{dt} &= \sum_{i=1}^{3} MortPhy_{i,X} + \sum_{i=1}^{3} Eges_{i,X} + \sum_{i=1}^{2} fr_{Det_L}^{MortZoo_i} MortZoo_{i,X} + \\ &\quad fr_{Det_L}^{MortZoo_3} PredZoo_{3,X} - Deg_{XDet_L} - \sum_{j=1}^{3} Graz_{j,XDet_L}\end{aligned} \tag{2.8}$$

$$\frac{dSiDet_L}{dt} = MortPhy_{3,Si} + fr_{Det_L}^{Eges_{Si}} \sum_{i=2}^{3} Eges_{i,Si} - Deg_{SiDet_L} \tag{2.9}$$

X ϵ [C, N, P]

$$\begin{aligned}\frac{dXDet_H}{dt} &= \sum_{i=1}^{2}(1 - fr_{Det_L}^{MortZoo_i}) MortZoo_{i,X} + (1 - fr_{Det_L}^{MortZoo_3}) PredZoo_{3,X} \\ &\quad - Deg_{XDet_H} - \sum_{i=1}^{3} Graz_{i,XDet_H}\end{aligned} \tag{2.10}$$

$$\frac{dSiDet_H}{dt} = (1 - fr_{Det_L}^{Eges_{Si}}) \sum_{i=2}^{3} Eges_{i,Si} - Deg_{SiDet_H} \tag{2.11}$$

The parameter fr and the value of 1-fr define the fractions of a process attributed to light and heavy detritus, respectively.

2.1.3.5 Dissolved organic matter (DOM)

DOM is usually released during phytoplankton exudation, as well as messy feeding by zooplankton. It also derives from the mortality of bacteria. DOM is consumed by bacteria. The equation below represents the rate of change of DOM. *DegDetL* and *DegDetH* are the light and heavy detritus degradtion. *UptBac* is the uptake of bacteria.
X ϵ [C, N, P]

$$\frac{dDOX}{dt} = \sum_{i=1}^{3} Exu_{i,X} + \sum_{i=1}^{3} MessyFeed_{i,X} + MortBac_X + Deg_{X,Det_L} + Deg_{X,Det_H} - UptBac_{DOX} \tag{2.12}$$

2.1.3.6 Dissolved inorganic matter (DIM) or nutrients

Four dissolved inorganic nutrients are considered in the model. For nitrogen, two nutrients are distinguished, nitrate and ammonium. They have distinctive roles in the functioning of the pelagic ecosystem. Nitrate is consumed by the phytoplankton, it is considered as part of the new primary production, and is the result of nitrification. The rate of change of nitrate is given by the balance between nitrification (*Nitrif*) and uptake by phytoplankton (*UptPhy*):

$$\frac{dNO_3}{dt} = Nitrif - \sum_{i=1}^{3} UptPhy_{i,NO_3} \tag{2.13}$$

Ammonium is considered part of regenerated production. It is consumed by phytoplankton and bacteria and also excreted by bacteria and zooplankton. Its nitrification by bacteria produces nitrate:

$$\frac{dNH_4}{dt} = \sum_{i=1}^{3} ExcZoo_{i,NH_4} + ExcBac_{NH4} - Nitrif - \sum_{i=1}^{3} UptPhy_{i,NH_4} - UptBac_{NH_4} \tag{2.14}$$

The inorganic phosphorus, phosphate, is consumed by heterotrophic bacteria and phytoplankton and excreted by heterotrophs:

$$\frac{dPO_4}{dt} = \sum_{i=1}^{3} ExcZoo_{i,PO_4} + ExcBac_{PO4} - \sum_{i=1}^{3} UptPhy_{i,PO_4} - UptBac_{PO_4} \tag{2.15}$$

Silicate is used by diatoms for their shell building. Silicate originates from exudation by phytoplankton as well as from the dissolution of small and large detritus. Index 3 represents the 3rd class of phytoplankton, micro-phytoplankton.

$$\frac{dSiO_4}{dt} = Excu_{3,Si} + Diss_{SiDet_L} + Diss_{SiDet_H} - UptPhy_{3,SiO_4} \tag{2.16}$$

2.1.3.7 Dissolved oxygen

The processes driving the dynamics of dissolved oxygen are gross primary production, autotrophic and heterotrophic respirations, and nitrification.

$$\begin{aligned}\frac{dDOx}{dt} = \sum_{i=1}^{3}(GPP_i - RespPhy_i)_{\gamma C/DOx} - \sum_{i=1}^{3}(RespZoo_i + RespZoo_i^{add})_{\gamma C/DOx} \\ -RespBac_{\gamma C/DOx} - Nitrif_{\gamma NH_4/DOx}\end{aligned} \tag{2.17}$$

The dissolved oxygen concentration is represented by *dDox*. *GPPi* and *RespPhyi* are gross primary production and respiration, respectively, for phytoplankton group i. *RespZooi* and $RespZooi^{add}$ are basal respiration and additional respiration fluxes to maintain constant N:C and P:C internal ratios, respectively, for zooplankton group I, *RespBac* is bacterial respiration and *Nitrif* nitrification. $\gamma_{C/DOx}$ and $\gamma_{NH_4/DOx}$, equal to 1 and 2, respectively, are the mole of *Dox*, used per mole of C in respiration and needed to oxidize one mol of ammonium in nitrification as described in Grégoire et al. (2008).

2.1.3.8 Benthic model

The model is coupled to a simplified benthic model described by Soetaert et al. (2001). This model calculates the upward nutrient flux at the water-sediment interface as a function of the deposit of particulate matter on the seafloor. To calculate the flux of inorganic nutrients (nitrate, ammonium, phosphate, and silicate) from the sediment to the water column and the oxygen flux integrated from the water column into the sediment, the benthic model uses the deposition flux of the organic matter from the biogeochemical model. The nitrate and ammonium fluxes are determined based on biogeochemical processes such as mineralization, nitrification, and denitrification. The phosphate flux is deduced from the inorganic ammonium based on an N:P ratio. As for the silicate flux, it represents the deposition flux of Si detritus.

2.1.4 Coupling of the hydrodynamic and biogeochemical models

The hydrodynamic model is used to describe the spatial and temporal evolutions of the biogeochemical state variables due to advection and mixing processes. The biogeochemical model calculates the biogeochemical source/sink terms of the biogeochemical state variables at each grid point. The evolution of each biogeochemical variable C is given by the following equation:

$$\frac{\partial C}{\partial t} + \frac{\partial uC}{\partial x} + \frac{\partial vC}{\partial y} + \frac{\partial (W - W_{sed})C}{\partial z} = \frac{\partial}{\partial z} k_v \frac{\partial C}{\partial z} + \frac{\partial C}{\partial t})_{bio} \tag{2.18}$$

Where u, v, and w are the three components of the current velocity, K_v is the vertical diffusivity calculated by the hydrodynamic model, w_{sed} is the settling velocity of the variable C, the last term represents the biogeochemical source/ sink term for the variable C.

To couple the models, the “Source splitting” technique (Butenschön et al., 2012) was used, because of the difference in the model’s time scales. Advection needs a shorter time step than the biogeochemical model. As a consequence, the biogeochemical source/sink term is calculated at a lower frequency than that of the Eulerian transport by the physical fields calculated from time-interpolated daily outputs from SYMPHONIE.

The photosynthetically available irradiance at the surface, PAR_{surf}, is assumed to be 43 % of the three-hourly fields of sea solar radiation provided by the meteorological ECMWF model. The percent of reflected irradiance, i.e. albedo, is set to 0.05. The attenuation with the depth of the light available for photosynthesis with depth is computed by distinguishing the parts of light penetrating in low and short wavelengths as follows:

$$\begin{aligned} PAR(z) = PAR_{surf}(1 - albedo)(p_1.e^{-\int_0^z k_{w,l}+k_{p,l}\sum_{i=1,3} ChlPhy_i(z)^{lc_l}dz}+ \\ (1-p_1)e^{-\int_0^z k_{w,s}+k_{p,s}\sum_{i=1,3} ChlPhy_i(z)^{lc_s}dz} \end{aligned} \tag{2.19}$$

where p_l is the percent of PAR with a long wavelength and is set to 0.5, k_w is the background extinction coefficient of water (m^{-1}), chosen as in Pope and Fry (1997), k_p is the extinction coefficient due to self-shading of phytoplankton cells and lc constants chosen as in Bricaud et al. (2004). *ChlPhyi* is the chlorophyll concentration in phytoplankton i. The indices “s” and “l” stand for short and long wavelengths (0.00635m, and 0.45m respectively).

2.1.4.1 Implementation of the biogeochemical model

To save computing time, the biogeochemical model is run offline using the daily average outputs (temperature, salinity, three current velocities, and turbulent coefficient) of the physical model. Then, the impacts of biogeochemical properties on hydrodynamics are not taken into account. We used a time step of 10 minutes for the advection and diffusion of the biogeochemical variables and a time step of 2 hours for the calculation of the source/sink terms. The model was run from June 2011 to December 2013. The first two years were considered as a spin-up and then not analyzed.

2.1.4.2 Initial and boundary conditions

We initialized the biogeochemical model with observation profiles averaged over 10 regions of the Mediterranean Sea for the summer of 2011. For inorganic nutrient profiles, we used the CARIMED (CARbon, tracer, and ancillary data In the MEDsea database (Álvarez et al., 2019), considering only summer data over the period 2011-2012 since the simulation starts in August.

Regarding the dissolved oxygen and chlorophyll concentrations, we initialized using summer in situ observations from BioGeoChemical-Argo floats (BGC-Argo, Argo, 2022) and the CARIMED database.

Solar radiation and wind forcing for the biogeochemical simulation are those used for the hydrodynamic simulation. Atmospheric depositions of inorganic nutrients were taken into account. Nitrate atmospheric depositions were applied as constant values based on the results of Kanakidou et al. (2012); Ribera d’Alcalà et al. (2003); Powley et al. (2017) and Richon et al. (2018) and silicate deposition was prescribed as constant values for western (west of the Sicily Strait) and eastern basins based on estimates given by Ribera d’Alcalà et al. (2003). It should be noted that in this study, we did not focus on the parametrization of the silicate because of the basin limitation in phosphate and nitrate. We deduced phosphate deposition from monthly Saharan dust deposition modeled with the regional model ALADIN-Climat (Nabat et al., 2015) and averaged over the period 1979-2016. We hypothesized that phosphorus represents 0.07 % of dust and that 15 % is in soluble form (Herut and Krom, 1996; Guerzoni et al., 1999; Ridame and Guieu, 2002; Richon et al., 2017). Nutrient fluxes at the water column/sediment interface have been obtained through a coupling of the biogeochemical model with a simplified version of the vertically integrated benthic model

described by Soetaert et al. (2000). At the river mouths, concentrations of nutrients were imposed at the sub-basin scale using the dataset of Ludwig et al. (2010). In the Atlantic Ocean, nutrients were prescribed using monthly profiles from the World Ocean Atlas 2009 climatology (https://odv.awi.de/en/data/ocean/world-ocean-atlas-2009/) at 5.5 °W. In the Marmara Sea, in order to represent a two-layer flow regime, we imposed a relaxation with a timescale of 1 day towards nitrate concentrations of 0.24 and 1.03 mmol N m^{-3} and phosphate concentrations of 0.06 and 0.05 mmol P m^{-3} for depths above and below 15 m respectively, based on the observations near the Dardanelles Strait from Tugrul et al. (2002).
As for the flux of oxygen at the air and sea interface, it was calculated using

$$DOx_{Flux} = Kw(DOx_{sat} - DOx_{surf}) \tag{2.20}$$

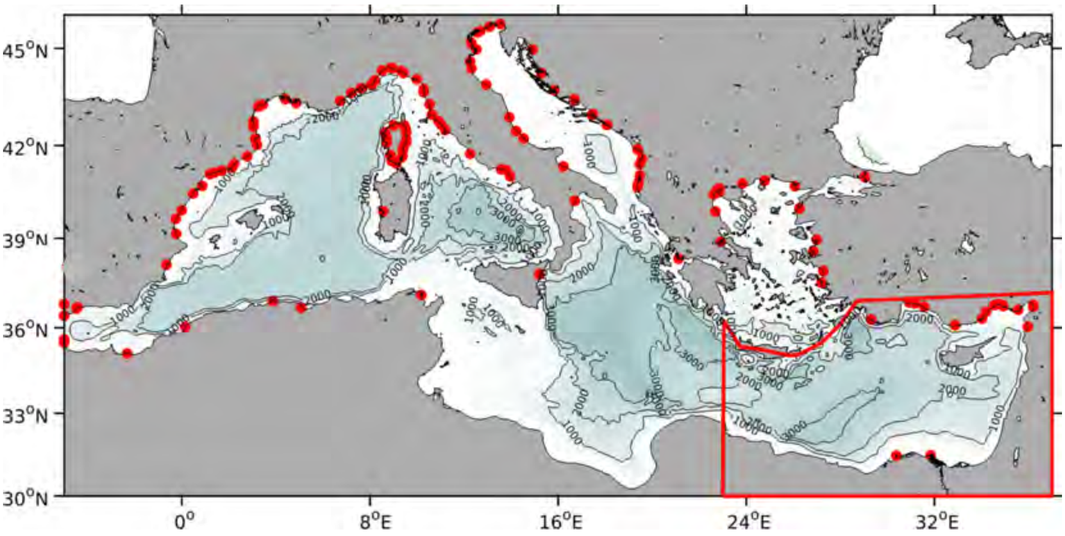

Figure 2.2: Bathymetry of Mediterranean. The red box shows the study area, and the red circles indicate the river input.

The dissolved oxygen at saturation (*Doxsat*) level is determined using the equation of Garcia and Gordon (1992). For the gas transfer velocity (*Kw*) we used the parameterization of Wanninkhof and McGillis (1999) with a cubic dependency to the wind.

2.2 Observations

During this thesis, 3 types of data have been used in order to assess the realism of the numerical models: data from satellite images, cruise, and BCG Argo floats.

Satellite images

We used the surface chlorophyll concentration derived from daily Level 4 reprocessed data, obtained from the EU Copernicus Marine Environment Monitoring Service (CMEMS) from the website (http://resources.marine.copernicus.eu/, OCEANCOLOUR_MED_CHL_L4_REP_OBSERVATIONS_009_078) with a spatial resolution of 1 km, for the period 2012-2020. This regional product is based on daily interpolated chlorophyll concentrations from multi-sensors (MODIS-Aqua, NOAA-20-VIIRS, NPP-VIIRS, MERIS sensors) for the Mediterranean Sea (Volpe et al., 2007, 2012). The data underwent a temporal averaging method and/or interpolation procedure to fill in missing data values. The applied regional color algorithm has increased the accuracy of the product, especially for the low chlorophyll values characterizing the eastern Mediterranean. The use of the MEDOC4 algorithm (Volpe et al., 2007, 2012) has reduced the overestimation (compared with in situ data) making this product suitable to study the oligotrophic eastern basin. To compare with model results, the data were interpolated on the model grid.

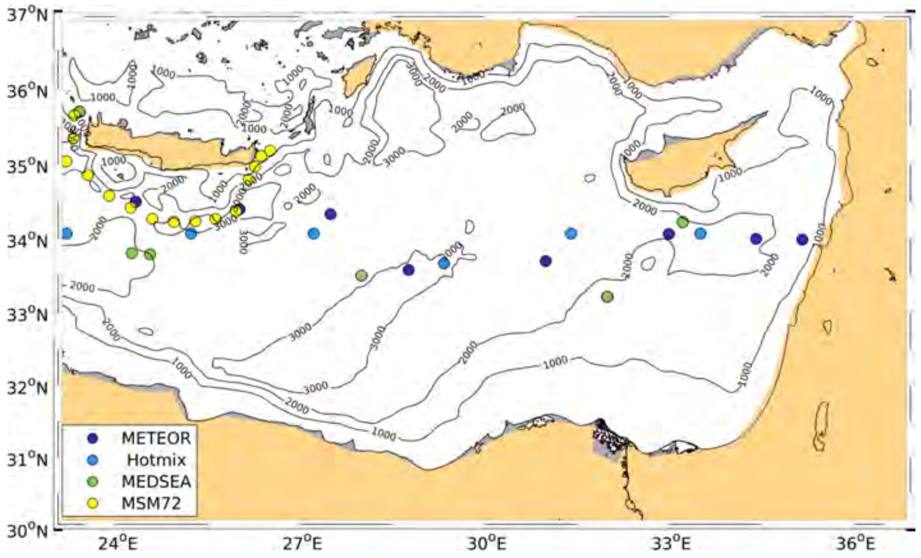

Figure 2.3: Map showing the CARIMED database. Each color represents a cruise.

Cruise database

Various observational cruises have been conducted in the Mediterranean Sea with the aim of sampling biogeochemical variables (O2, nutrients, carbon). Sampling was heavily concentrated in the western basin. The low number of observations in the East is an important obstacle to the evaluation of the model, especially for the Levantine Basin. Several efforts to compile the measurements made during campaigns at sea in a homogeneous and quality data set have been made. In this study we use the CARIMED database (CARbon in the MEDiterranean Sea) combining cruises all over the Mediterranean Sea from 2011-2019. Figure 2.3 shows the observation locations in the Levantine Sea. This dataset includes cruises with only best practiced standards for nutrients following the protocol of the GO-SHIP and the WOCE. Fourrier et al. (2020) added observations from 10 other cruises to the dataset and validated them. The data are available on figshare (Fourrier, 2020). We focused on observations collected during four cruises that covered the far-most east and south of the basin: the Meteor cruise M84/3 Tanhua (2013), Hotmix, MEDSEA(Ziveri and Grelaud, 2015)and MSM72 (Hainbucher et al., 2019)for the period between 2011-2018 (Álvarez et al., 2019)). All cruises followed the same sampling network. The seawater was collected using Niskin bottles from the surface to 4600 m using an SBE43 oxygen sensor for the oxygen concentrations followed by the modified Winkler potentiometric method (Hotmix, Martínez-Pérez et al. 2017). The inorganic nutrients were determined following the colorimetric methods of Wangersky (1978).

This study also takes advantage of biogeochemical measurements made in the context of the PERLE (Pelagic ecosystem response to dense water formation in the Levant experiment) experiment, during the period from October 2018 till March 2019 (D'Ortenzio et al., 2021). PERLE-1 covers the period of the preconditioning in the Levantine Basin in October 2018, and PERLE-2 (Durrieu de Madron and Conan, 2019)the dense water formation during February-March 2019. We used nutrient and O2 data from these cruises to validate our model. The spatial coverage of PERLE-1 and PERLE-2 observations is shown in Figure 2.4.

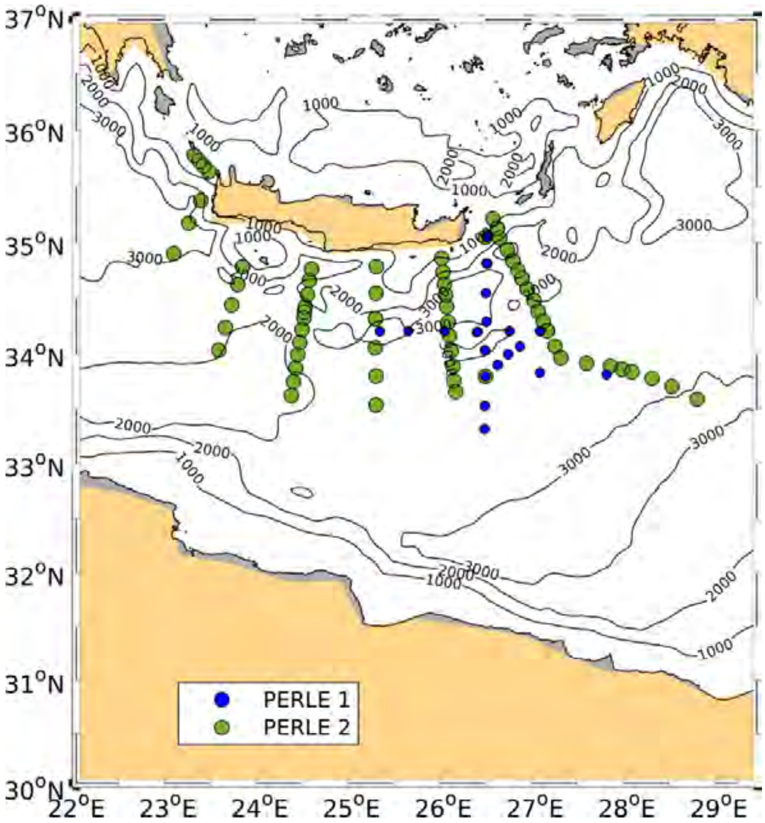

Figure 2.4: Map showing the PERLE1 and PERLE2 stations of observations used for the model assessment.

BGC Argo floats

We used observations from BGC Argo floats (Argo, 2022) deployed in the eastern basin downloaded from the Argo Global Data Assembly Center web portal accessible through the Coriolis database (http://www.coriolis.eu.org). 11 floats (10 floats provide chlorophyll data, 7 provide dissolved oxygen, 6 are in common) located in the eastern basin covering 2013-2021 were acquired. Downloaded parameters included float number, position, time, pressure, oxygen and chlorophyll. The data have been pre-processed with quality control methods and only values with "good" QC flag were kept. The floats' trajectories can be found in the

Appendix B.

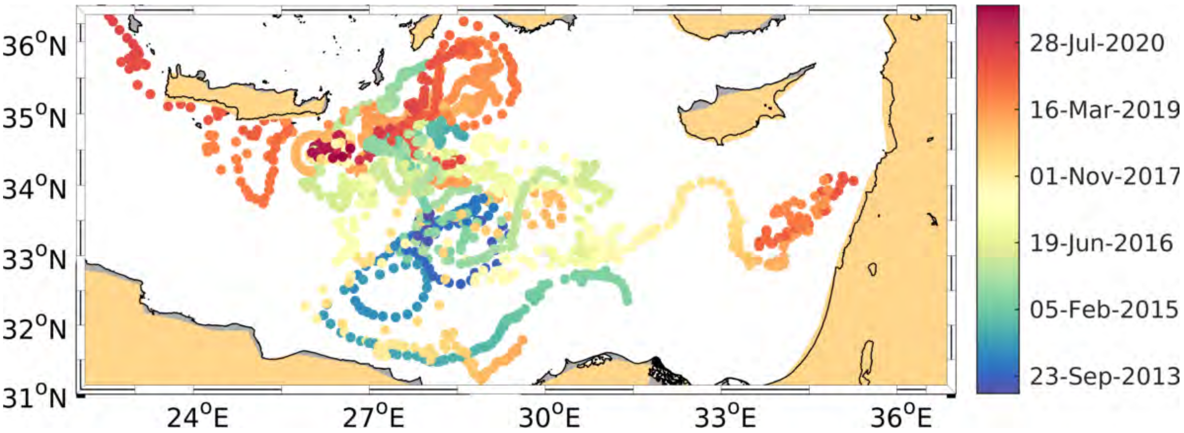

Figure 2.5: Map showing the temporal sequence of the BGC Argo floats profiles used in this study

Observation uncertainties

Ocean color constitutes an important tool to understand the functioning of the planktonic ecosystems in the Ocean. It has been used to gather information about different variables (e.g. chlorophyll, primary production,..), especially for regions with sampling and geopolitical constraints such as the Levantine Basin. Nonetheless, its efficient exploitation requires careful calibration and validation of the datasets. Ocean color has been widely used for observational as well as for modeling studies (Volpe et al., 2012). One of the most important organic carbon proxies is the surface chlorophyll concentration whose accuracy has been estimated to be 35 % for the global ocean (Mueller and Austin, 1995; McClain et al., 2006). Many studies have tried to assess the errors of the standard global products in the Mediterranean Sea (Bricaud et al., 2002; D'Ortenzio et al., 2002; Volpe et al., 2007). They found that uncertainties in satellite outputs might be the result of the optical properties of the Mediterranean water column characterized by oligotrophic waters, less blue and greener than the Global Ocean (Volpe et al., 2007), leading to an overestimation of the chlorophyll concentration by standard global algorithms e.g Bricaud et al., 2002; D'Ortenzio et al., 2002. Following D'Ortenzio and Ribera d'Alcalà (2009), this bias is of 30 % on average in the Mediterranean Sea when juxtaposed with in situ data. Recently, more accurate regional bio-optical algorithms (e.g., MedOC4 used for the comparisons) have been implemented in the Mediterranean Sea (Volpe et al., 2012). Yet, D'Ortenzio et al. (2021) when comparing the in situ surface chlorophyll to the satellite product, also used in this study, found an underestimation of the chlorophyll compared to the observed concentrations. This underestimation may be linked to the correction of white caps (due to recurrent winds in the area) reducing the number of available ocean color pixels in the Levantine Sea. They emphasized on the lack of ocean-color observations in this region.

The BGC Argo floats acquire a time series of vertical distribution (reaching 2000 m) of key physical and biogeochemical variables at all sea conditions and frequently over complete annual cycles (D'Ortenzio et al., 2014; Mignot et al., 2014). One of the goals of these Argo floats is to improve our knowledge of the seasonal and decadal-time variability of the biogeochemical parameters such as chlorophyll, oxygen, and nitrates. However, these measurements are also affected by uncertainties. Recent studies explored these uncertainties associated with the latest improvements in optical sensors. Systematic errors introduced by imperfect initial calibration, sensor drift, or changes in the environment during the measurement process can lead to the deviation of the float measurements from the true values. Mignot et al. (2019) revealed an additive bias of 2.9 µmol kg^{-1}, 0.46 µmol kg^{-1} and -0.06 mg m^{-3} and a relative error of 6.1 %, 3.2 %, and 5.4 %, respectively, for the float dissolved oxygen, nitrate, and chlorophyll concentrations. Roesler et al. (2017) confirmed an overestimation of Chl-a by a factor of 1.72 for the eastern Mediterranean basin; they found an uncertainty of +300 % even after the non-photo-chemical quenching correction. A lot of efforts have been made in order to improve the accuracy and to correct the systematic error of the measurements collected by BGC Argo floats see Bittig et al., 2019. As a matter of fact, the uncertainty associated with the last generation of optical sensors for oxygen has been reduced by a factor of 2-3 (Grégoire et al., 2021).

Finally, in situ data are also affected by uncertainties due to the sea conditions or the operator's ability to limit contaminations. They might also be due to the non-universal sampling method which explains the wide dispersion of the measurements in the same region. It should be noted that a lack of in situ data can cause products such as Argo floats and satellite data to be poorly characterized and inconsistent, causing uncertainty estimates to vary greatly between areas where extensive in situ data exist and where they are limited.

In conclusion, in this thesis, satellite data will be qualitatively analyzed due to the high uncertainties for the oligotrophic region. As for BGC floats, the low bias and uncertainties gave us confidence in using them for the validation of oxygen and chlorophyll. We will also compare quantitatively our model results with cruise data for oxygen and nutrients.

Statistical analyses

In order to quantify the performance of the model, we computed complementary metrics following the recommendations of (Allen et al., 2007):

The Pearson correlation coefficient (R)

$$R = \frac{\frac{1}{K}\sum_{k=1}^{K}(y_k^m - \overline{y^m})(y_k^o - \overline{y^o})}{\sigma_m \sigma_o} \tag{2.21}$$

Where K is the number of observations, y_k^m is the model output that corresponds to the observation k, y_k^o, $\overline{y^m}$, $\overline{y^o}$, σ_m and σ_o are the mean and the standard deviation of the model outputs and observations respectively.

The bias (B)

$$B = \overline{y^m} - \overline{y^o} \tag{2.22}$$

The percentage bias (PB)

$$PB = 100 \times \frac{\overline{y^m} - \overline{y^o}}{\overline{y^o}} \tag{2.23}$$

The normalized root mean square difference (NRMSD)

$$NRMSD = \frac{\frac{1}{K}\sum_{k=1}^{K}(y_k^o - y_k^m)^2}{\overline{y^o}} \tag{2.24}$$

Chapter 3

Model assesment

Contents

3.1 Introduction

In this chapter, we assess the coupled model's performance by comparing its outputs to available data (described in chapter 2) for the Levantine basin. These include satellite data (MEDOC4 for chlorophyll), in situ data (for nutrients, dissolved oxygen, and carbonate system), and float outputs (for dissolved oxygen and chlorophyll). The main objective of this step is to assess the performance of the model compared to what is really observed and to indicate its possible fallouts. The results here represent the simulation that showed the greatest statistical and realistic results. Some of these comparisons are also presented in the article in chapters 4 and 5.

3.2 Hydrology of water masses

The ability of the model to reproduce the characteristics of the different water masses has been evaluated through the confrontation of modeled data against SST and Argo floats data by (Estournel et al., 2021). The model reproduces the large and mesoscale features present in the basin: the Rhodes Gyre, Egyptian eddies, Ierapetra Eddy,... It positions the water masses well vertically. However, Estournel et al. (2021) found that the salinity in the Levantine basin is on average slightly underestimated by 0.027 units in the intermediate layer for 2012-2020. We compared available temperature and salinity data for the BGC-Argo floats used for the assessment of chlorophyll and dissolved oxygen. In this section, we present the comparisons for only two floats (6901528, 6901770) with different positions and time ranges in the Levantine basin.

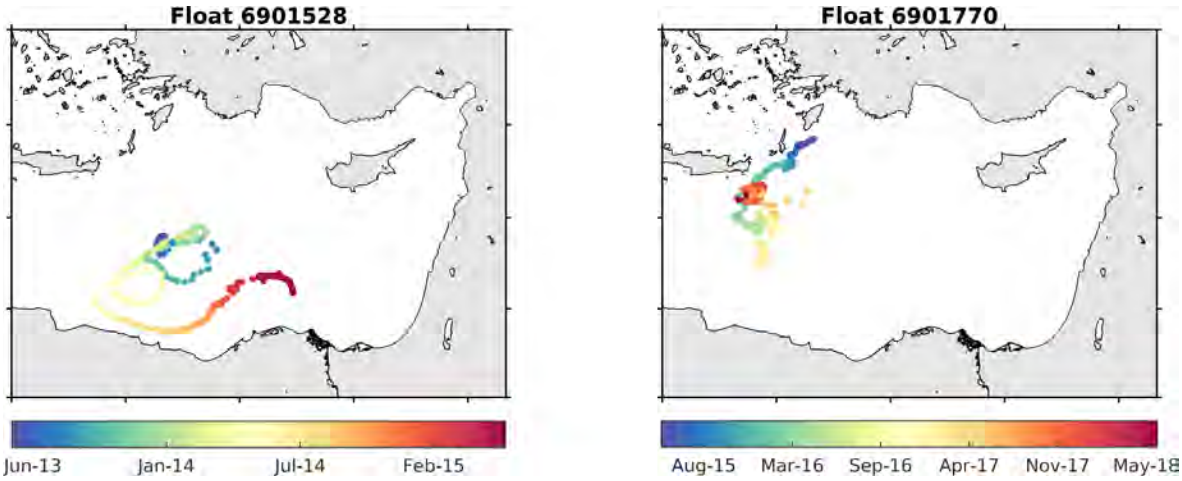

Figure 3.1: Trajectory of the Argo floats 6901528 and 6901770 deployed in the Levantine basin over the periods 2013/15 and 2015/18, respectively.

Figure 3.1 first presents the trajectory of the Argo float 6901528 composed of 181 profiles covering the southern Levantine basin from the surface to depths reaching 1019 m, and the period 15 May 2013 - 23 May 2015. The float 6901770 is located in the North-west of the Levantine and covers the period from 20 May 2015 to 14 June 2018 (Fig. 3.1). It moves along the eastern Cretan Arc along the Rhodes Gyre, Ierapetra and then to the South. The observed and modeled Theta-S diagrams are represented in Figure 3.2 (A 6901528 and B: 6901770). The color dots on diagrams represent the potential density anomaly.

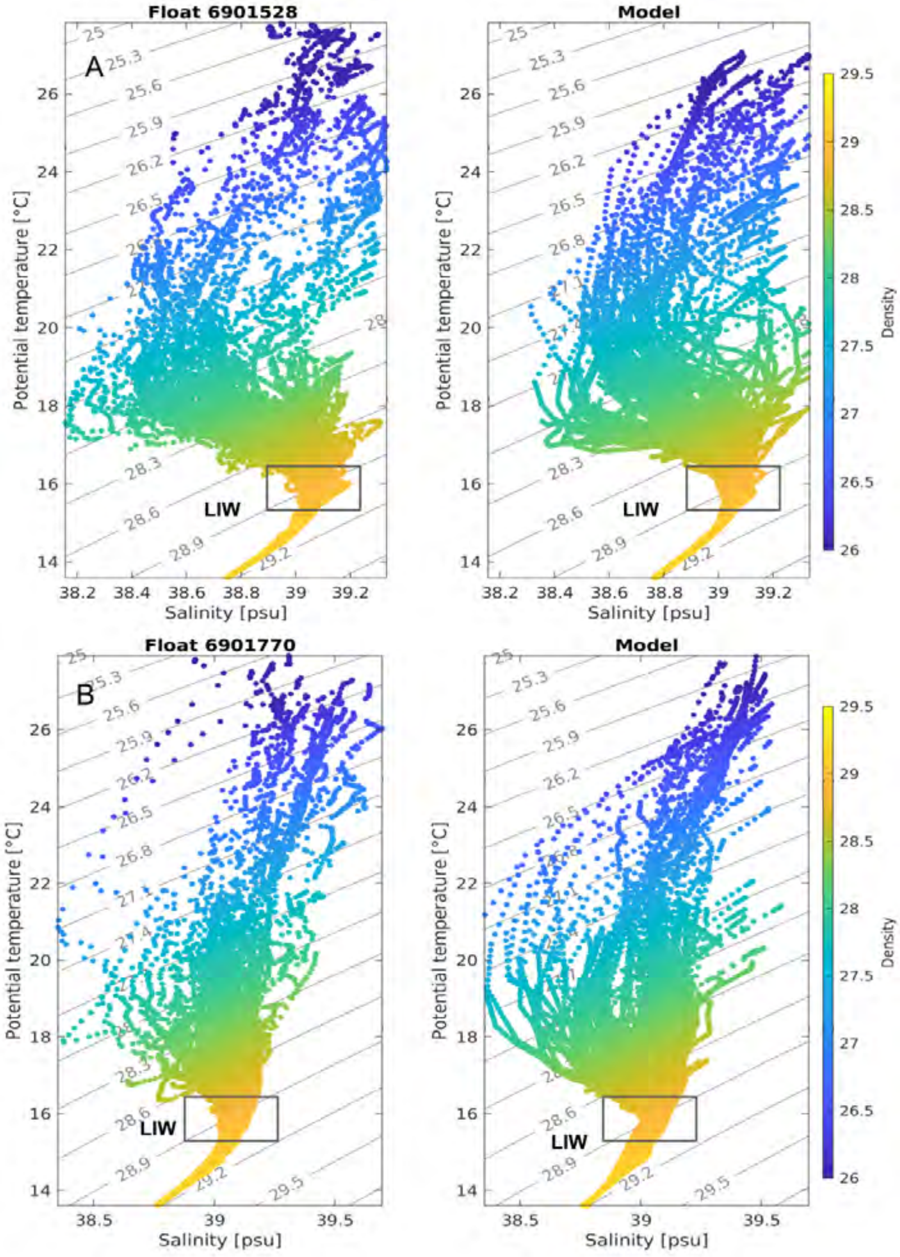

Figure 3.2: Theta-S diagram for (A) the float 6901528 data (left) and the corresponding model outputs (right) (B) the float 6901770 (left) and the corresponding model outputs (right). The colors refer to the density in kg m^{-3}. The color dots corresponding to LIW (Levantine Intermediate Water) are in the black rectangle.

The different masses of water are well represented in the simulation for both floats. We noticed a slight overestimation of the salinity in the surface and subsurface values for the model (see

Table 3.1: Statistical metrics of the model - observation comparison for temperature, salinity, and density for floats 6901528 and 6901770

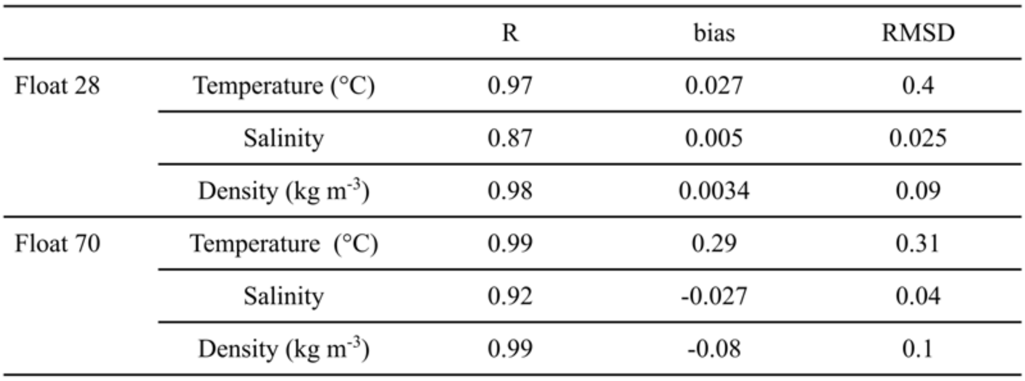

		R	bias	RMSD
Float 28	Temperature (°C)	0.97	0.027	0.4
	Salinity	0.87	0.005	0.025
	Density (kg m^{-3})	0.98	0.0034	0.09
Float 70	Temperature (°C)	0.99	0.29	0.31
	Salinity	0.92	-0.027	0.04
	Density (kg m^{-3})	0.99	-0.08	0.1

Estournel et al., 2021, Fig. 9). The Theta-S diagram confirms the slight underestimation of the salinity in the intermediate layer previously found by Estournel et al. (2021). The modeled LIW possesses a salinity of 39.1 psu, a potential density of 28.9 kg m^{-3} whereas the Atlantic Water (AW) is less salty as in the observations.

The observed and modeled salinity profiles for float 6901528 and 6901770 are represented in 3.3. The blue line represents the mixed layer depth (MLD) determined based on an increase of 0.01 kg m^{-3} relative to 10 m depth (Coppola et al., 2017). Both the model and the float data show the same seasonal cycle with discernible features such as the AW located below high salinity water in the surface layer from June till the end of December. During fall, wind stress and heat loss episodes favor evaporation in the surface layer. This leads to the gradual increase of salinity in the surface layer and its deepening with the mixed layer's depth. The salinity is homogeneous during winter along the mixed layer's depth. The high salinity layer and the AW water mix when heat loss events start to decrease, and with the increase in temperature, the surface layer begins its stratification. One can notice the overestimated AW inflow and the slight underestimation of the salinity of the intermediate layer in both modeled salinity reproductions previously mentioned for the TS diagram. We also noticed a slight underestimation of the modeled mixed layer specifically during the mixing period for both floats. We obtain a highly significant correlation coefficient ($R > 0.85$) between the modeled and the observed hydrodynamic variables. Both biases and Root Mean Square Difference (RMSD) remain low ($bias < 0.3$, $RMSD < 0.4$).

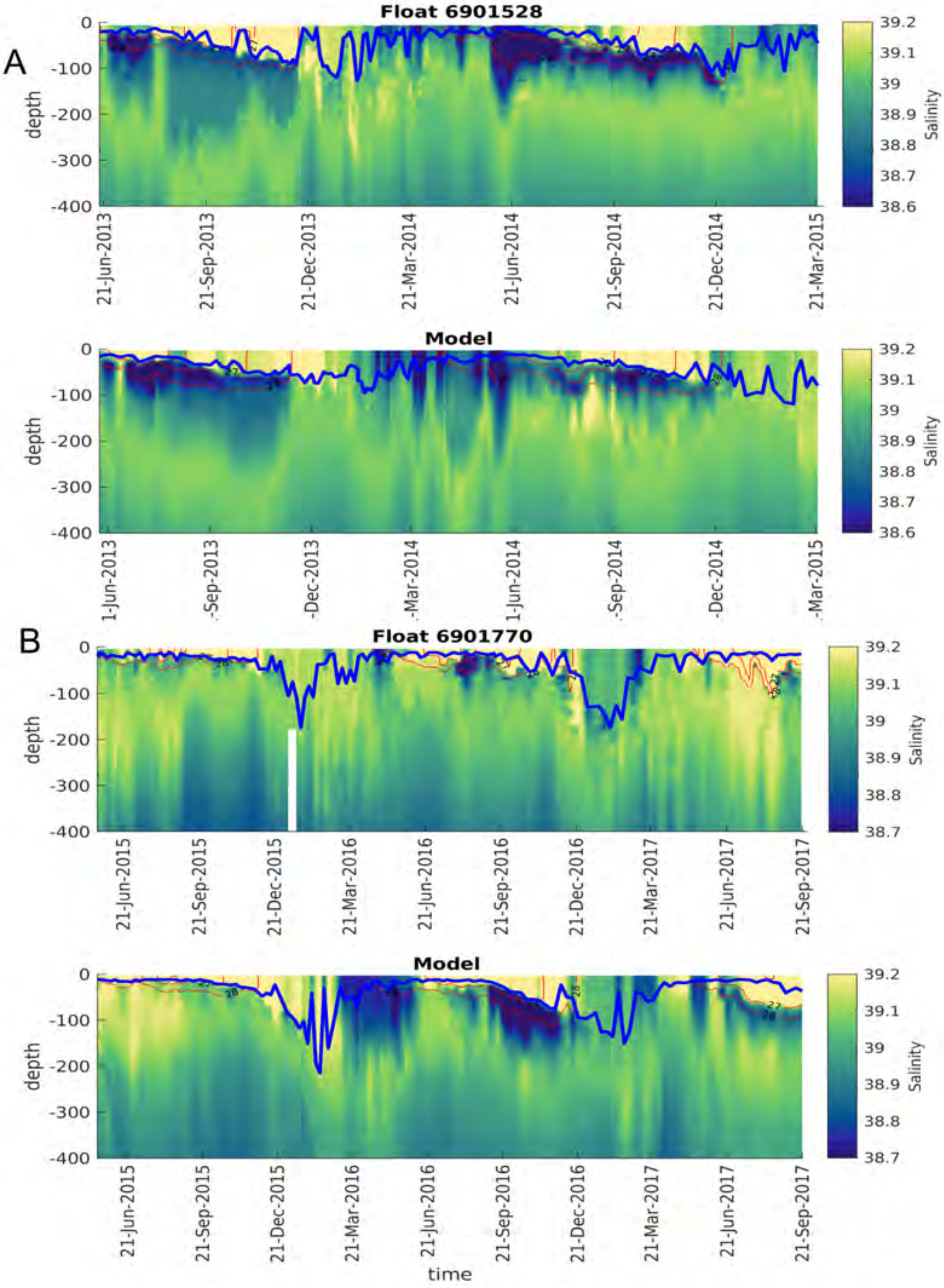

Figure 3.3: Hovmöller diagrams of observed and modeled salinity for (A) float 6901528 and (B) 6901770 in the first 400 m. The blue line represents the modeled and observed mixed layer depth (MLD) and the red thin lines are the density anomaly isolines (27 and 28 kg m^{-3}).

Table 3.2: Statistical indices of model-observation comparison for nitrate and phosphate over the water column. Mean^o and Mean^m are the means of the observations and the model, respectively, PB is the percent bias, R is the correlation coefficient and RMSD is the Root Mean Square Difference.

		Mean^o	Mean^m	PB	R	RMSD
PERLE-1	Nitrate	4.6	4.7	1.7%	0.97	0.39
	Phosphate	0.18	0.17	-5.9%	0.91	0.03
PERLE-2	Nitrate	4.9	4.8	-2.1%	0.95	0.39
	Phosphate	0.20	0.17	-17.6%	0.94	0.04
CARIMED	Nitrate	3.5	4.7	25.5%	0.98	1.31
	Phosphate	0.16	0.17	-6.3%	0.98	0.01

3.3 Nutrients

3.3.1 Seasonal variability

The modeled dissolved inorganic nutrients (nitrate, phosphate) are compared to observations for three seasons: winter, spring, and fall (Fig. 3.4) to estimate the reliability of the model to reproduce the correct vertical nutrient distribution for the considered seasons. The model reproduces correctly the surface nitrate and phosphate concentrations except for fall, where the observed low but non-zero values of PO_4 seem to be underestimated by the model which is close to null values. The modeled nitrate is within the range of the observations of CARIMED and PERLE-1 and -2 cruises. The main difference lies within the magnitude and the depth of the maximum nitrate concentration, located in the Intermediate and Transitional waters. During winter, the model underestimates the maximum of nitrate by about 1 μM. During spring, the modeled nutrients are in the observed ranges. During fall, the model is close to the mean profiles of PERLE-2. The magnitude of the maximum of nitrate in the simulation is 12 % lower than in the observations and the modeled nutriclines are shallower than those observed.

As for the phosphate, the shape of the vertical profile is qualitatively similar to observations but the simulation does not show such a pronounced maximum than the observations (Fig. 3.4). The modeled winter concentrations below 400 m are close to the lower range of the CARIMED concentrations, the model underestimates the maximum PO_4 by 25 % compared to PERLE-1. The model represents well the spring PO_4 concentration in all the layers. As for fall, the phosphate concentrations are underestimated by the model in the surface and deeper layers, PERLE-2 reaches a maximum of 0.24 µM whereas modeled outputs reach 0.19 µM.

Regarding the statistical metrics of the model-observation comparison, the modeled average of both nitrate and phosphate is close to what was observed for the different cruises (Table 3.2). The modeled bias is featured with negative values except for the nitrate for PERLE-

1 and CARIMED, emphasizing the general underestimation of the modeled concentrations. The percentage of bias was low for both nitrate and phosphate and for all cruises. Yet, the highest bias was recorded for CARIMED for the nitrate up to 25 % (Table 3.2). The statistical metrics R and RMSD indicate an overall good performance of the model. The correlation coefficient is high with values over 0.90 (p-value < 0.01). A more detailed comparison by layers can be found in Appendix B, Table B1.

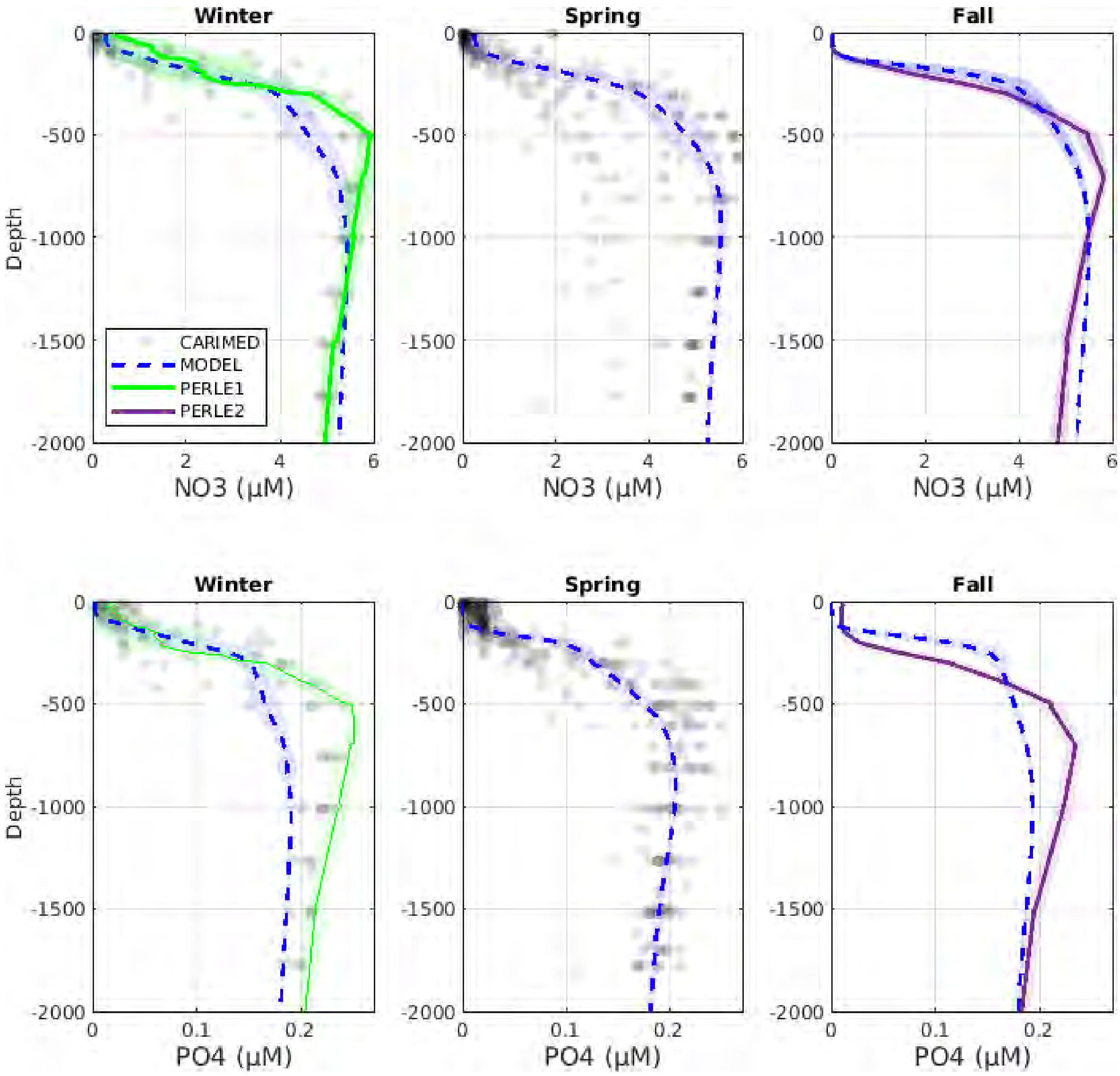

Figure 3.4: Observed and modeled profiles of nitrate and phosphate (µM) concentrations, averaged by season (winter: 21 December to 20 March, spring: 21 March to 20 June, fall: 21 September to 20 December), over the Levantine Sea.

3.4 Chlorophyll

One of the important products to compare with the results of the model, due to the large area covered, but also due to the frequency of the observations, is the satellite estimated surface Chl. But the use of this product in oligotrophic regions, and specifically in the Mediterranean Sea, is very delicate due to the shortcomings of the algorithms (see chapter 2). Another product that can be used is the chlorophyll measured by the BGC-Argo floats but these data are subjected to an overestimation of the concentrations or drifts with time.

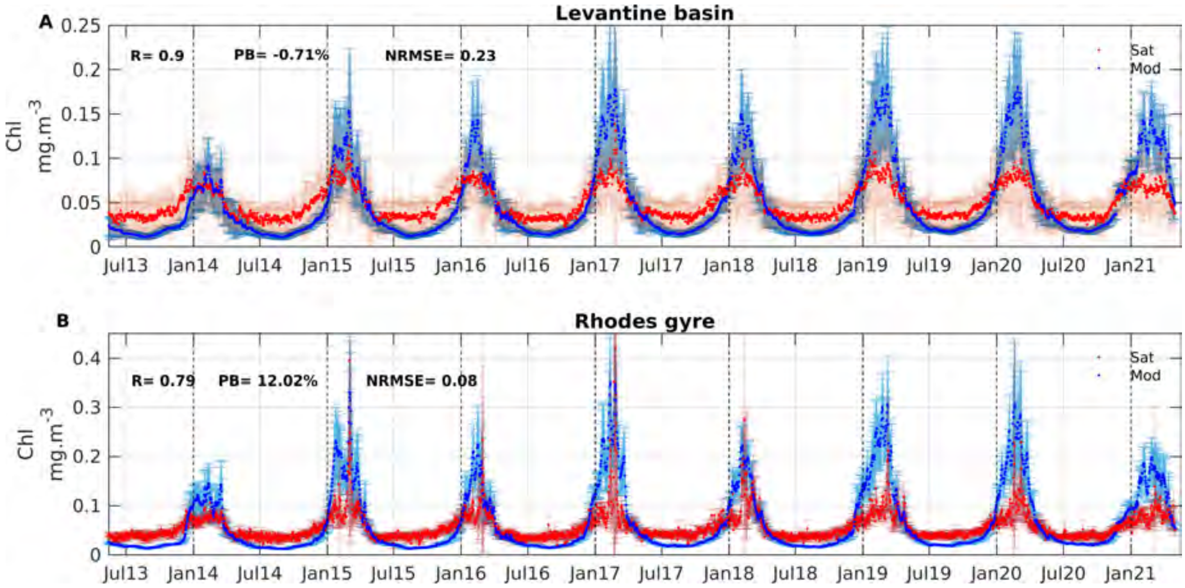

Figure 3.5: Observed (MEDOC satellite at 1 km resolution, in red) and modeled (blue) surface chlorophyll concentration (mg m^{-3}), averaged over the (A) whole Levantine basin and (B) Rhodes Gyre. Light blue and red bars represent the standard deviation in model and observation outputs respectively.

3.4.1 Satellite images

To assess the ability of the model to reproduce the surface chlorophyll concentration, we calculated the mean Chl for the Levantine basin. The Levantine basin can be separated into two different regimes: intermittent (Rhodes Gyre) and no bloom (the rest of the Levantine) regime (D'Ortenzio and Ribera d'Alcalà, 2009). The statistical metrics were calculated for both regions. Figure 3.5 represents a comparison between the modeled and observed Chl averaged over the Levantine basin (A) and over the Rhodes Gyre (B) for the period May 2013 - May 2021. The correlation coefficient between the data and the model is equal to 0.90 (*p-value* < 0.01) for the Levantine basin and 0.79 (*p-value* < 0.01) for the Rhodes Gyre. The model represents well the seasonal variation of the observed surface chlorophyll of MEDOC satellite, with minimum values during the stratification period and an increase in the chlorophyll concentration once the stratification weakens (at the end of fall). The timing of the maximum surface Chl is respected by the model for the Levantine and the Rhodes Gyre.

The annual mean of the model and observations is equal for both to 0.05 mg m^{-3} for the Levantine basin but the model underestimates the concentrations during the stratified period and the opposite in winter (overestimation of 31 %). The mean concentration of the modeled outputs for the Rhodes Gyre is also close to the observations (0.65, 0.59 mg m^{-3} for the model and satellite respectively) and the seasonal discrepancies are the same even if weaker. The metrics for both regions (PB: -0.71 and 12.01 %, NRMSE: 0.23 and 0.08, for the Levantine basin and Rhodes Gyre, respectively) are low indicating the relatively good representation of the surface chlorophyll by the model especially in the Rhodes Gyre.

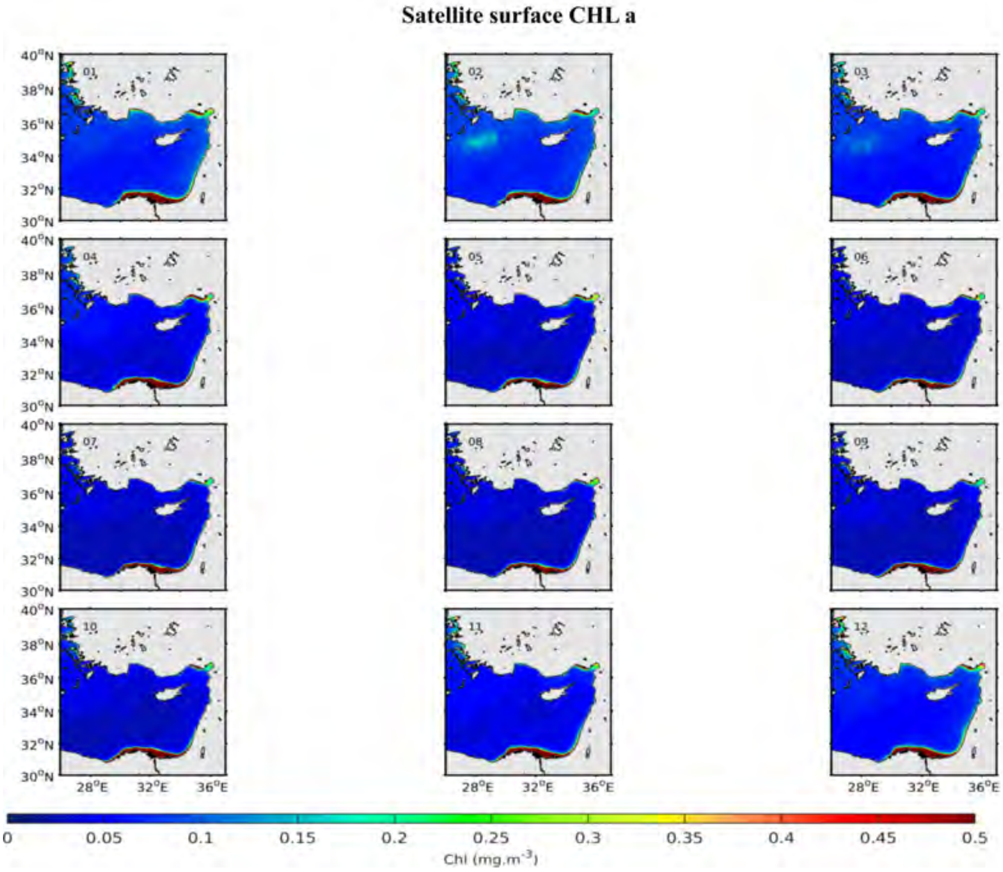

Figure 3.6: 7-year (2013-2020) average of observed monthly surface chlorophyll concentrations for the Levantine basin from satellite MEDOC product.

Figure 3.6 and 3.7 display the observed and simulated monthly surface chlorophyll concentration for the Levantine basin over the period 2013-2020. Chlorophyll concentration is generally low during the oligotrophic period, from May until November. The maximum is reached in February. Compared to the satellite data, the model seems to overestimate the spatial extension of the high Chl in the Rhodes Gyre. These differences between the model and the satellite data might be explained by the limiting number of available ocean color pixels in the area due to the cloud coverage and the intense wind in the Levantine Basin as was already reported by D'Ortenzio et al. (2021). As previously mentioned in chapter 2, D'Ortenzio et al. (2008) found a bias of 30 % in satellite data compared to in situ observations.

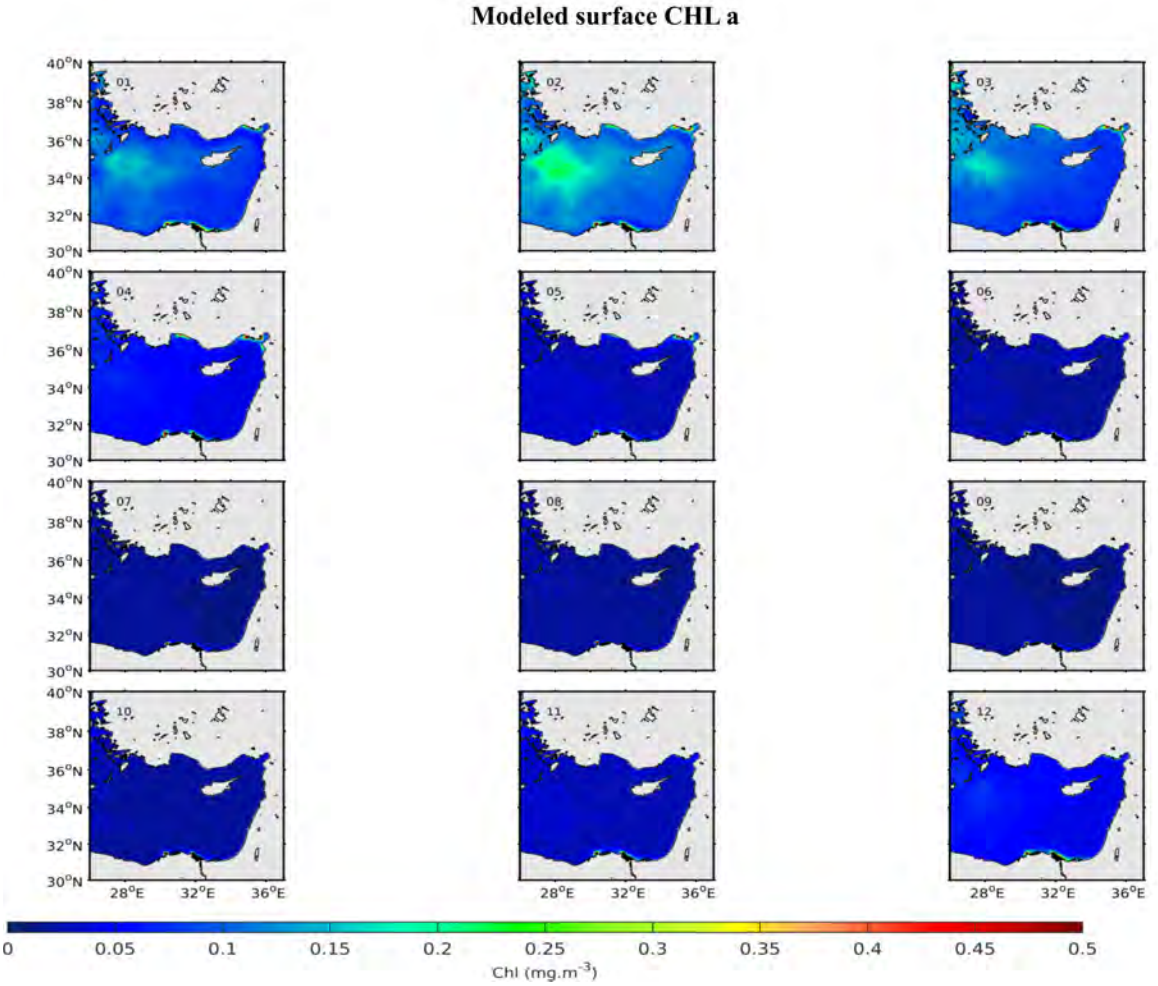

Figure 3.7: 7-year (2013-2020) average of modeled monthly surface chlorophyll concentrations for the Levantine basin.

3.4.2 Argo floats

Surface chlorophyll

The comparison of chlorophyll with Argo floats shows a good agreement as for the satellite (Fig. 3.8A). The model is also able to reproduce the observed interannual variability as shown by the interannual chlorophyll anomaly (Fig. 3.8B). As mentioned in chapter 2, Roesler et al. (2017) found an overestimation in float data chlorophyll by a factor of 1.72 for the eastern Mediterranean basin.

We have presented in this section both satellite and float data, to show the high variability between the different sources of observations. The model results for the surface chlorophyll are globally in good agreement with both data sources, the chlorophyll concentrations are within the satellite and the float range. The model reproduces adequately the seasonal variation in both cases. However, one can notice that each dataset is subject to different limitations with one dataset underestimating the chlorophyll concentrations while the other sometimes could overestimate it. These differences highlight the difficulties in obtaining reliable measurements for this region.

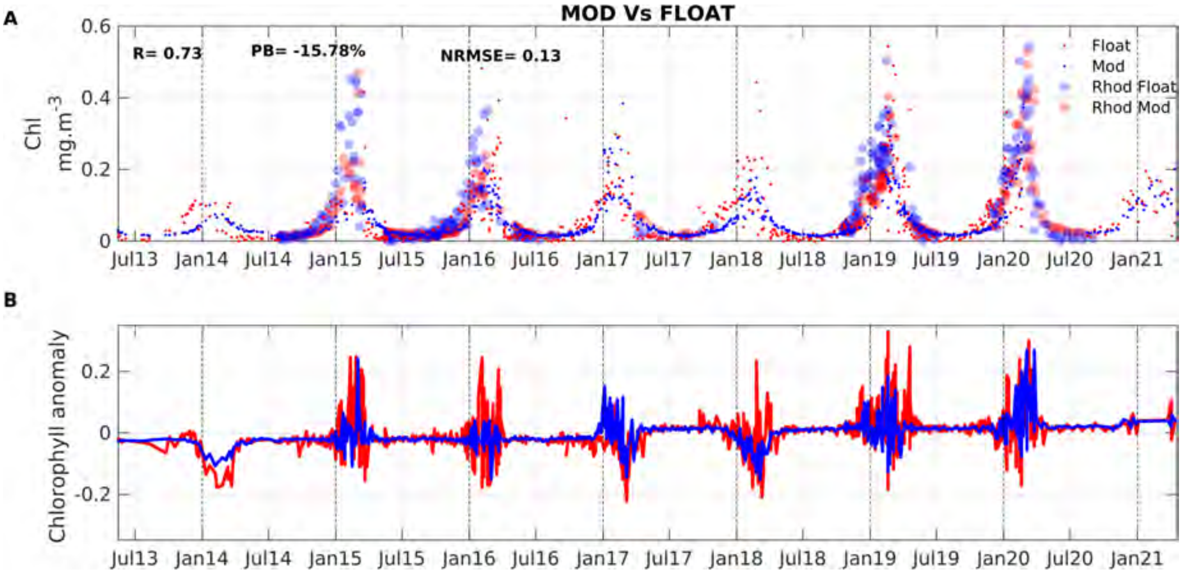

Figure 3.8: A. Observed (BGC float, in red) and modeled (blue) surface chlorophyll concentration (mg m^{-3}) for the Levantine basin and in the Rhodes gyre (light red, light blue) B. Chlorophyll anomaly for the Levantine basin for the period of study . All available float data was used in the comparison.

Spatial and temporal variability

We also evaluated the ability of the model to reproduce the chlorophyll concentration along the water column. We present in Figure 3.9 the temporal evolution of the chlorophyll along the path of float 6901773 in the Levantine basin. Float trajectories and all the comparisons between modeled and float chlorophyll can be found in the Appendix B.

The model estimates are in the range of the observations and follow the same seasonal cycle. The model and the observation chlorophyll concentration is homogeneous throughout the 100-200 first meters of the water column during the mixing period, the surface chlorophyll increases during spring and begins deepening when the stratification is accentuated forming the deep chlorophyll maximum (DCM). The temporal pattern of the surface chlorophyll is well reproduced by the model, with correct chlorophyll concentrations. A slight delay in the bloom initiation can be discerned for winter 2018 (Fig. 3.9c). The comparison between the modeled and float DCM depth shows a general trend of the model to overestimate the depth of the DCM after 2016. The statistical measures indicate a high correlation between the observations and the model (R $\sim$ 0.92) and low RMSD (0.02) and percentage bias (-4 %). They highlight the good performance of the model.

The statistical metrics of the comparisons of model outputs with BGC Argo floats located in the Levantine basin are represented in Table 3.3. Float trajectories can be found in Appendix B. Overall, the statistical scores show good agreement between the observed and modeled chlorophyll along the water column with high correlation coefficients except for floats 1770 and 3247. The RMSD values were low for all the floats indicating the close similitude of

Table 3.3: Statistical measures of model-observation comparison for chlorophyll over the water column for the BGC floats used for validation. RMSD was normalized using the mean.

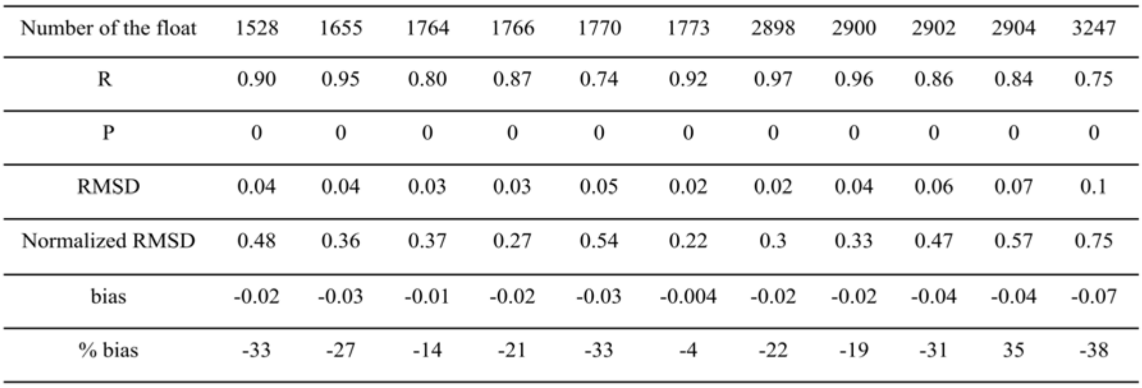

Number of the float	1528	1655	1764	1766	1770	1773	2898	2900	2902	2904	3247
R	0.90	0.95	0.80	0.87	0.74	0.92	0.97	0.96	0.86	0.84	0.75
P	0	0	0	0	0	0	0	0	0	0	0
RMSD	0.04	0.04	0.03	0.03	0.05	0.02	0.02	0.04	0.06	0.07	0.1
Normalized RMSD	0.48	0.36	0.37	0.27	0.54	0.22	0.3	0.33	0.47	0.57	0.75
bias	-0.02	-0.03	-0.01	-0.02	-0.03	-0.004	-0.02	-0.02	-0.04	-0.04	-0.07
% bias	-33	-27	-14	-21	-33	-4	-22	-19	-31	35	-38

the model and observations magnitudes. As for the bias, it was negative reflecting the slight underestimation of the modeled chlorophyll concentration compared to the float. The bias percentage was also low, the highest value was recorded for the float 3247 (-38 %). This float also had the highest RMSD.

Seasonal variability along the water column

We evaluated the vertical distribution of chlorophyll by averaging all the floats located in the Levantine basin for the period 2013-2020, based on the season (Fig 3.10). The comparison was also completed with a statistical analysis computed for each season (Table 3.4). Both the model and float data share the same profile shape for most of the seasons, except for winter. During winter (21 Dec - 20 Mar), the model overestimates the homogenization of the first 80 m, which leads to an overestimation of the surface chlorophyll concentration (model: 0.14 mg Chl m^{-3}, floats: 0.08 mg Chl m^{-3}) in the first 30 m, and on the contrary an underestimation in the 50-80 m layer. However, the modeled chlorophyll falls in range with the values presented by the Argo float. The model reproduced the development and deepening of a deep chlorophyll maximum (DCM) from spring to summer, and then its weakening and shallowing from summer to fall. The DCM concentration is underestimated in the model by 0.10 mg Chl m^{-3} and its depth is overestimated by 30 m in summer and fall and 20 m in spring.

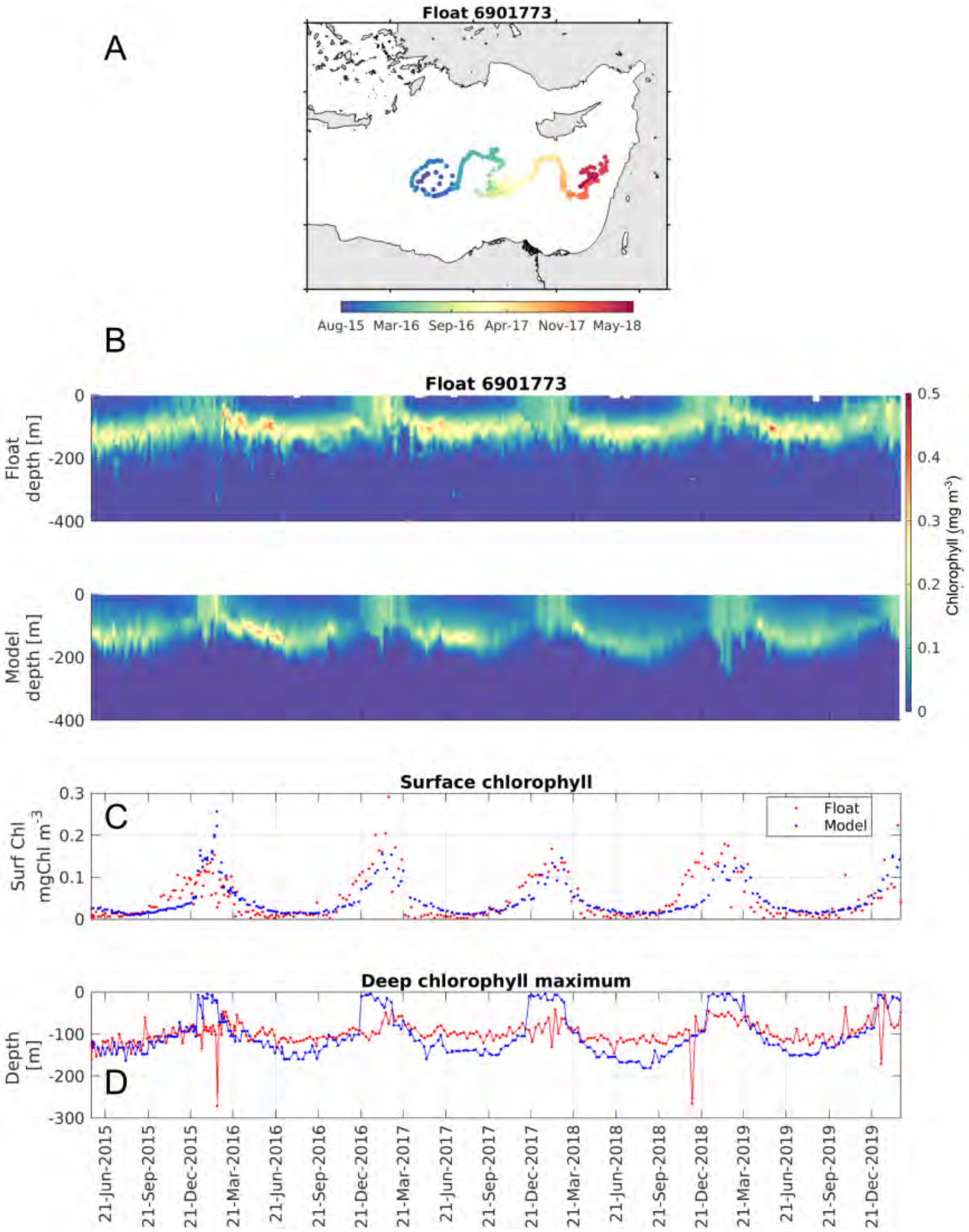

Figure 3.9: Time evolution of BGC-Argo float 6901773 observed and modeled data: (A) trajectory of the BGC-Argo float, (B) Hövmoller of observed and modeled chlorophyll for the first 400 m, respectively; temporal evolution of (C) surface chlorophyll concentration and(D) depth of deep chlorophyll maximum for the float (red) and model (blue).

The model shows high correlations (0.94, 0.91, 0.80, 0.91 for winter, spring, summer and fall, respectively, with p-value <0.01, Table 3.4). It also presents low RMSD (RMSD < 0.046) and bias when compared to the chlorophyll observations. The bias values are negative confirming the underestimation of the chlorophyll in the model.

Table 3.4: Statistical metrics of the chlorophyll (µmol kg^{-1}) seasonal vertical profiles for the modeled and the observed BGC Argo floats.

Metrics	Winter	Spring	Summer	Fall
R	0.94	0.91	0.80	0.91
RMSD	0.03	0.04	0.05	0.04
Normalized RMSD	0.36	0.56	0.68	0.62
Bias	-0.02	-0.02	-0.02	-0.02
Bias %	-21	-25	-22	-37

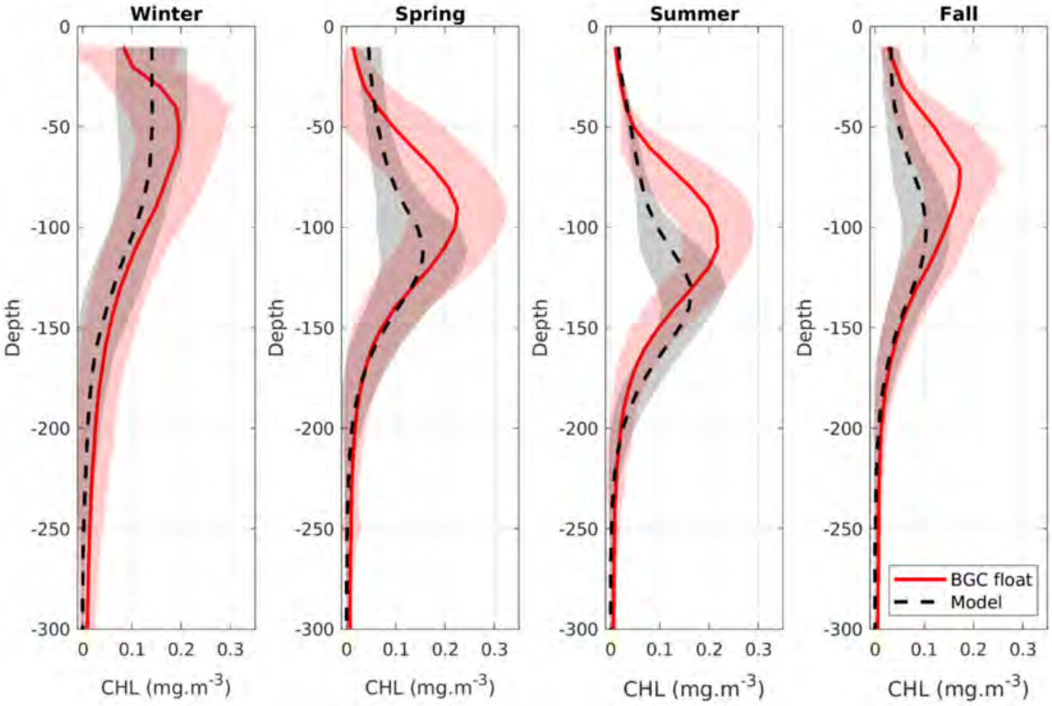

Figure 3.10: Comparison between observed (BGC-Argo float data, red) and modeled (black) profiles of chlorophyll (mg Chl m^{-3}) concentrations, averaged by season (winter: 21 December to 20 March, spring: 21 March to 20 June, summer: 21 June to 20 September, fall: 21 September to 20 December), over the Levantine Sea. Solid lines represent the mean, and shaded areas SD.

3.5 Oxygen

In this section, we will assess the modeled dissolved oxygen concentration by comparing it against different data sets. Observed dissolved oxygen concentrations from a Winkler analysis were used for the cruises (CARIMED, PERLE1, PERLE2). We also used oxygen concentrations from BGC Argo floats.

3.5.1 Surface oxygen

We compared the BGC Argo data of oxygen in the Levantine basin against the model outputs extracted at the same date and position. Figure 3.11 shows a comparison between the observed and modeled surface oxygen concentration along all the trajectories of the floats available in the Levantine basin. The comparison with the Argo starts in June 2013 and is extended till June 2020 with 1680 profiles covering 0 - 2075 m of depth. The simulated surface oxygen value seems to be often close to the float surface oxygen. The mean of the modeled oxygen is lower than in the float data by 2 µmol kg^{-1}, they possess the same SD (12 µmol kg^{-1}, Table 3.5). The statistical metrics show low bias (-0.49 %)and RMSD (RMSD: 6.8 µmol kg^{-1}, Normalized RMSD: 0.03, Table 3.5). The modeled surface oxygen is highly correlated with the measured surface oxygen (R: 0.85). In summary, the statistical quantities support our conclusions that the model generally successfully reproduces the spatial and temporal distribution of oxygen concentration in the surface layer.

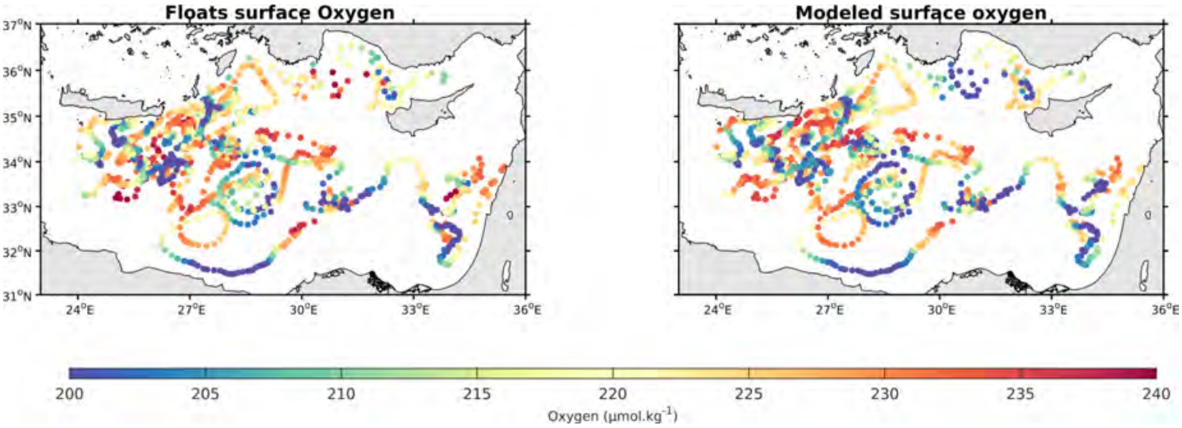

Figure 3.11: Oxygen surface concentration (µmol kg^{-1}) for BGC-Argo float data (left) and model (right) from 2013 - 2020 in the Levantine basin.

3.5.2 Seasonal variability along the water column

For the sake of clarity, we chose to represent in Figure 3.12, the modeled CARIMED oxygen concentrations in blue and the modeled float data in black. Statistical analysis was also conducted by comparing each data set with its corresponding modeled data. At the surface, the modeled oxygen concentrations seem to be in good agreement with the observations for all the seasons, except in fall when the model appears to overestimate compared to both cruise and Argo float data. In winter, the surface oxygen is maximum reaching 230 µmol

Table 3.5: Statistical metrics of the oxygen concentration (µmol kg^{-1}) for the modeled and the observed BGC Argo floats for the surface layer.

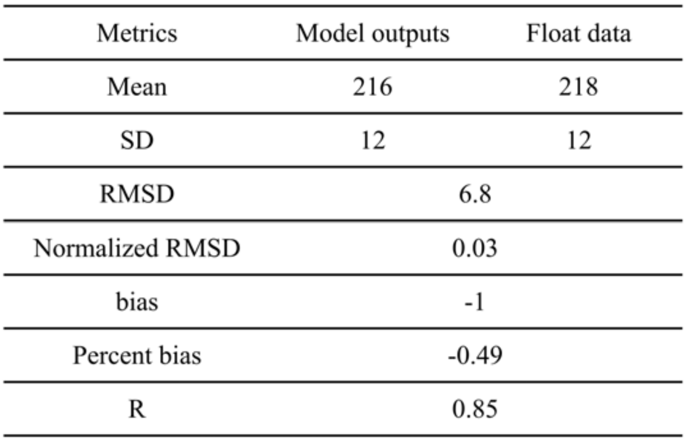

Metrics	Model outputs	Float data
Mean	216	218
SD	12	12
RMSD	6.8	
Normalized RMSD	0.03	
bias	-1	
Percent bias	-0.49	
R	0.85	

kg^{-1} for the model compared to 240 µmol kg^{-1} for the observations in the surface layer. The modeled oxygen concentrations are within the range of the observed oxygen values. As for spring, summer, and fall, the observed subsurface oxygen maximum is well captured by the model. It is located at 30 m for the model and the floats during spring, at 50 m for summer and fall (80 m for PERLE1) for the observations, and between 50 - 70 m for the model. The subsurface maximum magnitude is underestimated in the model by 10 µmol kg^{-1}. This could be partially caused by the underestimation of the inflow of MAW (see Section 3.1), or of the net community production suggested by an underestimation of modeled chlorophyll compared to float data (see Section 3.3). For the oxygen minimum layer (OML), modeled oxygen fits the observed oxygen values with a minimum of around 600 m. Further investigation, especially based on the location of the anomaly, would be necessary to identify the possible responsibility of too-deep mixing or remineralization processes. The model is able to capture the seasonal oxygen cycle and the oxygen's vertical distribution in the upper layers.

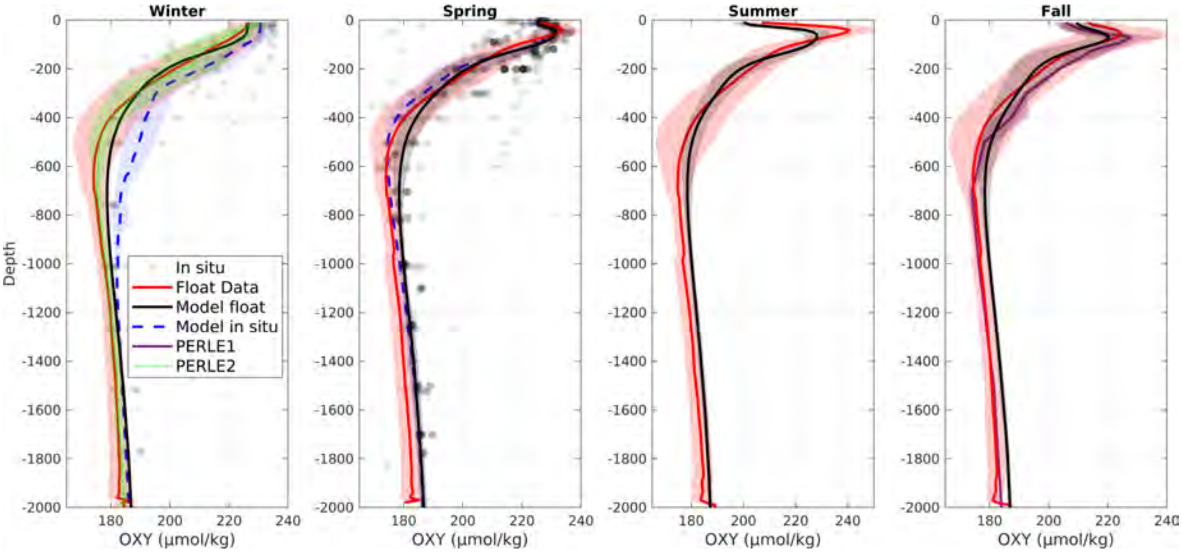

Figure 3.12: Comparison between observed (BGC-Argo float, CARIMED, PERLE-1, and PERLE-2 data, red, purple, and green lines, and grey dots) and modeled (black and blue lines) profiles of oxygen (µmol kg^{-1}) concentrations, averaged by season (winter: 21 December to 20 March, spring: 21 March to 20 June, summer: 21 June to 20 September, fall: 21 September to 20 December), over the Levantine Sea. Shaded areas correspond to SD.

Correlation, bias, and centered RMSD of dissolved oxygen between the model and various data sets are given in Figure 3.13. The statistics are calculated based on the available data and for the full water column during the study period to support the model validation. A strong positive correlation is found between the modeled and the observed dissolved oxygen ($R > 0.96$). The relatively low values of the RMSD indicate a close match between predicted and observed concentrations. In addition, all modeled datasets show a small residual between the modeled and the observed oxygen. However, there is a slight underestimation compared to the floats and PERLE-1 data, contrary to PERLE-2 and CARIMED.

3.5.3 Study case

We present here more in detail the comparison of modeled dissolved oxygen with data from an Argo float. All comparisons between modeled and float oxygen can be found in Appendix B. Float 6901773 was chosen because of its long period of coverage. We present the oxygen concentration of the float and the model for the period between 23 May 2015 and 28 September 2019. The model results fit observations in terms of seasonal variability (Fig 3.14A). The model reproduces qualitatively the surface oxygen maximum during spring, the deoxygenation at the surface during summer, and the homogenization in the first 100 m during winter. The simulated surface layer shows concentrations lower than the observations (Fig. 3.14C), with a difference of 5-10 µmol kg^{-1}. The surface statistical metrics R, PB, and NRMSD are 0.87, 0.99 %, and 0.04, respectively. The modeled oxygen saturation follows the same cycle as float 73 (Fig. 3.14D). There is a significant correlation of 0.96 between the modeled and observed oxygen saturation, and the normalized RMSD and the percent bias are low (0.03, -0.99 % respectively). We also investigated the subsurface oxygen maximum (SOM) depth and concentration for both the float and the model. The modeled depth of this layer seems to be deeper by 10 m at the beginning of the stratification period, reaching a maximum depth difference of 30 m during summer compared to the observed depth. The model underestimates the oxygen maximum concentrations by 15 µmol kg^{-1} in this layer.

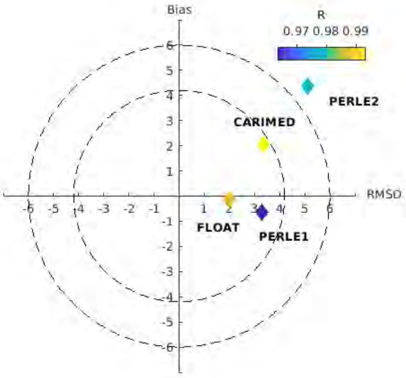

Figure 3.13: Statistical parameters of the modeled and the observed dissolved oxygen (µmol O_2 kg^{-1}) comparison along the vertical column in the Levantine basin. The correlation (CORR) color bar varies between 0.96 and 1.

As for the oxygen minimum layer, it is well located in the model during most of the float cycle. However, the OML (180 µmol kg^{-1} isoline, Fig. 3.14A) is deeper than the observations (float: 350 m, Model: 519 m) after March 2018. In detail, the model reproduces observed concentrations for depths below 200 m. High spatial correlations between the vertical profiles of modeled and observed oxygen for the first 1000 m are recorded during summer (close to 1), whereas lower correlations are present during the mixing and spring periods (Fig 3.14B). It is noteworthy to mention the decrease of the correlation for the period following June 2017, yet values are still above 0.8 and reflect the good performance of the model.

3.6 Carbonate system

3.6.1 Dissolved Inorganic Carbon

All vertical profiles of dissolved inorganic carbon (DIC) measured during the CARIMED and PERLE-2 cruises were compared to the model results (Fig 3.15). To assess the capacity of the model to reproduce the spatial and vertical variability of DIC in the water column, we present each dataset individually. CARIMED offers a global view of DIC in the Levantine basin for the mixing and stratification periods, while PERLE-2 is more focused on the western Levantine basin near Crete in February-March 2019.

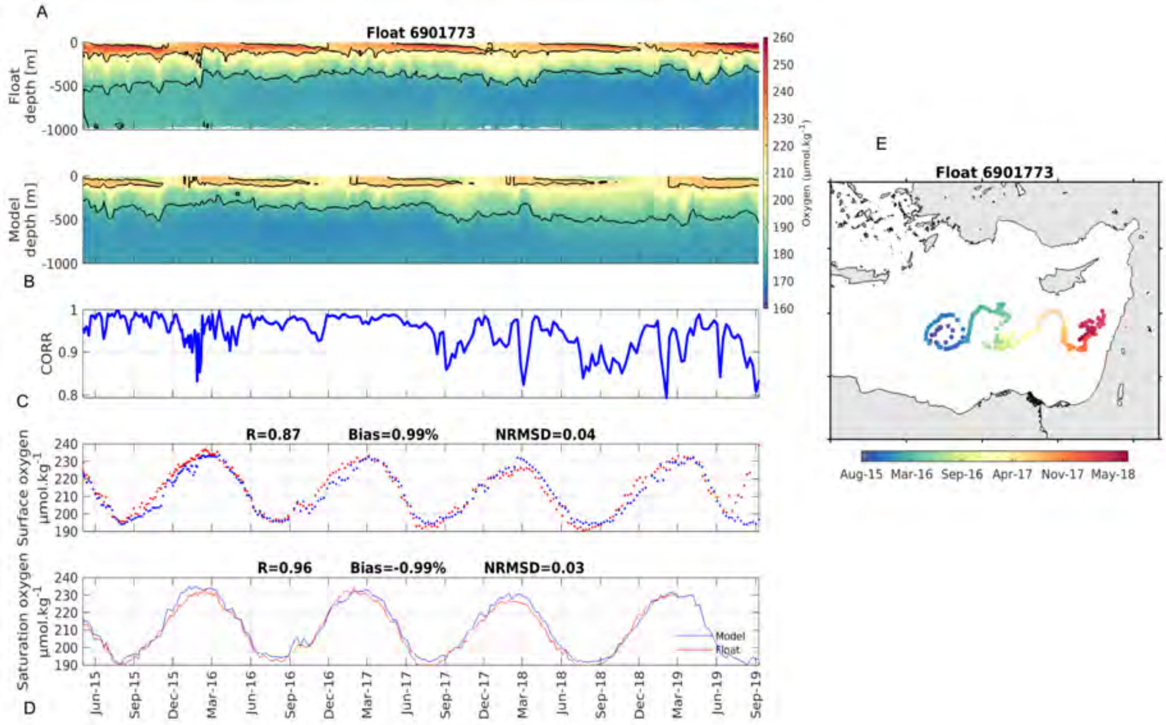

Figure 3.14: Comparison between observed (BGC-Argo float data) and modeled oxygen concentrations (µmol kg^{-1}) for float 6901773: (A) Hovmöller of observed and modeled oxygen for the first 1000 m, respectively, (B) correlation coefficient between both vertical profiles for the first 1000 m, (C),(D) time evolution of the surface oxygen and oxygen saturation between May 2015 and September 2019 and (E) trajectory of the float.

The DIC profiles presented minimum values at the surface. The modeled minimum varies between 2307 and 2310 µmol kg^{-1} for all the cruises, while observed DIC shows lower values, between 2280 and 2320 µmol kg^{-1} for CARIMED during winter, 2250 and 2332 µmol kg^{-1} for CARIMED during spring and 2290 and 2345 for PERLE2. The lowest values were observed during the cruises included in the CARIMED dataset. One can notice the important variability of observed surface DIC concentrations during PERLE-2, compared to the model. DIC reaches its maximum in the intermediate layer, between 200 and 700 m, with the modeled values in the observed range.

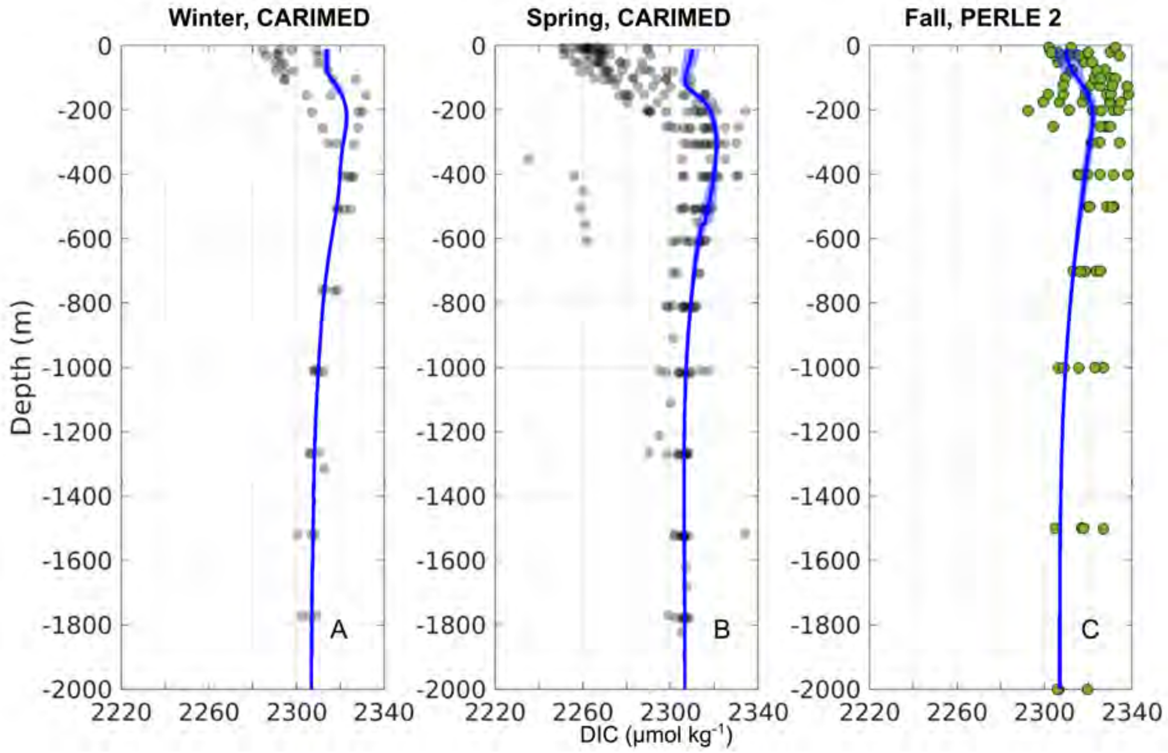

Figure 3.15: Observed (grey and green dots for CARIMED and PERLE-2, respectively) and modeled (blue line) DIC (µmol kg^{-1}) for the Levantine basin for ((A, C) CARIMED and (B): PERLE-2 datasets for winter, spring, and fall respectively.

3.6.2 Alkalinity

The total alkalinity (TA) concentration profiles show maximum values in the surface layer and lower values below 600 m. The surface TA concentration for the model is 2633 ± 8.5 µmol kg^{-1}. It is higher than most of the measured values during the CARIMED cruises (Fig 3.16), and in the upper range of values of PERLE-2. The model respects the vertical distribution and the concentrations in the different water masses for PERLE2.

DIC and TA in the surface layer are influenced by primary production that converts DIC to organic carbon and community respiration that consumes organic carbon and transforms it into DIC. They are also influenced by the increasing trend in evaporation and the associated increase in surface salinity. This slight overestimation for the AT during winter and spring might be the result of the slight overestimation of the production in the 0 - 30 m layer also spotted in the seasonal chlorophyll profiles in section 4.2.3. It might also be the consequence of cruise diversity and locations, as modeled TA of PERLE-2 did not show the same overestimation.

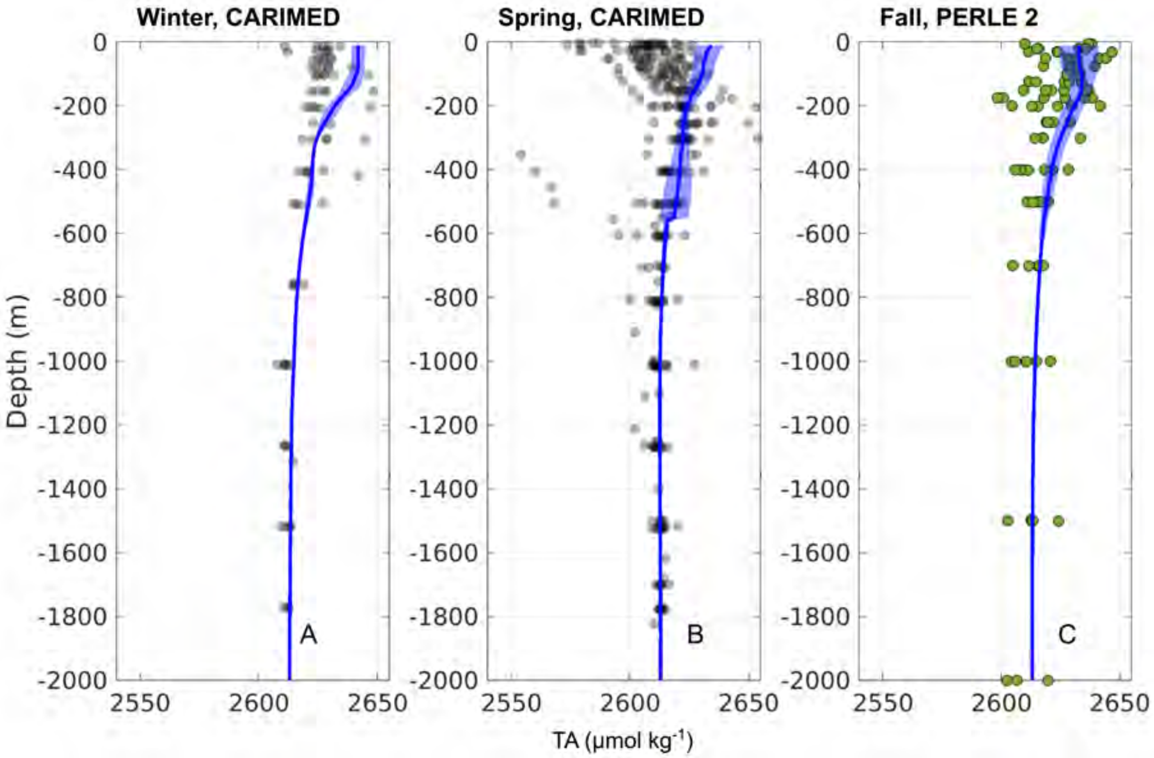

Figure 3.16: Observed (grey and green dots for CARIMED and PERLE-2, respectively) and modeled (blue line) TA (µmol kg^{-1}) for the Levantine basin for (A) CARIMED during winter (B) CARIMED during spring and (C) PERLE-2 cruises, respectively.

3.7 Conclusion

This chapter presents comparisons between the model outputs and in satellite, cruise and float data. Discrepancies were identified, but many positive points on the vertical distribution and seasonal cycle of the different variables make this simulation relevant for the study of interannual and seasonal variability of organic carbon and dissolved oxygen in the Levantine basin.

To summarize, the positive points are:

→ The modeled water mass characteristics were consistent with observed salinity, temperature and density.

→ The seasonal cycle and the orders of magnitude of the modeled mixed layer are realistic

→ The model is able to capture the observed seasonal cycle of the vertical profiles of chlorophyll and nutrients.

→ The observed spatial variability of the surface oxygen concentration is respected by the model.

→ The model captures relatively well the seasonal oxygen cycle and its vertical distribution.

→ Modeled alkalinity and dissolved organic carbon concentrations are in the range of the observations.

Some discrepancies have been noted:

→ The maximum modeled nutrient (PO_4) layer is shallower and the model underestimates the concentrations in the mixed layer during fall.

→ The model underestimates the chlorophyll and dissolved oxygen in the subsurface.

→ The DCM is deeper for the model for spring and summer.

→ The oxygen minimum is biased in winter.

It is necessary to keep in mind that comparing cruise, float, and remote sensing data involves not only model uncertainties but also data uncertainties (already developed in the previous chapter): both float chlorophyll and surface satellite data have been used in different studies covering the Mediterranean Sea. However, for our study, in the Levantine basin, the observed surface chlorophyll presented different magnitudes and thus it is difficult to judge if the model is overestimating or underestimating the surface chlorophyll. Therefore we assume that both model and data present uncertainties. Finally, it should be mentioned that the limited number of studies conducted in the basin makes model calibration difficult.

Chapter 4

The dynamics of organic carbon in the Rhodes Gyre

Contents

In the previous chapter, we assessed the coupled physical-biogeochemical models. The good agreement between the modeled outputs and the data gave us confidence in the model. In this chapter, we will examine the variability of the planktonic ecosystem and the biogeochemical cycles in the Rhodes Gyre. We will estimate the organic carbon budget in this region.

4.1 Context

The Rhodes Gyre is located in the northwest of the Levantine basin and is the area of formation of the LIW (Lascaratos et al., 1993; Lascaratos and Nittis, 1998). In spite of its importance, to date, studies focusing on the physical and biogeochemical characteristics of the gyre and the influence of the LIW on the Mediterranean Sea are still scarce. Therefore, there is a need to better understand the variability of the Rhodes Gyre at different scales.

First, let us summarize what has been done so far for the Rhodes Gyre. The hydrodynamics of this gyre has been well described in the literature (Ediger et al., 2005; Yilmaz et al., 1994; Theocharis et al., 1993; Özsoy et al., 1991, 1993) but it is not fully understood. The Rhodes Gyre is a cyclonic persistent feature of the Levantine basin with a low-temperature core (Özsoy et al., 1989) covering a large area centered upon the Rhodes Basin. Often detected by satellite images (Marullo et al., 2003), its center is a doming of the cold isotherms indicating a permanent upwelling (Özsoy et al., 1989). In winter, a dense water formation takes place within its center at intermediate depth (Marullo et al., 2003) producing the LIW which will eventually flow out of Gibraltar into the Atlantic ocean (Lascaratos et al., 1993; Nittis and Lascaratos, 1998). The winter mixed layer is marked in this area, heat loss and winds contribute to the winter mixed layer deepening and to the formation of intermediate and eventually deep waters. Estournel et al. (2021) using a 3D hydrodynamic model established the presence of two secondary cyclones inside the gyre smaller in winter. The overturning circulation of the deep and intermediate waters has been previously documented in the literature (Pinardi et al., 2015) but it has not been described in the Rhodes Gyre area.

Observational and modeling studies have also tried to describe the dynamics of the biogeochemical properties of this system. Events of surface chlorophyll increase have been recorded in the gyre following the mixing period, and have been reported through satellite data by Antoine et al. (1995) and through observational data by Vidussi et al. (2001). The bloom events are induced by the cyclonic circulation and the vertical mixing associated with intense air-sea interactions during winter allowing the injection of nutrients in the surface (Crise et al., 1999; D'Ortenzio and Ribera d'Alcalà, 2009; Lavigne et al., 2015). Nutrient stocks are uplifted into the surface layer. However, during cold and windy winters, significant nutrient concentrations are injected in the euphotic layer which in turn sustains the phytoplankton growth (Yilmaz and Tugrul, 1998; Ediger and Yilmaz, 1996). The hydrographic features of the Rhodes Gyre also determine the depth and the thickness of the nutricline (Yilmaz et al., 1994).

Napolitano et al. (2000) using a one dimensional coupled physical biological model, described the seasonal nutrient cycle of the gyre. They also showed that the vertical extent of mixing in the Rhodes influences the amplitude and the timing of the spring bloom. The MLD dynamic is therefore the primary factor in controlling the uptake and the availability of nutrients in the upper layers, and ultimately, the phytoplankton growth (Napolitano et al., 2000; Pedrosa-Pàmies et al., 2016; D'Ortenzio et al., 2021).

The Rhodes Gyre has been classified as a region characterized by intermittent blooms, surrounded by a no-bloom zone based on the trophic regimes of D'Ortenzio and Ribera d'Alcalà (2009). Napolitano et al. (2000) estimated the annual primary production to 97 g C m^{-2} yr^{-1}, comparable to the northwestern Mediterranean Sea (Antoine et al., 1995). The phytoplankton bloom fuels the biological carbon pump exporting carbon down to the ocean's interior. Pedrosa-Pàmies et al. (2016) estimated a total amount of 0.8 g C m^{-2} yr^{-1} of sinking organic carbon in the Rhodes Gyre during 2012. While Ediger et al. (2005) showed a temporal variation in the composition and abundance of particulate matter, high particulate organic matter concentrations being recorded in the gyre during late winter in the surface layer comparable to those of the more productive NW Mediterranean basin found by Doval et al. (1999).
This review of observational and modeling studies shows the limitation of the data and their lack in confirming what is presumed for the biogeochemical dynamic of the gyre and its forcing factors. In this chapter, we will provide new insights into the production and fate of the organic carbon in the Rhodes gyre, using 3D coupled physical-biogeochemical modeling. It is noteworthy to mention the choice of this specific region instead of conducting a study on a larger basin scale. The Rhodes Gyre is an "oasis" in the Levantine marine desert and appears to have an impact on the basin's widespread oligotrophic nature, it is interesting to investigate the carbon dynamics in this gyre and how it is likely to influence the oligotrophy of the surrounding area.

4.2 Résumé de l'article

Le Gyre de Rhodes est un cyclone permanent de la circulation générale du Bassin Levantin dans l'est de la Mer Méditerranée. Bien qu'il soit situé dans le bassin le plus oligotrophe de la mer Méditerranée, il s'agit d'une zone de production primaire relativement élevée en raison de l'important apport hivernal de nutriments associé à la formation des eaux intermédiaires levantines. Dans cette étude, un modèle 3D couplé hydrodynamique-biogéochimique (SYMPHONIE/Eco3M-S) a été utilisé pour caractériser la variabilité saisonnière et interannuelle de l'écosystème du Gyre de Rhodes et pour estimer un bilan annuel de carbone organique sur la période 2013-2020. Les comparaisons des sorties du modèle avec les données satellitaires et les données compilées in situ des campagnes à la mer et des flotteurs Argo biogéochimique ont révélé la capacité du modèle à reproduire les principales dynamiques biogéochimiques saisonnières et spatiales du Bassin Levantin. Les résultats du modèle ont montré que pendant la période de mélange hivernal, le phytoplancton se développe d'abord progressivement, soutenu par l'apport de nutriments. Ensuite, de courts épisodes de convection générés par des pertes de chaleur à la surface et des événements de vents intenses, favorisant les injections de nutriments dans la couche de surface, l'exportation de carbone organique vers le fond et induisant une légère limitation de la production primaire, alternent avec de courts épisodes de croissance phytoplanctonique. L'estimation du bilan annuel de carbone organique a montré que le Gyre de Rhodes est une zone autotrophe avec une production communautaire nette positive dans la couche supérieure (0-150 m) s'élevant à 31.2 ± 6.9 g C m^{-2} an^{-1}. La production communautaire nette dans la couche supérieure est presque équilibrée, sur la période d'étude de sept ans, par des transferts physiques, (1) via l'exportation vers le fond (16.8 ± 6.2 g C m^{-2} an^{-1}) et (2) par le transport latéral vers les régions environnantes (14.1 ± 2.1 g C m^{-2} an^{-1}). La couche intermédiaire (150-400 m) semble également être une source de carbone organique pour la Mer Levantine environnante (7.5 ± 2.8 g C m^{-2} an^{-1}) principalement par la subduction de l'Eau Intermédiaire Levantine après le mélange hivernal. Le Gyre de Rhodes montre une forte variabilité interannuelle avec une production primaire , une production communautaire nette et des exportations plus importantes au cours des années marquées par des fortes pertes de chaleur à la surface et un mélange vertical hivernal profond. Cependant, la production primaire annuelle ne semble être que partiellement influencée par le mélange vertical hivernal. Sur la base de nos résultats, nous pouvons supposer que l'augmentation future de la température et de la stratification pourrait avoir un impact important sur les flux de carbone dans cette région.

4.3 Article

Submitted article to Biogeosciences journal

Seasonal and interannual variability of the pelagic ecosystem and of the organic carbon budget in the Rhodes Gyre (Eastern Mediterranean): influence of winter mixing

Joelle Habib[1,2], Caroline Ulses[1], Claude Estournel[1], Milad Fakhri[2], Patrick Marsaleix[1], Mireille Pujo-Pay[3], Marine Fourrier[4], Laurent Coppola[4,5], Alexandre Mignot[6], Laurent Mortier[7], Pascal Conan[3]

[1] Laboratoire d'Etudes en Géophysique et Océanographie Spatiales (LEGOS), Université de Toulouse, CNES/CNRS/IRD/UT3, Toulouse, France

[2]National Center for Marine Sciences, National Council for Scientific Research (CNRS-L), Jounieh, Lebanon

[3]Sorbonne Université, CNRS, UMR7621, Laboratoire d'Océanographie Microbienne (LOMIC), Paris, France

[4] Laboratoire d'Océanographie de Villefranche, CNRS, Sorbonne Université, Villefranche-sur-Mer, France

[5]Sorbonne Université, CNRS, OSU STAMAR, UAR2017, 4 Place Jussieu, 75252 Paris cedex 05, France

[6]Mercator Océan International, Toulouse, France

[7]Sorbonne Université, UPMC Univ Paris 06 CNRS-IRD-MNHN, Laboratoire d'Océanographie et du Climat: Expérimentations et Approches Numériques (LOCEAN), 4 place Jussieu, 75005 Paris, France

Correspondence to: Joëlle Habib (joellehabib22@hotmail.com)

Abstract

The Rhodes Gyre is a cyclonic persistent feature of the general circulation of the Levantine Basin in the eastern Mediterranean Sea. Although it is located in the most oligotrophic basin of the Mediterranean Sea, it is a relatively high primary production area due to strong winter nutrient supply associated with the formation of Levantine Intermediate Water. In this study, a 3D coupled hydrodynamic-biogeochemical model (SYMPHONIE/Eco3M-S) was used to characterize the seasonal and interannual variability of the Rhodes Gyre's ecosystem and to estimate an annual organic carbon budget over the 2013-2020 period. Comparisons of model outputs with satellite data and compiled in situ data from cruises and BioGeoChemical-Argo floats revealed the ability of the model to reconstruct the main seasonal and spatial biogeochemical dynamics of the Levantine Basin. The model results indicated that during the winter mixing period, phytoplankton first progressively grow sustained by nutrient supply. Then, short episodes of convection driven by heat loss and wind events, favoring nutrient injections, organic carbon export and inducing light limitation on primary production, alternate with short episodes of phytoplankton growth. The estimate of the annual organic carbon budget indicated that the Rhodes Gyre is an autotrophic area with a positive net community production in the upper layer (0-150 m) amounting to 31.2 ± 6.9 g C m^{-2} $year^{-1}$. Net community production in the upper layer is almost balanced over the seven year period by physical transfers, (1) via downward export (16.8 ± 6.2 g C m^{-2} $year^{-1}$) and (2) through lateral transport towards the surrounding regions (14.1 ± 2.1 g C m^{-2} $year^{-1}$). The intermediate layer (150-400 m) also appears to be a source of organic carbon for the surrounding Levantine Sea (7.5 ± 2.8 g C m^{-2} $year^{-1}$) mostly through the subduction of Levantine Intermediate Water following winter mixing. The Rhodes Gyre shows high interannual variability with enhanced primary production, net community production and exports during years marked by intense heat losses and deep mixed layers. However, annual

primary production appears to be only partially driven by winter vertical mixing. Based on our results, we can speculate that future increase of temperature and stratification could strongly impact the carbon fluxes in this region.

1 Introduction

The ocean absorbs about 25% of the anthropogenic CO_2 emitted into the atmosphere (Friedlingstein et al., 2021). Various processes are involved in the ocean carbon sink: chemical processes driving the air-sea exchanges according to CO_2 solubility linked to sea surface temperature and salinity, biogeochemical processes in which dissolved inorganic carbon is first converted into organic carbon through photosynthesis, and then transferred to great depths, possibly after remineralization, and diffusive and advective physical processes (Palevsky and Quay, 2017; Palevsky and Nicholson, 2018). Those various chemical, biogeochemical and physical mechanisms interact, especially in highly dynamical regions such as water formation areas (Körtzinger et al., 2008), and it is crucial to understand those mechanisms and their interactions, as well as their variability and evolution in the context of increasing atmospheric CO_2 content and global warming.

The Levantine Basin, in the southeastern Mediterranean Sea (Fig. 1), is a concentration basin, i.e. there is a net loss of water by evaporation, balanced by an input of less salty water from the Atlantic Ocean flowing successively through the straits of Gibraltar and Sicily (Lascaratos et al., 1993). The Levantine Basin is also a warm and salty sea with surface temperature reaching 27.9 °C (El-Geziry, 2021) and salinity above 39.5 (Manca et al., 2004). Located in the northeastern part of the Levantine Basin, the Rhodes Gyre (Fig. 1) is a cyclonic persistent feature (Robinson et al. 2001; Millot and Taupier-Letage, 2005; Estournel et al., 2021) whose hydrodynamics has been well described in the literature, in particular following the POEM program in the 90s (Theocharis et al., 1993; Ozsoy et al., 1991; 1993; Marullo et al., 2003). During cold winter wind events, the high saline surface waters of the cyclonic Rhodes Gyre cool down, and their density increases, which generates deep mixing layers. During the following months, the newly formed dense water sinks to reach intermediate depths (130 - 400 m) forming the Levantine Intermediate Water (LIW, Hecht et al., 1988; Taillandier et al., 2022). Other studies have also reported LIW formations in the Gulf of Antalya (Sur et al., 1992; Kubin et al., 2019; Fach et al., 2021), in the southeastern margins of the basin, along the continental margins of the totality of the Levantine Basin (Brenner et al., 1991; Lascaratos et al. 1993; Özsoy et al. 1993) or in the Cretan Sea (Taillandier et al., 2022). However, the Rhodes Gyre remains the major area of LIW formation in the Levantine Basin (Lascaratos et al. 1999; Özsoy et al., 1989).

From a biogeochemical point of view, the eastern Mediterranean is a singular basin in terms of its oligotrophic to ultra oligotrophic regimes (Krom et al., 1991; Siokou-Frangou et al., 2010; Pujo-Pay et al., 2011; Kress et al. 2014) with chlorophyll concentrations reaching at most 0.5 mg m^{-3} in the deep chlorophyll maximum layer (Mignot et al., 2014). Considered an “oasis” in the Levantine Basin (Siokou-Frangou et al., 1999), the Rhodes Gyre is characterized by higher phytoplankton biomass and biological production than the surrounding region (Vidussi et al., 2011). Yilmaz and Tugrul (1998) detailed the coupling of hydrodynamic conditions and nutrient enrichment in the gyre. Under prolonged and cold winter conditions, the Rhodes Gyre presents chimney formations, where Levantine deep or intermediate water, moving to the surface due to mixing, enriches the euphotic layer in nutrients (Yilmaz and Tugrul, 1998; Ediger and Yilmaz, 1996). Observational studies also showed that cyclonic features of the Rhodes Gyre determine the depth and thickness of the nutricline (Yilmaz et al., 1994). Ediger and Yilmaz (1996) highlighted the interannual variability in nutrient supply into the euphotic layer in the area, with fewer injections during mild winters compared to cold winters. This was in agreement with the one-dimensional coupled physical-biological modeling study by Napolitano et al. (2000) who found an increase of nutrient supply with the intensification of winter cooling across the same year. They also showed that the vertical extent of mixing influences the magnitude and timing of the spring phytoplankton bloom. Based on an analysis of ocean color satellite data, D'Ortenzio and Ribera d'Alcalà (2009) classified the Rhodes Gyre as a trophic regime with an intermittent phytoplankton bloom. They reported a strong interannual variability in the spatial shape and timing of the bloom. Mayot et al. (2016) further showed the alternation between bloom, intermittent and no bloom regimes in the gyre.

After its formation, LIW spreads throughout the whole eastern Mediterranean Sea (Theocharis et al., 1993; Millot and Taupier-Letage, 2005; Estournel et al., 2021) and then heads towards the western Mediterranean and represents the main contribution to the outflow at the Strait of Gibraltar (Tanhua et al., 2013; Malanotte-Rizzoli et al., 2014). LIW is considered to play an important role in the formation of the Mediterranean intermediate and deep waters in the Aegean Sea, as well as in the southern Adriatic Sea and the northwestern Mediterranean Sea (Grignon et al., 2010; Velaoras et al., 2014; Margirier et al., 2020; Taillandier et al., 2022). This water mass may also have a critical impact on the biogeochemistry of the entire Mediterranean Sea (Astraldi et al., 1999; Malanotte-Rizzoli et al., 2014; Kress et al., 2014; Touratier and Goyet, 2009; Palmiéri et al., 2016). Thus, understanding its formation and propagation is a key to study its impact on biogeochemical dynamics first in the ultra oligotrophic Levantine Basin and then in the entire Mediterranean Sea.

In spite of the importance of LIW in the hydrodynamics and biogeochemistry of the eastern and western Mediterranean Sea, relatively few studies have been conducted since the POEM program in the 90s (The POEM group, 1992), partly because of the complex geopolitical situation and restricted access. In particular, in situ cruise data remain rare in the Rhodes Gyre (Napolitano et al., 2000; Marullo et al., 2003), with most studies having been conducted in the northeastern Levantine Basin (Krom et al., 2005; Hassoun et al., 2019; Alkalay et al., 2020; Fach et al., 2021) or through a limited section in the basin (Moutin and Raimbault, 2002; Pujo-Pay et al., 2011; Santinelli, 2015), and mostly during the stratification period. On the other hand, only one 1-D coupled hydrodynamic-biogeochemical model has been carried out in the Rhodes Gyre (Napolitano et al., 2000), while most 3D modeling studies investigated the whole Mediterranean Sea (Lazzari et al., 2012; Macias et al., 2014; Guyennon et al., 2016; Richon et al., 2017, 2018; Karaloni et al., 2020; Cossarini et al., 2021) or eastern Mediterranean Sea (Petihakis et al., 2009) without focusing on the LIW formation region of the Rhodes Gyre.

Along with the deployment of Argo floats in the Levantine Sea since 2015 (Pasqueron de Fommervault et al., 2015), the PERLE (Pelagic Ecosystem Response to deep water formation in the Levant Experiment) project, within the framework of which this study takes place, was conducted in order to obtain a better understanding of the formation and spreading of LIW and their impacts on the distribution of nutrients and planktonic ecosystems. In the frame of the PERLE project, D'Ortenzio et al. (2021) documented, using Biogeochemical-Argo floats and in situ data sampled during the cruise, a coupling between mixed layer and phytoplankton dynamics in the Rhodes Gyre. They found that winter deepening of the mixed layer induces a steady injection of nitrate into the surface followed by a rapid accumulation of phytoplanktonic biomass. However, this study is limited to parameters measured by biogeochemical floats, which does not allow for a more detailed exploration of biogeochemical and ecosystem dynamics. On the other hand, the intermittent trophic status of the area suggests significant interannual variability that remains poorly understood. In order to fill these gaps, the present study aims to gain insight into carbon dynamics through the examination of seasonal and interannual variabilities of the biogeochemical and physical fluxes of organic carbon, under particulate and dissolved forms, in the Rhodes Gyre and the estimate of an annual budget of organic carbon in the area over a multi-annual period. For that, we analyzed a simulation of a 3-D hydrodynamic-biogeochemical coupled model implemented over the Mediterranean Sea over the period from December 2013 - April 2021, and we focused on the Rhodes Gyre. The paper is organized as follows: first we describe in Sect. 2 the numerical models and the various data sets used to evaluate the model. Then, in Sect. 3 we present the assessment of the coupled model, the seasonal and interannual physical and biogeochemical variability and an annual budget of organic carbon . Results are discussed in Sect. 4 and conclusions are given in Sect. 5.

2 Material and methods

2.1 The coupled physical-biogeochemical model

2.1.1 The hydrodynamic model

The 3D primitive equation ocean model SYMPHONIE is described in detail in Marsaleix et al. (2006; 2008), Estournel et al. (2016) and Damien et al. (2017). This model has been primarily used to describe the circulation in response to wind forcing and the dynamics of river plumes (Estournel et al., 1997, 2001; Marsaleix et al., 1998), coastal circulations (Estournel et al., 2003; Petrenko et al., 2008), dense water formation (Estournel et al., 2005; Ulses et al., 2008; Herrmann et al., 2008; Estournel et al., 2016) and shelf-slope exchanges (Mikolajczak et al., 2020).

2.1.2 The biogeochemical model

Eco3M-S is a biogeochemical multi-nutrient and multi-plankton functional type model, representing the dynamics of the pelagic planktonic ecosystem previously described by Auger et al. (2011) and Ulses et al. (2021). It describes the cycles of carbon (C), nitrogen (N), phosphorus (P), silicon (Si), dissolved oxygen (O_2) and chlorophyll (Chl). The model is composed of eight compartments: dissolved inorganic nutrients (nitrate, ammonium, phosphate and silicate), dissolved oxygen, phytoplankton represented by three size classes (pico-, nano- and micro-phytoplankton), zooplankton formed of three size classes (nano-, micro- and meso-zooplankton), bacteria, particulate organic matter (POM), divided into two groups based on their settling speed (fast and slow settling speed) and dissolved organic matter (DOM). A summary diagram of the food web structure of the model and the interactions between the compartments is represented in Fig. S1.

The model was previously used in the Mediterranean Sea to study the pelagic ecosystem and biogeochemical processes in coastal areas (Auger et al. 2011; Many et al. 2021) and open-sea regions (Herrmann et al. 2013; Auger et al. 2014; Kessouri, 2015; Ulses et al. 2016; Kessouri et al. 2017; 2018; Ulses et al., 2021).

2.1.3 Implementation

The model configuration and implementation of the hydrodynamic simulation were described by Estournel et al. (2021). The model domain covers the Mediterranean Sea as well as the Marmara Sea and reaches 8° West in the Gulf of Cadiz. The horizontal grid is characterized by a resolution that varies between 2.3 and 4.5 km from the northwest to the southeast to account for the increase of the Rossby deformation radius therefore allowing an adequate representation of mesoscale processes. As for the Gibraltar Strait, the model resolution was further increased to 1.3 km grid for a better representation of the exchange area between the Mediterranean Sea and Atlantic Ocean. The vertical grid uses a VQS (vanishing quasi sigma) coordinate system with 60 levels and increased resolution near the surface. This model configuration was used to describe the surface and intermediate water circulations in the eastern Mediterranean Sea (Estournel et al., 2021).

The SYMPHONIE simulation is performed from 1 July 2011 to 2 May 2021. The meteorological parameters (with radiative fluxes) are hourly operational forecasts based on ECMWF 12 hour analyses at 1/8° horizontal resolution. A total of 142 rivers (Fig. S2) are considered in the model. As for the rivers of the Levantine Basin, monthly climatology discharges were based on the study of Poulos et al. (1997), except for the Nile River where the discharge value was set to 475 $m^3 s^{-1}$, following Nixon (2003).

We used the daily 3D current velocity, temperature, salinity and vertical diffusivity outputs of the hydrodynamic simulations as forcing fields for the biogeochemical model run on the same grid. The biogeochemical model runs for the period from 15 August 2011 to 2 May 2021 but outputs are analyzed from December 2013. The time step is 20 min for advection and diffusion of biogeochemical variables and 2 h for biogeochemical reactions. We initialized the biogeochemical model with observation profiles during the stratified period averaged over 10 regions of the Mediterranean Sea (indicated in Fig. S2). For inorganic nutrients profiles, we used the CARIMED (CARbon, tracer and ancillary data In the MEDsea) database (Àlvarez et al., 2019; see Sect. 2.2.2), considering only summer data over the period 2011-2012, when data were available. Due to the lack of summer observations for the Levantine region, we used spring observations. Regarding the dissolved oxygen and chlorophyll concentrations, we initialized using summer in situ observations from BioGeoChemical-Argo floats (BGC-Argo, Argo, 2022) (see Sect. 2.2.3) and the CARIMED database. Solar radiation and wind forcing for the biogeochemical simulation are those used for the hydrodynamic simulation. Atmospheric depositions of inorganic nutrients were taken into account. Nitrate and ammonium atmospheric depositions were applied as constant values based on the results of Kanakidou et al. (2012), Ribera d'Alcala et al. (2003), Powley et al. (2017) and Richon et al. (2018) and silicate deposition was prescribed as constant values for western (west of the Sicily Strait) and eastern basins based on estimates given by Ribera d'Alcalà et al. (2003). We deduced phosphate deposition from monthly Saharan dust deposition modeled with the regional model ALADIN-Climat (Nabat et al., 2015) and averaged over the period 1979-2016. We hypothesized that phosphorus represents 0.07 % of dust and that 15% is in soluble form (Herut and Krom, 1996; Guerzoni et al., 1999; Ridame and Guieu, 2002; Richon et al., 2017). Nutrient fluxes at the water column/sediment interface have been obtained through a coupling of the biogeochemical model with a simplified version of the vertically integrated benthic model described by Soetaert et al. (2000). At the river mouths, concentrations of nutrients were imposed using the results of Ludwig et al. (2010) who estimated the nutrient river discharge for the main rivers and 10 sub-regions of the Mediterranean Sea (Alboran, South-Western, North-Western, Tyrrhenian, Adriatic, Ionian, Central, Aegean, North-Levantine, South-Levantine). In the Atlantic Ocean, nutrients were prescribed using monthly profiles from the World Ocean Atlas 2009 climatology (https://odv.awi.de/en/data/ocean/world-ocean-atlas-2009/) at 5.5 °W. In the Marmara Sea, in order to represent a two-layer flow regime, we imposed a relaxation with a timescale of 1 day towards nitrate concentrations of 0.24 and 1.03 mmol N m^{-3} and phosphate concentrations of 0.06 and 0.05 mmol P m^{-3} for depths above and below 15 m respectively, based on the observations near the Dardanelles Strait from Tugrul et al. (2002).

2.1.4 Definition of the study area and budget calculation

In this paper, the analysis of the simulation of the whole Mediterranean basin is restricted to the Rhodes Gyre. Previous studies determined the Rhodes Gyre's location based on a Sea Surface Temperature (SST) criteria. Marullo et al. (2003) using AVHRR (Advanced Very High-Resolution Radiometer) images time series located the gyre in an area between the southeast of Rhodes and the east of Crete: 27°-30° E and 34-36° N with a threshold of 14°C. D'Ortenzio et al. (2021) identified the region using a SST threshold at 15°C based on satellite images. Other studies have also used the Sea Surface Height (SSH) from ADT (Absolute Dynamical Topography) maps to detect mesoscale features of the Mediterranean Sea such as Cornec et al. (2021).

In this study, we defined the Rhodes Gyre area based on modeled surface density. The winter mean surface density was calculated between January and mid-March, the period generally associated with deep vertical mixing (Malanotte-Rizzoli et al., 2003). The Rhodes Gyre was defined by the area where the density anomaly is above 28.8 kg m^{-3}. The resulting region (indicated in Fig. S3 and Fig. 1) designates a large area of the Rhodes Gyre, covering 27 500 km^{2}, that includes areas where the strongest mixing occurred over the period 2014-2021. The hydrodynamic and the biogeochemical variables presented in the following sections correspond to values averaged over this domain.

To calculate the organic carbon budget, the water column was divided into two layers. The surface layer is defined as the euphotic layer covering the surface to 150 m of depth, and the intermediate layer, from 150 to 400 m (Ozer et al., 2016; Menna et al., 2010, 2021), includes the LIW. Organic carbon englobes dissolved and particulate organic carbon (DOC and POC, respectively). The latter includes all modeled components of POC: low and fast sinking detritic particles and living organisms, i.e. the three size classes of phytoplankton, the three size classes of zooplankton and bacteria. The biogeochemical contribution to the organic carbon budget is the sum of gross primary production (GPP) and organic carbon consumption through community respiration (CR) (phytoplankton, zooplankton and bacteria respiration) (see Table S4 in Supplement Material by Many et al. (2021)). The physical contribution of the budget is divided into two components: lateral transport and vertical transport, both due to mixing and advection. Lateral transport represents the net transport at the lateral limits of the Rhodes Gyre area. Vertical transport represents the exchanges at the vertical boundaries of the layer. Positive values correspond to fluxes of organic carbon that enters the considered layer of the Rhodes Gyre area. Similarly, negative values correspond to fluxes of organic carbon that leaves the considered layer of the Rhodes Gyre area. The variation of organic carbon inventory, the biological term and lateral physical term were calculated online, i.e. during the simulation, while the vertical term was calculated as the residual based on values of all other terms. The equations of the budget are given in Supplement Material (Text S1).

2.2 Observations used for the coupled model assessment

In order to assess the performance of the model, we used remote sensing, in situ and BGC-Argo float data over the study period. Because the number of observations in the Rhodes Gyre area is limited,the comparison was conducted all over the Levantine Basin. The spatial coverage of the in situ dataset used in this study is shown in Fig. 1.

2.2.1 Satellite Data

To evaluate the modeled surface chlorophyll concentration, we used daily level 4 reprocessed data obtained from the European Copernicus Marine Environment monitoring Service (CMEMS) from the website (http://resources.marine.copernicus.eu/, products: OCEANCOLOUR_MED_CHL_L4_REP_OBSERVATIONS_009_078, last access: 16 June 2022) with a spatial resolution of 1 km. The latter is a regional product with daily interpolated chlorophyll concentrations from multi sensors (MODIS-Aqua, NOAA-20-VIIRS, NPP-VIIRS, MERIS sensors). To compare model results with those data, we interpolated the data on the model grid.

2.2.2 Cruise observations

We used the CARIMED (CARbon, tracer and ancillary data In the MEDsea) database with 862 profiles covering cruise observations available in the Mediterranean Sea for the period 2011-2018 (Àlvarez et al., 2019), to complete the assessment of the spatial distribution of the simulated variables. Data passed two quality controls following the GLODAP (Global Data Analysis Project) procedure (Key et al., 2004) adapted to the Mediterranean Sea. This dataset included cruises with only best-practiced standards for nutrients following the GO-SHIP (The Global Ocean Ship-based hydrographic investigations Program) and the WOCE (World Ocean Circulation Experiment) protocols. Fourrier et al. (2020) added data from 10 other cruises to the dataset and validated them. The data are available on figshare (https://doi.org/10.6084/m9.figshare.12452795.v2, last access: 10 October 2022, Fourrier, 2020). Sea water was collected using Niskin bottles from the surface to 4600 m of depth. An SBE43 oxygen sensor was used during the cruises and adjusted with Winkler measurements. The inorganic nutrients were determined following the colorimetric methods of Grasshoff et al. (1999).

We also used the PERLE cruise dataset: PERLE 1 (25 profiles) covering the Levantine Basin in October 2018 and PERLE 2 (29 profiles) in February-March 2019 (D’Ortenzio et al., 2021). At all stations water samples were collected from Niskin bottles for nutrient analysis. This dataset passed a primary quality control.

It is important to mention that we used validation data different from calibration data to prevent over fitting of model parameters and to have a better assessment of the model’s reaction capacity when the validation patterns are different from those used in the calibration; this method was supported by Robson (2014) .

2.2.3 BGC-Argo floats

To evaluate the temporal and the spatial variability of the modeled dissolved oxygen and chlorophyll, we used observations from BGC-Argo floats providing O_2 (1566 profiles) and Chl-a (1171 profiles) measurements (Argo, 2022) deployed in the eastern Mediterranean, downloaded from the Argo Global Data Assembly Center web portal accessible through the Coriolis database (http://www.coriolis.eu.org, last access: 21 June 2022). Regarding O_2 measurements made by Argo floats, air measurements and optode calibration protocols have led to a significant improvement in the quality and accuracy of these data (Bittig et al. 2018; Bittig and Körtzinger 2015). These can now reach accuracies of 1-1.5 µmol kg^{-1} close to those achieved in situ by the Winkler method. Mignot et al. (2019) conducted a similar study to try to quantify the observational errors for dissolved oxygen and chlorophyll concentrations. They found a bias of 2.9 ± 5.5 µmol kg^{-1} and -0.06 ± 0.02 mg m^{-3} for the oxygen and the chlorophyll respectively and a relative Root Mean Square Difference (RMSD) of 6.1% for oxygen and 5.4 % for chlorophyll in the Mediterranean Sea.

3 Results

3.1 Assessment of the coupled physical-biogeochemical model

The hydrodynamical model was evaluated by Estournel et al. (2021) by computing model/observations statistics using salinity and temperature observations from Argo floats and satellite data. The authors showed the ability of the model to reproduce the hydrological characteristics of the surface and intermediate waters in the eastern Mediterranean Sea. In the following section, we focus on the evaluation of the biogeochemical model in the Levantine Sea.

3.1.1 Surface chlorophyll concentration

Figure 2 shows the temporal variation of the satellite and modeled surface chlorophyll averaged all over the Levantine Sea (panel (a)), as well as the BGC-Argo float data, and the modeled surface chlorophyll along the trajectory of floats located in the Levantine Sea (panel (c), data located specifically in the Rhodes Gyre are indicated in lighter colors (panel (b,d)), over the study period. To quantify the differences between model outputs and observations, we calculated the percent bias (PB, $100 \times \frac{Mean\,mod - Mean\,obs}{Mean\,obs}$, where *Mean mod* and *Mean obs* are the mean of the model outputs and observations respectively) and the Normalized Root Mean Square Difference (NRMSD, $\sqrt{\frac{\sum_{k=1}^{k}(Obs - Mod)^2}{Max\,obs - Min\,obs}}$ where *Obs* and *Mod* are the observation and model output, respectively, *Max obs* and *Min obs* are the maximum and minimum observation values for the chlorophyll).

The model captures the seasonal dynamics of the observed satellite chlorophyll over the Levantine basin (Fig. 2a) and more particularly in the Rhodes Gyre (Fig. 2b). At the end of fall, the chlorophyll concentration begins to increase progressively and reaches its maximum in February/March, with higher maxima in the Rhodes Gyre compared to the surrounding Levantine Sea, in both the data and the model. The surface concentration is minimal in summer, for both the model and satellite. The model and satellite show differences in magnitude: in the model the winter maximum is generally higher, and the summer minimum values are lower, compared to the satellite data for both regions. The standard deviation (SD) of the model in the Levantine basin (0.04 mg Chl m^{-3}) and the Rhodes Gyre (0.07 mg Chl m^{-3}) is close to the mean chlorophyll concentration (0.05 mg Chl m^{-3}, 0.06 mg Chl m^{-3} respectively) which underlines the high variability of this oligotrophic system. The mean surface chlorophyll concentration in the satellite data for the Levantine basin and the Rhodes Gyre is 0.05 ± 0.02 and 0.06 ± 0.02 mg Chl m^{-3}. We obtain a highly significant correlation coefficient equal to 0.90 and 0.79 (p-value < 0.01), and low values for the NRMSD (an error of 23%, and 8%) and percent bias (-0.71, 12%), between model outputs and satellite data over the whole study period for the Levantine basin and the Rhodes Gyre, respectively. Regarding the comparison with BGC-Argo float data in the Levantine Sea (Fig. 2c) and the Rhodes Gyre (Fig. 2d), the model reproduces correctly both the seasonal cycle and the magnitude of chlorophyll during the different periods of the year. Both model and float data show high variability in late winter/early spring in the Rhodes Gyre in agreement with previous studies (D'Ortenzio and Ribera d'Alcalà, 2009; Salgado-Hernanz et al., 2019; Kotta and Kitsiou, 2019). The statistical metrics show a significant correlation equal to 0.66 (p-value <0.01) between the observed and modeled values in the Levantine Sea. The NRMSD is equal to 13% and the percent bias remains low (-13%). Similar statistical scores were obtained between the model outputs and the float data in the Rhodes Gyre, i.e. correlation (0.78, p-value <0.01) as well as low bias (-19%) and NRMSD (15

%). The difference between the comparisons of model results with satellite data and those with BGC-Argo float data could be attributed in part to an underestimation of satellite chlorophyll concentration during winter in the Levantine Sea as suggested by Vidussi et al. (2001) and reported by D'Ortenzio et al. (2021).

3.1.2 Seasonal variation of vertical distribution

Figure 3 shows a comparison of modeled and observed mean seasonal profiles of chlorophyll, dissolved oxygen, nitrate and phosphate, in the Levantine Sea from both BGC-Argo floats and the oceanographic cruises. The model results are compared with the observations at the same dates and positions. This comparison is completed by a statistical analysis computed over the whole period of study (Fig. S4).

The model reproduces the general features of the nitrate and phosphate concentration profiles with an increase from the surface to 500-1000 m and a gradual, low decrease below, close to the profiles imposed at the initialization, showing a stability over the simulation period (Fig. 3). The modeled phosphate concentrations in the transitional layer (500-1000), located between the intermediate and deep layers, are in the lower range values of observations. The surface nutrient profiles show low concentrations from the surface to 50 m during winter while in spring and fall the layer depleted in nutrients reaches 100 m, in both observations and model outputs.

The statistical analysis (Fig. S4) shows that the model displays high correlation ($R > 0.90$, $p\text{-value} < 0.01$, for all the cruise datasets) and low RMSD (~ 0.01, 0.03 and 0.02 mmol P m^{-3} for CARIMED, PERLE 1 and PERLE 2, respectively) and bias (0.006,-0.01 -0.03 mmol P m^{-3} for CARIMED, PERLE 1 and PERLE 2, respectively) compared to the phosphate observations. PERLE 1 and PERLE 2 phosphate observations show high variability, with a SD ~ 0.065 and 0.062 mmol P m^{-3} respectively. The modeled SD for both cruises is slightly smaller in comparison with observations (0.05 and 0.04 mmol P m^{-3}). As for nitrate, the metrics confirm the good agreement between model outputs and observations with significant correlations above 0.95 ($p\text{-value} < 0.01$), a bias of 0.1, -0.1 and 1.4 mmol N m^{-3} for PERLE 1, PERLE 2 and CARIMED, respectively, and a RMSD close to 0.4 mmol N m^{-3} for PERLE 1 and PERLE 2 and 1.3 mmol N m^{-3} for CARIMED.

The model reproduces the development of a deep chlorophyll maximum (DCM) in spring, and its presence in summer and fall, reaching a maximal depth in summer (Fig. 3). During winter, the model overestimates the surface chlorophyll by 0.05 mg Chl m^{-3} and homogenization in the first 50 m. It generally underestimates the DCM concentration by 25 % and overestimates its depth by 20 m (130 m and 110 m for the model and the float, respectively).

The magnitude and seasonal variation of the vertical profile of dissolved oxygen concentration are well reproduced (Fig. 3). As with chlorophyll, the surface oxygen concentration is maximum during winter. It reaches 230 µmol kg^{-1} and 240 µmol kg^{-1} for the model and the float data respectively. The model reproduces the presence of a subsurface oxygen maximum in spring, summer and fall, between 40 and 60 m depth as observed, with an underestimation of its concentration by 10 µmol kg^{-1}. The oxygen minimum layer concentration stands within the range of the observed values. The model is highly correlated with the different data sets ($R > 0.95$, $p\text{-value} < 0.01$). The observations show a SD close to 16.5 µmol kg^{-1} for the floats. The modeled float oxygen concentrations also show a high SD of ~ 14.5 µmol kg^{-1}.

3.1.3 Study case: BGC-Argo float/model comparison

Figure 4 represents the evolution of the chlorophyll and oxygen concentrations for Float 6901764 and those extracted from the model at the same time and location (both indicated on panel (b)). The choice of the float was done based on both the temporal extension and the localization of the platform: this float covers both the Rhodes Gyre and the surrounding region for a long period, 2015 – 2019 (Fig. 4b). The model represents the seasonal cycle, with an increase in the surface chlorophyll during winter (Fig. 4d) followed by the formation and deepening of the DCM (Fig. 4a). The DCM is mostly well localized in the model (10-20 m deeper than in the observations during summer). The model accurately reproduces the vertical distribution of chlorophyll although some differences exist, such as the slight underestimation of the intensity of the maximum chlorophyll also noted in Fig. 3. The surface chlorophyll concentrations for the first 10 m from the simulation and the float data (Fig. 4d) are significantly correlated (R=0.83, p-value < 0.01).

The modeled and observed oxygen display a similar seasonal cycle, with an increase in surface oxygen concentration during winter (Fig. 4e) followed by a decrease at the surface and a deepening of the oxygen maximum (Fig. 4c) during the stratification period. In both the model outputs and observations the oxygen minimum layer is located, at depths between 300 and 1000 m. The model and the float show a good temporal correlation for the surface concentration of dissolved oxygen (R=~0.96, p-value < 0.01, Fig. 4e).

3.2 Meteorological and hydrodynamic variability

Figure 5 exhibits the time series of surface heat fluxes, mixed layer depth (MLD) and temperature profile anomaly (computed based on the difference in temperatures from the mean daily temperature over the seven years), spatially averaged over the Rhodes Gyre area (defined in Sect. 2.1.4). The mixed layer depth is defined as the depth where the potential density exceeds by 0.01 kg m^{-3} its value at 10 m depth (Coppola et al., 2017). This density based criteria is more appropriate than shallower temperature-based MLD estimates to represent mixing in the dense water formation zone, such as the Rhodes Gyre, as suggested by Houpert et al. (2015).

The domain displays a seasonal cycle, characterized by a heat loss at the air-sea interface from October to March followed by a heat gain from April to the end of September (Fig. 5a). During autumn, the strong heat losses, induced by cold northerly wind events (Horton et al., 1997), weaken the stratification and induce mixing until depths around 40-50 m (Fig. 5b). The following northerly wind/heat loss events in winter further favor the deepening of the mixed layer, with the maximum depth ranging between 90 and 180 m in February/March. After March, the sea gains heat, restratifying the surface layer, and the MLD abruptly decreases. The seasonal pattern of modeled heat flux and mixed layer is in agreement with the climatology of the heat storage rates reported by D’Ortenzio et al. (2005) and Houpert et al. (2015). The Rhodes Gyre area displays a minimum winter temperature lower than 16.5 °C in the Levantine Basin (Fig. S5a).

A strong wintry interannual variability of surface heat flux, as well as of wind stress magnitude and MLD, is clearly visible (Fig. 5 and S6, Table S1). Winters 2014-15, 2016-17, 2018-19 and 2019-20 are characterized by a winter mean heat loss higher than the seven year winter average, i.e. 130 W m^{-2} (Table S1, Fig. S6), and with mean winter mixed layer depth close to or higher than the seven year mean mixed layer of 68 m (Table S1). Cold winters (2014-15, 2018-19 and 2019-20) are also marked by strong winter wind stresses, except for 2016-17 characterized by the highest winter heat loss (Fig. S6). Among the mild winters, winter 2013-14 presents both a strong positive winter heat flux anomaly and a strong negative winter wind stress anomaly, as a consequence of the absence of cold winds from January onwards, leading to the shallowest mixed layers (Table S1). Negative anomalies of temperature are generally visible over the ML in winter and in subsurface during the stratification period for years of high winter heat losses (2014-15, 2016-17, 2018-19 and 2019-20, Fig. 5c). These anomalies extend below the subsurface for years 2014-15 and 2016-17 marked by deep winter mixing.

3.3 Variability of the pelagic planktonic ecosystem

Figure 6 presents the modeled time series of vertical profiles of nutrients, phytoplankton, zooplankton and dissolved organic carbon concentrations, spatially averaged over the Rhodes Gyre area.

During fall, nutrient concentrations gradually increase in the surface layer with the weakening of the stratification and the gradual rise of the nutricline (defined here as isoline 1 mmol N m^{-3} for nitracline and 0.05 mmol P m^{-3} for phosphacline) up to the surface (Fig. 6a, 6b and S7) induced by the reduction of solar insolation and the shallowing of the DCM, possibly reinforced by the intensification of the cyclonic circulation,. As for the DOC, it starts decreasing gradually in the first 100 m in mid-fall with the weakening of the stratification (Fig. 6e and S7).

During winter, surface phytoplankton concentration starts to increase when the mixed layer depth increases and persistently reaches the nutriclines (Fig. 6a-c and S7a-d). The Rhodes Gyre area is enriched in nutrients at the surface (Fig. S5c) and is characterized by surface maximum chlorophyll concentrations over the Levantine Sea (Fig. S5b). The zooplankton concentration generally begins to increase after the onset of the phytoplankton accumulation in winter (Fig. 6d and S7e). The DOC concentration in the 0-100 m layer further decreases during the winter mixing period, from January to March (Fig. 6e and S7f). One can also notice that the deepening of the mixed layer in winter is also responsible for the transfer of both plankton and DOC under 150 m where their concentrations increase (Fig. 6). The maximum surface concentration of organic carbon for phytoplankton reaches values higher than 0.5 mmol C m^{-3} between February and March (Fig. 6c, Table S1). Zooplankton concentration reaches its maximum (1-1.5 mmol C m^{-3}) near the surface in March-April (Fig. 6d). Phytoplankton growth stops at the surface when it becomes depleted in phosphate, the surface nitrate concentration ranging between 0.3 and 1 mmol N m^{-3} during winter, in agreement with the observations of Yilmaz and Tugrul (1998) (Fig. 6a-c). Then, the deep chlorophyll maximum (DCM, green dotted line in Fig. 6c) forms. The DOC concentration progressively increases during spring (Fig. 6e).

During summer, the depletion in nutrients increases and deepens: phosphate and nitrate concentrations in the first 150 m are lower than 0.01 mmol P m^{-3} and 0.1 mmol N m^{-3}, respectively (Fig. 6a and 6b). The summer averaged nitracline and phosphacline are localized at 131 m and 144 m, respectively. The averaged DCM for all summer periods is at a mean depth of 128 m with magnitudes between 0.2 and 0.3 mg Chl m^{-3} (Fig. 6c). One should notice that the depth of DCM coincides with the depth of deep carbon maximum. Throughout the summer, the biomass of phytoplankton decreases. The decline of phytoplankton at the end of summer induces a zooplankton decrease (Fig. 6d). On the contrary, DOC accumulates due to stratification and reaches its maximum ranging from 52 to 55 mmol C m^{-3} in early August (Fig. 6e).

Interannual variability of nutrient and phytoplankton concentrations is strong during the mixing period when deep nutrients are injected into the surface layer (Fig. 6a and 6b, S7). During the cold winters (noted C in Figure 6) of 2014-15, 2016-17, 2018-19 and 2019-20, the mixed layer reaches the nutriclines over a larger area (not shown) and period, allowing higher nutrient supplies into the surface layer (Table 1). The interplay between vertical mixing, deep nutrient injection and increase in surface phytoplankton shows interannual variability as illustrated in Fig. 11 for the mild winter 2023-14 and the cold winter 2014-15. When the mixed layer punctually reaches the nutriclines in early winter or throughout a mild winter as in 2013-14 (Fig. 11a), surface nutrients and chlorophyll increase gradually and nearly synchronously. When the winter is severe as in 2014-15 (Fig. 11b), gales expand the area in which MLD breaks through the nutriclines. The surface nutrient response is each time a rapid increase (<1 day see for example early January and early February 2015), while the chlorophyll response depends on the depth of the MLD. When it is shallower than the euphotic layer, chlorophyll increases gradually (~12 days in January 2015). When the MLD exceeds the euphotic layer as in February 2015, chlorophyll development is delayed due to dilution of phytoplankton cells in the deep ML and light limitation for phytoplankton growth. Thus, surface phytoplankton concentrations reach higher values (> 1.5 mmol C m^{-3} and 0.3 mg Chl m^{-3}) during cold winters compared to mild winters (< 1 mmol C m^{-3} and 0.23 mg Chl m^{-3}) (Table S1). These differentiated chlorophyll responses to the mixed layer described here as a function of time also appear simultaneously at different points in space. As an example, Fig. S8 shows a low chlorophyll concentration on 20 February 2015 in the core of the Rhodes Gyre where vertical mixing is the most intense, and higher concentrations in the border of the gyre (panels (a) and (c)). Modeled surface chlorophyll averaged over the Rhodes Gyre area is then maximum 12 days later, on 4 March 2015, when it reaches higher concentrations in the center of the gyre as soon as the water column restratified (Fig. S8b-d). With regard to the date of the maximum surface chlorophyll no clear link with winter severity can be established. The former is instead related to the timing and history of wind events favoring the deepening of the ML, submitted to high interannual variability. For example, it was found on 11 and 12 February during the mild winter 2015-16 and the severe winter 2016-17 respectively (Table S1).

Regarding zooplankton, the spring surface concentration is minimal during the mild year 2013-14 and maximum during the cold years 2016-17, 2018-19 and 2019-20 (Fig. 6d). High concentrations are also visible along the DCM layer for those years, as well as in 2018. DOC concentrations show similar interannual variability as zooplankton (Fig. 6e).

3.4 Organic carbon inventory and fluxes

Figures 7 and 8 represent, respectively in the surface (0 – 150 m) and intermediate (150 - 400 m) layers of the Rhodes Gyre area, the variability of the organic carbon inventory, the biogeochemical fluxes and the vertical and horizontal exchanges at the limits of the two boxes.

In the surface layer, the inventory of organic carbon is minimum in January and maximum in June/July (Fig. 7a). The modeled gross primary production (GPP) generally follows the cycle of the solar insolation (not shown) with minimum values in December and maximum values at the end of June. A secondary peak is visible between February and April (Fig. 7b). Its vertical distribution (not shown) is close to the one of phytoplankton (Fig. 6c) and mostly relies on recycled production (ammonium uptake represents 78% of total nitrogen uptake).. The community respiration (CR) follows a similar pattern to the GPP with a temporal shift of a few weeks. The resulting net community production (NCP, corresponding to GPP minus CR) shows a peak value in February/March, during the secondary peak in the GPP, and negative values from August to January (Fig. 7c), indicating that the region is autotrophic from January to April and heterotrophic for the rest of the year.

The physical transport of organic carbon (POC plus DOC), by lateral and vertical mixing and advection, at the limits of the Rhodes Gyre area is negative almost all year round, and especially during the winter mixing period, which indicates an export of organic carbon from the surface layer (Fig. 7d). Winter export is mainly dominated by vertical downward fluxes, which concern both particulate and dissolved forms (Fig. 7e). Lateral export is more important for DOC, with values exceeding 10 mmol C m^{-2} d^{-1} over several months for some summer/fall periods, when the POC lateral export shows little variation along the period (Fig. 7f). This could be explained by higher current velocities near the surface where the DOC concentration is maximal, compared to 100-150 m where the POC is maximum. The vertical export of total OC is reduced from spring onwards and becomes low (< 10 mmol C m^{-2} d^{-1}) in summer and autumn, when DOC can be injected from the intermediate layer into the surface layer due to upwelling events.

GPP shows interannual variability characterized by higher peak values during the restratification periods at the end of winter, for years 2014-15, 2016-17, 2018-19 and 2019-20 (Fig 7b) marked by strong winter mixing (Fig. 5b). Interannual variability of the seasonal cycle is less pronounced for CR, showing higher peaks following the late winter phytoplankton blooms for the same years (Fig. 7b). As a result, interannual variability of NCP is then linked with the variability of GPP, with higher winter NCP maxima reaching 40 mmol C m^{-2} d^{-1} for the strong mixing winters (Fig. 7c). The model results show that vertical export of POC and DOC at 150 m displays strong interannual variability during the winter mixing period with total OC export reaching 36 mmol C m^{-2} d^{-1} during severe winter years, and remaining lower than 10 mmol C m^{-2} d^{-1} during mild winter years for the surface layer (Fig. 7e). Thus the increase in total OC transport during cold winters seems to be counterbalanced by an increase in NCP. For instance in winter 2014-15 peaks reaching 60 mmol C m^{-2} d^{-1} are visible for both NCP and OC total transport .

The seasonal cycle of the organic carbon inventory in the intermediate layer is generally marked by a first peak during the winter mixing periods and a second peak in summer (Fig. 8a). The OC lateral exchange flux is negative from January to September, indicating a divergence of organic carbon from the Rhodes Gyre to the surrounding regions (Fig. 8b). During fall, it shows small inputs of organic carbon in the Rhodes Gyre. The vertical exchange flux (net difference between vertical fluxes at 150 m and vertical fluxes at 400 m), representing a net gain for the intermediate layer, generally shows an opposite sign to the lateral flux. The total (lateral plus vertical) OC transport (not shown) follows a similar pattern to the vertical flux variations, as vertical exchange flux dominates the lateral one. Finally, OC consumption shows maximum values during winter mixing periods, when heterotrophic respiration follows the downward input of surface OC (Fig. 8c). A secondary peak of OC respiration is visible in fall when the OC stock increases. This can be explained by the deepening of the ecosystem due to the increase in solar radiation at that period. However, the overestimation of the depth of the DCM shown in Sect. 3.1.2 suggests that it could be overestimated in the model results..

Interannual variability can also be discerned in the intermediate layer (Fig. 8). Lateral flux is characterized by higher negative peaks during cold winters: the maximum lateral export exceeds 10 mmol C m^{-2} d^{-1} for cold years while it is limited to 3 mmol C m^{-2} d^{-1} during mild winters (Fig. 8b). OC consumption in February-March is more pronounced during cold years ranging between 5 and 8 mmol C m^{-2} d^{-1} compared to mild years, when it is limited to 2 mmol C m^{-2} d^{-1} (Fig. 8c).

3.5 Annual budget of organic carbon

Figure 9 presents the annual budget of organic carbon for the surface and intermediate layers of the Rhodes Gyre area, averaged over the seven year period (December 2013-December 2020), and Table 1 provides the terms of the budget for each year. The model results show that, over the seven studied years, the annual biogeochemical flux (NCP) in the surface layer is positive (31.2 ± 6.9 g C m^{-2} $year^{-1}$) and more than three times higher than the OC consumption in the intermediate layer (-8.5 ± 3.1 g C m^{-2} $year^{-1}$) (Fig. 9). The annual downward export amounts to 16.8 ± 6.2 g C m^{-2} $year^{-1}$ and takes place under the form of POC and DOC (11.9 ± 3.4 versus 4.9 ± 2.8 g C m^{-2} $year^{-1}$, Table 1). The Rhodes Gyre appears as a source of organic carbon for the surface layer of the surrounding region (14.1 ± 2.1 g C m^{-2} $year^{-1}$). Then, we found that 54% of OC imported into the intermediate layer is locally remineralized into inorganic carbon (8.5 ± 3.1 g C m^{-2} $year^{-1}$), the remaining is mostly exported laterally to the surrounding area (7.5 ± 2.8 g C m^{-2} $year^{-1}$). The organic carbon export towards the deeper layer is 16 times weaker (1.01± 0.5 g C m^{-2} $year^{-1}$) than the downward export from the surface layer. The variation in organic carbon inventory remains low in the surface and intermediate layers (0.44 and 0.09 g C m^{-2} $year^{-1}$, respectively), indicating a quasi-balance between biogeochemical production and physical transfers over the seven year period.

The biogeochemical fluxes, i.e. PP, CR and NCP, all show an annual mean stronger than the seven year average during the cold winter years 2016-17, 2018-19 and 2019-20 (Table 1). However, the magnitude of PP and CR appears to be higher for the mild winter year 2017-18 compared to the cold winter year 2014-15. Regarding the physical transfer, we found that particulate and dissolved OC downward export show clearly stronger annual mean during all cold winter years (2014-15, 2016-17, 2018-19 and 2019-20). The lateral export in the surface is generally also stronger during cold years, except during the year 2016-17 which shows the lowest lateral OC export. Nevertheless, this latter year shows both the highest OC downward export from the surface and the highest lateral export in the intermediate layer towards the surrounding region, suggesting that lateral export is deepened during this very cold winter (Fig. 5c). Finally, the excess of biological production during cold winters is almost entirely compensated by an excess in total OC export.

4 Discussion

4.1 Model skill assessment

The comparisons of model results with the available data sets, presented in Sect. 3.1, show an overall good agreement in the seasonal dynamics and vertical distribution of chlorophyll, nutrients and dissolved oxygen in the Levantine Sea. We notice however an underestimation in the magnitude of the modeled subsurface maximum of chlorophyll and dissolved oxygen concentration when comparing with both the BGC-Argo float and cruise data. The model also produces chlorophyll maxima that are too deep in summer and profiles that are too mixed in winter. Concerning the first point, further studies will be necessary to improve the model parameterizations (optical model, POC degradation processes, particle sinking). In winter, mixed chlorophyll and DCM-like profiles alternate indicating small scale (few kilometers) or temporal variability related to meteorological conditions. The study of the physical processes driving this variability and their impact on phytoplankton deserves a dedicated study of physical and biogeochemical Argo profiles and probably a higher spatial resolution modeling.

One should notice that ocean color and in situ data remain scarce in the Levantine Sea, and especially in the Rhodes Gyre (D'Ortenzio et al., 2021) making the evaluation exercise difficult and partial. Additional in situ observations in the study area are required to further refine the biogeochemical model results. Comparisons with complementary biological (in particular composition and biomass of phytoplankton and zooplankton) and biogeochemical observations carried out during the PERLE cruises whose analyses are in progress will be used in near future studies to continue the evaluation.

Here, we complete the direct comparisons with in situ and satellite observations comparisons from the literature. In the model result, DOC concentrations show a rapid decrease with depth from values ranging between 45 and 64 mmol C m^{-3} in the surface layer to values around 40 mmol C m^{-3} below 300 m depth (Fig. 6e). These results are in agreement with what was reported in previous observational studies in the Levantine Sea (Krom et al., 2005; Santinelli et al., 2010; Pujo-Pay et al., 2011; Martinez Perez et al., 2017). The surface values fall in the lower range of observations (41-100 mmol C m^{-3}), which could be partly explained by the locations of the observations, mostly outside the Rhodes Gyre in more stratified and less productive regions. The model DOC concentrations exhibit a clear seasonal cycle in the surface layer, with maximum values at the end of summer and low values during winter mixing periods when surface waters are mixed with deeper DOC-poorer waters and DOC is transported towards intermediate depths. This variability is in line with the few observational studies documenting the seasonal cycle in the Ligurian and southern Adriatic seas characterized by strong winter mixing (Avril et al., 2002; Santinelli et al., 2013).

Regarding the organic carbon biological fluxes, the seven year averaged annual NPP that amounts to 115 ± 15 g C m^{-2} year^{-1} falls in the range of the previous annual estimates for the northern Levantine Sea based on both the satellite ocean color data (60-152 g C m^{-2} year^{-1}, Antoine et al., 1995 ; Bosc et al., 2004; Uitz et al., 2012), or more specifically for the Rhodes Gyre based on modeling studies (92-180 g C m^{-2} year^{-1}, Napolitano et al., 2000; Kalaroni et al., 2020; Cossarini et al., 2021). The higher magnitude of annual and winter NPP values in the Rhodes Gyre area compared to the surrounding Levantine Basin (Fig. S5d), by 13% and 21% respectively, is in line with the findings of Vidussi et al. (2001), Uitz et al. (2012) and Cossarini et al. (2021).

The mean annual POC export at 150 m depth in the Rhodes Gyre is estimated in the model at 11.9 ± 3.4 g C m^{-2} year^{-1}. The POC export data in the Mediterranean are almost all located in other regions (Gulf of Lion, Gogou et al. (2014); Adriatic Sea, Boldrin et al. (2002); Ionian Sea, Gogou et al. (2002)) and show values at 100-150 m measured or extrapolated between 3 and 23 g C m^{-2} year^{-1}. Only Moutin and Raimbault (2002) reported POC export for the Rhodes Gyre but limited to May-June 1996. These values are twice our mean values for the same months. It does not seem possible with these too rare and ephemeral observations, to conclude on a possible bias of the model.

The mean fraction of NPP exported from the surface under the particulate form represents 10 % of the total NPP in the model. This is in the range of what was estimated for the measured carbon export by Buesseler (1998) for the global ocean (2-20%), similar to the estimates of 11% for the western and eastern Mediterranean sites by Gogou et al. (2014) and to the estimates of 9 % by Moutin and Raimbault (2002) for the Rhodes Gyre.

Our estimate of the annual DOC export at 150 m depth amounts to 4.9 ± 2.8 g C m^{-2} year^{-1}. It shows a high interannual variability, which is discussed in Sect. 4.3. It is smaller than the annual DOC flux estimated at 100 m at 12 g C m^{-2} yr^{-1} in the Ligurian Sea by Avril (2002) and at 50 m depth at 15.4 g C m^{-2} yr^{-1} in the southern Adriatic Sea by Santinelli et al. (2013), both sites being characterized by strong winter mixing. On the contrary, our estimate is greater than the DOC flux at 50 m of 3.2 g C m^{-2} yr^{-1} estimated in the stratified Tyrrhenian Sea by Santinelli et al. (2013).

The modeled organic carbon fluxes appear to be in the order of magnitude of those deduced from observations, although we are conscious that the comparisons between both estimates are not straightforward, due notably to the definition of the processes (Ducklow and Doney, 2003; Di Biagio et al., 2022), the composition of OC considered (Gali et al., 2022) and the difference in time and locations.

Finally, though the model results show positive and negative annual variations of organic carbon inventory, an increasing trend in the OC inventory of 0.44 mol C m^{-2} $year^{-1}$ is found over the period 2013-20. This is in general agreement with the observations by Ozer et al. (2022). In their study, these authors found a general long positive trend for the depth-integrated chlorophyll measured offshore Haifa, to the east of the Levantine Basin, between 2002 and 2021, superimposed by interannual variations. They suggested that the long-term warming and salinification result in an increased buoyancy and a shallowing of the LIW (up to 110 m) enabling a higher level of nutrients to become available to the photic zone from below, supporting the observed rise of the integrated chlorophyll a. Considering the lack of data in the study area to assess this point in the model and the high interannual variability, an extension of the simulation over a longer period would be needed to detect a possible drift in the model.

4.2 Influence of winter mixing on phytoplankton growth

The model results display a similar general seasonal cycle of phytoplankton net growth from years 2013-14 to 2019-20 in the Rhodes Gyre area. On average, the period of phytoplankton accumulation at the surface is concomitant with the global period of vertical mixing. This is in agreement with the modeling results for the whole Levantine Sea by Lazzari et al. (2012) and the satellite and BGC-Argo observations in the Rhodes Gyre reported by Lavigne et al. (2013), Mignot el al. (2014) and D’Ortenzio et al. (2021). Although this similar general pattern of ecosystem dynamics can be found for all the studied years, the model results exhibit pronounced interannual variability over the period in terms of magnitude and timing of nutrient injection into the surface and phytoplankton growth. Our model results show that during cold winters (years 2014-15, 2016-17, 2018-19 and 2019-20), deeper mixing leads to higher nutrient supply into the euphotic layer, with nutrient injection being more than twice as high during severe winters compared to mild winters (Table 1). The significant correlation found between nutrient injection and mean winter HL (heat loss, Fig. 10a) or mean winter MLD (higher than 0.85) is in line with previous observational (Ediger and Yilmaz, 1996; Yilmaz and Tugrul, 1998) and modeling (Napolitano et al, 2000) studies in the Rhodes Gyre.

The model shows that during cold winters phytoplankton growth is interrupted during strong mixing periods, and is explosive at the end of strong mixing periods, with higher winter and summer PP during cold winter years (not shown). This is in line with the study of Ediger et al. (2005) who reported higher PP and biomass at the periphery of the gyre than in its homogenized center, based on observations collected in March 1992 when a deep convection event occurred. In the Rhodes Gyre, the episodes of strong surface phytoplankton growth, as well as of its interruption due to vertical mixing deeper than the base of the euphotic zone, remain short. They are markedly shorter than in the other Mediterranean regions of deep water formation, especially compared to the northwestern Mediterranean region where deep mixing can last for two months during intense convection years (i.e. 2004-05, 2005-06, 2012-13; Bernardello et al., 2012; Ulses et al., 2016; Mayot et al., 2017; Kessouri et al., 2018). These results are consistent with the characterization proposed by D’Ortenzio and Ribera d'Alcala et al. (2009) and Mayot et al. (2016) as an intermittent or intermediate bloom regime.

Although winter and spring NPP is higher under cold winters, annual NPP is not significantly correlated with heat loss if 2013-14 is not considered (Fig. 10e). The modeled NPP depends on the nitrate and ammonium uptake supporting, respectively, 30 and 70% of the NPP. Nitrate uptake is significantly correlated with HL (R= 0.88, p-value < 0.01, Fig. 10g) and MLD, whereas the ammonium uptake shows no significant correlation with HL (R= 0.69, p-value < 0.01, Fig. 10h). Thus the intensity of mixing that determines the amount of new deep nutrient available for primary production doesn’t strongly impact recycled production. Other driving factors such as trends in temperature and nutricline depth as observed in the southeastern Levantine Basin (Ozer et al., 2022) or low solar insolation in summer / fall that we don’t address in this study could also influence the variability of annual PP.

4.3 Influence of winter mixing on organic carbon export

Figures 10b and 10c- show the relationship between winter heat loss and annual vertical export of organic carbon at 150 m and the lateral flux of organic carbon from the intermediate layer (150-400 m) exported from the Rhodes Gyre to the Levantine Basin. The correlation for those annual exports is greater than 0.86 (p-value <0.02) for the seven years data set and increases to more than 0.90 (p-value <0.005) if 2013-14, the warmest winter, is removed indicating that it is an atypical year. Compared to the linear regression inferred from the other six years (red line), 2013-14 is above the regression line, meaning stronger vertical and horizontal fluxes than predicted by the regression (values approaching 0 or even negative). Unlike the other years, the seasonal cycle of export at 150 m indeed shows no clear signal in winter (Fig. 7e), and in the surface layer GPP also shows no notable peak in winter and spring (Fig. 7b). For this exceptionally warm year, the fluxes are therefore not driven by winter conditions. It is likely that the fluxes of the year 2013-14 which are close but weaker to those of the second warmest year (2017-18), can be considered minimum values for the Rhodes Gyre. Compared to this minimum value, the annual export is increased by a factor of 2 to 2.5 for the coldest years of the sequence, with this increase thus representing the contribution of cold winters.

The order of magnitude of the winter contribution to the annual vertical export is similar to that found by Kessouri et al. (2018) at the same depth in the deep convection zone of the Gulf of Lion. The main difference is on the timing of the vertical export. Bernardello et al. (2012) and Kessouri et al. (2018) showed that in the Gulf of Lion, the production and export phases alternate, the former mainly between gales when the layer is stratified, and the latter during gales and mixing due to the deepening of the mixed layer. In the Rhodes Gyre where convection is intermediate, the depth of mixing is not sufficient to persistently inhibit production, which allows for more continuous export throughout the winter period. Intermittency of convection is thus less necessary to trigger the export than for deep convection. This could explain the compensation between the excess in NCP and OC export during cold winters.

The annual lateral OC flux from the Rhodes Gyre to the Levantine Basin in the intermediate layer is clearly related to winter severity (Fig. 10c), with OC vertical export at 150 m allowing to identify the responsibility of physical processes of LIW formation followed by subduction from the Rhodes Gyre to the Levantine Basin. Taillandier et al. (2022) indicated that the volume of dense water in the Rhodes Gyre region returns to its pre-convection level in two to three months which gives an estimate of the time scale of lateral export that is in agreement with the model's assessment showing lateral export of organic carbon from the intermediate layer of the Rhodes Gyre that becomes low from April onwards (Fig. 8b). Regarding organic carbon, these physical processes (convection/subduction) are modulated by biogeochemical processes, for example, consumption by respiration which competes with physical export. The regression between vertical and lateral export over the seven years indicates that 45% of organic carbon exported below 150 m depth is exported to the Levantine Basin while 50% is consumed by respiration inside the Rhodes Gyre intermediate layer.

4.4 Influence of winter mixing on carbon sequestration

The modeled NCP in the surface layer indicates that the planktonic ecosystem has an autotrophic metabolism from January to August, with maximum values during the phytoplankton bloom, and an heterotrophic metabolism from September to December. This is consistent with the study by Wimart-Rousseau et al. (2021) based on cruise observations of the carbonate system at three different seasons, and the biogeochemical reanalysis by Cossarini et al. (2021). At the annual scale, the planktonic ecosystem in the Rhodes Gyre acts as a sink of atmospheric CO_2 with an estimate of mean NCP at 31.2 ± 6.9 g C m^{-2} yr^{-1}. This OC net biological production (DIC consumption) is almost balanced by both the OC lateral and vertical transports with a quasi-evenly distribution. The OC exported towards the intermediate layer is further respired or laterally exported by subduction towards the surrounding Levantine Basin. We estimate that 1% and 3% of the NPP and NCP, respectively, is then transferred towards the deeper depths.

The ~~H~~high interannual variability of annual NCP (SD of 22%) in the Rhodes Gyre appears to be primarily linked to the intensity of winter atmospheric HL and vertical mixing (significant correlation > 0.88 between annual NCP and winter HL, Fig. 10f), which indicates an enhanced autotrophic metabolism during cold years, that is almost counterbalanced by an enhanced OC export. One can also notice a significant correlation (0.88, p-value < 0.01) between winter HL and respiration in the intermediate layer (Fig. 10d).

In this study, we describe only partially the cycle of DIC through its biological consumption. Air-sea flux and transport terms of the inorganic form of carbon are not considered here. This limits the determination of the role of the Rhodes Gyre relative to atmospheric CO_2 uptake and of the influence of winter mixing intensity on this uptake. Previous studies reported that a significant amount of OC exported below the euphotic layer could be reinjected back under organic or remineralized form during the following winters in convection regions (Oschlies et al., 2004; Körtzinger et al., 2008; Palevsky and Quay, 2017). Over the study period, one can notice the succession of two convective years, 2018-19 and 2019-20, however the second year does not display particularly low net OC downward export compared to the other cold years (Fig. 10b). The impact of winter mixing on total carbon sequestration is thus difficult to establish and requires the description of the dynamics of the carbonate system in the model that will be investigated in a near-future study.

Based on a 1D coupled model combined with satellite data, D'Ortenzio et al. (2008) and Taillandier et al. (2012), reported a CO_2 air-sea flux between -1.5 and -0.5 mol C m^{-2} yr^{-1}, in the Rhodes Gyre and the whole Levantine Sea acting thus as a source for the atmosphere. Cossarini et al. (2021) modeled the temporal evolution of CO_2 air-sea fluxes from 1999 to 2019. They found that the Rhodes Gyre is a small sink of atmospheric CO_2 (< 0.25 mol C m^{-2} yr^{-1}), whereas the surrounding Levantine Basin is a source for the atmosphere. Besides, they reported an increasing absorption of atmospheric CO_2 in both the eastern and western Mediterranean Sea, leading to a change in the sign of air-sea exchanges averaged over the eastern Mediterranean, and a switch from source to sink, at the end of the period (2019), in response to the increase of atmospheric CO_2. Hassoun et al. (2019) and Wimart-Rousseau et al. (2021) derived an increasing trend in inorganic carbon content in the coastal and open-sea Levantine Basin, based on observations. The predictions for the carbon cycle in the Mediterranean Sea over the 21st century by Solidoro et al. (2022) and Reale et al. (2022) showed a further increase in atmospheric CO_2 absorption, which, together with the increasing temperature and stratification (Somot et al., 2006; Soto-Navarro et al. 2020), leads to an increase in carbon content.

5 Conclusion

In this study we have used a 3D coupled hydrodynamic – biogeochemical model to investigate the pelagic ecosystem functioning and estimate a budget of organic carbon in the Rhodes Gyre, over the period of 2013-2020, marked by the alternation of cold and mild winter years. The assessment of the model results based on satellite, cruise, and BGC-Argo float observations in the Levantine Basin demonstrates that the model was able to reproduce reasonably well the main seasonal and spatial evolution of physical and biogeochemical observed variables.

The model confirms that the intensity of winter surface heat loss and vertical mixing events significantly influences the magnitude of nutrient supplies into the euphotic layer and of surface phytoplankton growth. The development of phytoplankton at the surface is always concomitant with the winter mixing period. It is characterized by a first phase of progressive growth with the deepening of the mixed layer, and a second phase consisting of alternating short periods (< 2 weeks) of vertical mixing and of phytoplankton growth episodes during temporary restratification. This second phase only occurs during severe winters due to the dilution of phytoplankton biomass over the mixed layer and the reduction of light availability. A spatial variability is also depicted in the gyre during the mixing period. Under prolonged winter conditions, the characteristics of the phytoplankton bloom are present at the periphery of the Rhodes Gyre, when vertical mixing is intense, and reappear in the center of the gyre at the restratification. At the end of the mixing period, a DCM forms and progressively deepens until mid-summer.

Our results show that the Rhodes Gyre is characterized by an alternation between phytoplankton growth and OC export from the upper layer, favored by vertical mixing episodes. OC is transported vertically towards intermediate depths and laterally towards the surrounding regions, partly by subduction during the dispersion of LIW. The annual downward OC export is strongly enhanced with the intensity of winter surface heat flux, with annual export 2 to 3 times higher during cold winter years compared to mild winter years. 50% of the organic carbon exported below 150 m depth in the Rhodes Gyre is remineralized at intermediate levels inside the gyre and 45% is exported towards the surrounding Levantine Basin. The Rhodes Gyre acts as a source of organic carbon for the surrounding areas.

The Rhodes Gyre is found to be an autotrophic ecosystem, with net community production in the surface layer accounting for 31.2 ± 6.9 g m^{-2} $year^{-1}$. Finally, our modeling study is constrained to the Rhodes Gyre and a seven year period. Its spatial and temporal extension could allow the examination of (i) the fate of the organic carbon produced in the Rhodes Gyre after its export to the Levantine Basin and to the other regions of the eastern Mediterranean Sea, as well as (ii) the influence of remote drivers on biological activity and physical processes in the Levantine Basin.

Code availability

The SYMPHONIE model and the MATLAB codes used to process the model outputs are available from the authors on request.

Data availability

Data used to validate the model are available on different websites specified in the main text of the manuscript. These data and the model outputs are also available from the authors on request.

Competing interests

The authors declare that they have no conflict of interest.

Acknowledgments

This study is a contribution to the MerMex (Marine Ecosystem Response in the Mediterranean Experiment) project of the MISTRALS international program. The numerical simulations were performed using the SYMPHONIE model, developed by the SIROCCO group (https://sirocco.obs-mip.fr/, last access: 17 October 2022), and computed on the cluster of Laboratoire d'Aérologie and HPC resources from CALMIP grants (P1325, P09115 and P1331). We acknowledge the scientists and crews of the Flotte océanographique française (https://www.flotteoceanographique.fr/, last access: November 2022) who contributed to the cruises carried out in the framework of the PERLE project. The authors would like to acknowledge the National Council for Scientific Research of Lebanon (CNRS-L), Campus France, the University of Toulouse and LEGOS for granting a doctoral fellowship to Joëlle Habib. We thank Marta Álvarez (IEO, La Coruña) and collaborators for making available the CARIMED database to us. We also warmly thank Pierre Nabat from CNRM for providing the atmospheric deposition data.

References

Alkalay, R., Zlatkin, O., Katz, T., Herut, B., Halicz, L., Berman-Frank, I., and Weinstein, Y.: Carbon export and drivers in the southeastern Levantine Basin, Deep Sea Research Part II: Topical Studies in Oceanography, 171, 104 713, https://doi.org/10.1016/j.dsr2.2019.104713, 2020.

Álvarez, M., Velo, A., Tanhua, T., Key, R., Heuven, S. V., Español, I., Ieo, D. O., Coruña, A., and Marinas, I. D. I.: Carbon, tracer and ancillary data in the MEDSEA, CARIMED: an internally consistent data product for the Mediterranean Sea., Tech. Rep. 2019, Instituto Español de Oceanografía, 2019.655

Antoine, D., Morel, A., and Andre, J. M.: Algal pigment distribution and primary production in the eastern Mediterranean as derived from coastal zone color scanner observations, Journal of Geophysical Research, 100, https://doi.org/10.1029/95jc00466, 1995.

Argo: Argo float data and metadata from Global Data Assembly Centre (Argo GDAC), SEANOE, https://doi.org/https://doi.org/10.17882/42182, 2022.

Astraldi, M., Balopoulos, S., Candela, J., Font, J., Gacic, M., Gasparini, G. P., Manca, B., Theocharis, A., and Tintoré, J.: The role of straits and channels in understanding the characteristics of Mediterranean circulation, Progress in Oceanography, 44, 65–108, https://doi.org/10.1016/S0079-6611(99)00021-X, 1999.

Auger, P. A., Diaz, F., Ulses, C., Estournel, C., Neveux, J., Joux, F., Pujo-Pay, M., and Naudin, J. J.: Functioning of the planktonic ecosystem on the Gulf of Lions shelf (NW Mediterranean) during spring and its impact on the carbon deposition: A field data and 3-D modelling combined approach, Biogeosciences, 8, 3231–3261, https://doi.org/10.5194/bg-8-3231-2011, 2011.

Auger, P. A., Ulses, C., Estournel, C., Stemmann, L., Somot, S., and Diaz, F.: Interannual control of plankton communities by deep wintermixing and prey/predator interactions in the NW Mediterranean: Results from a 30-year 3D modeling study, Progress in Oceanography,124, 12–27, https://doi.org/10.1016/j.pocean.2014.04.004, 2014.

Avril, B.: DOC dynamics in the northwestern Mediterranean sea (DYFAMED site), Deep-Sea Research Part II: Topical Studies in Oceanography, 49, 2163–2182, https://doi.org/10.1016/S0967-0645(02)00033-4, 2002.670

Bernardello, R., Cardoso, J. G., Bahamon, N., Donis, D., Marinov, I., and Cruzado, A.: Factors controlling interannual variability of vertical organic matter export and phytoplankton bloom dynamics-a numerical case-study for the NW Mediterranean Sea, Biogeosciences, 9, 4233–4245, https://doi.org/10.5194/bg-9-4233-2012, 2012.

Bittig, H. C. and Körtzinger, A.: Tackling oxygen optode drift: Near-surface and in-air oxygen optode measurements on a float provide an accurate in situ reference, Journal of Atmospheric and Oceanic Technology, 32, 1536–1543, https://doi.org/10.1175/JTECH-D-14-00162.1, 2015

Bittig, H. C., Körtzinger, A., Neill, C., van Ooijen, E., Plant, J. N., Hahn, J., Johnson, K. S., Yang, B., and Emerson, S. R.: Oxygen optode sensors: Principle, characterization, calibration, and application in the ocean, Frontiers in Marine Science, 4, 1–25, https://doi.org/10.3389/fmars.2017.00429, 2018.

Boldrin, A., Miserocchi, S., Rabitti, S., Turchetto, M. M., Balboni, V., and Socal, G.: Particulate matter in the southern Adriatic and Ionian Sea: Characterisation and downward fluxes, Journal of Marine Systems, 33-34, 389–410, https://doi.org/10.1016/S0924-7963(02)00068-4,675,2002.

Bosc, E., Bricaud, A., and Antoine, D.: Seasonal and interannual variability in algal biomass and primary production inthe Mediterranean Sea, as derived from 4 years of SeaWiFS observations, Global Biogeochemical Cycles, 18,https://doi.org/10.1029/2003gb002034, 2004.

Bosse, A., Testor, P., Damien, P., Estournel, C., Marsaleix, P., Mortier, L., Prieur, L., and Taillandier, V.: Wind-forced submesoscale symmetric instability around deep convection in the northwestern mediterranean sea, Fluids, 6, 1–26, https://doi.org/10.3390/fluids6030123, 2021.

Brenner, S., Rozentraub, Z., Bishop, J., and Krom, M.: The mixed-layer/thermocline cycle of a persistent warm core eddy in the eastern Mediterranean, Dynamics of Atmospheres and Oceans, 15, 457–476, https://doi.org/10.1016/0377-0265(91)90028-E, 1991.

Buesseler, K. O.: The decoupling of production and particulate export in the surface ocean, Global Biogeochemical Cycles, 12, 297–310, https://doi.org/10.1029/97GB03366, 1998.

Copin-Montégut, C., Bégovic, M., and Merlivat, L.: Variability of the partial pressure of CO2 on diel to annual time scales in the Northwestern Mediterranean Sea, Marine Chemistry, 85, 169–189, https://doi.org/10.1016/j.marchem.2003.10.005, 2004.

Coppola, L., Prieur, L., Taupier-Letage, I., Estournel, C., Testor, P., Lefevre, D., Belamari, S., LeReste, S., and Taillandier, V.: Observation of oxygen ventilation into deep waters through targeted deployment of multiple

Argo-O2 floats in the north-western Mediterranean Sea in 2013, Journal of Geophysical Research: Oceans, 122, 6325–6341, https://doi.org/10.1002/2016JC012594, 2017.

Cornec, M., Laxenaire, R., Speich, S., and Claustre, H.: Impact of Mesoscale Eddies on Deep Chlorophyll Maxima, Geophysical Research Letters, 48, https://doi.org/10.1029/2021gl093470, 2021.

Cossarini, G., Feudale, L., Teruzzi, A., Bolzon, G., Coidessa, G., Solidoro, C., Di Biagio, V., Amadio, C., Lazzari, P., Brosich, A., and Salon, S.: High-Resolution Reanalysis of the Mediterranean Sea Biogeochemistry (1999–2019), Frontiers in Marine Science, 8, 1–21, https://doi.org/10.3389/fmars.2021.741486, 2021.

Dall'Olmo, G., Dingle, J., Polimene, L., Brewin, R. J., and Claustre, H.: Substantial energy input to the mesopelagic ecosystem from the seasonal mixed-layer pump, Nature Geoscience, 9, 820–823, https://doi.org/10.1038/ngeo2818, 2016.

Damien, P., Bosse, A., Testor, P., Marsaleix, P., and Estournel, C.: Modeling Postconvective Submesoscale Coherent Vortices in the North-western Mediterranean Sea, Journal of Geophysical Research: Oceans, 122, 9937–9961, https://doi.org/10.1002/2016JC012114, 2017.

Di Biagio, V., Salon, S., Feudale, L., and Cossarini, G.: Subsurface oxygen maximum in oligotrophic marine ecosystems: mapping the interaction between physical and biogeochemical processes, Biogeosciences, 2018, 1–33, https://doi.org/10.5194/bg-2022-70,2022

D'Ortenzio, F. and Ribera d'Alcalà, M.: On the trophic regimes of the Mediterranean Sea: a satellite analysis, Biogeosciences Discussions,5, 2959–2983, https://doi.org/10.5194/bgd-5-2959-2008, 2009.

D'Ortenzio, F., Ragni, M., Marullo, S., and Ribera d'Alcalà, M.: Did biological activity in the Ionian Sea change after the Eastern Mediterranean Transient? Results from the analysis of remote sensing observations, Journal of Geophysical Research: Oceans, 108,https://doi.org/10.1029/2002jc001556, 2003.

D'Ortenzio, F., Iudicone, D., de Boyer Montegut, C., Testor, P., Antoine, D., Marullo, S., Santoleri, R., and Madec, G.: Seasonal variability of the mixed layer depth in the Mediterranean Sea as derived from in situ profiles, Geophysical Research Letters, 32, 1–4, https://doi.org/10.1029/2005GL022463, 2005.

D'Ortenzio, F., Antoine, D., and Marullo, S.: Satellite-driven modeling of the upper ocean mixed layer and air-sea CO2 flux in the Mediterranean Sea, Deep-Sea Research Part I: Oceanographic Research Papers, 55, 405–434, https://doi.org/10.1016/j.dsr.2007.12.008, 2008.

D'Ortenzio, F., Taillandier, V., Claustre, H., Coppola, L., Conan, P., Dumas, F., Durrieu du Madron, X., Fourrier, M., Gogou, A., Karageorgis, A., Lefevre, D., Leymarie, E., Oviedo, A., Pavlidou, A., Poteau, A., Poulain, P. M., Prieur, L., Psarra, S., Puyo-Pay, M., Ribera d'Alcalà, M., Schmechtig, C., Terrats, L., Velaoras, D., Wagener, T., and Wimart-Rousseau, C.: BGC-Argo Floats Observe Nitrate Injection and Spring Phytoplankton Increase in the Surface Layer of Levantine Sea (Eastern Mediterranean), Geophysical Research Letters, 48, 1–11, https://doi.org/10.1029/2020GL091649, 2021.

Ducklow, H. W. and Doney, S. C.: What Is the Metabolic State of the Oligotrophic Ocean? A Debate, Ann. Rev. Mar. Sci., 5(1), 525–533, doi:10.1146/annurev-marine-121211-172331, 2013.

Ediger, D. and Yilmaz, A.: Characteristics of deep chlorophyll maximum in the Northeastern Mediterranean with respect to environmental conditions, Journal of Marine Systems, 7963, 1996.

Ediger, D., Tuˇgrul, S., and Yilmaz, A.: Vertical profiles of particulate organic matter and its relationship with chlorophyll-a in the upper layer of the NE Mediterranean Sea, Journal of Marine Systems, 55, 311–326, https://doi.org/10.1016/j.jmarsys.2004.09.003, 2005.

El-Geziry, T.M. Long-term changes in sea surface temperature (SST) within the southern Levantine Basin. Acta Oceanol. Sin. 40, 27–33. https://doi.org/10.1007/s13131-021-1709-2, 2021

Estournel, C., Kondrachoff, V., Marsaleix, P., and Vehil, R.: The plume of the Rhone: Numerical simulation and remote sensing, Continental Shelf Research, 17, 899–924, https://doi.org/10.1016/S0278-4343(96)00064-7, 1997.

Estournel, C., Broche, P., Marsaleix, P., Devenon, J. L., Auclair, F., and Vehil, R.: The rhone river plume in unsteady conditions: Numerical and experimental results, Estuarine, Coastal and Shelf Science, 53, 25–38, https://doi.org/10.1006/ecss.2000.0685, 2001.

Estournel, C., De Madron, X. D., Marsaleix, P., Auclair, F., Julliand, C., and Vehil, R.: Observation and modeling of the winter coastal oceanic circulation in the Gulf of Lion under wind conditions influenced by the continental orography (FETCH experiment), Journal of Geophysical Research: Oceans, 108, 1–19, https://doi.org/10.1029/2001jc000825, 2003.

Estournel, C., Zervakis, V., Marsaleix, P., Papadopoulos, A., Auclair, F., Perivoliotis, L., and Tragou, E.: Dense water formation and cascading in the Gulf of Thermaikos (North Aegean), from observations and modelling, Continental Shelf Research, 25, 2366–2386, https://doi.org/10.1016/j.csr.2005.08.014, 2005.

Estournel, C., Testor, P., Taupier-Letage, I., Bouin, M. N., Coppola, L., Durand, P., Conan, P., Bosse, A., Brilouet, P. E., Beguery, L., Belamari, S., Béranger, K., Beuvier, J., Bourras, D., Canut, G., Doerenbecher, A., de Madron, X. D., D'Ortenzio, F., Drobinski, P., Ducrocq, V., Fourrié, N., Giordani, H., Houpert, L., Labatut, L., Brossier, C. L., Nuret, M., Prieur, L., Roussot, O., Seyfried, L., and Somot, S.: HyMeX-SOP2: The field campaign dedicated to dense water formation in the northwestern Mediterranean, Oceanography, 29,196–206, https://doi.org/10.5670/oceanog.2016.94, 2016.

Estournel, C., Marsaleix, P., and Ulses, C.: A new assessment of the circulation of Atlantic and Intermediate Waters in the Eastern Mediterranean, Progress in Oceanography, 198, 102 673, https://doi.org/10.1016/j.pocean.2021.102673, 2021.

Fach, B. A., Orek, H., Yilmaz, E., Tezcan, D., Salihoglu, I., Salihoglu, B., and Latif, M. A.: Water Mass Variability and Levantine Intermediate Water Formation in the Eastern Mediterranean between 2015-2017, Journal of Geophysical Research: Oceans, 2, https://doi.org/10.1029/2020jc016472, 2021.

Fourrier, M.: Dataset used for CANYON-MED training and validation., figshare, https://doi.org/Fourrier, Marine (2020): Dataset used for CANYON-MED training and validation. figshare. Dataset. https://doi.org/10.6084/m9.figshare.12452795.v1, 2020.

Fourrier, M., Coppola, L., Claustre, H., D'Ortenzio, F., Sauzède, R., and Gattuso, J. P.: A Regional Neural Network Approach to Estimate Water-Column Nutrient Concentrations and Carbonate System Variables in the Mediterranean Sea: CANYON-MED, Frontiers in Marine Science, 7, https://doi.org/10.3389/fmars.2020.00620, 2020.

Friedlingstein, P., Jones, M. W., Sullivan, M. O., Andrew, R. M., Bakker, D. C. E., Hauck, J., Quéré, C. L., Peters, G. P., and Peters, W.:Global Carbon Budget 2021, Earth System Science Data, 14, 1917–2005, 2022.

Galí, M., Falls, M., Claustre, H., Aumont, O., and Bernardello, R.: Bridging the gaps between particulate backscattering measurements and modeled particulate organic carbon in the ocean, Biogeosciences, 19, 1245–1275, https://doi.org/10.5194/bg-19-1245-2022, 2022

Gardner, W. D., Chung, S. P., Richardson, M. J., and Walsh, I. D.: The oceanic mixed-layer pump, Deep-Sea Research Part II, 42, https://doi.org/10.1016/0967-0645(95)00037-Q, 1995.

Gogou, A., Sanchez-Vidal, A., Durrieu de Madron, X., Stavrakakis, S., Calafat, A. M., Stabholz, M., Psarra, S., Canals, M., Heussner, S., Stavrakaki, I., and Papathanassiou, E.: Reprint of: Carbon flux to the deep in three open sites of the Southern European Seas (SES), Journal of Marine Systems, 135, 170–179, https://doi.org/10.1016/j.jmarsys.2014.04.012, 2014.

Grasshoff, K., Kremling, K., and Ehrhardt, M.: Methods of seawater analysis, Marine Chemistry, 7, 86–87, https://doi.org/10.1016/0304-4203(78)90045-2, 1999.

Grignon, L., Smeed, D. A., Bryden, H. L., and Schroeder, K.: Importance of the variability of hydrographic preconditioning for deep convection in the Gulf of Lion, NW Mediterranean, Ocean Science, 6, 573–586, https://doi.org/10.5194/os-6-573-2010, 2010.

Guerzoni, S., Chester, R., Dulac, F., Herut, B., Loÿe-Pilot, M. D., Measures, C., Migon, C., Molinaroli, E., Moulin, C., Rossini, P., Saydam, C., Soudine, A., and Ziveri, P.: The role of atmospheric deposition in the biogeochemistry of the Mediterranean Sea, Progress in Oceanography, 44, 147–190, https://doi.org/10.1016/S0079-6611(99)00024-5, 1999.

Guyennon, A., Baklouti, M., Diaz, F., Palmieri, J., Beuvier, J., Lebaupin-Brossier, C., Arsouze, T., Beranger, K., Dutay, J. C., and Moutin, T.: New insights into the organic carbon export in the Mediterranean Sea from 3-D modeling, Biogeosciences, 12, 7025–7046,https://doi.org/10.5194/bg-12-7025-2015, 2015.

Hassoun, A. E. R., Fakhri, M., Raad, N., Abboud-Abi Saab, M., Gemayel, E., and De Carlo, E. H.: The carbonate system of the Eastern-most Mediterranean Sea, Levantine Sub-basin: Variations and drivers, Deep-Sea Research Part II: Topical Studies in Oceanography, 164, 54–73,https://doi.org/10.1016/j.dsr2.2019.03.008, 2019.

Hecht, A., Robinson, A. R., and Pinardi, N.: Currents, water masses, eddies and jets in the Mediterranean Levantine Basin., 1988.

Hermann, M., Somot, S., Sevault, F., Estournel, C., and Déqué, M.: Modeling the deep convection in the northwestern Mediterranean sea using an eddy-permitting and an eddy-resolving model: Case study of winter 1986-1987, Journal of Geophysical Research: Oceans, 113,1–25, https://doi.org/10.1029/2006JC003991, 2008.

Herrmann, M., Diaz, F., Estournel, C., Marsaleix, P., and Ulses, C.: Impact of atmospheric and oceanic interannual variability on the North-western Mediterranean Sea pelagic planktonic ecosystem and associated carbon cycle, Journal of Geophysical Research: Oceans, 118,5792–5813, https://doi.org/10.1002/jgrc.20405, 2013.

Herut, B. and Krom, M.: Atmospheric Input of Nutrients and Dust to the SE Mediterranean, in: Guerzoni, S., Chester, R. (eds) The Impact of Desert Dust Across the Mediterranean., pp. 349–358, springe,dordrecht, https://doi.org/10.1007/978-94-017-3354-0_35, 1996.

Hood, E. M. and Merlivat, L.: Annual to interannual variations of fCO2 in the northwestern Mediterranean Sea: Results from hourly measurements made by CARIOCA buoys, 1995-1997, Journal of Marine Research, 59, 113–131, https://doi.org/10.1357/002224001321237399, 2001.

Horton, C., Clifford, M., and Schmitz, J.: A real-time oceanographic nowcast / forecast system for the Mediterranean Sea. Journal of Geophysical Research: Oceans, 102, C11, https://doi.org/10.1029/97JC005331997.

Houpert, L., Testor, P., de Madron, X. D., Somot, S., D'Ortenzio, F., Estournel, C., and Lavigne, H.: Seasonal cycle of the mixed layer, the seasonal thermocline and the upper-ocean heat storage rate in the Mediterranean Sea derived from observations, Progress in Oceanography, 132, 333–352, https://doi.org/10.1016/j.pocean.2014.11.004, 2015.

Kalaroni, S., Tsiaras, K., Petihakis, G., Economou-Amilli, A., and Triantafyllou, G.: Modelling the mediterranean pelagic ecosystem using the POSEIDON ecological model. Part II: Biological dynamics, Deep-Sea Research Part II: Topical Studies in Oceanography, 171, 104 711, https://doi.org/10.1016/j.dsr2.2019.104711, 2020.

Kanakidou, M., Duce, R. A., Prospero, J. M., Baker, A. R., Benitez-Nelson, C., Dentener, F. J., Hunter, K. A., Liss, P. S., Mahowald, N.,Okin, G. S., Sarin, M., Tsigaridis, K., Uematsu, M., Zamora, L. M., and Zhu, T.: Atmospheric fluxes of organic N and P to the global ocean, Global Biogeochemical Cycles, 26, 1–12, https://doi.org/10.1029/2011GB004277, 2012.

Kessouri, F.,~~ Mer, D., and Processus, M.:~~ Cycles biogéochimiques de la Mer Méditerranée : Processus et bilans, Ph.D. thesis, Paul Sabatier,201~~6~~5.

Kessouri, F., Ulses, C., Estournel, C., Marsaleix, P., Severin, T., Pujo-Pay, M., Caparros, J., Raimbault, P., Pasqueron de Fommervault, O., D'Ortenzio, F., Taillandier, V., Testor, P., and Conan, P.: Nitrogen and Phosphorus Budgets in the Northwestern Mediterranean Deep Convection Region, Journal of Geophysical Research: Oceans, 122, 9429–9454, https://doi.org/10.1002/2016JC012665, 2017.

Kessouri, F., Ulses, C., Estournel, C., Marsaleix, P., D'Ortenzio, F., Severin, T., Taillandier, V., and Conan, P.: Vertical Mixing Effects on Phytoplankton Dynamics and Organic Carbon Export in the Western Mediterranean Sea, Journal of Geophysical Research: Oceans, 123, 1647–1669, https://doi.org/10.1002/2016JC012669, 2018.

Key, R. M., Kozyr, A., Sabine, C. L., Lee, K., Wanninkhof, R., Bullister, J. L., Feely, R. A., Millero, F. J., Mordy, C., and Peng, T. H.:A global ocean carbon climatology: Results from Global Data Analysis Project (GLODAP), Global Biogeochemical Cycles, 18, 1–23, https://doi.org/10.1029/2004GB002247, 2004.

Körtzinger, A., Schimanski, J., Send, U., and Wallace, D.: The ocean takes a deep breath, Science, 306, 1337, https://doi.org/10.1126/science.1102557, 2004.

Kotta, D. and Kitsiou, D.: Chlorophyll in the eastern mediterranean sea: Correlations with environmental factors and trends, Environments MDPI, 6, https://doi.org/10.3390/environments6080098, 2019.

Kress, N., Gertman, I., and Herut, B.: Temporal evolution of physical and chemical characteristics of the water column in the Easternmost Levantine basin (Eastern Mediterranean Sea) from 2002 to 2010, Journal of Marine Systems, 135, 6–13, https://doi.org/10.1016/j.jmarsys.2013.11.016, 2014.

Krom, Brenner, S., Kress, N., Neori, A., and Gordon, L. I.: Nutrient dynamics and new production in a warm core eddy from the eastern Mediterranean Sea, Deep-Sea Research Part I, 39, 467–480, 1991.

Krom, M. D., Woodward, E. M., Herut, B., Kress, N., Carbo, P., Mantoura, R. F., Spyres, G., Thingsted, T. F., Wassmann, P., Wexels-Riser, C., Kitidis, V., Law, C., and Zodiatis, G.: Nutrient cycling in the south east Levantine basin of the eastern Mediterranean: Results from a phosphorus starved system, Deep-Sea Research Part II: Topical Studies in Oceanography, 52, 2879–2896, https://doi.org/10.1016/j.dsr2.2005.08.009, 2005.

Kubin, E., Poulain, P. M., Mauri, E., Menna, M., and Notarstefano, G.: Levantine intermediate and levantine deep water formation: An Argo float study from 2001 to 2017, Water (Switzerland), 11, https://doi.org/10.3390/w11091781, 2019.

Lascaratos, A., Williams, R. G., and Tragou, E.: A mixed-layer study of the formation of Levantine Intermediate Water, Journal of Geophysical Research, 98, 1993.

Lascaratos, A., Roether, W., Nittis, K., and Klein, B.: Recent changes in deep water formation and spreading in the Eastern Mediterranean Sea: A review, Progress in Oceanography, 44, 5–36, https://doi.org/10.1016/S0079-6611(99)00019-1, 1999.

Lavigne, H., D’Ortenzio, F., Migon, C., Claustre, H., Testor, P., D’Alcalà, M. R., Lavezza, R., Houpert, L., and Prieur, L.: Enhancing the comprehension of mixed layer depth control on the Mediterranean phytoplankton phenology, Journal of Geophysical Research: Oceans, 118, 3416–3430, https://doi.org/10.1002/jgrc.20251, 2013.

Lazzari, P., Solidoro, C., Ibello, V., Salon, S., Teruzzi, A., Béranger, K., Colella, S., and Crise, A.: Seasonal and inter-annual variability of plankton chlorophyll and primary production in the Mediterranean Sea: A modelling approach, Biogeosciences, 9, 217–233, https://doi.org/10.5194/bg-9-217-2012, 2012.

Leonard, B.P. A stable and accurate convective modelling procedure based on quadratic upstream interpolation, Comput. Methods Appl. Mech. Eng., 19, 59–98, https://doi.org/10.1016/0045- 7825(79)90034-3, 1979.

Ludwig, W., Bouwman, A. F., Dumont, E., and Lespinas, F.: Water and nutrient fluxes from major Mediterranean and Black Sea rivers: Past and future trends and their implications for the basin-scale budgets, Global Biogeochemical Cycles, 24, 1–14,https://doi.org/10.1029/2009GB003594, 2010.

Macías, D., Stips, A., and Garcia-Gorriz, E.: The relevance of deep chlorophyll maximum in the open Mediterranean Sea evaluated through 3D hydrodynamic-biogeochemical coupled simulations, Ecological Modelling, 281, 26–37,830 https://doi.org/10.1016/j.ecolmodel.2014.03.002, 2014.

Malanotte-Rizzoli, P., Manca, B. B., Marullo, S., D’Alcala, R., Roether, W., Theocharis, A., Bergamasco, A., Budillon, G., Sansone, E.,Civitarese, G., Conversano, F., Gertman, I., Herut, B., Kress, N., Kioroglou, S., Kontoyannis, H., Nittis, K., Klein, B., Lascaratos, A., Latif, M. A., Ozsoy, E., Robinson, A. R., Santoleri, R., Viezzoli, D., and Kovacevic, V.: The Levantine Intermediate Water Experiment (LIWEX) Group: Levantine basin - A laboratory for multiple water mass formation processes, Journal of Geophysical Research C: Oceans,108, https://doi.org/10.1029/2002jc001643, 2003.

Malanotte-Rizzoli, P., Artale, V., Borzelli-Eusebi, G. L., Brenner, S., Crise, A., Gacic, M., Kress, N., Marullo, S., Ribera D’Alcalà, M., Sofianos, S., Tanhua, T., Theocharis, A., Alvarez, M., Ashkenazy, Y., Bergamasco, A., Cardin, V., Carniel, S., Civitarese, G., D’Ortenzio, F., Font, J., Garcia-Ladona, E., Garcia-Lafuente, J. M., Gogou, A., Gregoire, M., Hainbucher, D., Kontoyannis, H., Kovacevic, V., Kraskapoulou, E., Kroskos, G., Incarbona, A., Mazzocchi, M. G., Orlic, M., Ozsoy, E., Pascual, A., Poulain, P. M., Roether, W., Rubino, A., Schroeder, K., Siokou-Frangou, J., Souvermezoglou, E., Sprovieri, M., Tintoré, J., and Triantafyllou, G.:

Physical forcing and physical/biochemical variability of the Mediterranean Sea: A review of unresolved issues and directions for future research, Ocean Science, 10, 281–322, https://doi.org/10.5194/os-10-281-2014, 2014.

Manca, B., Burca, M., Giorgetti, A., Coatanoan, C., Garcia, M. J., and Iona, A.: Physical and biochemical averaged vertical profiles in the Mediterranean regions: An important tool to trace the climatology of water masses and to validate incoming data from operational oceanography, Journal of Marine Systems, 48, 83–116, https://doi.org/10.1016/j.jmarsys.2003.11.025, 2004.

Many, G., Ulses, C., Estournel, C., and Marsaleix, P.: Particulate organic carbon budget of the Gulf of Lion shelf (NW Mediterranean) using a coupled hydrodynamic-biogeochemical model, Biogeosciences Discussions, pp. 1–41, https://doi.org/10.5194/bg-2021-82, 2021.

Margirier, F., Testor, P., Heslop, E., Mallil, K., Bosse, A., Houpert, L., Mortier, L., Bouin, M. N., Coppola, L., D’Ortenzio, F., Durrieu de Madron, X., Mourre, B., Prieur, L., Raimbault, P., Taillandier, V., de Madron, X., Mourre, B., Prieur, L., Raimbault, P., and Taillandier, V.: Abrupt warming and salinification of intermediate waters interplays with decline of deep convection in the Northwestern Mediterranean Sea, Scientific Reports, 10, 1–11, https://doi.org/10.1038/s41598-020-77859-5, 2020.

Marsaleix, P., Estournel, C., Kondrachoff, V., and Vehil, R.: A numerical study of the formation of the Rhone River plume, Journal of Marine Systems, 14, 99–115, https://doi.org/10.1016/S0924-7963(97)00011-0, 1998.

Marsaleix, P., Auclair, F., and Estournel, C.: Considerations on open boundary conditions for regional and coastal ocean models, Journal of Atmospheric and Oceanic Technology, 23, 1604–1613, https://doi.org/10.1175/JTECH1930.1, 2006.

Marsaleix, P., Auclair, F., Floor, J. W., Herrmann, M. J., Estournel, C., Pairaud, I., and Ulses, C.: Energy conservation issues in sigma coordinate free-surface ocean models, Ocean Modelling, 20, 61–89, https://doi.org/10.1016/j.ocemod.2007.07.005, 2008.

Martínez-Pérez, A. M., Osterholz, H., Nieto-Cid, M., Álvarez, M., Dittmar, T., and Álvarez-Salgado, X. A.: Molecular composition of dissolved organic matter in the Mediterranean Sea, Limnology and Oceanography, 62, 2699–2712, https://doi.org/10.1002/lno.10600,2017.

Marullo, S., Napolitano, E., Santoleri, R., Manca, B., and Evans, R.: Variability of Rhodes and Ierapetra Gyres during Levantine Intermediate Water Experiment: Observations and model results, Journal of Geophysical Research: Oceans, 108, 1–18,https://doi.org/10.1029/2002jc001393, 2003.

Mayot, N., D’Ortenzio, F., D’Alcalà, M. R., Lavigne, H., and Claustre, H.: Interannual variability of the Mediterranean trophic regimes from ocean color satellites, Biogeosciences, 13, 1901–1917, https://doi.org/10.5194/bg-13-1901-2016, 2016.

Mayot, N., D’Ortenzio, F., Taillandier, V., Prieur, L., de Fommervault, O. P., Claustre, H., Bosse, A., Testor, P., and Conan, P.: Physical and Biogeochemical Controls of the Phytoplankton Blooms in North Western Mediterranean Sea: A Multiplatform Approach Over a Complete Annual Cycle (2012–2013 DEWEX Experiment), Journal of Geophysical Research: Oceans, 122, 9999–10 019,https://doi.org/10.1002/2016JC012052, 2017.

Mémery, L., Lévy, M., Vérant, S., and Merlivat, L.: The relevant time scales in estimating the air-sea CO2 exchange in a mid-latitude region, Deep-Sea Research Part II: Topical Studies in Oceanography, 49, 2067–2092, https://doi.org/10.1016/S0967-0645(02)00028-0, 2002.

Menna, M. and Poulain, P. M.: Mediterranean intermediate circulation estimated from Argo data in 2003-2010, Ocean Science, 6, 331–343, https://doi.org/10.5194/os-6-331-2010, 2010.

Menna, M., Gerin, R., Notarstefano, G., Mauri, E., Bussani, A., Pacciaroni, M., and Poulain, P. M.: On the Circulation and Thermohaline Properties of the Eastern Mediterranean Sea, Frontiers in Marine Science, 8, 1–19, https://doi.org/10.3389/fmars.2021.671469, 2021.

Mignot, A., Claustre, H., Uitz, J., Poteau, A., Ortenzio, F. D., and Xing, X.: Understanding the seasonal dynamics and the deep chlorophyll maximum in oligotrophic, AGU. Global Biogeochemical Cycles, 856–876, https://doi.org/10.1002/2013GB004781, 2014.

Mikolajczak, G., Estournel, C., Ulses, C., Marsaleix, P., Bourrin, F., Martín, J., Pairaud, I., Puig, P., Leredde, Y., Many, G., Seyfried, L., and Durrieu de Madron, X.: Impact of storms on residence times and export of coastal waters during a mild autumn/winter period in the Gulf of Lion, Continental Shelf Research, 207, https://doi.org/10.1016/j.csr.2020.104192, 2020.

Millot, C. and Taupier-Letage, I.: Circulation in the Mediterranean Sea, Life in the Mediterranean Sea: A Look at Habitat Changes, 5, 99–125, https://doi.org/10.1007/b107143, 2005.

Moutin, T. and Raimbault, P.: Primary production, carbon export and nutrients availability in western and eastern Mediterranean Sea in early summer 1996 (MINOS cruise), Journal of Marine Systems, 33-34, 273–288, https://doi.org/10.1016/S0924-7963(02)00062-3, 2002.

Nabat, P., Somot, S., Mallet, M., Michou, M., Sevault, F., Driouech, F., Meloni, D., Di Sarra, A., Di Biagio, C., Formenti, P., Sicard, M., Léon, J. F., and Bouin, M. N.: Dust aerosol radiative effects during summer 2012 simulated with a coupled regional aerosol-atmosphere-ocean model over the Mediterranean, Atmospheric Chemistry and Physics, 15, 3303–3326, https://doi.org/10.5194/acp-15-3303-2015, 2015.

Napolitano, E., Oguz, T., Malanotte-Rizzoli, P., Yilmaz, A., and Sansone, E.: Simulations of biological production in the Rhodes and Ionian basins of the eastern Mediterranean, Journal of Marine Systems, 24, 277–298, https://doi.org/10.1016/S0924-7963(99)00090-1, 2000.

Nixon, S. W.: Replacing the Nile: Are anthropogenic nutrients providing the fertility once brought to the Mediterranean by a great river?,Ambio, 32, 30–39, https://doi.org/10.1579/0044-7447-32.1.30, 2003.

Oschlies, A.: Feedbacks of biotically induced radiative heating on upper-ocean heat budget, circulation, and biological production in a coupled ecosystem-circulation model, Journal of Geophysical Research: Oceans, 109, 1–12, https://doi.org/10.1029/2004JC002430, 2004.

Ozer, T., Gertman, I., Kress, N., Silverman, J., and Herut, B.: Interannual thermohaline (1979–2014) and nutrient (2002–2014) dynamics in the Levantine surface and intermediate water masses, SE Mediterranean Sea, Global and Planetary Change, 151, 60–67, https://doi.org/10.1016/j.gloplacha.2016.04.001, 2016.

Ozer, T., Rahav, E., Gertman, I., Sisma-Ventura, G., Silverman, J., and Herut, B.: Relationship between thermohaline and biochemical patterns in the levantine upper and intermediate water masses, Southeastern Mediterranean Sea (2013–2021), Frontiers in Marine Science, 9, 1–11, https://doi.org/10.3389/fmars.2022.958924, 2022.

Özsoy, E., Hecht, A., and Ünlüata, : Circulation and hydrography of the Levantine Basin. Results of POEM coordinated experiments 1985-1986, Progress in Oceanography, 22, 125–170, https://doi.org/10.1016/0079-6611(89)90004-9, 1989.

Özsoy, E., Hecht, A., Ünlüata, , Brenner, S., Oˇguz, T., Bishop, J., Latif, M. A., and Rozentraub, Z.: A review of the Levantine Basin circulation and its variability during 1985-1988, Dynamics of Atmospheres and Oceans, 15, 421–456, https://doi.org/10.1016/0377-0265(91)90027-D, 1991.

Özsoy, E., Hecht, A., Ünlüata, , Brenner, S., Sur, H. I., Bishop, J., Latif, M. A., Rozentraub, Z., and Oˇguz, T.: A synthesis of the Levantine Basin circulation and hydrography, 1985-1990, Deep-Sea Research Part II, 40, 1075–1119, https://doi.org/10.1016/0967-0645(93)90063-S, 1993.

Palevsky, H. I. and Nicholson, D. P.: The North Atlantic Biological Pump Insights from the ocean observatoriess initiative irminger sea array, Oceanography, 31, 42–49, 2018.

Palevsky, H. I. and Quay, P. D.: Influence of biological carbon export on ocean carbon uptake over the annual cycle across the North Pacific Ocean, Global Biogeochemical Cycles, 31, 81–95, https://doi.org/10.1002/2016GB005527, 2017.

Palmiéri, J., Dutay, J.-C., D'Ortenzio, F., Houpert, L., and Bopp, L.: The Mediterranean subsurface chlorophyll dynamic and its impact on the Mediterranean bioregions, Progress in Oceanography, 2016.

Pasqueron De Fommervault, O., D'Ortenzio, F., Mangin, A., Serra, R., Migon, C., Claustre, H., Lavigne, H., Ribera D'Alcalà, M., Prieur, L., Taillandier, V., Schmechtig, C., Poteau, A., Leymarie, E., Dufour, A., Besson, F., and Obolensky, G.: Seasonal variability of nutrient concentrations in the Mediterranean Sea: Contribution of Bio-Argo floats, Journal of Geophysical Research: Oceans, 120, 8528–8550,https://doi.org/10.1002/2015JC011103, 2015.910

Petihakis, G., Triantafyllou, G., Tsiaras, K., Korres, G., Pollani, A., and Hoteit, I.: Eastern Mediterranean biogeochemical flux model -Simulations of the pelagic ecosystem, Ocean Science, 5, 29–46, https://doi.org/10.5194/os-5-29-2009, 2009.

Petrenko, A., Dufau, C., and Estournel, C.: Barotropic eastward currents in the western Gulf of Lion, north-western Mediterranean Sea, during stratified conditions, Journal of Marine Systems, 74, 406–428, https://doi.org/10.1016/j.jmarsys.2008.03.004, 2008.

Poulos, S. E., Drakopoulos, P. G., and Collins, M. B.: Seasonal variability in sea surface oceanographic conditions in the Aegean Sea (Eastern Mediterranean), Journal of Marine Systems, 13, 225–244, 1997.

Powley, H. R., Krom, M. D., and Van Cappellen, P.: Understanding the unique biogeochemistry of the Mediterranean Sea: Insights from a coupled phosphorus and nitrogen model, Global Biogeochemical Cycles, 31, 1010–1031, https://doi.org/10.1002/2017GB005648, 2017.

Pujo-Pay, M., Conan, P., Oriol, L., Cornet-Barthaux, V., Falco, C., Ghiglione, J. F., Goyet, C., Moutin, T., and Prieur, L.: Integrated survey of elemental stoichiometry (C, N, P) from the western to eastern Mediterranean Sea, Biogeosciences, 8, 883–899, https://doi.org/10.5194/bg-8-883-2011, 2011.

Reale, M., Cossarini, G., Lazzari, P., Lovato, T., Bolzon, G., Masina, S., Solidoro, C., and Salon, S.: Acidification, deoxygenation, and nutrient and biomass declines in a warming Mediterranean Sea, Biogeosciences, 19, 4035–4065, https://doi.org/10.5194/bg-19-4035-2022, 2022.

Ribera d'Alcalà, M., Civitarese, G., Conversano, F., and Lavezza, R.: Nutrient ratios and fluxes hint at overlooked processes in the Mediterranean Sea, Journal of Geophysical Research: Oceans, 108, https://doi.org/10.1029/2002jc001650, 2003.

Richon, C., Dutay, J. C., Dulac, F., Wang, R., Balkanski, Y., Nabat, P., Aumont, O., Desboeufs, K., Laurent, B., Guieu, C., Raimbault, P., and Beuvier, J.: Modeling the impacts of atmospheric deposition of nitrogen and desert dust-derived phosphorus on nutrients and biological budgets of the Mediterranean Sea, Progress in Oceanography, 163, 21–39, https://doi.org/10.1016/j.pocean.2017.04.009, 2017.

Richon, C., Dutay, J. C., Dulac, F., Wang, R., and Balkanski, Y.: Modeling the biogeochemical impact of atmospheric phosphate deposition from desert dust and combustion sources to the Mediterranean Sea, Biogeosciences, 15, 2499–2524, https://doi.org/10.5194/bg-15-2499-2018, 2018.

Ridame, C. and Guieu, C.: Saharan input of phosphate to the oligotrophic water of the open western Mediterranean sea, Limnology and Oceanography, 47, 856–869, https://doi.org/10.4319/lo.2002.47.3.0856, 2002.

Robinson, A., Leslie, W., Theocharis, A., and Lascaratos, A.: Mediterranean Sea Circulation, Encyclopedia of Ocean Sciences, pp. 1689–1705, https://doi.org/10.1006/rwos.2001.0376, 2001.

Robson, B. J.: State of the art in modelling of phosphorus in aquatic systems: Review, criticisms and commentary, Environmental Modelling and Software, 61, 339–359, https://doi.org/10.1016/j.envsoft.2014.01.012, 2014.

Salgado-Hernanz, P. M., Racault, M. F., Font-Muñoz, J. S., and Basterretxea, G.: Trends in phytoplankton phenology in the Mediterranean Sea based on ocean-colour remote sensing, Remote Sensing of Environment, 221, 50–64, https://doi.org/10.1016/j.rse.2018.10.036, 2019.

Sanders, R., Henson, S. A., Koski, M., De La Rocha, C. L., Painter, S. C., Poulton, A. J., Riley, J., Salihoglu, B., Visser, A., Yool, A., Bellerby, R., and Martin, A. P.: The Biological Carbon Pump in the North Atlantic, Progress in Oceanography, 129, 200–218, https://doi.org/10.1016/j.pocean.2014.05.005, 2014.

Santinelli: DOC in the Mediterranean Sea, Biogeochemistry of Marine Dissolved Organic Matter: Second Edition, pp. 579–608, https://doi.org/10.1016/B978-0-12-405940-5.00013-3, 2015.

Santinelli, Nannicini, L., and Seritti, A.: DOC dynamics in the meso and bathypelagic layers of the Mediterranean Sea, Deep-Sea Research Part II: Topical Studies in Oceanography, 57, 1446–1459, https://doi.org/10.1016/j.dsr2.2010.02.014, 2010.

Santinelli, C., Hansell, D. A., and Ribera d'Alcalà, M.: Influence of stratification on marine dissolved organic carbon (DOC) dynamics: The Mediterranean Sea case, Progress in Oceanography, 119, 68–77, https://doi.org/10.1016/j.pocean.2013.06.001, 2013.

Siokou-Frangou, I., Gotsis-Skretas, O., Christou, E. D., and Pagou, K.: Plankton Characteristics in the Aegean, Ionian and NW Levantine Seas, The Eastern Mediterranean as a Laboratory Basin for the Assessment of Contrasting Ecosystems, pp. 205–223, https://doi.org/10.1007/978-94-011-4796-5_15, 1999.

Siokou-Frangou, I., Christaki, U., Mazzocchi, M. G., Montresor, M., Ribera D'Alcala, M., Vaque, D., and Zingone, A.: Plankton in the open mediterranean Sea: A review, Biogeosciences, 7, 1543–1586, https://doi.org/10.5194/bg-7-1543-2010, 2010.

Soetaert, K., Middelburg, J. J., Herman, P. M., and Buis, K.: On the coupling of benthic and pelagic biogeochemical models, Earth Science Reviews, 51, 173–201, https://doi.org/10.1016/S0012-8252(00)00004-0, 2000.

Solidoro, C., Cossarini, G., Lazzari, P., Galli, G., Bolzon, G., Somot, S., and Salon, S.: Modeling Carbon Budgets and Acidification in the Mediterranean Sea Ecosystem Under Contemporary and Future Climate, Frontiers in Marine Science, 8, 1–15, https://doi.org/10.3389/fmars.2021.781522, 2022.

Somot, S., Sevault, F., Déqué, M., Somot, S., Sevault, F., and Déqué, M.: Transient climate change scenario simulation of the Mediterranean Sea for the 21st century using a high-resolution ocean circulation model To cite this version : HAL Id : hal-00195045 Transient climate change scenario simulation of the Mediterranean Sea f, Climate Dynamics, 27, 851–879, 2006.

Soto-Navarro, J., Jordá, G., Amores, A., Cabos, W., Somot, S., Sevault, F., Macías, D., Djurdjevic, V., Sannino, G., Li, L., and Sein, D.:Evolution of Mediterranean Sea water properties under climate change scenarios in the Med-CORDEX ensemble, Climate Dynamics, 54, 2135–2165, https://doi.org/10.1007/s00382-019-05105-4, 2020.

Sur, H., Ozsoy, E., and Unluata, U.: Simultaneous deep and intermediate depth convection in the Northem Levantine Sea ,, oceanologica, 16, 33–43, 1992.

Taillandier, V., D'Ortenzio, F., and Antoine, D.: Carbon fluxes in the mixed layer of the Mediterranean Sea in the 1980s and the 2000s, Deep-Sea Research Part I: Oceanographic Research Papers, 65, 73–84, https://doi.org/10.1016/j.dsr.2012.03.004, 2012.

Taillandier, V., D'Ortenzio, F., Prieur, L., Conan, P., Coppola, L., Cornec, M., Dumas, F., Durrieu de Madron, X., Fach, B., Fourrier, M., Gentil, M., Hayes, D., Husrevoglu, S., Legoff, H., Le Ster, L., Örek, H., Ozer, T., Poulain, P. M., Pujo-Pay, M., Ribera d'Alcalà, M., Salihoglu, B., Testor, P., Velaoras, D., Wagener, T., and Wimart-Rousseau, C.: Sources of the Levantine Intermediate Water in Winter 2019, Journal of Geophysical Research: Oceans, 127, 1–19, https://doi.org/10.1029/2021JC017506, 2022.

Tanhua, T., Hainbucher, D., Schroeder, K., Cardin, V., Álvarez, M., and Civitarese, G.: The Mediterranean Sea system: A review and an introduction to the special issue, Ocean Science, 9, 789–803, https://doi.org/10.5194/os-9-789-2013, 2013.

The POEM group: General circulation of the Eastern Mediterranean, Earth Science Reviews, 32, 285–309, https://doi.org/10.1016/0012-8252(92)90002-B, 1992.

Theocharis, A., Georgopoulos, D., Lascaratos, A., and Nittis, K.: Water masses and circulation in the central region of the Eastern Mediterranean, Deep-Sea Research II, 40, 1121–1142, 1993.

Touratier, F. and Goyet, C.: Decadal evolution of anthropogenic CO2 in the northwestern Mediterranean Sea from the mid-1990s to the mid-2000s, Deep-Sea Research Part I: Oceanographic Research Papers, 56, 1708–1716, https://doi.org/10.1016/j.dsr.2009.05.015, 2009.

Tuˇgrul, S., Be ¸siktepe, T., and Salihoˇglu, I.: Nutrient exchange fluxes between the Aegean and Black Seas through the marmara sea, Mediterranean Marine Science, 3, 33–42, https://doi.org/10.12681/mms.256, 2002.

Uitz, J., Stramski, D., Gentili, B., D'Ortenzio, F., and Claustre, H.: Estimates of phytoplankton class-specific and total primary production in the Mediterranean Sea from satellite ocean color observations, Global Biogeochemical Cycles, 26, 1–10,https://doi.org/10.1029/2011GB004055, 2012.

Ulses, C., Estournel, C., Bonnin, J., Durrieu de Madron, X., and Marsalei, P.: Impact of storms and dense water cascading on shelf-slope exchanges in the Gulf of Lion (NW Mediterranean), Journal of Geophysical Research: Oceans, 113, https://doi.org/10.1029/2006JC003795,2008.

Ulses, C., Estournel, C., Kessouri, F., Hermann, M., and Marsaleix, P.: Modeling, Budget of organic carbon in the North-Western Mediterranean open sea over the period 2004–2008 using 3-D coupled physical Modeling, Journal of Geophysical Research : Oceans, 121,7026–7055, https://doi.org/10.1002/2016JC011818, 2016.

Ulses, C., Estournel, C., Fourrier, M., Coppola, L., Kessouri, F., Lefèvre, D., and Marsaleix, P.: Oxygen budget of the north-western Mediterranean deep-convection region, Biogeosciences, 18, 937–960, https://doi.org/10.5194/bg-18-937-2021, 2021.

Velaoras, D., Krokos, G., Nittis, K., & Theocharis, A.: Dense intermediate water outflow from the Cretan Sea: A salinity driven, recurrent phenomenon, connected to thermohaline circulation changes. Journal of Geophysical Research: Oceans, 119, 3868–3882. https://doi.org/10.1002/2014JC009937, 2014.

Vidussi, F., Claustre, H., Manca, B. B., Luchetta, A., and Jean-Claude, M.: Phytoplankton pigment distribution in relation to upper thermocline circulation in the eastern Mediterranean Sea during winter, Journal of Geophysical Research, 106, 939–956, 2001.

Vidussi, F., Mostajir, B., Fouilland, E., Le Floc'H, E., Nouguier, J., Roques, C., Got, P., Thibault-Botha, D., Bouvier, T., and Troussellier, M.: Effects of experimental warming and increased ultraviolet B radiation on the Mediterranean plankton food web, Limnology and Oceanography, 56, 206–218, https://doi.org/10.4319/lo.2011.56.1.0206, 2011.

Wimart-Rousseau, C., Wagener, T., Álvarez, M., Moutin, T., Fourrier, M., Coppola, L., Niclas-Chirurgien, L., Raimbault, P., D'Ortenzio, F.,Durrieu de Madron, X., Taillandier, V., Dumas, F., Conan, P., Pujo-Pay, M., and Lefèvre, D.: Seasonal and Interannual Variability of the CO2 System in the Eastern Mediterranean Sea: A Case Study in the North Western Levantine Basin, Frontiers in Marine Science, 8, 1–18, https://doi.org/10.3389/fmars.2021.649246, 2021.

Yilmaz, A. and Tugrul, S.: The effect of cold- and warm-core eddies on the distribution and stoichiometry of dissolved nutrients in the northeastern Mediterranean, Journal of Marine Systems, 16, 253–268, https://doi.org/10.1016/S0924-7963(97)00022-5, 1998.

Yilmaz, A., Ediger, D., Basturk, O., and Tugrul, S.: Phytoplankton fluorescence and deep chlorophyll maxima in the northeastern Mediterranean, Oceanologica Acta, 17, 69–77, 1994.

Figures

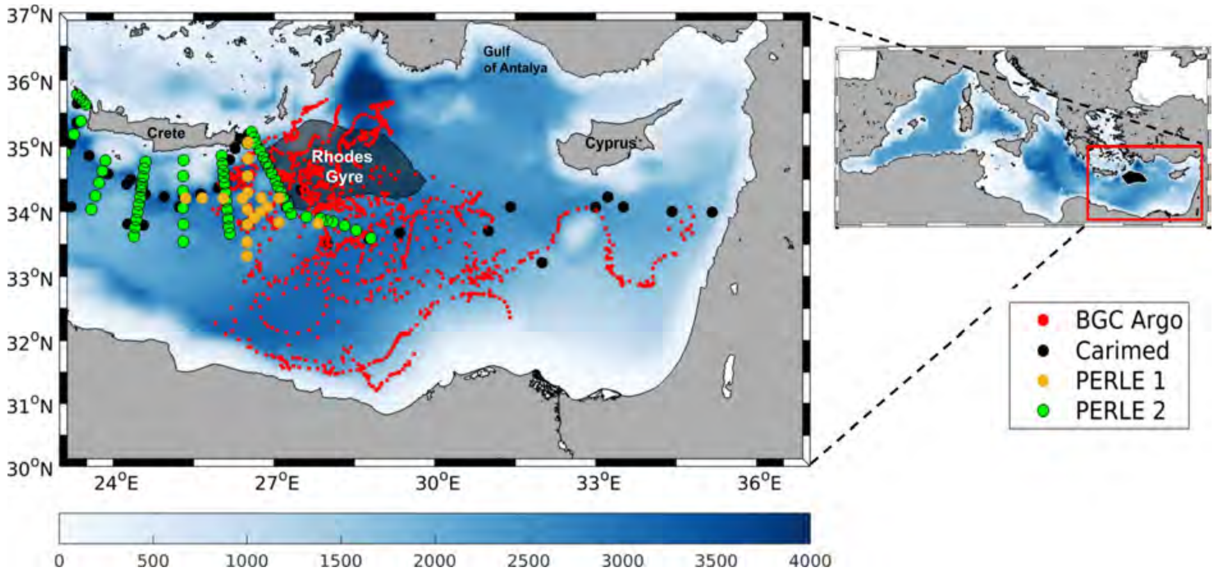

Figure 1: Model domain (right) and bathymetry (m) in the Mediterranean Sea and Levantine Basin. Red, black, yellow and green dots indicate positions of BGC-Argo floats, CARIMED, PERLE 1 and PERLE 2 cruise data, respectively, from 2013 to 2020. The black patch represents the Rhodes Gyre.

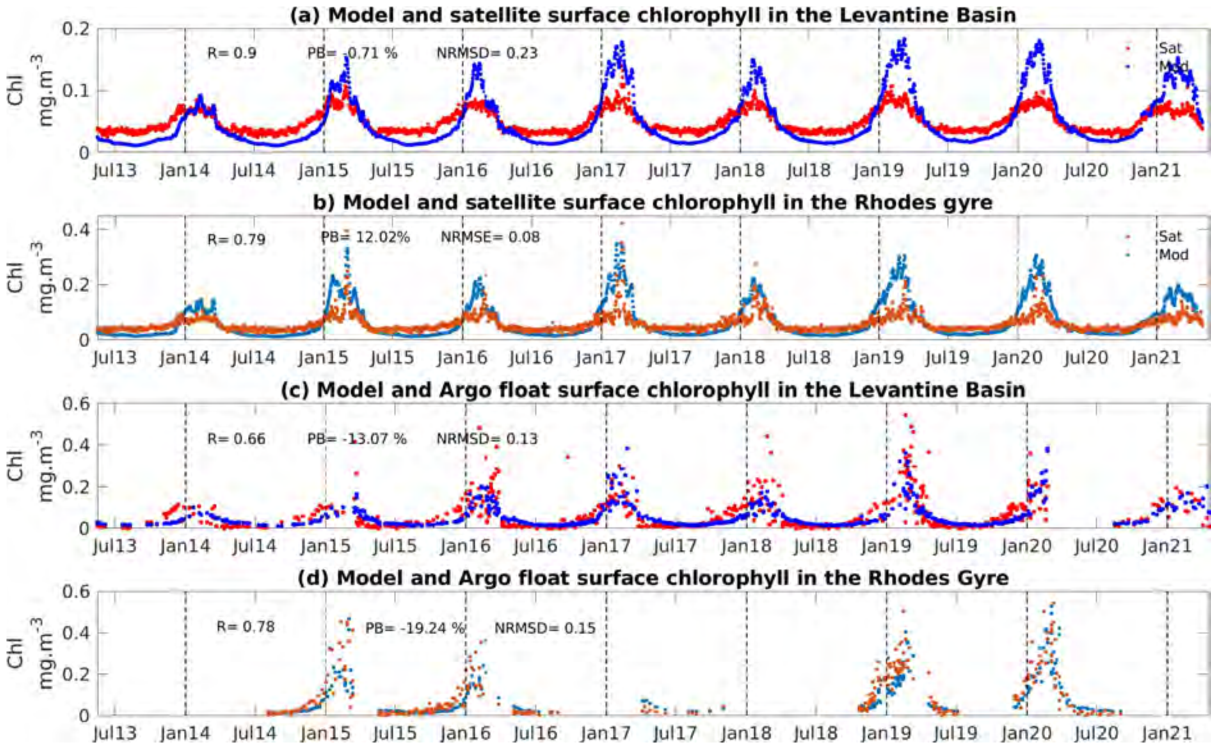

Figure 2: Time series of modeled (in blue) and satellite (in red) surface chlorophyll-a concentration (mg m^{-3}) averaged over (a) the Levantine Basin and (b) the Rhodes Gyre. Time series of (c)-modeled (in blue) and BGC-Argo float (in red) surface chlorophyll-a concentration (mg m^{-3}) (c) in the Levantine Basin and (d) in the Rhodes Gyre. Coefficient correlation (R), percent bias (PB) and Normalized Root Mean Square Deviation (NRMSD) between model outputs and observations are indicated in (a), (b), (c) and (d).

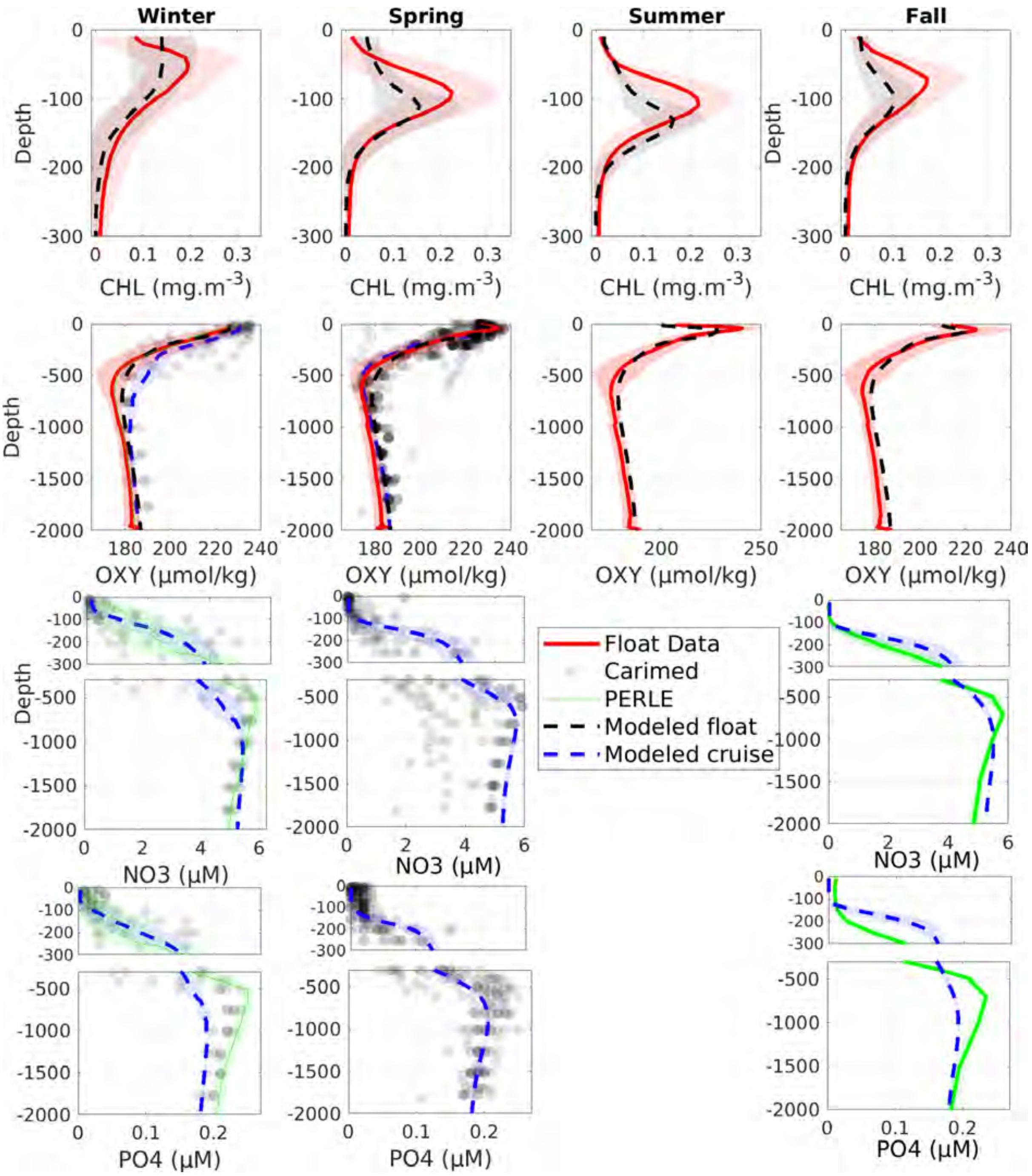

Figure 3: Comparison over the Levantine Sea between observed (gray points for CARIMED, green lines for PERLE1 and PERLE2, red line for BGC-Argo float data) and modeled (blue and black lines) profiles of chlorophyll (mg Chl m^{-3}), dissolved oxygen (µmol kg^{-1}), nitrate (µM) and phosphate (µM) concentrations, averaged by season (winter: 21 December to 20 March, spring: 21 March to 20 June, summer: 21 June to 20 September, fall: 21 September to 20 December). Shaded areas represent standard deviation.

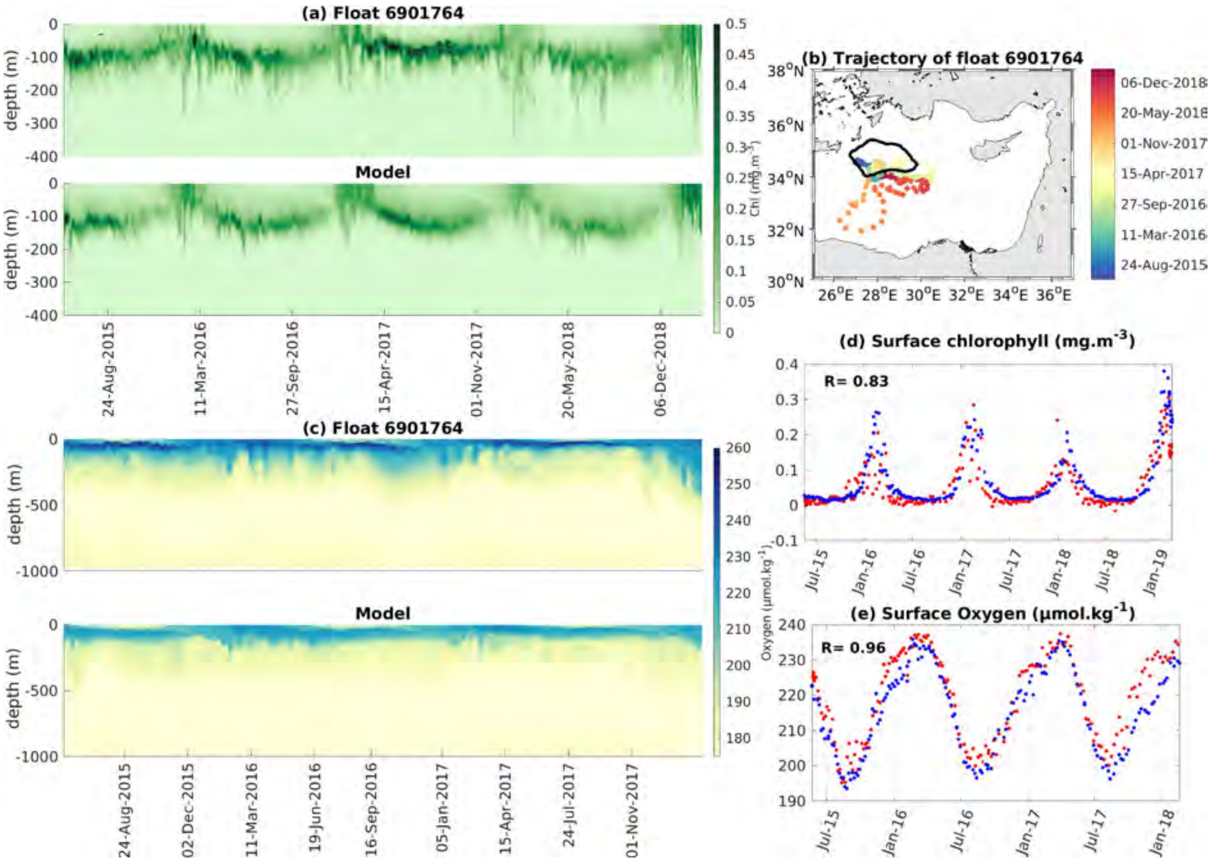

Figure 4: Time evolution of BGC-Argo float 6901764 observed and modeled data: (a) Hovmöller diagrams of chlorophyll concentration (mg m^{-3}), (b) trajectory of the BGC-Argo float, (c) Hovmöller diagrams of dissolved oxygen concentration (µmol kg^{-1}), (d) surface chlorophyll (mg m^{-3}) in the first 10 m, (e) surface dissolved oxygen (µmol kg^{-1}) observed in the first 10 m. Red dots represent the float data and the blue dots the model outputs in (d) and (e).

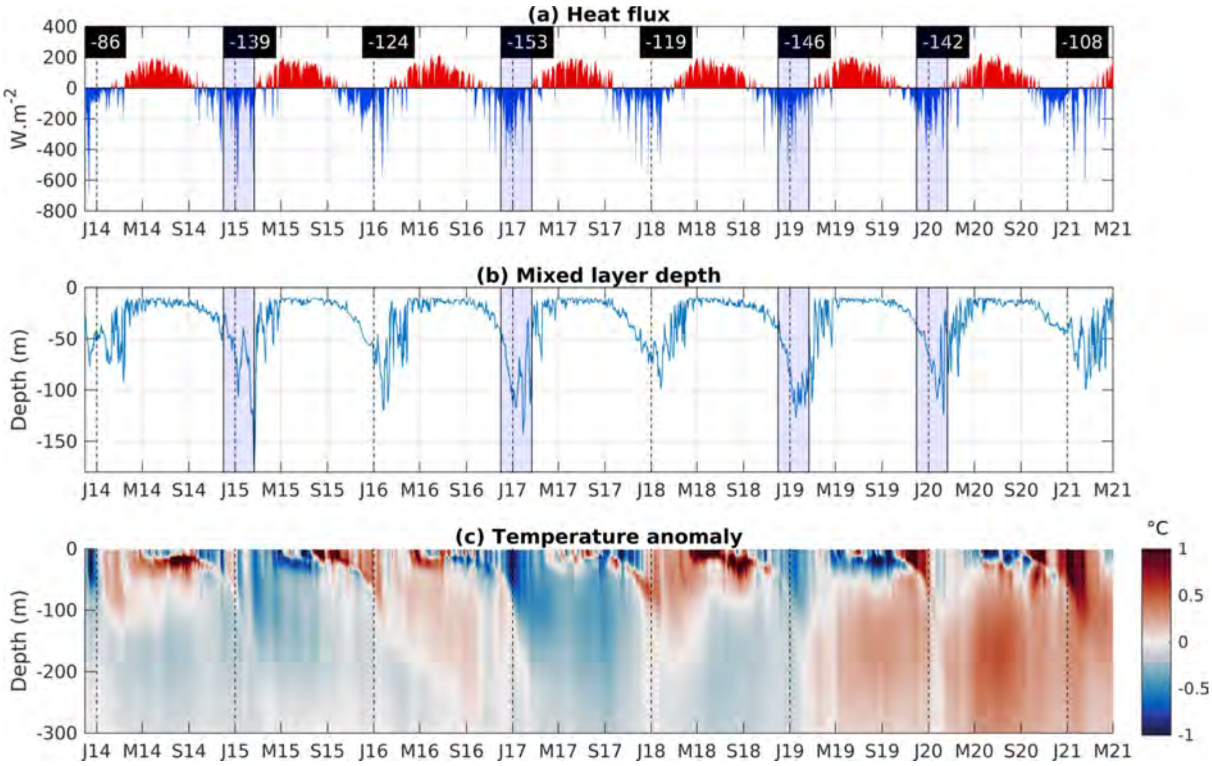

Figure 5: Time series of modeled (a) surface heat fluxes (W m^{-2}), (b) mixed layer depth (m) and (c) temperature anomaly (°C), averaged over the Rhodes Gyre area. The winter (December-January-February) mean heat flux is

indicated in black rectangles in (a). J: January M: May S: September. Winters with strong heat loss and deeper mixed layers are emphasized in blue in (a) and (b).

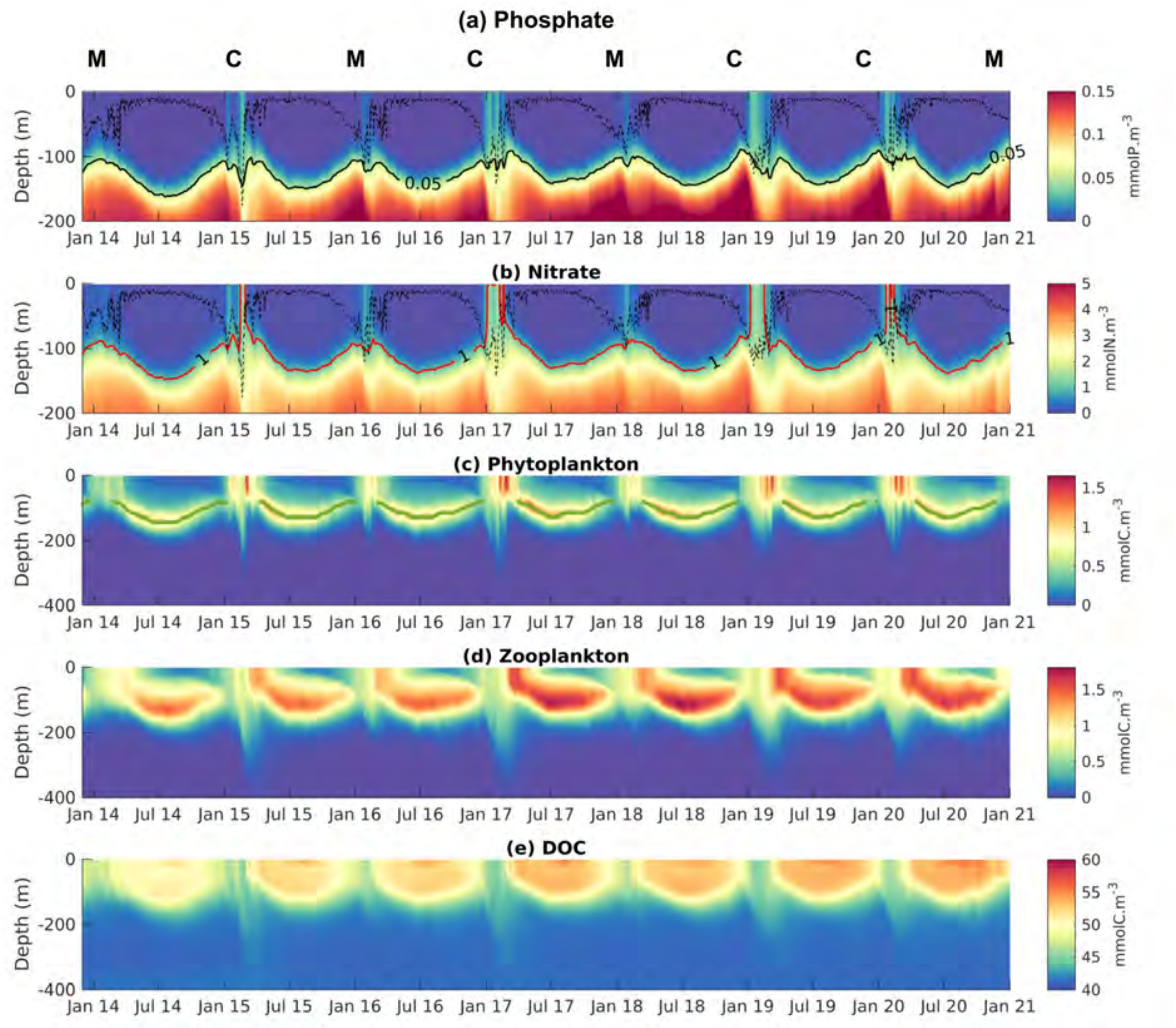

Figure 6: Hovmöller diagrams of modeled (a) phosphate (mmol P m^{-3}), (b) nitrate (mmol N m^{-3}), (c) phytoplankton (mmol C m^{-3}), (d) zooplankton (mmol C m^{-3}) and (d) dissolved organic carbon (mmol C m^{-3}) concentrations averaged over the Rhodes Gyre, from December 2013 to January 2021. The black dotted line in (a) and (b) indicates the mixed layer depth. The red line represents the depth of the nitracline in (b), and the black one of the phosphacline in (a). The green dotted line in (c) indicates the deep chlorophyll maximum. C refers to cold winter years and M to mild winter years.

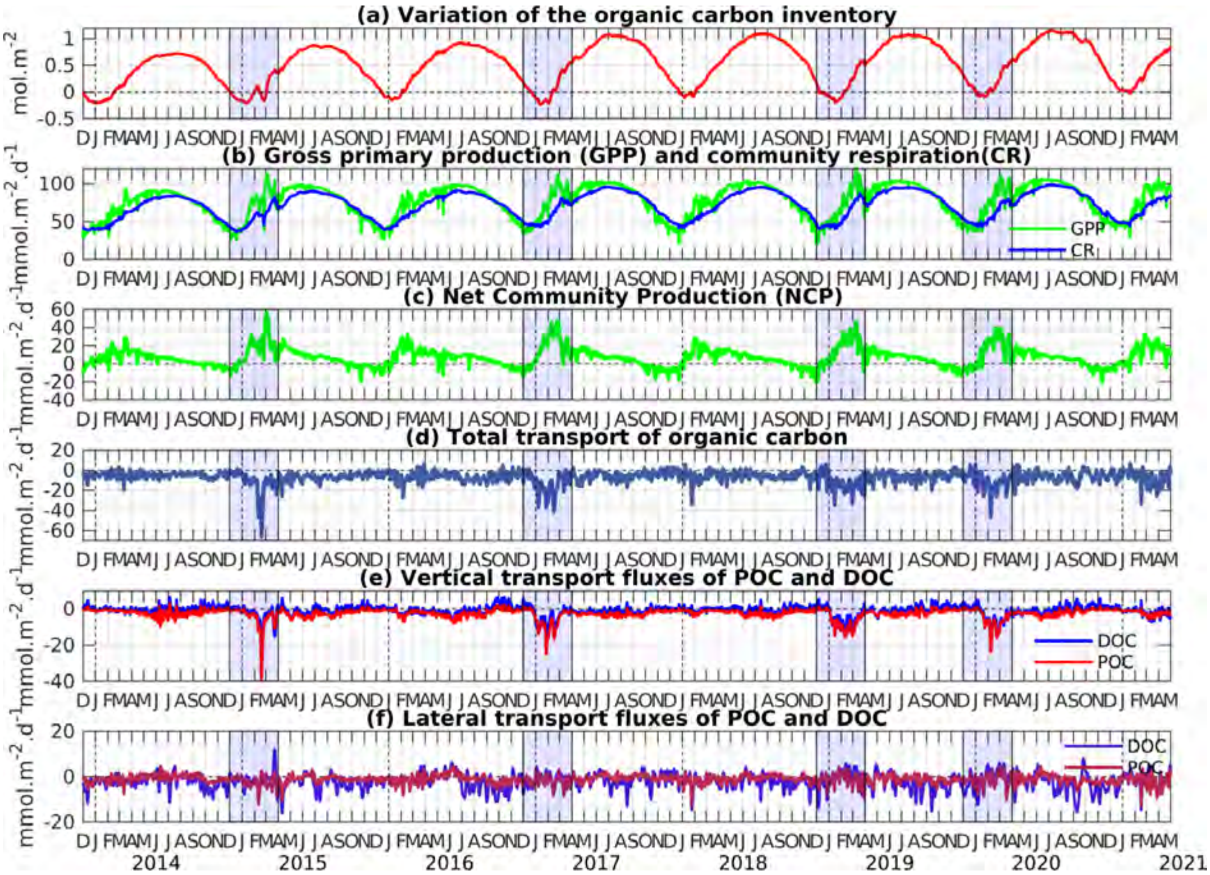

Figure 7: Time evolution of (a) the variation of the organic carbon inventory (from 1st December 2013, mol C m^{-2}), (b) gross primary production (GPP) (in green), and community respiration (CR) in the surface layer (in blue) (mmol C m^{-2} d^{-1}), (c) net community production (NCP) (mmol C m^{-2} d^{-1}), (d) total transport of organic carbon at the limits of the area (mmol C m^{-2} d^{-1}), (e) vertical transport fluxes of POC and DOC at the base of the surface layer (mmol C m^{-2} d^{-1}) and (f) lateral transport fluxes of POC and DOC at the limits of the area (mmol C m^{-2} d^{-1}), averaged over the Rhodes Gyre surface layer (0-150 m). Cold winters/early springs are emphasized in blue.

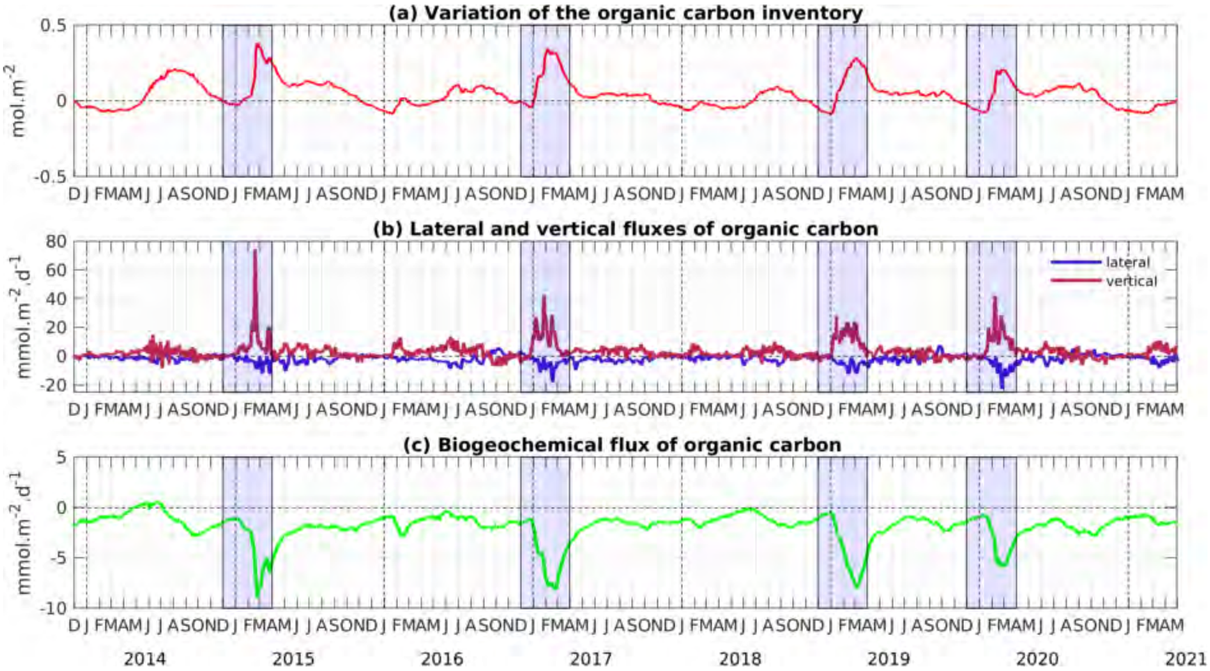

Figure 8: Time evolution of (a) variation of the organic carbon inventory (from 1st December 2013, mol C m^{-2}), (b) lateral and vertical transport fluxes of organic carbon (mmol C m^{-2} d^{-1}) at the limits of the area and (c)

biogeochemical flux of organic carbon (mmol C m^{-2} d^{-1}), averaged over the Rhodes Gyre intermediate layer (150-400 m). Cold winters/early springs are emphasized in blue.

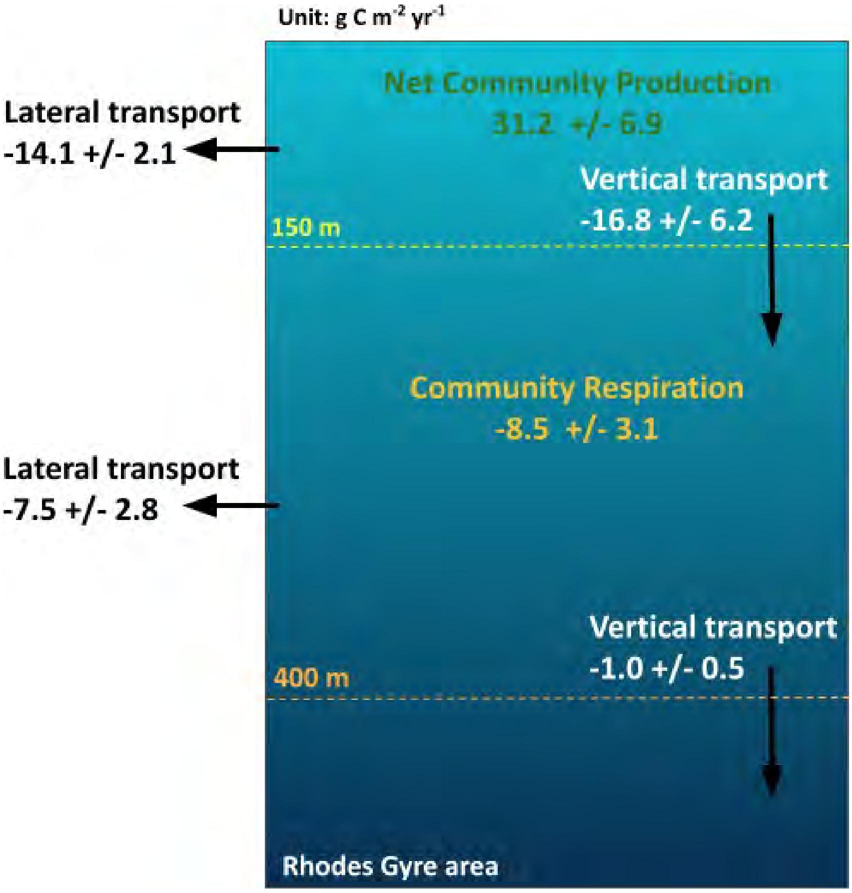

Figure 9: Annual organic carbon budget (g C m^{-2} yr^{-1}) in the surface and intermediate layers of the Rhodes Gyre for the seven year period 2013-2020.

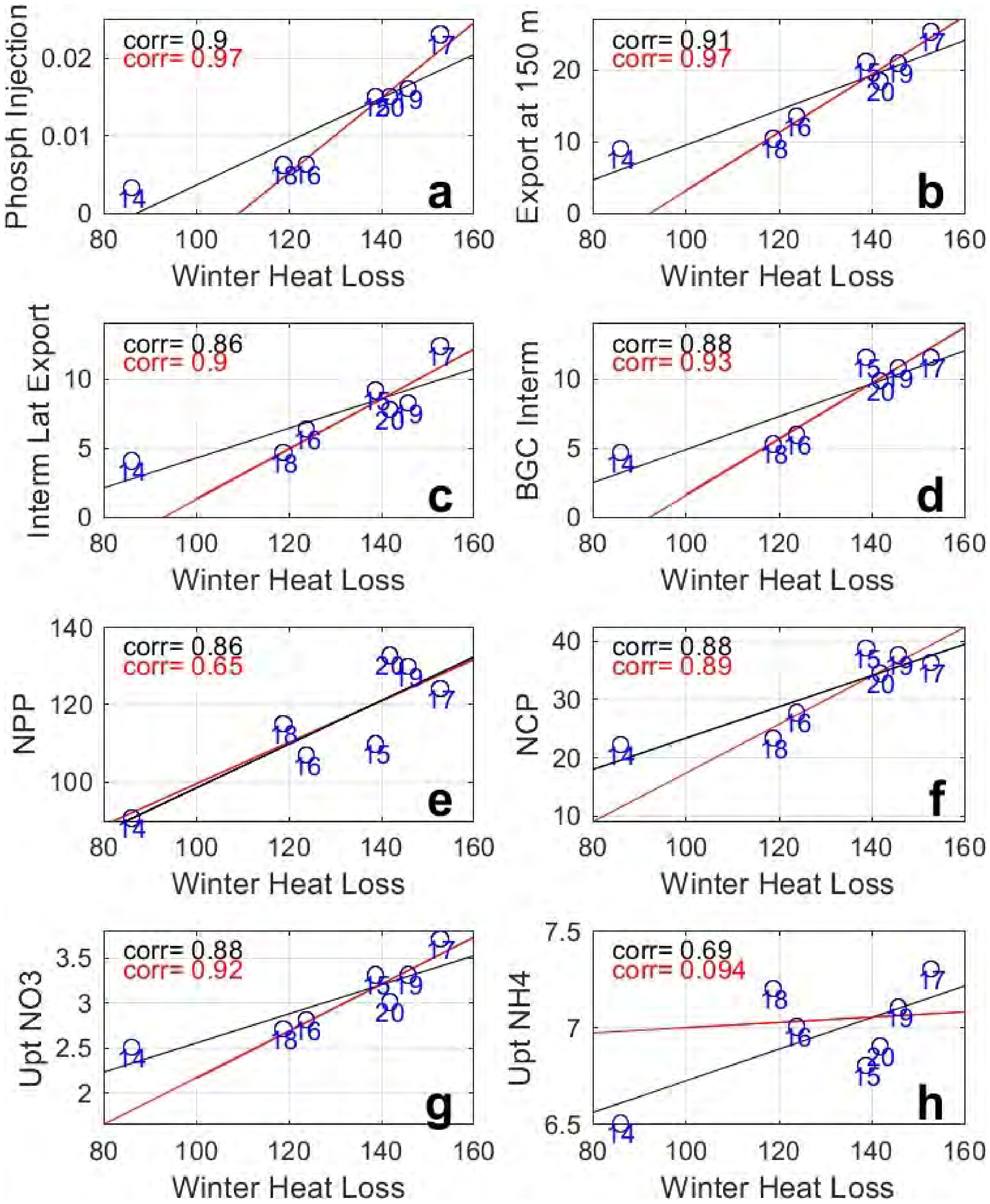

Figure 10: Scatter-plot of winter surface heat loss (W m^{-2}) vs. (a) winter phosphate injection (mol P m^{-2}) into the surface layer and mean annual values of (b) downward export of OC (Organic Carbon) at 150 m (gC m^{-2} yr^{-1}),, (c) lateral export from the intermediate layer (gC m^{-2} yr^{-1}),; (d) biogeochemical consumption in the intermediate layer (gC .m^{-2} .yr^{-1}), (e) NPP, (f) NCP (gC m^{-2} yr^{-1}), (g,h) uptake of nitrate and ammonium (mmol N m^{-2} yr^{-1}). The years are identified by the numbers in blue, e.g. 14 stands for 2013-14. The black line shows the seven years linear regression and the red line shows the linear regression when excluding 2013-14. The corresponding correlations are shown with the same color code.

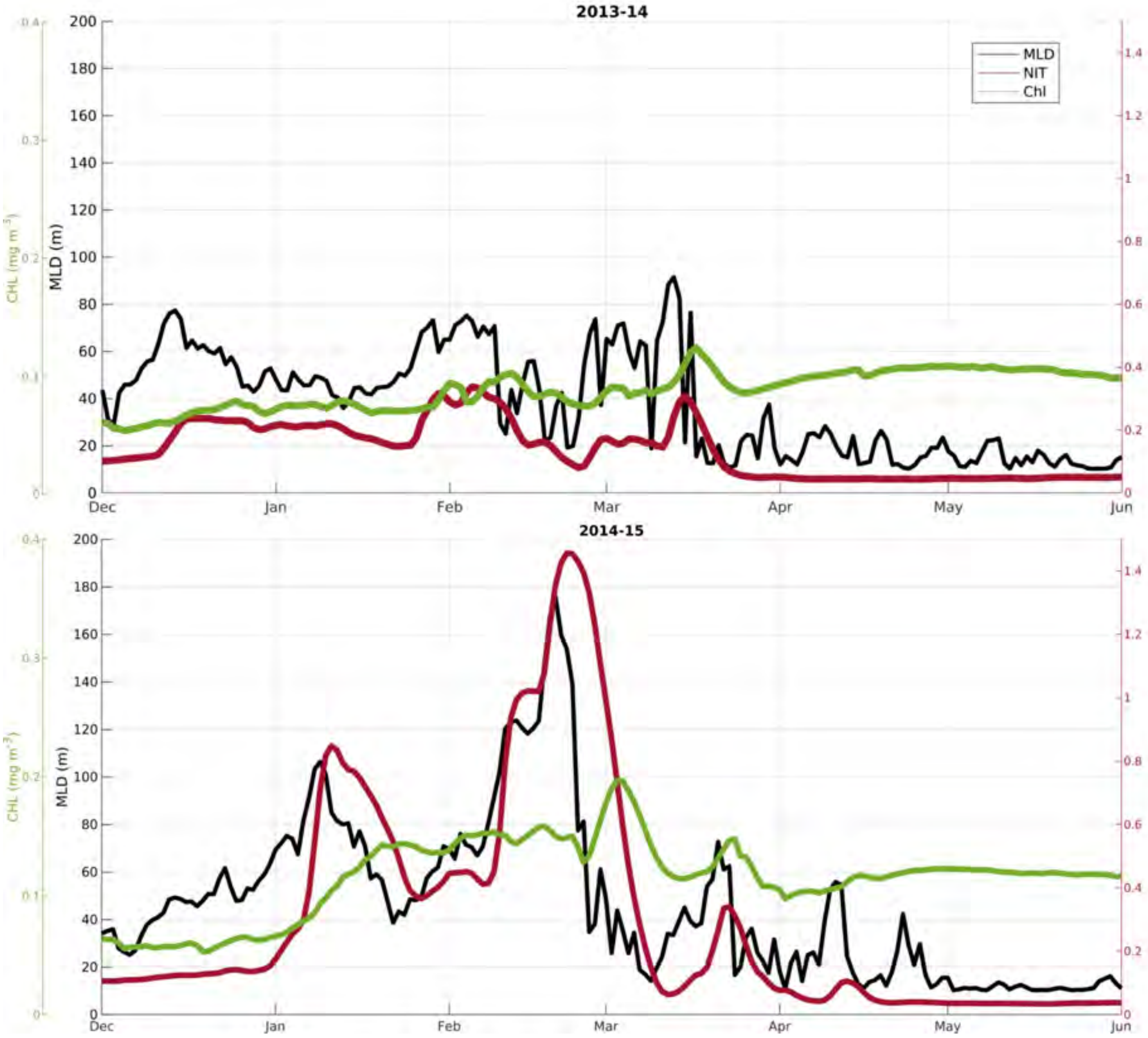

Figure 11: Annual cycle of the Mixed Layer Depth (MLD, m) (black), surface chlorophyll (CHL, mg m^{-3}) (green) and nitrate (NIT, mmol N m^{-3}) (red) concentration for years 2013-14, and 2014-15~~.~~

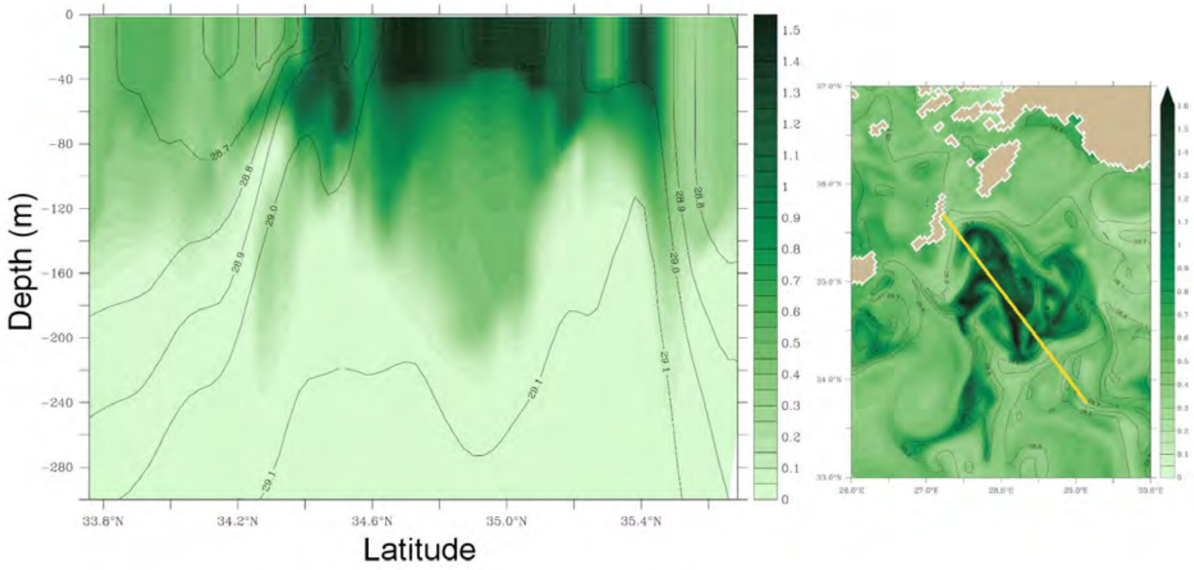

Figure 12: Vertical section of phytoplankton concentration (expressed in mmol C m^{-3}) across the Rhodes Gyre on March 27, 2015. The potential density anomaly (kg m^{-3}) is overlaid with contours. The position of the section is indicated on the map of surface phytoplankton (right panel).

Tables

Table 1. Amount of nutrients injected into the surface layer in winter (December - January - February) in the Rhodes Gyre; annual biogeochemical carbon flows (gross and net primary production (GPP and NPP), net community production (NCP), community respiration (CR)), downward export flux of particulate and dissolved organic carbon (POC and DOC) and lateral export at 150 and 400 m for the different years and averaged over the 7-year period, estimated from the model. Positive values correspond to an input for the considered layer of the study area. The annual budget is calculated from December.

			Units	2013-14	2014-15	2015-16	2016-17	2017-18	2018-19	2019-20	Mean (SD)
Surface layer (0 - 150m)	**Winter (DJF)**	Amount of nitrate injected in winter in the surface layer	*mol N m*$^{-2}$	0.09	0.33	0.14	0.47	0.14	0.31	0.30	0.25 (0.14)
		Amount of phosphate injected in winter in the surface layer	*mol P m*$^{-2}$	0.003	0.015	0.006	0.023	0.006	0.016	0.015	0.012 (0.007)
	Annual	GPP	$gC.m^{-2}.yr^{-1}$	298.7	330.2	328.8	350.3	337.9	354.2	357.9	336.9 (20.4)
		CR	$gC.m^{-2}.yr^{-1}$	281.5	303.8	307.9	326.3	320.2	327.8	333.9	314.5 (18.2)
		NCP	$gC.m^{-2}.yr^{-1}$	22.1	38.6	27.5	36.2	23.2	37.4	34.3	31.2 (6.9)
		NPP	$gC.m^{-2}.yr^{-1}$	90.5	109.6	106.7	123.9	114.9	129.6	132.5	115.0 (14.7)
		POC vertical export at 150 m	$gC.m^{-2}.yr^{-1}$	-7.8	-14.2	-9.7	-16.4	-8.1	-14.3	-12.8	-11.9 (3.4)
		DOC vertical export at 150 m	$gC.m^{-2}.yr^{-1}$	-1.1	-6.8	-3.6	-8.8	-2.2	-6.5	-5.5	-4.9 (2.8)
		OC vertical export at 150 m	$gC.m^{-2}.yr^{-1}$	-8.9	-21	-13.3	-25.2	-10.3	-20.8	-18.3	-16.8 (6.2)
		OC lateral export	$gC.m^{-2}.yr^{-1}$	-13.1	-16.3	-13.5	-10.6	-13.6	-14.7	-16.8	-14.1 (2.1)
		OC inventory variation	$gC.m^{-2}.yr^{-1}$	0.1	1.4	0.7	0.4	-0.6	2.0	-0.8	0.44 (1)
Intermediate layer (150 - 400 m)	**Annual**	CR	$gC.m^{-2}.yr^{-1}$	-4.6	-11.5	-5.9	-11.5	-5.2	-10.7	-9.8	-8.5 (3.1)
		POC vertical	$gC.m^{-2}.yr^{-1}$	-1.5	-1.9	-1.7	-2.3	-1.7	-2.2	-2.1	-1.9 (0.3)

		export at 400 m									
		DOC vertical export at 400 m	$gC.m^{-2}.yr^{-1}$	1.3	1.1	0.9	0.7	0.8	0.6	1.0	0.9 (0.2)
		OC vertical export at 400 m	$gC.m^{-2}.yr^{-1}$	-0.2	-0.8	-0.8	-1.6	-0.9	-1.6	-1.1	-1.0 (0.5)
		OC lateral export	$gC.m^{-2}.yr^{-1}$	-4.0	-9.1	-6.3	-12.3	-4.6	-8.2	-7.7	-7.5 (2.8)
		OC inventory variation	$gC.m^{-2}.yr^{-1}$	0.02	-0.4	0.3	-0.2	-0.3	0.3	-0.4	-0.1 (0.3)

Supplementary Material

Text S1: Equation of OC balance

The variation of the OC inventory in the upper layer of the Rhodes Gyre between times t_1 and t_2 ($\Delta\ OC\ I_{upper}$), in mol C m^{-2}, is equal to the sum of all OC fluxes within the Rhodes Gyre area between t_1 and t_2:

$$\Delta\, OC\, I_{upper} = OC\, I_{upper,\, t2} - OC\, I_{upper, t1} = \int_{t_1}^{t_2} \left(F_{OC,lat} + F_{OC,vert} + F_{OC,bgc}\right) dt \qquad \text{(S1)}$$

where $F_{OC,lat}$ and $F_{OC,vert}$ are the lateral and vertical exchange fluxes at the boundaries of the upper layer (150 m to the surface) of the Rhodes Gyre area, and $F_{OC,bgc}$ is the biogeochemical flux inside the Gyre.

$OC\ I_{upper,t}$ was computed from:

$$OC\, I_{upper,t} = \int\int \int_{(x,y)\in\, RG/z\in upper\ layer} OC(x, y, z, t)\ dx\ dy\ dz \qquad \text{(S2)}$$

OC is the sum of organic carbon fast- and slow-sinking detritus, dissolved organic carbon and the carbon biomass of phytoplankton, zooplankton and bacteria.

The lateral exchange flux was computed from:

$$F_{OC,lat} = \int\int_{A} OC * (x, y, z, t)\ v_t(x, y, z, t)\ dA \qquad \text{(S3)}$$

where v_t is the current velocity normal to the limit of the Rhodes Gyre area, A is the area of the vertical section limiting the Rhodes Gyre and extending from the base of the upper layer (150 m) to the surface, and where OC* is a function of OC which results from the use of the QUICKEST advection scheme (Leonard, 1979):

$$OC *= OC - \frac{Dx}{2} Cr\ GRAD - \frac{1}{3}(1 - Cr^2)\ CURV \qquad \text{(S4)}$$

where Dx is the grid horizontal resolution, CURV and GRAD are given by Leonard (1979) and *Cr* is the Current number.

$F_{OC,bgc}$ was computed from:

$$F_{OC,bgc} = \int \int \int_{(x,y)\in\, RG\ /\ z\ \in\ upper\ layer} BGCflux(x, y, z, t)\ dx\ dy\ dz \qquad \text{(S5)}$$

where *BGCflux* is the biogeochemical flux, i.e. GPP - CR (see Table S4 in Supplement Material by Many et al. (2021)).

Finally, the vertical transport flux, $F_{OC,vert}$, was derived from all other terms of Eq. (S1).

The computation of OC balance in the intermediate layer is computed in a similar way between 150 and 400 m

.

Table S1: Metrics computed from chlorophyll (Chl) concentration, winter (December-January-February) mixed layer depth (MLD) and surface heat flux for the Rhodes Gyres over the period of 2013-2020. For the mean, the values in parenthesis represent the standard deviation (SD).

	Units	2013-14	2014-15	2015-16	2016-17	2017-18	2018-19	2019-20	Mean (SD)
Mean winter surface heat flux	W m^{-2}	-86	-139	-124	-153	-119	-146	-142	-130 (23)
Maximum MLD	m	92	176	120	143	98	127	124	126 (28)
Mean winter MLD	m	51	72	61	79	62	84	65	68 (11)
Maximum Chl	mg m^{-3}	0.15	0.33	0.23	0.35	0.22	0.31	0.31	0.27 (0.07)
Date of maximum Chl	-	12 Feb	4 Mar	17 Feb	11 Feb	7 Feb	10 Mar	20 Feb	-

Figures

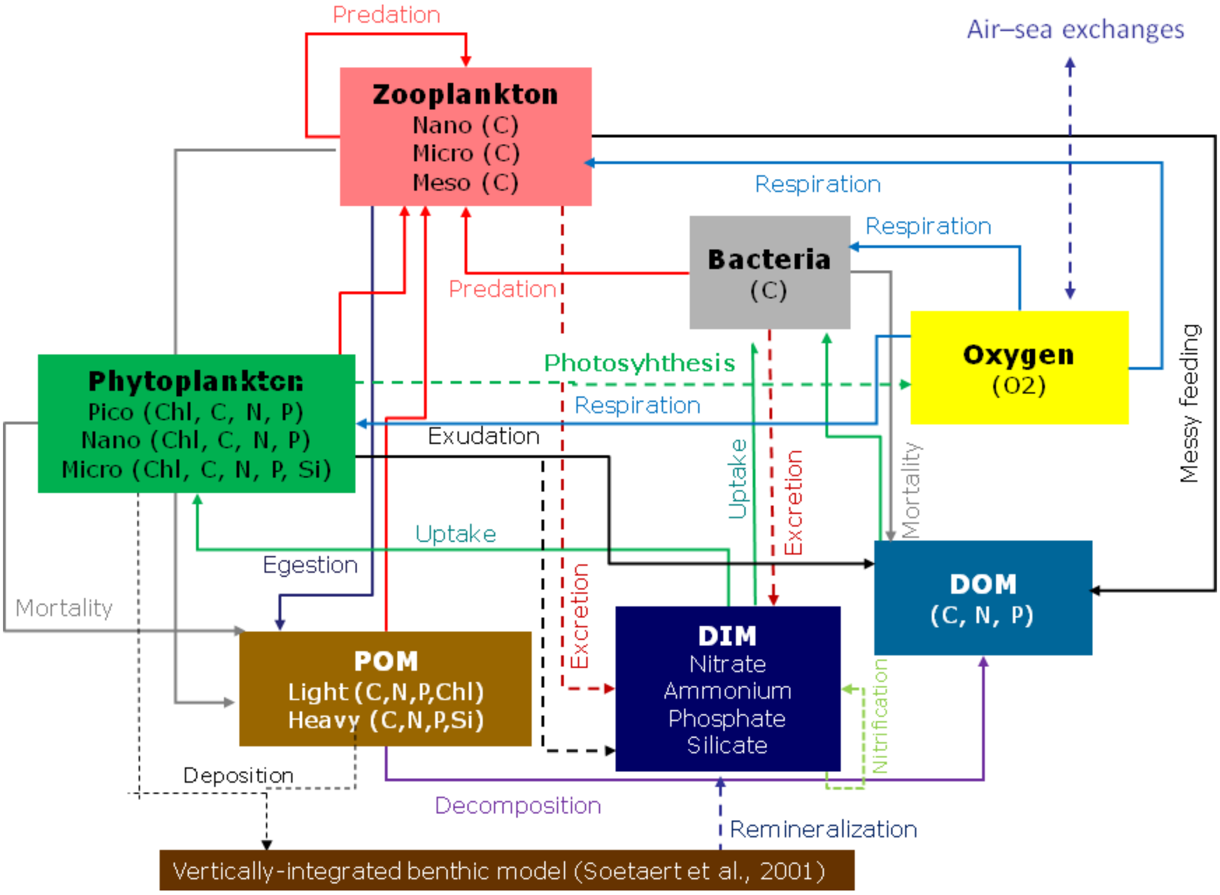

Figure S1: Schematics of the biogeochemical model Eco3M-S (from Ulses et al. 2021).

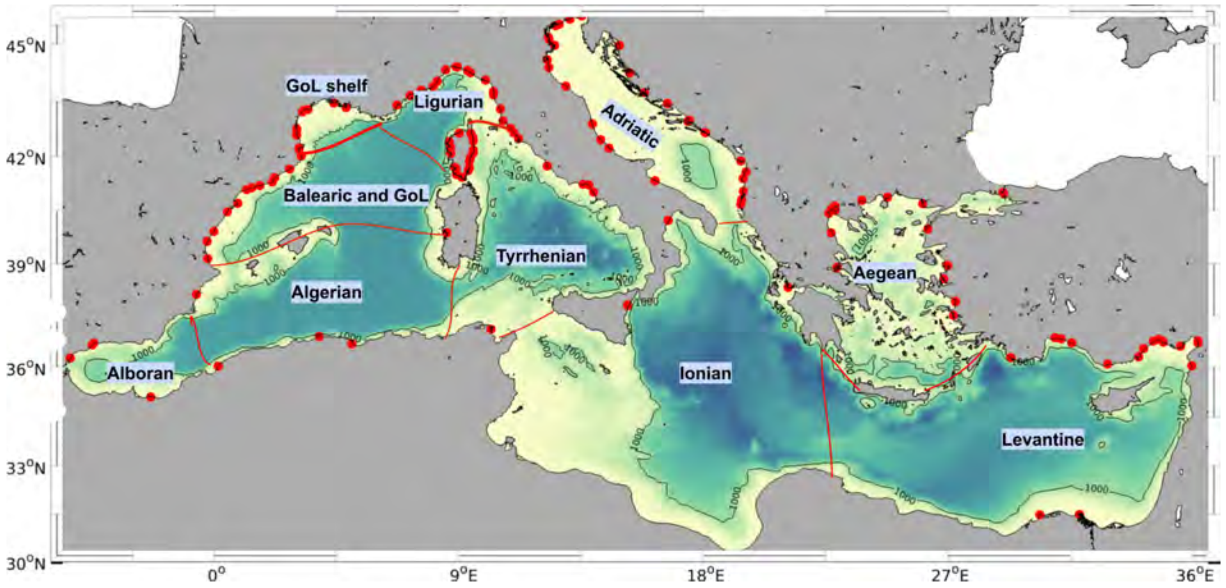

Figure S2: Subregions of the modeled Mediterranean Sea considered for the initialisation of the biogeochemical simulation. GoL: Gulf of Lion. Red dots represent river mouths, red lines indicate the limits of the sub-basins in the model.

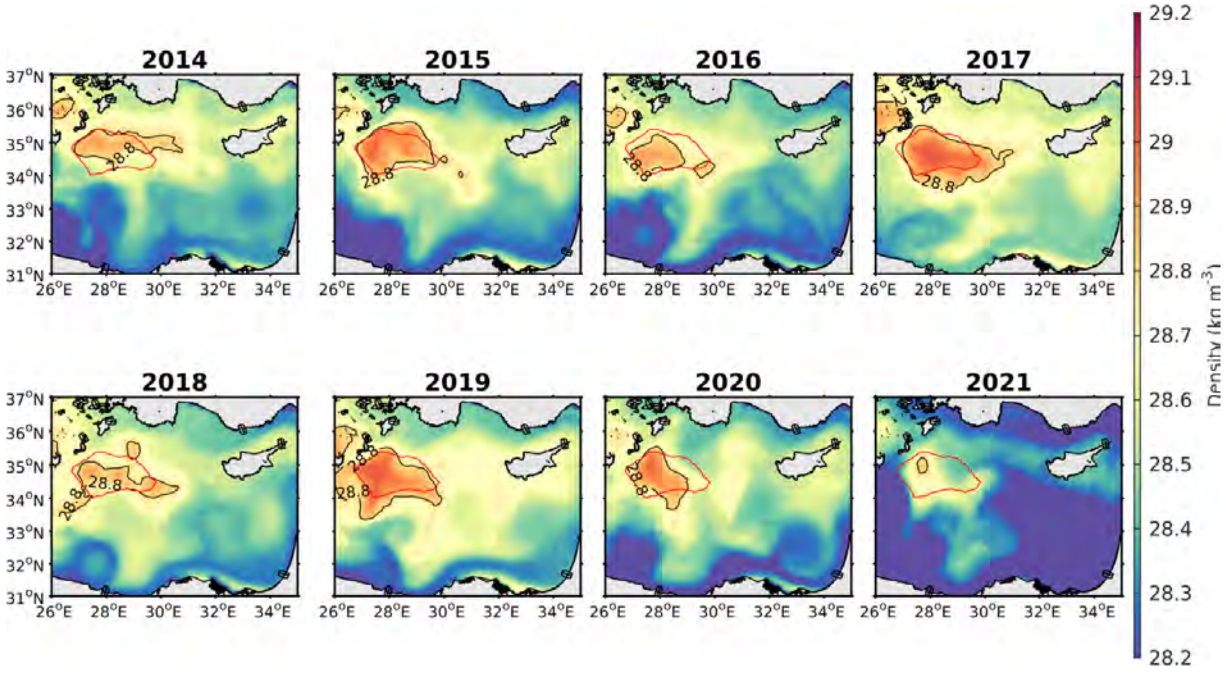

Figure S3: Surface density anomaly (kg m^{-3}) averaged over the mixing period (January-February-mid-March) from year 2014 to year 2021. The red line indicates the limit of the defined Rhodes Gyre area.

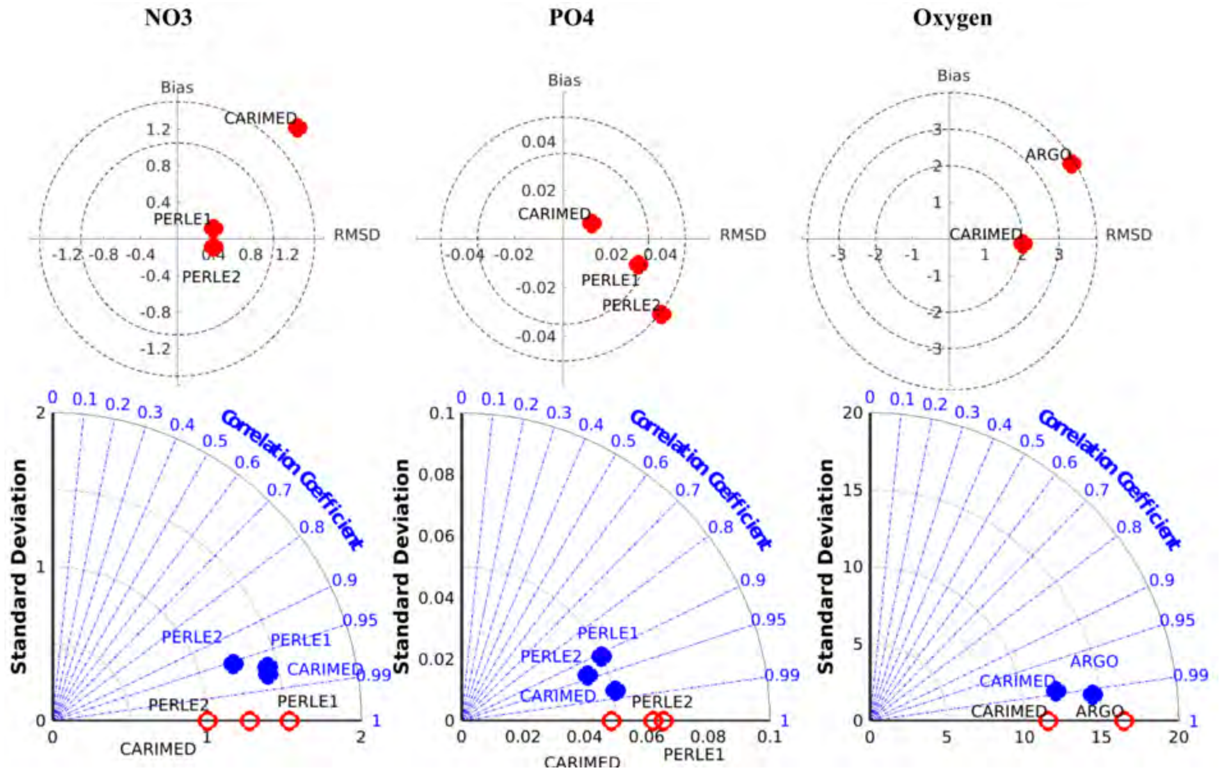

Figure S4: Statistical parameters of the modeled and observed nitrate (mmol N m^{-3}), phosphate (mmol P m^{-3}) and dissolved oxygen (µmol O$_2$ kg^{-1}) concentrations in the Levantine Basin: Top: target diagram of the bias and the~~ centered~~ RMSD, bottom: Taylor diagram with the correlation coefficient and the standard deviation. Blue ~~pots~~ dots indicate model outputs and red circles and dots observations. The angle represents the correlation coefficient.

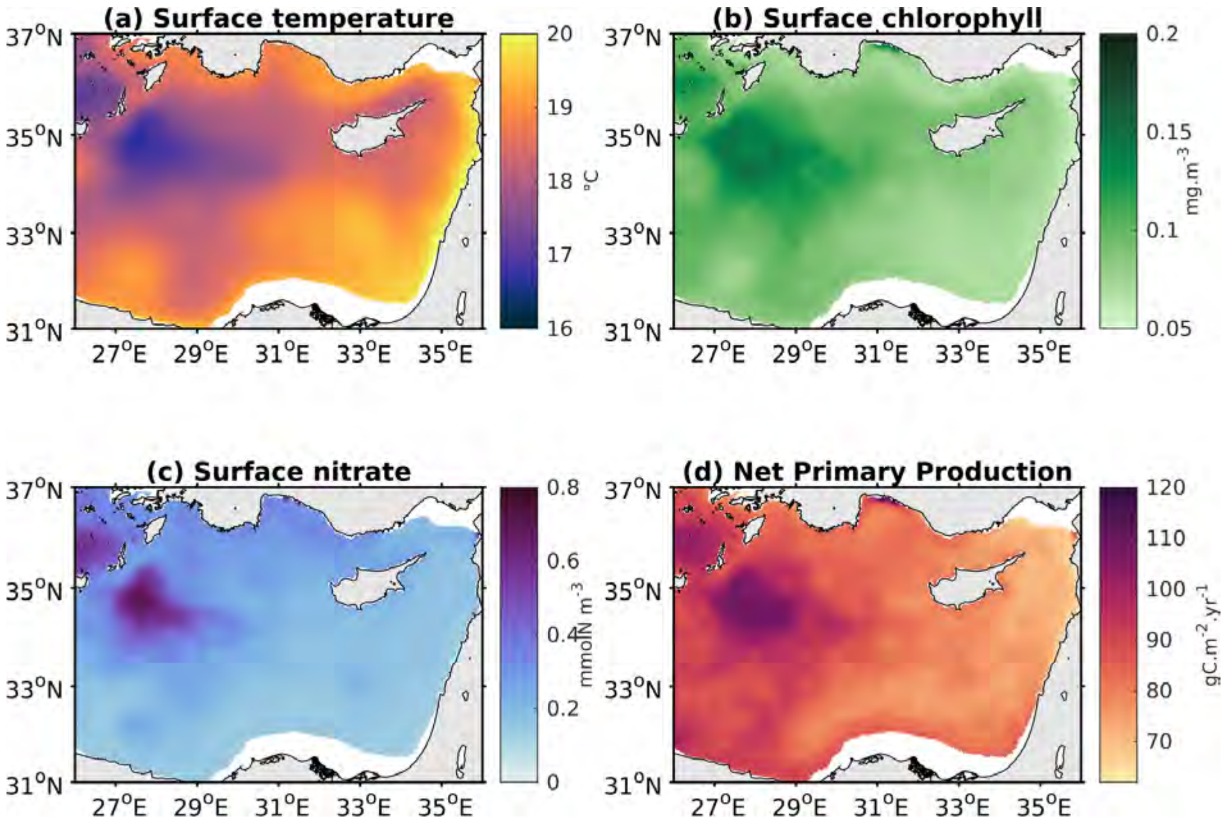

Figure S5: Modeled surface temperature (°C), chlorophyll (mg m^{-3}), nitrate (mmol N m^{-3}) concentrations and net primary production integrated over the surface (0-150 m) layer (g C m^{-2} yr^{-1}), averaged over the 2013-2020 winters (December-January-February).

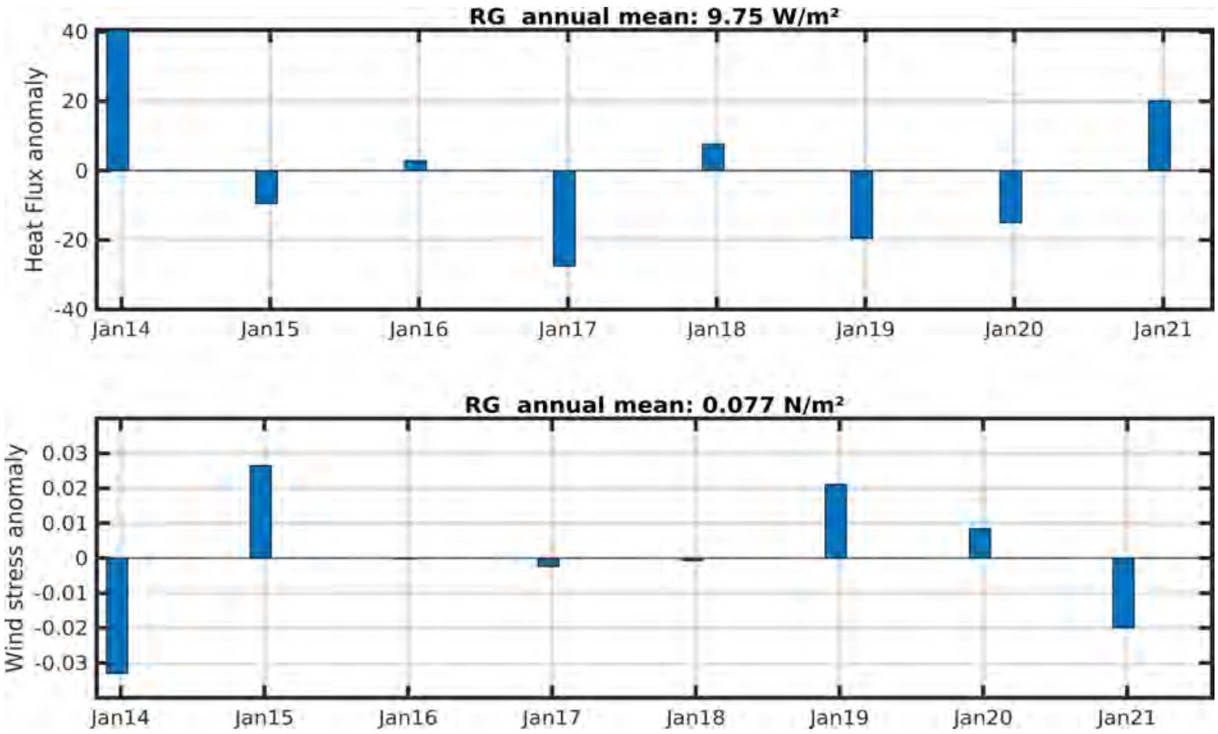

Figure S6: The seasonal surface heat flux (W m^{-2}) and wind stress (N m^{-2}) anomalies for the Rhodes Gyre (winter: December to February, spring: March to May, summer: June to August, fall: September to November).

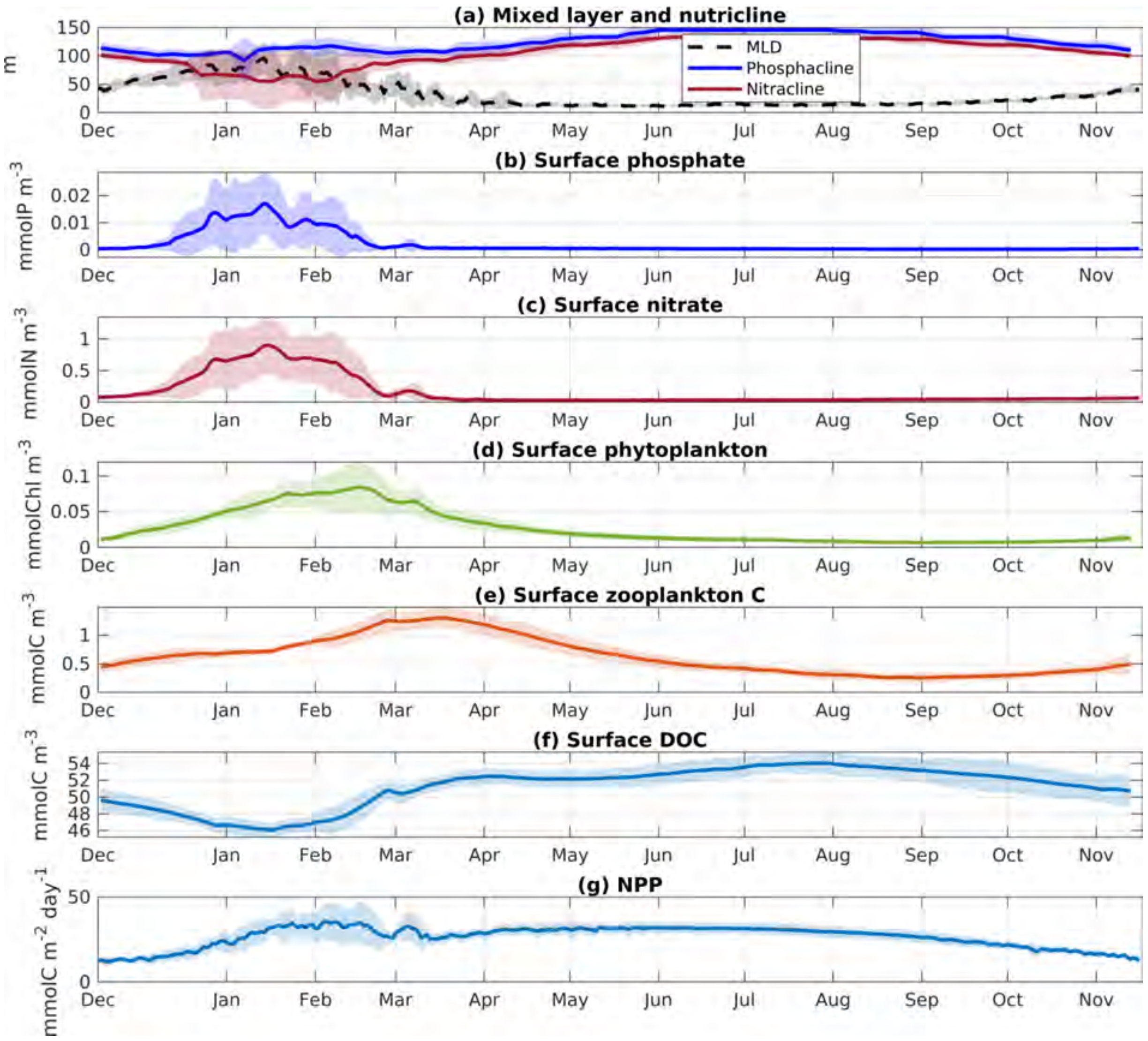

Figure S7: Seasonal cycle of (a) the mixed layer and nutricline depths, (b) surface phosphate, (c) nitrate, (d) phytoplankton, (e) zooplankton, (f) DOC concentrations and (g) NPP in the Rhodes Gyre averaged over the period 2013-20 (solid line for mean daily value, shaded areas for standard deviation).

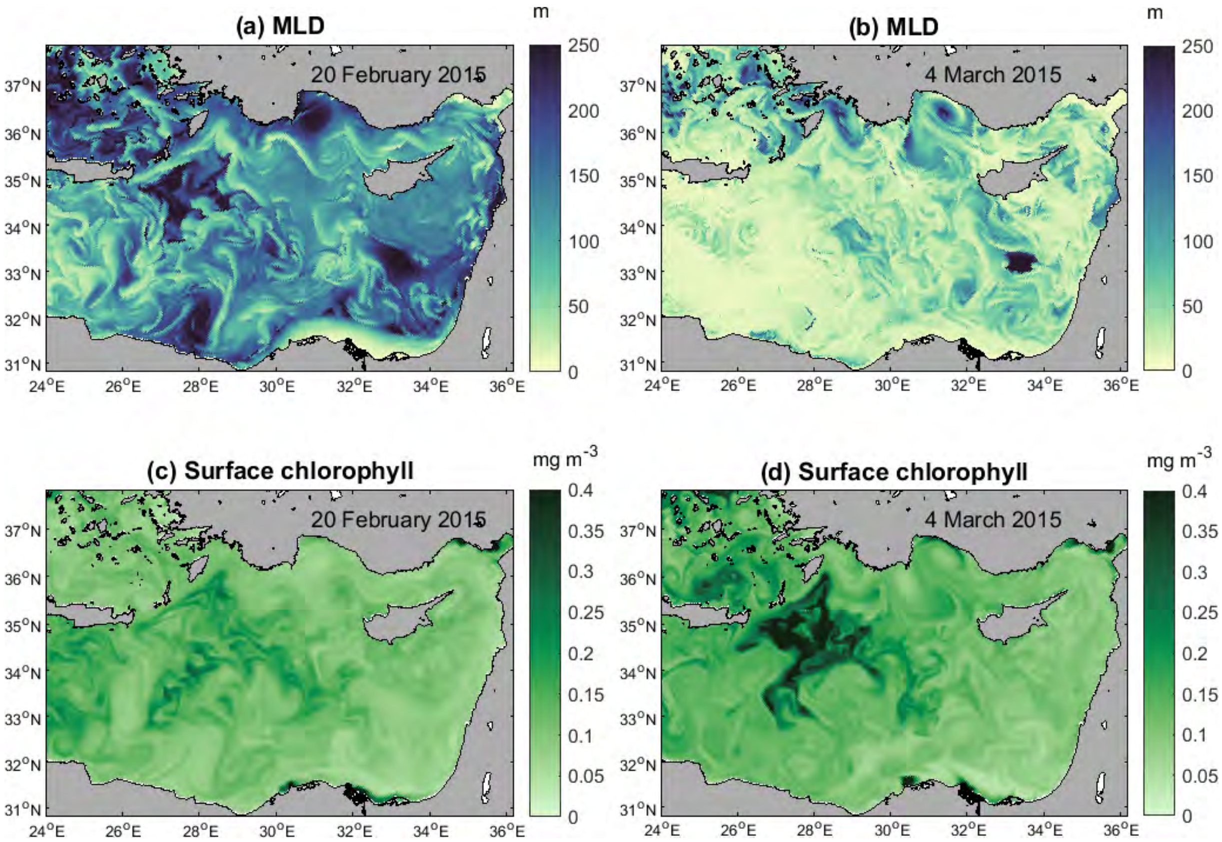

Figure S8: (a,b) Mixed layer depth (MLD, m) and (c,d) surface chlorophyll concentration (mg Chl m^{-3}), modeled for 20 February 2015 and 4 March 2015, respectively.

4.4 Conclusion

The coupled hydrodynamic-biogeochemical model has been validated for the period of our study in the Levantine Basin using satellite, float, and cruise data. Globally, the model was able to reproduce the seasonal cycle of the nutrients, chlorophyll, and dissolved oxygen in the surface and along the water column. Although the model gives some realistic spatial and temporal patterns, the comparisons of model results with observations highlight possible discrepancies in some of the biogeochemical variables, which require investigations for further improvements in the future.

The intensity of winter sea heat loss and vertical mixing affects the nutrient supply, the phytoplanktonic growth, and therefore the organic carbon dynamics. During mixing events, when the mixed layer reaches the nutriclines, nutrients are injected into the surface layer leading to the growth of phytoplankton. We show then an alternation between phytoplankton growth and punctual mixing events. The Rhodes ecosystem shows high interannual variability with enhanced nutrient supply and phytoplankton growth, and organic carbon export and production, during cold winters.

Our results showed that the Rhodes Gyre acts as a biological production area with a net community production of 31.2 ± 6.9 g m^{-2} $year^{-1}$ in the surface layer and an 8.5 ± 3.1 g m^{-2} $year^{-1}$ consumption in the intermediate layer. Part of the produced organic carbon is exported through downward or lateral export, maxima were detected during intense winter events, which is consistent with the interannual variability of the vertical and lateral organic carbon fluxes. The surface layer of the gyre acts as a source of organic carbon to the surrounding areas, and to the intermediate layer.

Finally, this analysis is constrained to the Rhodes gyre. A similar study on a larger domain such as the Levantine Basin could allow us to evaluate the fate of the organic carbon produced in the Rhodes Gyre after their export. It could also contribute to the understanding of the contribution of this gyre to the Aegean, Ionian, and Adriatic sub-basins and subsequently the Western Mediterranean Sea.

Chapter 5

Seasonal and interannual variabilities of dissolved oxygen in the Levantine Sea

Contents

In this chapter, we use the model to analyze the spatial and temporal evolution of dissolved oxygen in the surface and intermediate layers of the Levantine Basin. We start by evaluating the model performance against observational data (a more detailed comparison is described in Chapter 3). Then, based on the model results, the seasonal and interannual variabilities of dissolved oxygen are presented and the dissolved oxygen budget for the Levantine Basin is estimated. Finally, the influence of the circulation and the winter mixing on oxygen dynamics is discussed. Conclusions are given in the last section.

5.1 Introduction

Dissolved oxygen (O_2) is vital for marine life and forms an essential component of the biogeochemical cycles by controlling the oxidation and respiration of organic matter and thus the carbon and nutrient cycles in the ocean. The key factors controlling the oxygen inventory in the ocean are photosynthesis, and remineralization, the temperature and salinity-dependent oxygen solubility and the air-sea exchange, and the mixing and advective fluxes influencing the ventilation of water masses. During the recent decades, the oxygen inventory has decreased by 2 % in the Global Ocean (Schmidtko et al., 2017). Global warming leads to the reduction of oxygen solubility which explains $\sim$15 % of the current total global oxygen loss (Schmidtko et al., 2017). The remaining loss could be caused by the increase of upper ocean stratification between 1970-1990 which generated a reduction of ventilation and circulation of deep ocean layers (Helm et al., 2011).

The Mediterranean Sea is a well-ventilated basin compared to the World Ocean (Tanhua et al., 2013; Schneider et al., 2014). The low salinity Atlantic Water that enters in the surface layer through the Gibraltar Strait with nutrients and travels towards the Eastern Basin while gradually transforming into a more saline Mediterranean Water due to the air-sea heat and moisture fluxes (Malanotte-Rizzoli et al., 2014). Reaching the Levantine Basin (Fig. 5.1), the AW subducts under the Levantine Surface Water (LSW) in summer. During winter time, heat loss at the surface leads to an increase of density and deep mixing Levantine Intermediate Water (LIW) forms and then propagates between 200-600 m in the whole Mediterranean (Brasseur et al., 1996) while progressively gaining nutrients, before heading towards the Atlantic explaining the ultra-oligotrophic nature of the basin. This water impacts the deep water formation in the Adriatic Sea (Gačić et al., 2010; Lascaratos et al., 1999) and in the Western Basin (Schneider et al., 2014), playing a role of a preconditioning factor for these water formations with its high salinity. The Rhodes Gyre, a permanent cyclone in the northwest of the Levantine Basin (Sur et al., 1993; Lascaratos and Nittis, 1998; Lascaratos et al., 1999) has been identified as the main area of LIW formation.

The Levantine Basin is considered as an ultra-oligotrophic region, except the Rhodes Gyre where winter vertical convection accounts for the nutrient enrichment in the surface layer and leads to organic carbon production (Lavigne et al., 2013; D'Ortenzio et al., 2021) and export to the intermediate and surrounding areas (see Chapter 4). Previous studies have investigated the oxygen dynamics in this region (Schlitzer et al., 1991; Klein et al., 2003; Manca et al., 2004; Tanhua et al., 2013; Mavropoulou et al., 2020). The cross section in the basin during the stratified period presents an oversaturated surface water with dissolved oxygen, and an oxygen maximum (235 µmol kg^{-1}) present between 50-80 m (Kress et al., 2003; Mavropoulou et al., 2020). Whereas, the winter cross section oxygen shows an upper mixed layer with maximum dissolved oxygen concentrations of 240 µmol kg^{-1}. Deeper layers of the Levantine basin exhibit lower oxygen concentrations compared to the surface. Along the vertical profile, an oxygen minimum layer is located between 600-1200 m and present oxygen minimum concentration of 170/180 µmol kg^{-1}, it corresponds to the *Oxygen Minimum Layer* (OML) (Tanhua et al., 2013). Below this layer, the distribution of oxygen is relatively homogeneous with values slightly higher than the ones recorded for the OML (Mavropoulou et al., 2020).

Deep waters and LIW formations are at the origin of ventilation of the eastern basin. Roether and Schlitzer (1991) depicted fast ventilation in deeper layers of the Levantine Basin through the inflow of dense waters formed in the Adriatic and Aegean seas and Stratford and Williams (1997) have estimated LIW ventilation process to 10-20 years in the eastern basin. Di Biagio et al. (2022) highlighted various processes influencing the presence of oxygen maximum in the sub-surface during the stratified period. They show that it could be explained by primary or spring residual production at that layer or the downwards transport such as subduction.

Previous studies have investigated changes in oxygen distribution in the Mediterranean. The modeling study by Cossarini et al. (2021) showed a negative trend in oxygen at the surface of the Mediterranean Sea due to the surface temperature increase during the past two decades (Ozer et al., 2016, 2022; Escudier et al., 2021). A net decrease in the oxygen inventory in deeper layers (1200-2000 m) for the southeastern Levantine Basin using observational data over a 20 year period (2002 - 2020) has also been pointed out by Sisma-Ventura et al. (2021). Biogeochemical projections suggested that future warming and respiration increase will lead to the deoxygenation of the Mediterranean Sea in the surface and subsurface layers of 3-6 % at the end of the 21st century (Reale et al., 2022) with the Levantine being the most affected sub-basin. Hence, this region shows temporal and vertical changes occurring at short, annual, and decadal time scales (Kress et al., 2014; Sisma-Ventura et al., 2016) and modeling predicts further evolutions (Reale et al., 2022). However, the oxygen inventory in the eastern basin remains little known, with limited observations in time and space for the Levantine Basin.

The PERLE (Pelagic Ecosystem Response to deep water formation in the Levant Experiment) project aims at gaining insights on the biogeochemical cycles in the oligotrophic Levantine Sea, especially in the LIW formation areas. In this study, which took place in the frame of this project we quantify the variation of the oxygen inventory of the Levantine surface and intermediate waters and detail the contribution of the oxygen air-sea exchange, biological and physical processes in this variation, based on a 3D coupled hydrodynamical-biogeochemical modeling.

This paper is organized as follows: Sect. 2 describes the coupled models implemented in the Levantine Basin. In Sect. 3 we first present an assessment of the model results using in situ observations, then we investigate the seasonal and interannual dynamics of oxygen in the surface and intermediate layers for the Levantine Basin, describe its spatial variability across the basin, and finally estimate an annual budget of oxygen in the Levantine Basin. This section is followed by a discussion of the results and a conclusion in Sect. 4 and 5, respectively.

5.2 Material and Method

5.2.1 Modeling

5.2.1.1 The coupled hydrodynamic-biogeochemical model

The modeling presented in this study is based on a biogeochemical model forced offline by the outputs (temperature, salinity, three current velocities, and turbulent coeffcient) of the 3D ocean circulation model SYMPHONIE, described in detail in Marsaleix et al. (2006, 2008); Estournel et al. (2016) and Damien et al. (2017). This latter is a 3D primitive equation model with a free surface and generalized sigma vertical coordinate previously used to simulate the hydrodynamic conditions of the Mediterranean Sea: in river plumes (Estournel et al., 1997, 2001; Marsaleix et al., 1998), for dense water formation (Estournel et al., 2005; Ulses et al., 2008; Herrmann et al., 2008; Estournel et al., 2016) and shelf-slope exchanges (Mikolajczak et al., 2020).

We used the biogeochemical model Eco3M-S. It is a biogeochemical multi-nutrients and multi-plankton functional type model, representing the dynamics of the pelagic plankton ecosystem and the cycles of multiple biogenic elements: carbon, nitrogen, phosphorus, silicon and oxygen (Auger et al., 2011; Ulses et al., 2021). The plankton is classified based on their size. The phytoplankton is represented by three size classes: pico-, nano- and micro-phytoplankton (class 1, 2 and 3, respectively). The zooplankton is also represented by three size classes: nano-, micro- and meso-zooplankton (class 1, 2 and 3, respectively). The biogeochemical model was previously used to study the dynamic of the planktonic ecosystems and organic carbon (Herrmann et al., 2013; Auger et al., 2014; Ulses et al., 2016; Kessouri et al., 2018; Many et al., 2021), as well as the nitrogen and phosphorus cycles (Kessouri et al., 2017), and the oxygen dynamics(Ulses et al., 2021) in the northwestern Mediterranean Sea. The description of the oxygen compartment is detailed in Ulses et al. (2021). The rate of change of dissolved oxygen concentration due to biogeochemistry in the water column is calculated based on the following equation:

$$\begin{aligned}\frac{dDOx}{dt} = \sum_{i=1}^{3}(GPP_i - RespPhy_i)_{\gamma C/DOx} - \sum_{i=1}^{3}(RespZoo_i + RespZoo_i^{add})_{\gamma C/DOx} \\ - RespBac_{\gamma C/DOx} - Nitrif_{\gamma NH_4/DOx}\end{aligned} \quad (5.1)$$

The dissolved oxygen concentration is represented by DOx. GPP_i and $RespPhy_i$ are gross primary production and respiration, respectively, for phytoplankton group i. The $RespZoo_i$ and $RespZoo_i$ add are basal respiration and additional respiration fluxes to maintain constant N:C and P:C internal ratios, respectively, for zooplankton group i, *RespBac* is bacterial respiration and *Nitrif* nitrification. *C/DOx* and *NH4/DOx*, equal to 1 and 2, respectively, are the mole of DOx , used per mole C in respiration and needed to oxidize one mole of ammonium in nitrification as described in Grégoire et al. (2008). The flux of dissolved oxygen at the air-sea interface is governed by the following equation:

$$DOxFlux = Kw(DoxSat - DOxSurf) \quad (5.2)$$

$DOxSat$ represents the oxygen saturation and $DOxSurf$ the concentration of dissolved oxygen at the surface. The dissolved oxygen at saturation level is determined using the Garcia and Gordon (1992)equation. The oxygen saturation anomaly percentage is defined as the difference between the dissolved oxygen and the oxygen saturation :

$$(DOx - DOxSat)/DOxSat \times 100\%. \tag{5.3}$$

Kw represents the gas transfer velocity in m s^{-1}. We determined it based on the parametrization of Wanninkhof and McGillis (1999)with a cubic dependency to the 10m wind speed following the study of Ulses et al. (2021) in the north-western deep convection area, which obtained the best results for the air–sea exchange using this parametrization.

5.2.1.2 Implementation

The hydrodynamic model covers the Mediterranean Sea plus a buffer zone including the Marmara Sea and reaches 8° west in the Gulf of Cadiz. The horizontal resolution varies between 2.3 and 4.5 km north–south and west–east. The model grid reaches the Gibraltar Strait; a narrowing was conducted with a 1.3 km grid for a better representation of the exchange area between the Mediterranean and the Atlantic Ocean. The model has 60 vertical levels with closer levels near the surface. This model configuration was used to describe the surface and intermediate water circulations in the eastern Mediterranean Sea (Estournel et al., 2021). Atmospheric forcings were provided by the ECMWF model with a horizontal resolution of 1/8° using the 3 hourly fields (the direction and speed of the wind, air temperature and humidity, pressure, solar and downward long-wave radiation, and precipitation). The model accounts for a total of 142 rivers.

The biogeochemical model Eco3M-S was forced by daily fields of temperature, salinity, current and vertical diffusivity from the SYMPHONIE model. The period simulated by the hydrodynamic model runs from 1 July 2011 to 2 May 2021. The two first years were considered as a spin-up and were not considered in the analysis. We used the same 3-hour fields of wind speed and solar radiation atmospheric forcings provided by the ECMWF model as for the hydrodynamic simulation. The biogeochemical model was initialized on 15 August 2011, in 10 sub-regions, using climatological fields of in situ nutrient and dissolved oxygen concentrations from CARIMED (CARbon in the MEDiterranean Sea) database and Biogeochemical-Argo (BGC-Argo) float data over the 2011-2012 summer periods. At the river mouths, concentrations of nutrients were imposed by sub-basin using the dataset of Ludwig et al. (2010). Dissolved oxygen at river mouths was set at saturation values. In the Atlantic Ocean, nutrients were prescribed using monthly profiles from World Ocean Atlas 2009 climatology at 5.5 °W. In the Marmara Sea, in order to represent a two-layer flow regime, we imposed a daily relaxation towards a nutrient concentration of 0.24 and 1.03 mmol N m^{-3} and a phosphate concentration of 0.06 and 0.05 mmol P m^{-3} for depths above and below 15 m, respectively, based on the observations near the Dardanelles Strait from Tugrul et al. (2002). Nutrient fluxes at the water column/sediment interface have been obtained through a coupling of the biogeochemical model with a simplified version of the vertically-integrated benthic model described by Soetaert et al. (2000). The latter transforms organic matter into inorganic nutrients while consuming oxygen directly in the mineralization or indirectly through the re-oxidation of reduced substances formed upon anoxic mineralization reaction.

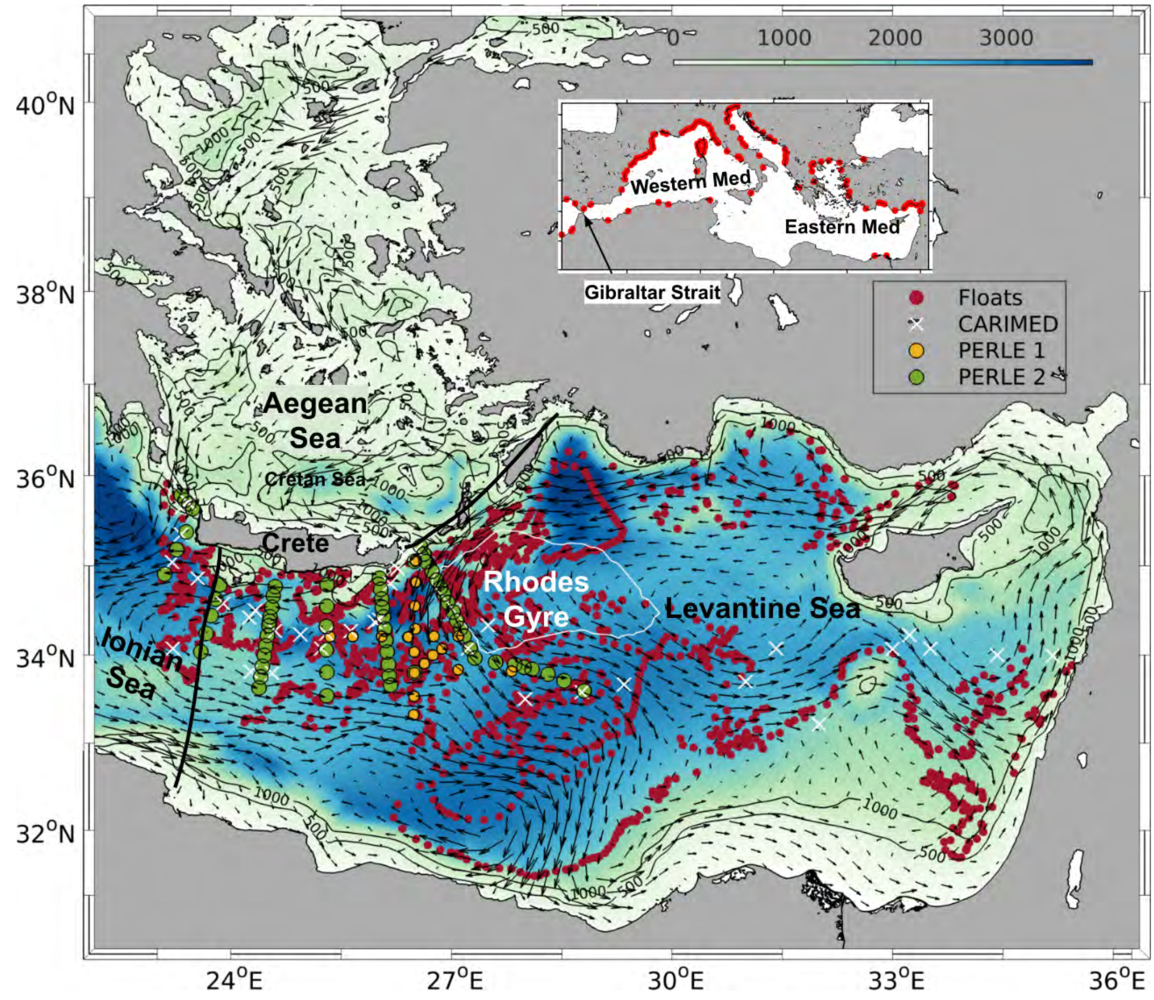

Figure 5.1: Model domain and bathymetry (m, background) in the Eastern Mediterranean. The arrows represent the surface currents averaged over the period of study, black lines delimit the basins for the budget calculation. Red, yellow, and green dots indicate BGC-Argo float PERLE-1 and PERLE-2 observations, respectively, and white crosses CARIMED cruise observations from 2013 to 2021.

5.2.1.3 Study area and budget calculation

In this study, we analyze the seasonal cycle of oxygen and we estimate the annual oxygen budget over the Levantine Basin. This study area covers 540 000 km^2. For budget calculation, the water column was divided into two layers based on the biogeochemical processes: the surface layer defined as the euphotic layer covering the surface to 150 m of depth where photosynthesis takes place, and the underlying intermediate layer from 150 to 400 m where flows the LIW. The biogeochemical term of the oxygen budget is the sum of oxygen production due to gross primary production and of oxygen consumption through nitrification and community respiration. The physical term is divided into two components: the lateral and the vertical transports due both to advection and mixing. The lateral transport represents the exchanges with the Ionian and Aegean seas. A negative lateral transport indicates a net export of oxygen towards the areas mentioned above. The oxygen inventory, biogeochemical fluxes and lateral fluxes were calculated online while the vertical transport, defined as a net flux at the layer interface, was deduced from the other terms of the budget. The budget calculation is detailed in Text S1 in Supplementary material.

5.2.2 Observations

5.2.2.1 Argo float data

In order to assess the modeled temporal and vertical evolution of the oxygen concentration, we used observations from Argo floats that were deployed in the Levantine Basin during the periods of 2013-15 and 2015-18. In particular, we present comparisons with data provided by the two BGC-Argo floats 6901528/lovbio18c and 6901764 (151 and 173 vertical profiles, respectively). Temperature and salinity measurements were also extracted to calculate the oxygen saturation at the surface. The oxygen data were downloaded from the Argo Global Data Assembly Center web portal accessible through the Coriolis database (http://www.coriolis.eu.org). Calibration of dissolved oxygen was performed at the deployment using in situ observations from 0 to 1000 m depth. The calibration and the deployment strategy are detailed in Thierry et al. (2021). The uncertainties of the measurements were estimated at $\sim$ 2-10 µmol kg^{-1} depending on the sensor (Grégoire et al., 2021).

5.2.2.2 Cruise data

During the period from October 2018 to March 2019, biogeochemical measurements were made in the context of the PERLE (Pelagic ecosystem response to dense water formation in the Levant experiment) (D'Ortenzio et al., 2021). An in situ survey was carried out in the Levantine Basin to describe the formation and dispersion of the Levantine Intermediate Water (LIW) and to assess its role in structuring the phytoplankton ecosystem in this area. In this study, we use data from two PERLE cruises: PERLE-1 (PROTEVSMED_PERLE_2018, SHOM 2018) on board R/V l'Atalante in October 2018 and PERLE-2 on board R/V Pourquoi Pas? in February-March 2019 (PERLE2, Durrieu de Madron and Conan, 2019). PERLE-1 covers the period of the pre-conditioning of LIW formation; an array of 25 profiling floats was set up. PERLE-2 covers the dense water formation period with 29 profiling oxygen floats. Stations of PERLE cruise are indicated in Fig. 5.1 (Fourrier, 2021). Winkler analyses (Winkler, 1888) was performed onboard using photometric endpoint detection to adjust the SBE43 raw data. The accuracy of the SBE43 sensor is estimated at around 2 µmol kg^{-1}.
We also used the observations included in the CARIMED database, collected during four cruises that covered the far most east and south of the basin: the Meteor M84/3 (Tanhua, 2013), Hotmix, MEDSEA (Ziveri and Grelaud, 2015)and MSM72 (Hainbucher et al., 2019)cruises conducted during the period between 2011-2018. The seawater was collected using Niskin bottles from the surface to 4600 m of depth using an SBE43 oxygen sensor for the oxygen concentrations followed by the modified Winkler potentiometric method Martínez-Pérez et al. (2017). The spatial coverage of the datasets is shown in Fig. 5.1.

5.3 Results

5.3.1 Assessment of the model

An assessment of the hydrodynamic simulation was performed by Estournel et al. (2021) who showed the capacity of the model to reproduce the observed hydrology, as well as the surface and intermediate circulations. In Habib et al. (submitted), the results of the biogeochemical model were evaluated against satellite, cruise, and Argo float data, showing correct spatial and temporal modeled variabilities of chlorophyll, dissolved inorganic nutrients, and dissolved oxygen. Here, we further assess the dissolved oxygen dynamics by providing supplementary comparisons with PERLE cruise and Argo float data.

5.3.1.1 Comparaison with BGC-Argo float data

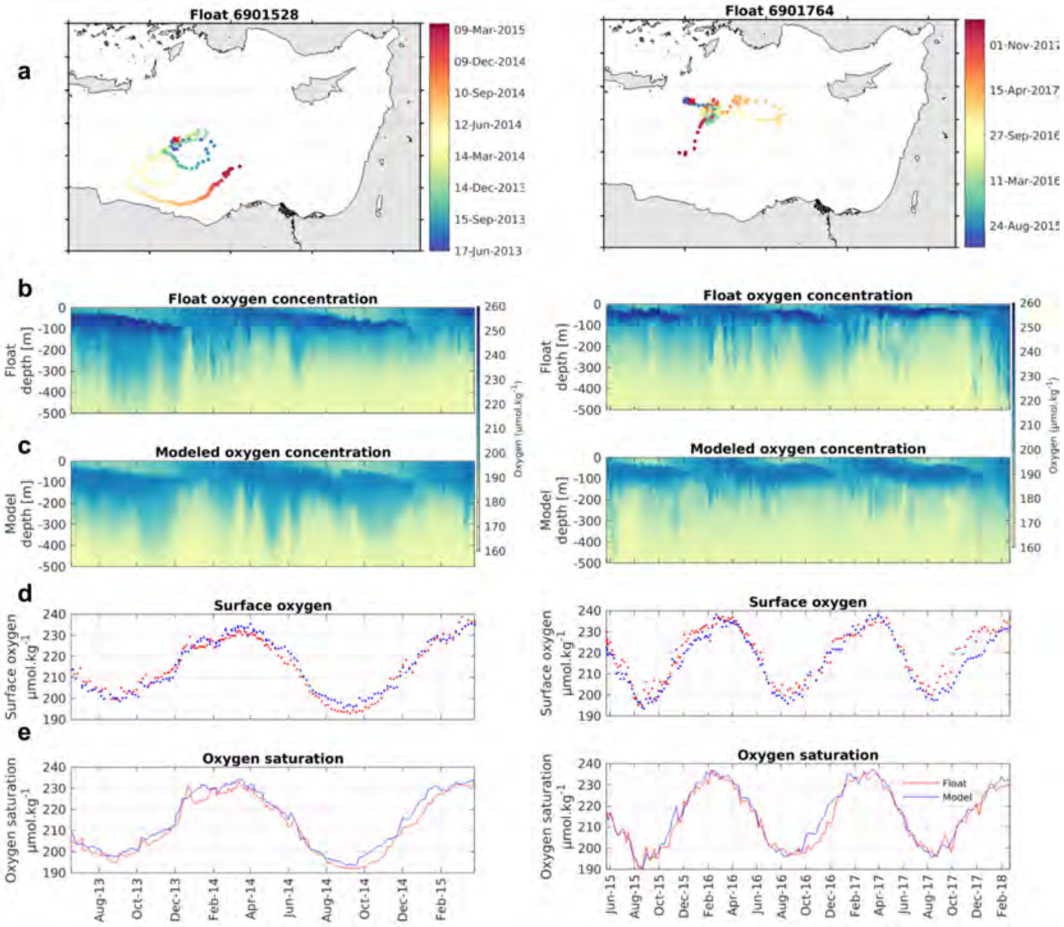

Figure 5.2: From top to bottom: (a) trajectory of the BGC-Argo floats with deployment position (red cross); Hovmöller diagrams of oxygen concentration (µmol O_2 kg-1) from (b) float data and (c) model outputs; (d) surface oxygen concentration (µmol O_2 kg-1) from the float data (red dots) and the model (blue dots); (e) oxygen saturation (µmol O_2 kg-1) from the float data (red) and the model (blue) for the period of float life.

Figure 5.2 represents the temporal evolution of vertical profiles of oxygen from the model and float observations for the first 500 m, as well as the surface oxygen concentration and oxygen saturation, along two float trajectories covering two different periods. We chose these floats because of their spatiotemporal extension, both floats cover stratification and mixing periods in two different locations. The observations and the model outputs exhibit the same seasonal variability. At the end of fall, the oxygen saturation begins increasing progressively and reaches maximum values in March; it is minimum at the end of summer (Fig. 5.2d-e). When comparing modeled surface oxygen concentrations and dissolved oxygen at saturation level against observations, the model shows high correlation coefficients of 0.97 and 0.98 (*p-value* < 0.01), respectively, for Float 6901528, and 0.95 and 0.98 (*p-value* < 0.01), respectively for Float 6901764. The biases for the surface oxygen of - 0.29 µmol O_2 kg^{-1} and - 3.9 µmol O_2 kg^{-1} for the two floats indicate an underestimation of the oxygen in the surface visible in Fig. 5.2b-c. The low values of RMSD (Root Mean Square Difference) for the surface oxygen concentration (3.27 µmol O_2 kg^{-1} and 5.37 µmol O_2 kg^{-1} for floats 6901528 and 6901764, respectively) and for the oxygen saturation (3.41 µmol O_2 kg^{-1} and 3.01 µmol O_2 kg^{-1} for floats 6901528 and 6901764, respectively) show the accuracy of the model to reproduce their concentrations.

The general features across the water column observed using the BGC-Argo floats were respected by the model with (i) the formation of a subsurface oxygen maximum in March/April when the water column restratified permanently, (ii) a deepening of oxygen maximum until December and (iii) the erosion of the oxygen maximum followed by a homogenization of the mixed layer when vertical mixing intensifies (Fig. 5.2b-c). The modeled maximum oxygen in the subsurface layer is underestimated by $\sim$ 10 µmol kg^{-1} by the model along the trajectory of both floats (bias = - 10 µmol kg^{-1}, RMSD= 10.9). As for the subsurface oxygen maximum depth, it is well located in the model compared to the observations. Further deep, the concentration and the localization of the OML observed from floats 6901528 and 6901764 are well reproduced by the model: in both data and model, the OML is localized between 300 and 400 m and has a magnitude of 180 µmol kg^{-1} (Fig. 5.2). Overall, the simulation reproduces correctly the spatial and temporal variability of the oxygen observed at the surface and the water column for both floats.

5.3.1.2 Comparison with cruise data

The comparisons of the modeled dissolved oxygen with in situ data from PERLE-1, PERLE-2 and CARIMED databases are shown in Fig.5.3. This comparison is completed with statistical metrics computed across the water column (indicated on Fig. 5.3).

The magnitude and variation of oxygen concentrations are well reproduced in the different water layers. The model reproduces the presence of a subsurface maximum reaching 230 µmol O_2 kg^{-1} at 70 m during the fall PERLE-1 cruise (Fig. 5.3a). Over the CARIMED cruise periods, it is located at a 50 m depth in the model outputs and shows high variability in the observations averaged over the CARIMED dataset during the stratification period (Fig. 5.3c). The maximum concentrations (230 µmol O_2 kg^{-1}) are located at the surface during winter PERLE-2 cruise and CARIMED observations collected during the mixing period, for both model and observations (Fig. 5.3b and d) Modeled dissolved oxygen concentrations below 100 m generally stand within the range of the observed values, except for the comparison with

PERLE-2 observations for which the model shows higher values all over the water column. On the other hand, the model presents smaller values (less than 5 %) of oxygen below 150 m compared to the CARIMED dataset during the stratification period. Between 200 and 500 m depth, the model shows a SD (standard deviation) of 5.2 µmol O_2 kg^{-1}, while the CARIMED data shows an SD of 7.1 µmol O_2 kg^{-1} potentially reflecting differences in the sampling methods between each campaign of the dataset or a spatial heterogeneity not sufficiently taken into account by the model.

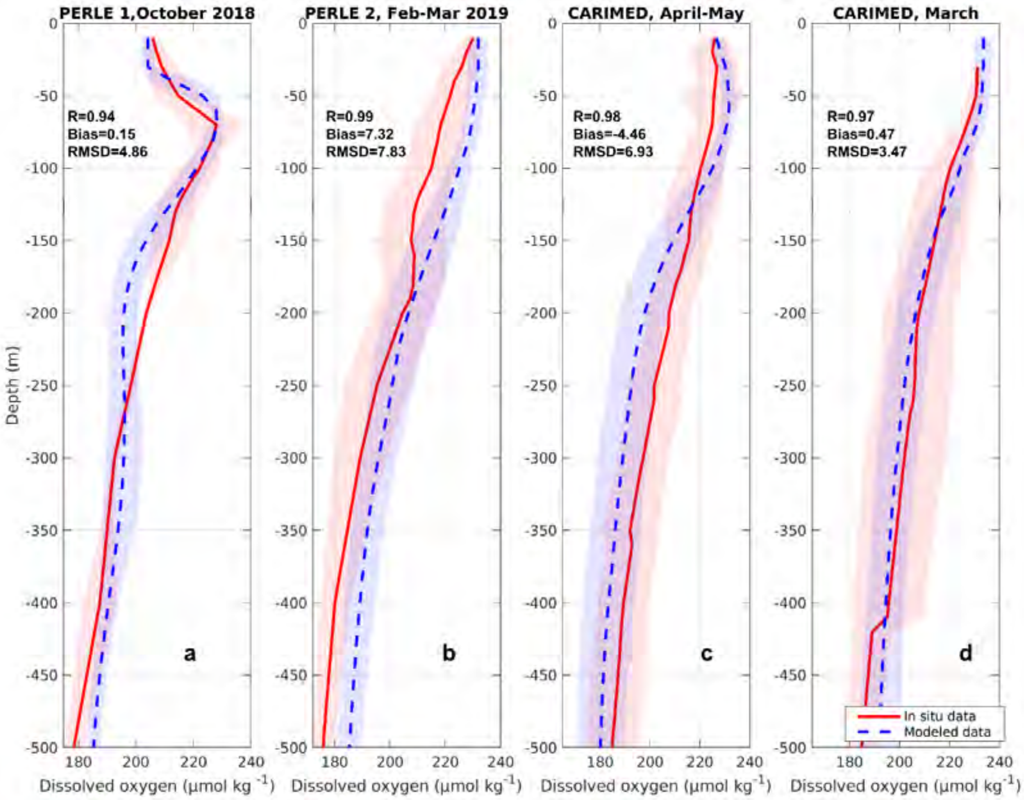

Figure 5.3: Comparison between the mean modeled (blue dotted line) and (a) PERLE-1 (10-20 October 2018), (b) PERLE-2 (25 February-16 March 2019), and CARIMED (2011-2018) (c) during stratification and (d) during mixing period observed (red solid line) profiles of the dissolved oxygen concentration (µmol O_2 kg^{-1}). The shaded areas represent the standard deviation. Coefficient correlation, bias and RMSD between model outputs and observations are indicated on figures.

The metrics confirm the good agreement between the modeled and the observed dissolved oxygen, for all the cruises. The model and PERLE-1, PERLE-2 and CARIMED data are significantly correlated (correlation coefficient of 0.94, 0.99, 0.97 and 0.98, respectively). The RMSD are 4.5, 7.8, 3.5 and 6.9 µmol O_2 kg^{-1}, respectively, and biases 0.2, 7.3, 0.5 and -4.5 µmol O_2 kg^{-1} , respectively.

5.3.1.3 Atmospheric forcing and vertical mixing

Figure 5.4 presents the time series of the modeled heat air-sea flux, wind stress, mixed layer depth (MLD), and surface temperature, spatially averaged over the Levantine Sea, from December 2013 to May 2021. A seasonal hydrodynamic cycle for the surface layer is clearly visible. During fall, a strong sea heat loss, induced by the air temperature decrease and the intensification of northern winds, weakens the stratification and the mixed layer begins deepening progressively (Fig. 5.4a-c). The surface temperature strongly decreases (Fig. 5.4d). The sea heat loss events continue in winter, accompanied by minimum surface temperature and a gradual increase in the mixed layer depth. The maximum depth is reached during February-March, the seven-year averaged mixed layer maximum is 110 m (Table S1, Supplementary material). From April, the sea surface starts gaining heat and the surface temperature is increasing (Fig. 5.4a and 5.4d). The mixed layer abruptly shallows and shows a large variation of its depth for the period of early spring, in response to the passage of continental winds over the surface and a localized sea heat loss. The frequency of intense wind events starts decreasing in late spring/summer (Fig. 5.4b). The surface temperature reaches maximum values around 28 °C in August (Fig. 5.4d) and a thin ML of 10 m depth settles until October.

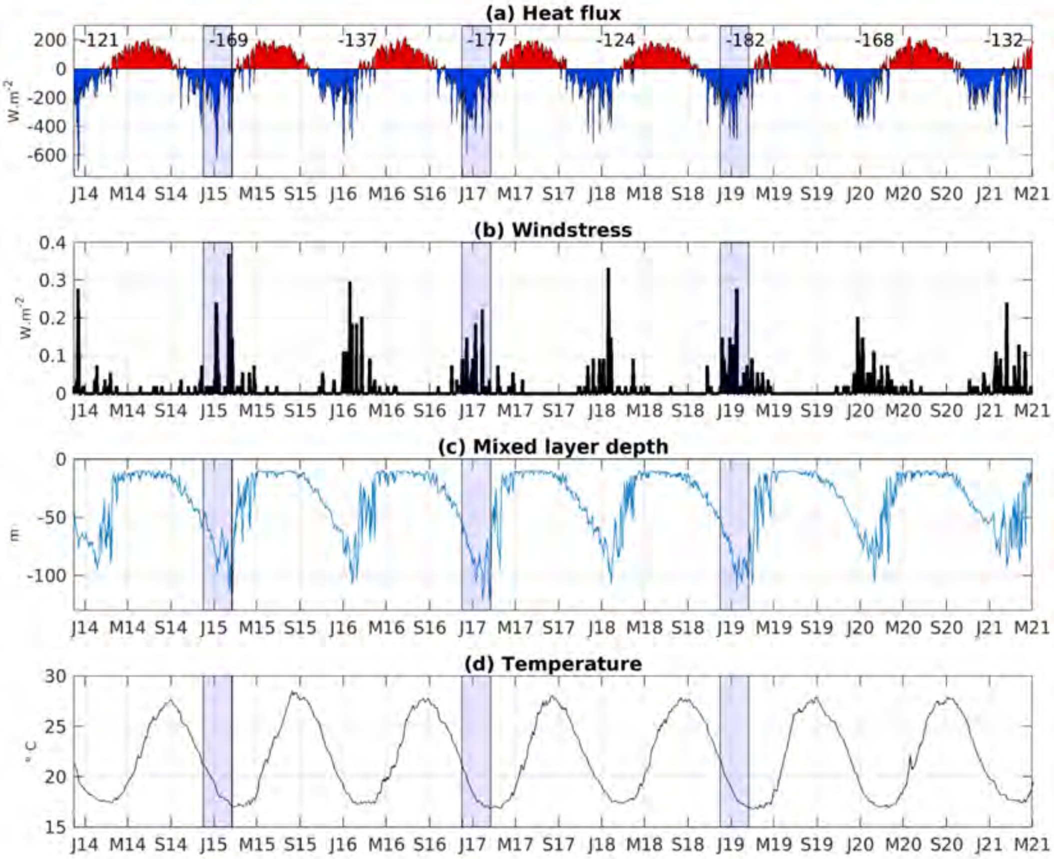

Figure 5.4: Time series of modeled (a) air-sea heat fluxes (W m^{-2}), (b) wind-stress (W m^{-2}), (c) mixed layer depth (m), (d) surface temperature (°C) averaged over the Levantine Sea. The mean winter (December-January-February) sea heat loss is indicated in (a).

Beyond the seasonal pattern, the surface heat flux and the mixed layer present interannual variability. The winter heat loss is higher than the seven-year mean value of 152 ± 25 W m^{-2}, for winters 2014-15, 2016-17, 2018-19, and 2019-20 (heat loss of 169, 177, 182, and 168 W m^{-2}, respectively, Table S1, Supplementary material). The mixed layer depth shows higher values than the mean value of 108 ± 11 m during the winters 2014-15, 2016-17, and 2018-19 (MLD of 123, 121, and 112 m, respectively, Table S1, Supplementary material). Based on the winter heat flux and maximum spatially averaged MLD, the years were classified as mild and cold winter years. Years with both winter heat loss and maximum MLD above the seven-year mean, i.e. 2014-15, 2016-17, and 2018-19, are considered cold years. Mild winter years possess a heat loss smaller than 152 W m^{-2} and are associated with shallower MLD than 108 m. The mild winter years are 2013-14, 2015-16, 2017-18, and 2020-21.

5.3.2 Variability of the dissolved oxygen

5.3.2.1 Seasonal oxygen dynamic in the surface and intermediate layers

Autumn was defined from September to November. During this period, oxygen solubility begins increasing (Fig. 5.5b) with the decrease of the surface temperature (Fig. 5.4d) following heat loss events. The gradual deepening of the mixed layer inducing the mixing of surface O_2 poorer waters with deeper O_2 enriched water (Fig. 5.8c) favors an increase in the surface oxygen concentrations (Fig. 5.5b). The increase in oxygen saturation is stronger than the increase in surface oxygen concentration and the Levantine Sea becomes, in October, to be undersaturated in oxygen compared to the atmosphere and absorb atmospheric oxygen at the surface. Over the whole fall period, which represents a transition period, the mean fall air-sea flux remains weak (0.005 mol O_2 m^{-2} $month^{-1}$, Fig. 5.7a). The transport fluxes in the surface and intermediate layers generally show low values for the fall season (Fig. 5.5e-g, Fig. 5.6c-e), with a mean fall value for the total transport of -0.01 and 0.06 mol O_2 m^{-2} $month^{-1}$, respectively (Fig. 5.7a and 5.7c). In the surface layer, lateral transport shows an input of 0.48 mol O_2 m^{-2} $month^{-1}$ from the Ionian Sea and a loss of 0.30 mol O_2 m^{-2} $month^{-1}$ towards the Aegean Sea (Fig. 5.7b). The fluxes are opposite in the intermediate layer which loses oxygen through lateral export towards the Ionian Basin (- 0.11 O_2 mol m^{-2} $month^{-1}$) and gains 0.07 mol O_2 m^{-2} $month^{-1}$ of oxygen from the Aegean Sea (Fig. 5.7d). Regarding the vertical transport, 0.19 mol O_2 m^{-2} $month^{-1}$ of oxygen are exported from the surface layer to the intermediate layer on average (Fig. 5.7b). Oxygen consumption by community respiration (CR) and nitrification dominate the oxygen production by gross primary production (GPP) across the water column (Fig. 5.5d, 5.6b, 5.9). Surface and intermediate layers show a fall mean net consumption of oxygen of -0.24 mol O_2 m^{-2} $month^{-1}$ (Fig. 5.7a) and - 0.19 O_2 mol m^{-2} $month^{-1}$ (Fig. 5.7c), respectively. Thus, the Levantine Sea loses oxygen in the surface layer mostly through biogeochemical processes, with an oxygen inventory decrease of 0.25 O_2 mol m^{-2} $month^{-1}$.

Over the winter period (December-January-February), the vertical mixing increases and reaches the nutricline (not shown). The supply of inorganic nutrients into the surface layer favors primary production and phytoplankton growth near the surface (Fig. 5.8b and 5.9a) leading to a switching from a net consumption to a net production of oxygen from January (Fig. 5.5d). The winter mean biogeochemical flux amounts to 0.03 mol O_2 m^{-2} $month^{-1}$, which represents a contribution to only 3 % of the total O_2 gain (air-sea flux plus biogeochemical flux) in this layer (Fig. 5.7a). The air-sea flux cumulated during this period that amounts to 0.9 mol O_2 m^{-2} $month^{-1}$ remains the highest contributor of this total gain. This high atmospheric oxygen uptake can be explained by the high oxygen saturation level, following the decrease in surface temperature (Fig. 5.4d) due to cooling and winter mixing, compared to the surface oxygen concentration which is influenced by the mixing with O_2 -poorer intermediate waters (Fig. 5.5b and 5.8c). This accentuates the under-saturation of the Levantine Basin compared to the atmosphere and thus the absorption of atmospheric oxygen, especially during intense wind events where air-sea flux exceeds 50 mmol O_2 m^{-2} day^{-1} (Fig. 5.5c). The lateral transport is characterized by an increasing net inflow of oxygen at the Ionian boundary and an increasing outflow at the boundary with the Aegean Sea (Fig. 5.5g). The vertical transport shows a clear downward export of oxygen towards the intermediate layer, during intense wind and mixing events (Fig. 5.4b-c, Fig. 5.5f). The winter mean total transport represents a loss of 0.37 mol O_2 m^{-2} $month^{-1}$ (Fig. 5.7a) resulting from a net downward flux of 0.74 mol m^{-2} $month^{-1}$ from the surface layer, a loss of O_2 through lateral transfer of 1.29 mol O_2 m^{-2} $month^{-1}$ towards the Aegean Sea and a lateral gain of 1.66 mol O_2 m^{-2} $month^{-1}$ from the Ionian Sea (Fig. 5.7b). The sum of the different processes in this layer indicate an increase of 0.57 mol O_2 m^{-2} $month^{-1}$ in the oxygen inventory. The intermediate layer also shows an increase in the oxygen inventory with a winter mean gain of 0.26 mol O_2 m^{-2} $month^{-1}$.

The biogeochemical flux in this layer is generally marked by an abrupt decrease when the vertical mixing intensifies (Fig. 5.4c and 5.6b). The lateral exchanges show the same pattern as in the surface layer, with an increasing net inflow from the Ionian Sea and an increasing outflow towards the Aegean Sea, but with a 2 times weaker intensity (Fig. 5.6e). Peaks of exchanges are visible during intense wind-induced mixing episodes. Over the winter period, the net outflow of oxygen towards the Aegean Sea exceeds the net inflow of oxygen from the Ionian by a factor of 2 (Fig. 5.7d). However, due to the high downward flux the net physical transfer is positive and dominates the net biogeochemical consumption (Fig. 5.7c).

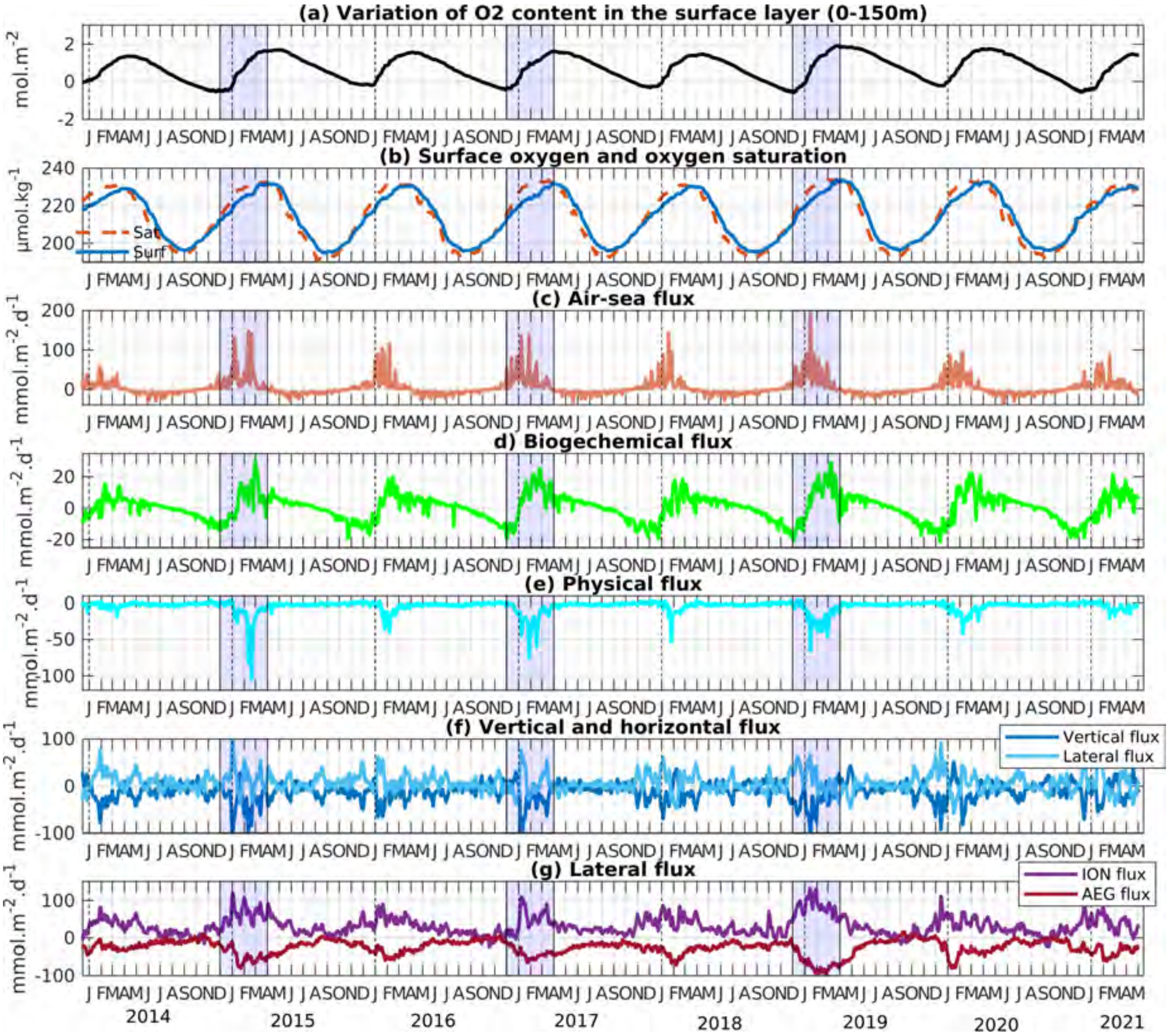

Figure 5.5: (a) Variation of the dissolved oxygen inventory (mol m^{-2}) from 1st December 2013 and time series of (b) surface oxygen concentration (blue) and oxygen saturation (orange) (µmol O_2 kg-1), (c) air-sea flux (mmol O_2 m^{-2} d^{-1}), (d) biogeochemical flux (mmol O_2 m^{-2} d^{-1}), (e) total vertical and horizontal transport (mmol O_2 m^{-2} d^{-1}), (f) vertical flux (light blue) and lateral (dark blue) flux (mmol O_2 m^{-2} d^{-1}), and detailed lateral flux at the boundary with the (g) Ionian (purple) and Aegean (red) seas (mmol O_2 m^{-2} d^{-1}), in the surface (0-150 m) layer and averaged over the Levantine Basin.

During spring, from early March to the end of June, the biogeochemical flux shows maximum magnitudes during the phytoplankton bloom that can occur in early March, decreases first rapidly just after the bloom and then more slowly (Fig. 5.5d, 5.8b, 5.9). The spring mean reaches 0.2 mol O_2 m^{-2} month^{-1}. The O_2 production in the surface layer favors the increase of surface oxygen concentration reaching 230 µmol kg^{-1} in April (Fig. 5.5b), the latter surpassing the oxygen saturation. The Levantine Basin then becomes a source of oxygen for the atmosphere (Fig. 5.5c). We estimate a net release of 0.09 mol O_2 m^{-2} month^{-1} of oxygen to the atmosphere during the whole spring period (Fig. 5.7a). The vertical and lateral fluxes decrease compared to the previous season. The water column restratifies (Fig. 5.4c) leading to a 61 % decrease in the downward export of O_2 towards the intermediate layer (0.29 mol O_2 m^{-2} $month^{-1}$). The lateral exchanges at the two lateral boundaries present the same sign than in winter but with lower rates (Fig. 5.5g and 5.7b, outflow: 1.07 mol O_2 m^{-2} $month^{-1}$, inflow: 1.25 mol O_2 m^{-2} $month^{-1}$). Finally, the oxygen inventory in the surface layer slightly decreases by 0.003 mol O_2 m^{-2} $month^{-1}$ during spring due to the out-gassing of oxygen to the atmosphere, the downward transport and the lateral export towards the Aegean. The intermediate layer also displays a decrease in the rate of the cummulated lateral and vertical flux by 18 and 45 %, respectively (Fig. 5.6e and 5.7d). The vertical transport of oxygen at 400 m indicates an export of 0.1 mol m^{-2} $month^{-1}$ towards the deeper layer. The oxygen consumption by the planktonic ecosystem through respiration and nitrification decreases (Fig. 5.6b) and contributes to a loss of 0.18 mol O_2 m^{-2} $month^{-1}$ of oxygen (Fig. 5.7c). The balance between physical and biogeochemical fluxes leads to a slight decrease of the oxygen inventory by 0.01 mol m^{-2} $month^{-1}$.

During summer (July-August-September), the surface oxygen concentration continues to present higher values than the oxygen saturation (Fig. 5.5b), which leads to a continuous out-gassing of O_2 (Fig. 5.5c) and a cumulative loss of 0.32 mol O_2 m^{-2} $month^{-1}$ (Fig. 5.7a). The biogeochemical fluxes are weak both in the surface (Fig. 5.5d) and intermediate (Fig. 5.6b) layers. The cumulative summer flux amounts to 0.05 and -0.13 mol O_2 m^{-2} $month^{-1}$ in the surface and intermediate layers, respectively. In addition, the surface Levantine Basin still exports O_2 towards the Aegean Sea (0.4 mol m^{-2} $month^{-1}$) and the intermediate layer (0.13 mol m^{-2} $month^{-1}$) and receives O_2 from the Ionian Sea (0.53 mol m^{-2} $month^{-1}$) but at lower rates (Fig. 5.5g and 5.7b). The Levantine Basin intermediate layer acts as a source of oxygen to both the Ionian (36 % of the lateral transport) and the Aegean (64 %) seas during the summer period. Finally, the oxygen inventory decreases by 0.32 and 0.05 mol m^{-2} $month^{-1}$ in the upper and intermediate layers, respectively.

5.3.2.2 Interannual variability of the dissolved oxygen fluxes in the surface and intermediate layers

All years display a similar seasonal oxygen cycle described in the Sect. 5.3.2.1. However, high fluxes and higher variation in the oxygen inventory are clearly visible for cold years (2014-15, 2016-17, 2018-19). For example, the O_2 inventory variation reaches 1.64 mol O_2 m^{-2} during winter 2014-15 while it is 1.33 mol O_2 m^{-2} for winter 2013-14 (Fig. 5.5a). Regarding the biogeochemical flux they exceed 20 mmol m^{-2} day^{-1} during the phytoplankton bloom occurring during the cold winter years (Fig. 5.5d). The lateral and vertical transports of dissolved oxygen at the interfaces of the surface layer show peaks of oxygen inflow from the Ionian Sea, outflow towards the Aegean Sea and downward export into the intermediate layer exceeding 100, 75 and 100 mmol O_2 m^{-2} $year^{-1}$, respectively, during the cold winters (Fig. 5.5f-g). The cold years are also characterized by higher O_2 air-sea fluxes during winter (Fig. 5.5c).

In the intermediate layer, cold winter years also present higher O_2 winter fluxes and oxygen inventory variation compared to mild years (Fig. 5.6). Biogeochemical fluxes indicate important negative peaks exceeding 10 mmol m^{-2} day^{-1} during cold winter years (Fig. 5.6b). Physical fluxes also are marked by a higher magnitude (Fig. 5.6c-f). As found in the surface layer, higher lateral oxygen exchanges occur during the cold winters, with peaks ranging between 37 and 68 mmol m^{-2} day^{-1} at the boundary with the Aegean Sea and between 34 and 58 mmol m^{-2} day^{-1} at the boundary with the Ionian Sea. The downward fluxes were also higher during cold years. Along with the seasonal internal variation, an increasing trend in the inventory is visible from 2013-14 to 2018-19, followed by a decreasing trend until the end of the study period (Fig. 5.6a).

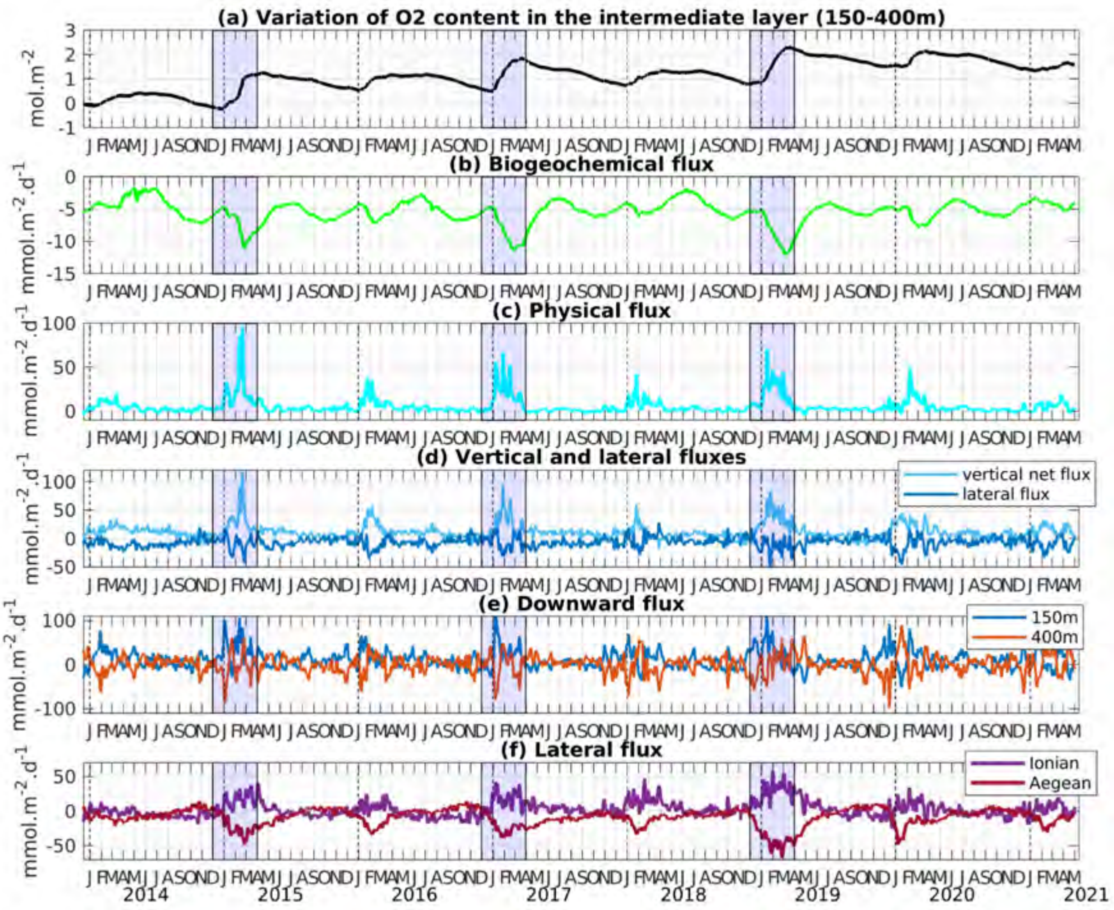

Figure 5.6: Time series of (a) variation of the dissolved oxygen inventory (mol m^{-2}) in the 150-400 m layer, (b) biogeochemical flux, (c) the total vertical and horizontal transport (mmol m^{-2} d^{-1}), (d) downward flux (light blue) and lateral flux (dark blue) , and (g) The lateral Ionian (purple) and Aegean fluxes (red) (mmol m^{-2} d^{-1}) in the intermediate layer and averaged over the Levantine Basin.

5.3.2.3 Annual oxygen budget in the surface and intermediate layers

The annual budget of the Levantine Basin was calculated in the surface (0-150 m) and intermediate layers (150-400 m) for the seven year period from December 2013 to December 2020 (Fig. 5.10), and for each of the seven studied years (Fig. 5.11).

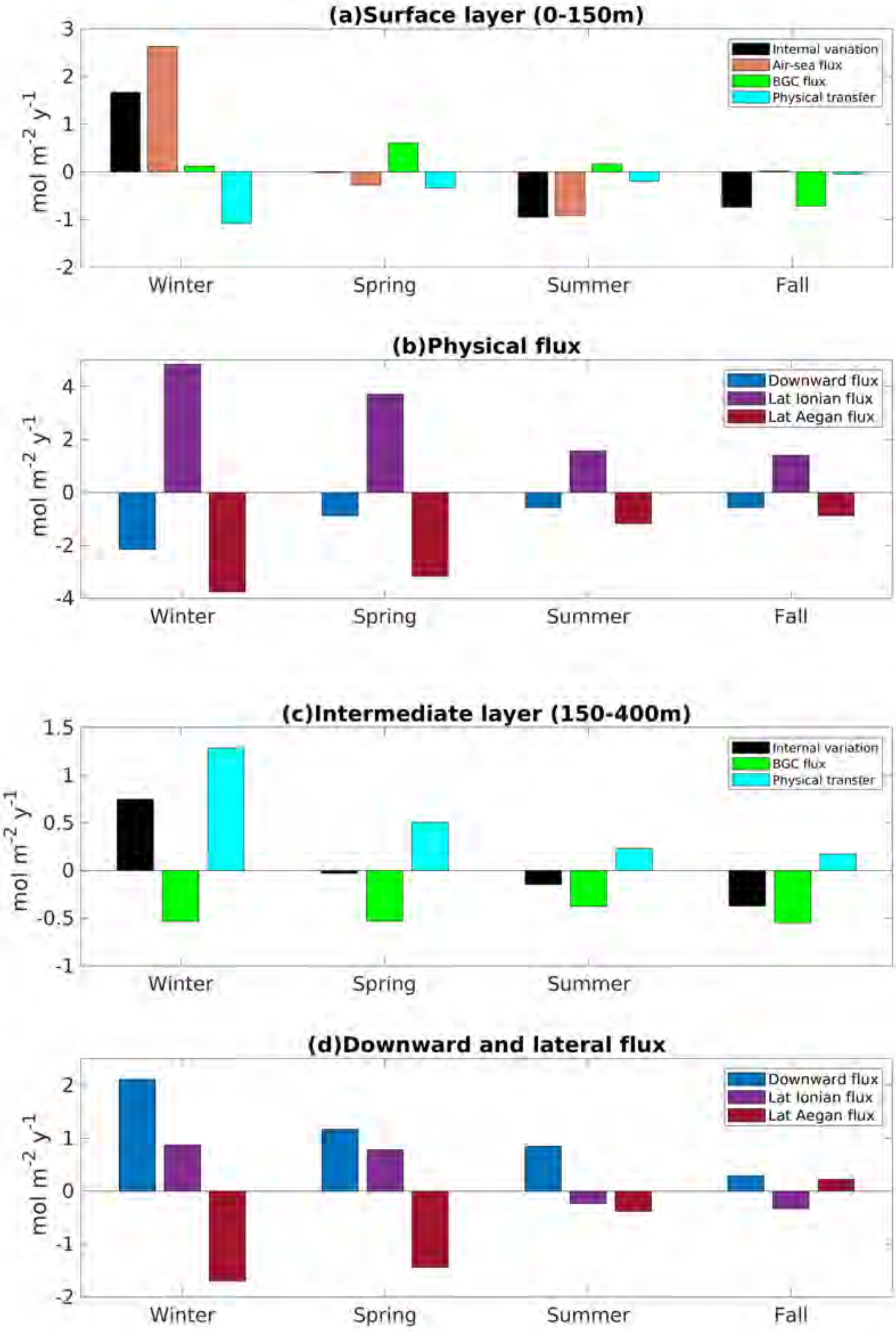

Figure 5.7: Modeled seasonal oxygen fluxes (a) in the surface layer and (c) intermediate layers, and the downward and lateral fluxes (b) in the surface and (d) intermediate layer for the period of study, 2013-2020.

At the annual scale and over the seven-year period 2013-2020, the surface layer gains oxygen through air-sea flux and biogeochemical flux and loses oxygen through physical transport at the limits of the domain (Fig. 5.10 and 5.11a). The net oxygen loss by transport (Fig. 5.11a) is composed of a lateral input of oxygen at the limit with the Ionian Sea, and a release of oxygen towards the Aegean Sea and the intermediate layer of the Levantine Basin (Fig. 5.10 and 5.11b). The lateral exchanges dominate vertical transport. One should notice that the net biogeochemical term is one order of magnitude smaller than physical transfer and air-sea flux.

The annual SD (Table S2, Supplementary material) of the internal variation and various fluxes is strong, showing a high interannual variability. The Levantine Basin acts as a sink for atmospheric oxygen for the seven studied years, with a higher uptake than average during colder years (2014-15, 2016-17 and 2018-19, Fig. 5.11a). The annual lateral and vertical transports at the limits show the same direction for all years, with higher magnitudes during the three colder years (2014-15, 2016-17 and 2018-19, Fig. 5.11b). The surface ecosystem of the Levantine Basin appears to be generally productive in oxygen, except during the mild winter years 2013-14 and 2017-18 (Fig. 5.11a). The oxygen inventory is increasing by 0.3, 0.06 and 0.36 mol O_2 m^{-2} for the cold years 2014-15, 2016-17, and 2018-19 respectively (Fig. 5.11a).

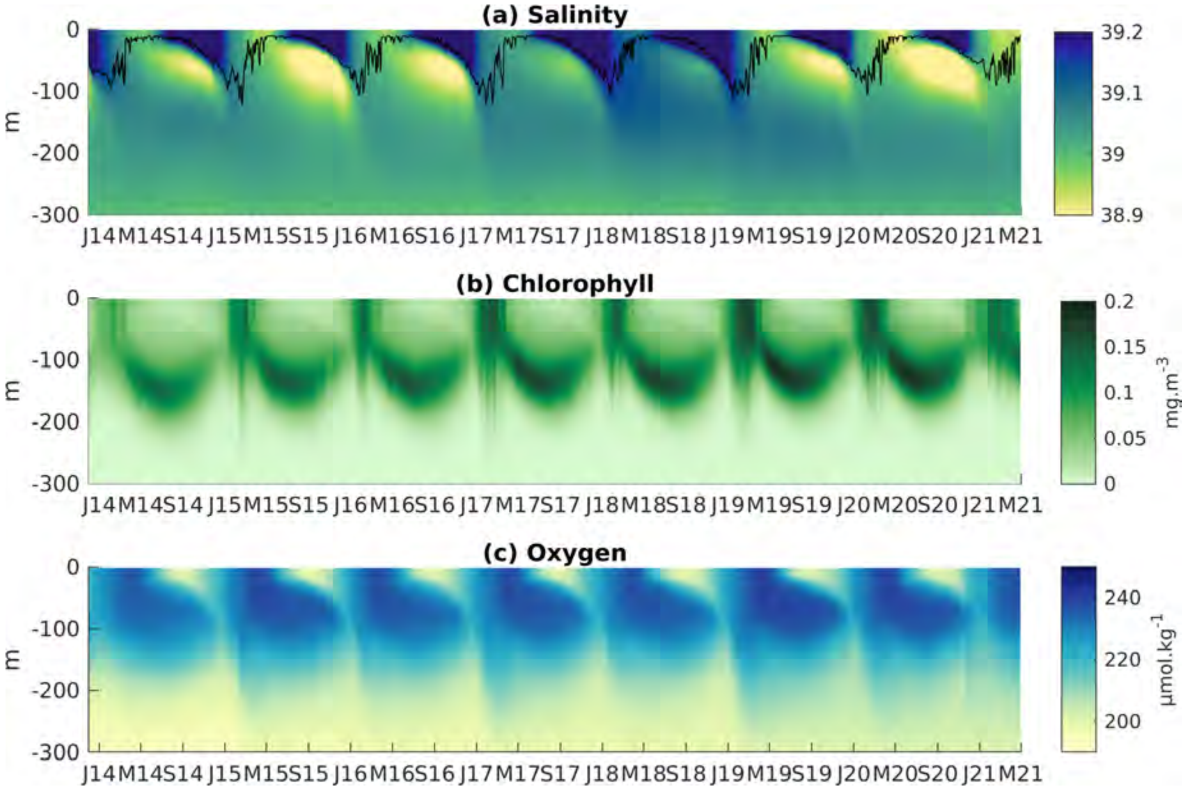

Figure 5.8: Hovmöller diagrams of (a) salinity, (b) chlorophyll (mg m^{-3}), and (c) dissolved oxygen concentration (µmol kg-1), averaged over the Levantine Basin, from December 2013 to May 2021. The black line in (a) indicates the mixed layer depth.

On average the intermediate layer loses 1.25 mol O_2 m^{-2} of oxygen through biogeochemical consumption and gains 2.19 mol O_2 m^{-2} of oxygen through net physical transfer (Fig. 5.10 and 5.11c). The physical oxygen supply results from an inflow from the Ionian Sea (1.08 mol O_2 m^{-2})and the upper layer (4.18 mol O_2 m^{-2}) and an outflow towards the Aegean Sea (3.3 mol O_2 m^{-2}) (Fig. 5.11d).

Both the physical and biogeochemical fluxes also show higher magnitudes during cold winter years in the intermediate layer (Fig. 5.11c). The lateral exchange at the Aegean boundary represents an export for the Levantine Basin for all studied years, with more important fluxes for the cold years 2014-15, 2016-17 and 2018-19 (Fig. 5.11d). The lateral exchanges with the Ionian Sea change direction: while during mild years, the dissolved oxygen is transported from the Levantine Basin towards the Ionian Sea (1.4 and 1.0 mol O_2 m^{-2} for 2013-14 and 2015-16, respectively), cold years show an oxygen injection in the Levantine Basin originating from the Ionian Sea. It should be noted that during 2017-18 considered as a mild year, the lateral Ionian flux is positive (2.2 O_2 mol m^{-2}).

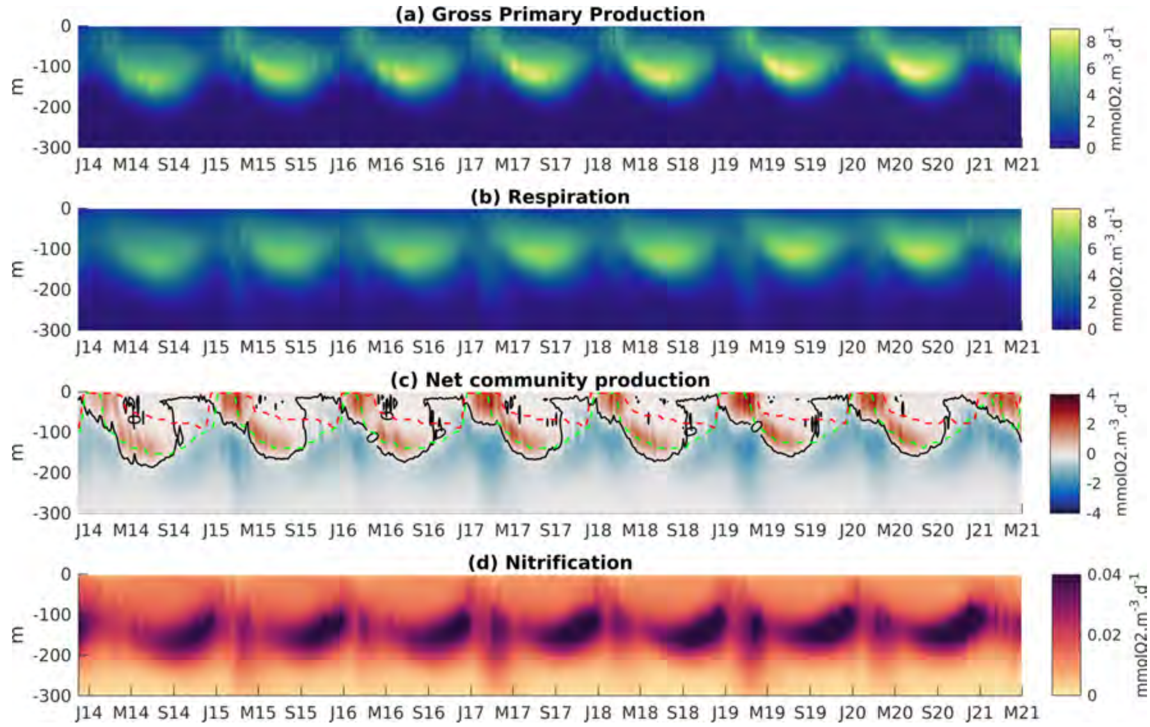

Figure 5.9: Hovmöller diagrams of (a) gross primary production (mmolC m^{-3} d^{-1}), (b) community respiration (mmolC m^{-3} d^{-1}), (c) net community production (mmolC m^{-3} d^{-1}), and (d) nitrification (mmolN m^{-3} d^{-1}) averaged over the Levantine Basin, from December 2013 to May 2021. The green dotted line represents the depth of the deep chlorophyll maximum, the red dotted line the subsurface oxygen maximum depth.

5.4 Discussion

5.4.1 Impact of biological processes on the oxygen inventory

The model results show that the Levantine Basin ecosystem in the surface layer produces dissolved oxygen from January to August (winter, spring and summer) and consumes dissolved oxygen the following four months (Fig. 5.5d and 5.7a). The biological production presents maximum magnitudes (> 2 mmol O_2 m^{-2} d^{-2}) near the surface during the winter mixing and phytoplankton bloom period, and then in the subsurface when the DCM forms in spring and early summer (Fig. 5.9c). The consumption is maximum in fall between 100 and 200 m depth, and during the mixing period below the ML. Nitrification is maximum at the DCM level in fall (Fig. 5.9d) and represents less than 4 % of the annual CR (community respiration).

In summer, the relatively thick subsurface oxygen maximum (SOM) layer remains around 70 m depth, above the subsurface maximum biological production located at around 140 m depth close to the DCM. The difference of locations of the DCM and SOM depths is in agreement with the observations of Pujo-Pay et al. (2011) and modeling results of Di Biagio et al. (2022). On the other hand, the oxygen maximum is located in the less salty subsurface Modified Atlantic Water (MAW), characterized by a metabolism close to equilibrium, suggesting that the location of the maximum is rather the result of the subduction of more oxygenated waters, in agreement with the findings of Di Biagio et al. (2022) at an eastern site of the Levantine Sea. This is also in line with the findings of Kress and Herut (2001) who observed that the MAW, subducted in summer below the mixed layer constituted of Levantine Surface Water and prevented from out-gassing, showed similar oxygen concentrations as they did in winter, around 230 µmol kg^{-1}.

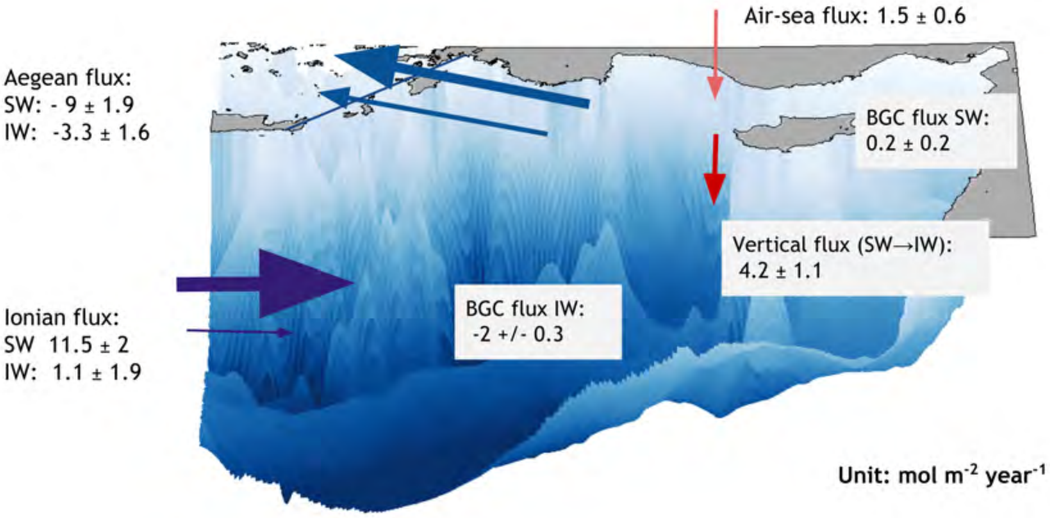

Figure 5.10: Schematic showing the terms of the annual oxygen budget (in mol O_2 m^{-2} yr^{-1}) for the Levantine Basin over the period from December 2013 to December 2020. The terms of the budget are estimated for the upper, euphotic layer (surface-150 m), and the intermediate layer (150 -400 m).SW: surface layer, IW: intermediate layer.

At the annual scale, over the seven studied years, the Levantine Basin acts as a weak autotrophic ecosystem (NCP: 1.2 ± 2.9 mol O_2 m^{-2} $year^{-1}$). The NCP represents the difference between growth primary production (GPP) and respiration (CR). However, the relatively strong SD reveals high interannual variability and we found that its status could change, becoming a very weak heterotrophic ecosystem during the mild winter years 2013-14 and 2015-16 when winter sea heat loss remains weak, MLD depth shallow and vertical supplies of nutrients low (see chapter 4). A significant correlation (R=0.91, *p-value* < 0.01) is obtained between mean winter heat loss (W-HL) and NCP in the surface layer (Fig. S1, Supplementary material) suggesting a switch from autotrophic to heterotrophic status when the W-HL is below 135 W m^{-2}. Figure 5.12 illustrates the spatial heterogeneity of the balance between GPP and CR, with positive NCP values in a central area including the Rhodes Gyre and the West Cyprus Gyre, an area extending to the South along the eastern fronts of the Mersa-Matruh Eddies (Herodotus Trough Eddies) and the coastal areas influenced by rivers. NCP is negative in the along-slope circulation, the Mersa-Matruh Eddies and the Shikmona Eddy (see Fig. 1.6 for eddies locations).

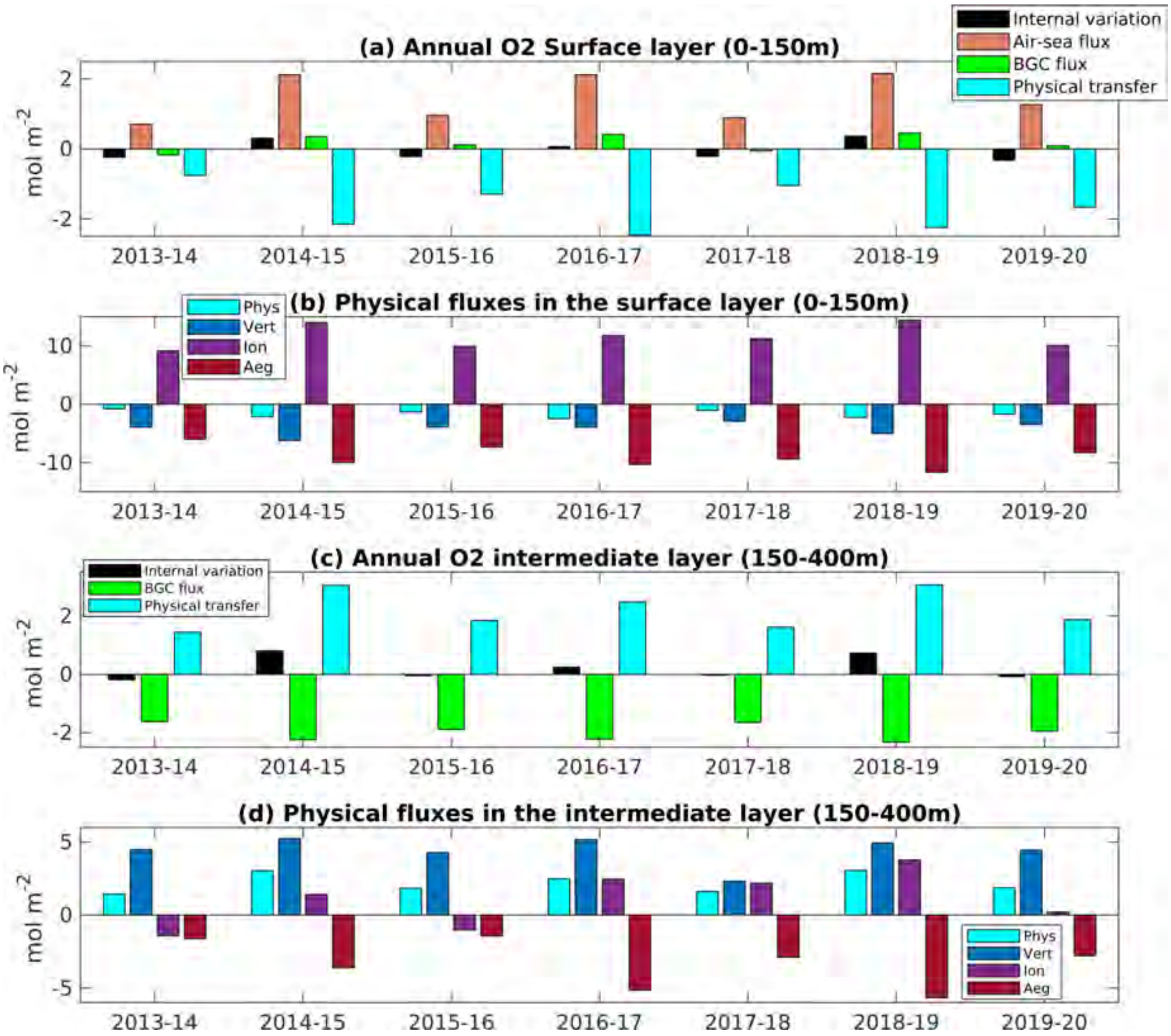

Figure 5.11: (a) Modeled annual dissolved oxygen fluxes (b) and the vertical and lateral transport across the 0 -150 m layer (c) Modeled annual dissolved oxygen fluxes (d) and the vertical and lateral transport across the 150 - 400 m layer for the period of study .

In the intermediate layer, the annual budget shows an annual consumption of 2.0 ± 0.3 mol O_2 m^{-2} yr^{-1}. Interannual variability of oxygen consumption remains weak, with the magnitude significantly correlated with mean W-HL (R=0.94, *p-value* < 0.01). By considering both surface and intermediate layers, the Levantine Sea appears as an heterotrophic system. This is consistent with the budget of organic carbon (Supplementary material). This budget shows in the surface layer a lateral supply from the Ionian Sea, exceeding the lateral export towards the Aegean Sea, as well as a downward export from the surface layer to the intermediate layer. The downward export of organic matter, produced in the surface and originating from the Ionian Sea is higher than the net carbon production in the surface layer. In the intermediate layer, the lateral export of organic carbon towards the Aegean exceeds the organic carbon input from the Ionian Sea. However, the net lateral input of organic carbon in the surface layer is higher than the net lateral export in the intermediate layer (1856 versus 304 Gmol C yr^{-1}). Thus, the strong downward organic carbon export relative to the low carbon production in

the surface layer favors an heterotrophic status and recycling role of the Levantine Sea for the Mediterranean Sea.
Considering the surface area (540 000 km^2), the Levantine Basin produces 91 Gmol yr^{-1} of oxygen in the surface layer. It is noteworthy that, in this layer, the biogeochemical term of the budget is one order of magnitude lower than the air-sea flux and the physical transfer over the period of 2013-2020. The Rhodes Gyre shows the highest annual biogeochemical production rates, amounting to 1.3 ± 0.6 mol O_2 m^{-2} yr^{-1} in the surface layer. This area, representing 5 % of the Levantine Basin area, contributes to 41 % of the oxygen production of the whole surface layer. The annual consumption in the intermediate layer amounts to 1074 ± 155 mol O_2 m^{-2} yr^{-1} . It represents 70 % of the biogeochemical consumption in the whole Mediterranean Sea estimated by Huertas et al. (2009) based on in situ observations at the Gibraltar Strait.
Our results are consistent with the review by Siokou-Frangou et al. (2010) and the study by Christaki et al. (2011) depicting a large temporal and spatial heterogeneity in the trophic status in the oligotrophic Levantine Sea, where the plankton ecosystem is dominated with the heterotrophic component the open sea, except in areas such as the Rhodes Gyre marked by deep mixing.

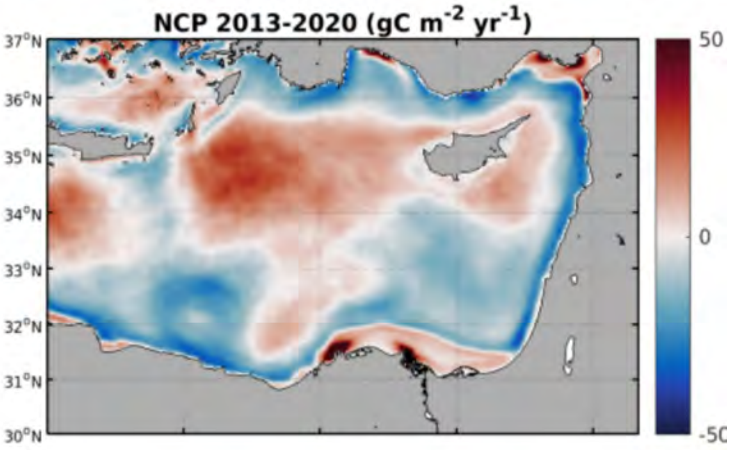

Figure 5.12: Modeled annual net community production (g C m^{-2} yr^{-1}) in the surface layer (0-150 m) for the period from December 2013 to December 2020.

There is very few data on metabolism rates in the eastern Mediterranean Sea and most of them were deduced from observations during stratified periods. The comparisons between model results averaged over periods from mid-June to mid-July and the process rates measured near the surface in the core of an anticyclonic eddy in the eastern Levantine during the BOUM cruise show that the modeled GPP and CR are in the upper range of the measurements (1.36 versus 0.12 ± 0.90 mmol O_2 m^{-3} day^{-1} for GPP and 1.27 versus 0.38 ± 0.92 mmol O_2 m^{-3} day^{-1}) with a low modeled NCP of 0.09 mmol O_2 m^{-3} day^{-1} as in the observations displaying a rapid change of sign (-0.26 ± 0.22 mmol O_2 m $^{-3}$ day^{-1}, (Lagaria et al., 2011)). The comparisons with the rates integrated over the surface layer (145 m) at the same site show high rates in the model for GPP (68 versus 28-75 mmol O_2 m^{-2} day^{-1}) and CR (67 versus 39-58 mmol O_2 m^{-2} day^{-1}) and a NCP is the range of observations (0.9 versus 4 ± 15 mmol

O_2 m^{-2} day^{-1}) (Christaki et al., 2011). The comparisons between model results averaged for the month of May over the Levantine Basin and the rates measured by Regaudie-De-Gioux et al. (2009) during the THRESHOLD cruises in the 5-110 m surface layer (GPP varying between 0.16 and 2.93 mmol O_2 m^{-3} day^{-1}, CR between 0.1 and 8.2 mmol O_2 m^{-3} day^{-1} and NCP -6.4 and 8.2 mmol O_2 m^{-3} day^{-1} in the eastern Mediterranean Sea) show also high values for modeled GPP (ranging between 1 and 8 mmol O_2 m^{-3} day^{-1}), and values in the range of observations for CR (between 1 and 7 mmol O_2 m^{-3} day^{-1}) and NCP (between 0 and 2 mmol O_2 m^{-3} day^{-1}).

5.4.2 Air-sea flux

The model results display a similar seasonal cycle of the air-sea flux for the seven studied years, in the Levantine Sea. From April to September, the Levantine Sea is oversaturated compared to the atmosphere and oxygen is released into the atmosphere, while the rest of the year the Levantine Sea is undersaturated and absorbs atmospheric oxygen (Fig. 5.5b-c). The air-sea flux is particularly strong in winter when the wind is intense and the O_2 saturation anomaly, between 2 and 3 %, is maximum. Our results highlight a significant correlation between surface temperature and both surface oxygen concentration and oxygen saturation ($R > 0.8$, *p-value* < 0.01), in agreement with the previous observational study of Mavropoulou et al. (2020).

At the annual scale, the Levantine Basin acts as a net sink for the atmospheric oxygen at a rate of 1.5 ± 0.6 mol O_2 m^{-2} yr^{-1}, between December 2013 and December 2020. The modeled air-sea flux exhibits strong interannual variability in terms of magnitude, with a SD of 44 %. Our model results show that during the cold years 2014-15, 2016-17 and 2018-19 annual air-sea flux are higher than average. A significant correlation is found between winter heat loss (W-HL) and both annual and winter air-sea flux ($R=0.92$ and $R=0.93$, respectively, *p-value* < 0.01). The annual air-sea flux shows a strong spatial variability (Fig. 5.13). Except in the coastal area influenced by the Nile River in the South-east, the whole Levantine Sea appears as an atmospheric oxygen sink. The highest uptake rates are found in the Rhodes Gyre area, which is a LIW formation area, where they exceed 5 mol O_2 m^{-2} yr^{-1}. One can also notice the presence of other regions characterized by higher uptake rates, located in the North, in the Antalya Bay and the Cilician basin. Those regions were also identified by Fach et al. (2021) as potential LIW formation areas. The annual air-sea flux is also spatially mostly controlled by the winter air-sea O_2 flux. The annual anomalies show that the cold years (2014-15, 2016-17 and 2018-19) absorb more atmospheric oxygen in the whole sea, especially in the Rhodes Gyre. On the contrary, during the mild years (2013-14, 2015-16 and 2017-2018) a smaller uptake is general and is more pronounced in the Rhodes Gyre.

The strong wind stress during the undersaturation period favors a positive budget at the air-sea interface for the Levantine Basin. The winter air-to-sea flux amounts to 10.7 ± 2.8 mol O_2 m^{-2} yr^{-1}. This is accentuated in the Rhodes Gyre which is the main area of LIW formation (Nielsen, 1912; Ovchinnikov, 1984; Lascaratos and Nittis, 1998). In fall and winter, the cyclonic circulation intensifies and the mixed layer deepens below 130 m on average. A winter budget for the Rhodes Gyre shows that surface water enriched in oxygen through air-sea flux and biological production is exported laterally towards the surrounding Levantine Sea, while deeper water poorer in oxygen is supplied from the intermediate layer. This enhances an undersaturation in this area that shows maximum values varying between 2 and 5 %, and a mean winter uptake of 20.0 ± 7.4 mol m^{-2} yr^{-1}. Such intensification of oxygen uptake was previously observed and modeled in other water formation areas. In the central Labrador Sea Gyre, Körtzinger et al. (2004) reported a large increase in oxygen inventory during the deep convection period and Körtzinger et al. (2008) and Wolf et al. (2018) observed high undersaturation reaching 6-7 % at the sea surface during winter mixing. The estimates of air-sea flux during deep convection in this area ranges between 12 and 37 mol m^{-2} (Körtzinger et al., 2008; Wolf et al., 2018). Closer, in the NW Mediterranean deep and intermediate convection areas, previous studies based on in situ observations (Copin-Montegut and Begovic, 2002; Coppola et al., 2017, 2018) documented increases in oxygen inventory over the water column during the deepening of the mixed layer varying between 11 and 25 mol m^{-2} during the deep mixing periods. Strong undersaturation levels between 10 and 20 % were estimated (Ulses et al., 2021; Fourrier et al., 2022). Copin-Montegut and Begovic (2002) calculated an air-to-sea flux of 5.0 and 2.3 mol m^{-2} for the winter mixing periods of 1998-99 (26 days) and 1999-2000 (23 days), respectively. Using 3D coupled hydrodynamic-biogeochemical modeling, Ulses et al. (2021) estimated the intake of atmospheric oxygen at 18 mol m^{-2} (in 63 days) during the intense deep convection event of 2012-13 for the whole deep convection area. Thus the Rhodes Gyre shows comparable uptake rate as other deep convection areas.

Considering the area of the Levantine Basin, the uptake of oxygen from the atmosphere amounts to 786 Gmol O_2 yr^{-1}. The Rhode Gyre, which represents 5 % of the Levantine Basin, contributes to 14% of this annual atmospheric oxygen intake. As a matter of comparison, the uptake in the warm Levantine Basin, characterized by relatively low solubility, represents 64% of the oxygen uptake by the NW Mediterranean deep convection estimated for the cold years 2012-13 by Ulses et al. (2021).

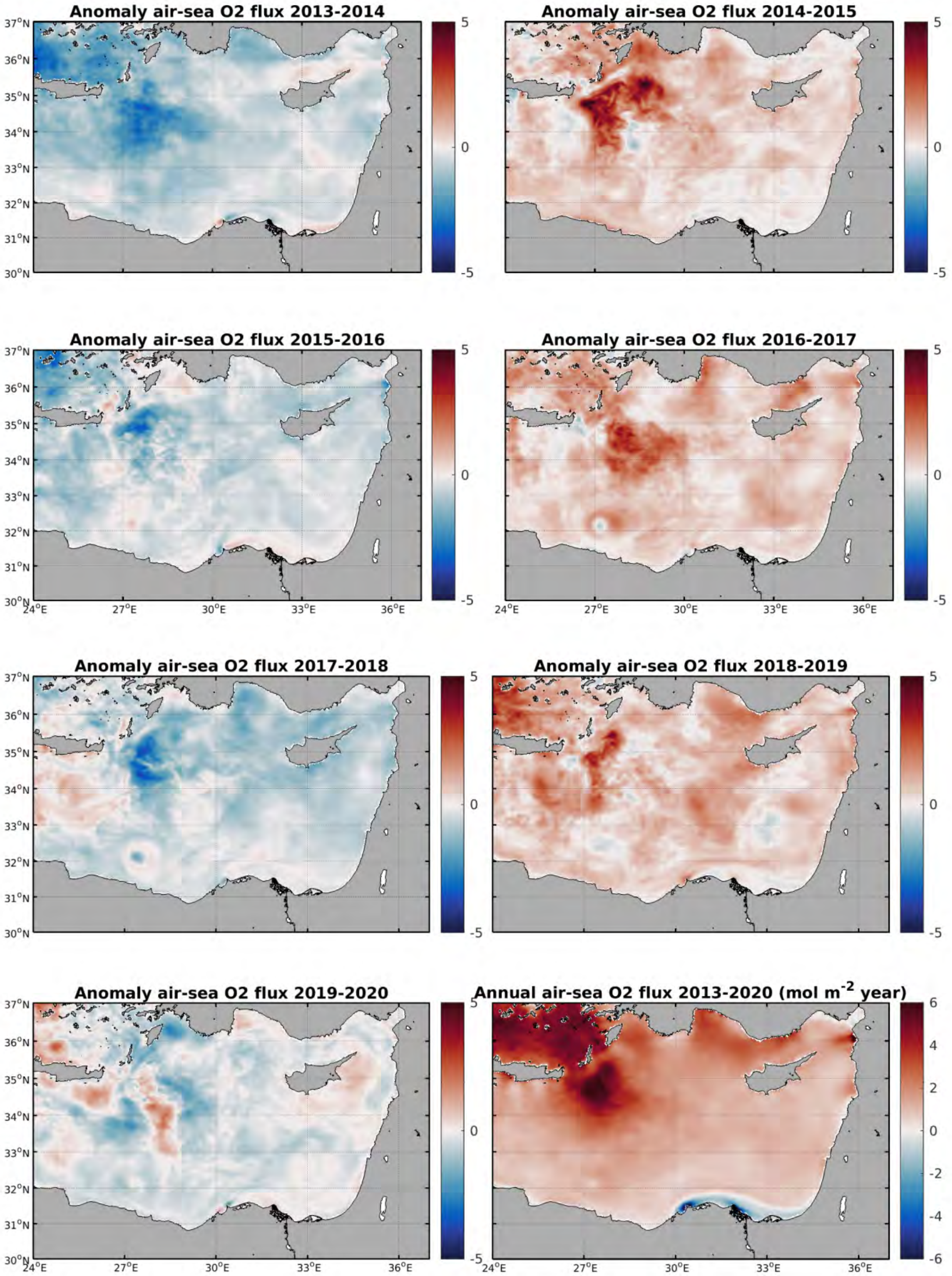

Figure 5.13: Modeled annual air-sea oxygen anomaly and the annual air and sea O_2 flux for the period of study.

5.4.3 Ventilation and exchanges with the surrounding regions

The oxygen budget shows an annual O_2 downward transport from the surface layer towards the intermediate layer of 4.2 ± 1.1 mol O_2 m^{-2} yr^{-1} (Fig. 5.10, Table S2 in Supplementary material). This vertical transfer occurs in all seasons, with maximum intensity in winter, when ML is the deepest, and a progressive decrease until fall. The annual SD of 26% shows a moderate interannual variability. The severe winters 2014-15 and 2018-19 were characterized by intense mixing yielding a deeper and stronger ventilation of the water column than average (Fig. 5.8c, Fig. 5.11d, Table S2 in Supplementary material). A significant correlation was found between winter oxygen vertical export and winter heat loss (W-HL, R=0.76, *p-value* < 0.05, respectively), but not between annual vertical export and W-HL (R=0.53, *p-value*=0.22).

The Levantine Basin is characterized by the presence of numerous anticyclonic and cyclonic gyres that may affect the vertical distribution of oxygen (Minas and Bonin, 1988; Moutin and Raimbault, 2002; Coppola et al., 2017; Mavropoulou et al., 2020). Figure 5.14 illustrates from January to May 2015 the spatial repartition of oxygen at 200 m depth over the Levantine Basin and along a vertical section crossing the Rhodes Gyre to the northeast of the section and an anticyclone to the southwest (see position of the section on the horizontal maps in left panel).

Between January and February, the air-sea fluxes transfer energy to the surface layer through wind and heat fluxes. The mixed layer depth increases as well as the intensity of the cyclonic current around the basin. In February (5.14b), some fronts become unstable and the potential energy is converted into kinetic energy mainly at submesoscale with the formation of many filaments and eddies. This is clearly the case of the Rhodes Gyre where the finest structures of the basin are observed. The along-slope current develops mesoscale instabilities with meanders and anticyclonic eddies that appear later from the Egyptian coast to the Middle Eastern coast and to the Turkish coast.

Between February and May, the fine structures tend to disappear (Fig. 5.14b-d). Some larger eddies on the contrary develop as at the southwestern end of the section plotted on the map of May (5.14d). This continues later with eddy-eddy interactions (not shown). The direct and inverse energy cascades result in a few months in smoother fields dominated by large mesoscale structures ($\sim$ 150 km see for example January, Fig. 5.14a).

Regarding oxygen, the concentration at 200 m increases significantly between January and February (Fig. 5.14a-b) with the deepening of the mixed layer in the submesoscale filaments and eddies of the Rhodes Gyre as well as in the slope current and anticyclonic eddies. Despite very different water masses, dense in the Rhodes Gyre, light in the slope current, the lack of stratification allows oxygen to reach 200 to 300 meters depth in both cases. Outside of these areas, the mixed layer is shallower which restricts the penetration of oxygen. In March, the Rhodes Gyre re-stratifies. Vertically homogeneous oxygen concentrations are now limited to the first 100 meters (5.14c). Between 100 and 200 meters, the concentration has clearly decreased compared to February. The horizontal section at 200 m shows indeed a spreading of the concentrations even if filamentary structures are still visible in the gyre. The vertical section between 27.5 and 28°E shows in the globally cyclonic structure marked by the doming of isopycnal 29.1, an alternation of submesoscale cyclones and anticyclones (see the 29.1 isopycnal ripples) with oxygen-poor ascending and oxygen-rich descending water columns, respectively. Small eddies have detached from the gyre and populate the region between the Rhodes Gyre and Cyprus around 30 -31°E. The anticyclones that have recently developed along the Turkish coast, of relatively small size compared to those of the Egyptian coast, store oxygen down to a depth of about 300 m. The same is true for the anticyclone that forms southwest of the section at about 26°E. However, it seems that in this case, oxygen is distributed in two cores, the first on the first 200 m in which the transfer of oxygen is done vertically from the atmosphere and the surface layer, the second at 400 m, separated from the first by a less rich layer that suggests that it is decoupled from the surface layer. The origin of this core is a filament coming from the Rhodes Gyre that wraps around the anticyclone. It is likely that the subduction of dense water from the Rhodes Gyre allows the burial of oxygen in depth in the anticyclones located at its periphery. The Ierapetra anticyclone, in cases where it has not disappeared in winter, is a good candidate for this process because of its proximity to the Rhodes Gyre.

Two months later, in May, the oxygen at 200 m is much more homogeneous(Fig. 5.14d). The filaments of the Rhodes Gyre are very attenuated. The horizontal section shows that the Gyre at this depth is beginning to recover the low concentrations that characterize it (see for example January, Fig.5.14a) linked to the vertical upward velocities. We can also note the presence of small cyclones for example along the Egyptian coast around 26 and 29°E or south of Cyprus that also show subsurface waters poor in oxygen. The highest concentrations are in the numerous anticyclones that characterize the Levantine basin at this time.

In the Rhodes Gyre, we found that the vertical transfer of oxygen, averaged over the whole year, is directed, as the water transport, from the deeper layers towards the surface (Table S3, Supplementary material). On average, oxygen gained from vertical advection and air/sea flux is laterally exported (9.4 ± 3.1 mol O_2 m^{-2} yr^{-1} in the surface layer and 5.6 ± 2.3 mol O_2 m^{-2} yr^{-1} in the intermediate layer, Table S3). This lateral transfer is strong in winter as seen in Fig. 14 and takes place notably through the dispersal of LIW by subduction (Taillandier et al., 2022; Estournel et al., 2021) as it was reported by Malanotte-Rizzoli et al. (2003) for January 1995 during the POEM cruise. The net annual biological production (1.3 ± 0.6 mol O_2 m^{-2} yr^{-1}, Table S3) and the large amount of absorbed atmospheric oxygen (3.9 ± 1.7 mol O_2 m^{-2} yr^{-1}, Table S3) are important contributions for the redistribution to the surrounding Levantine Basin.

Regarding the Levantine, our results show a weak transfer from the deep layer into the intermediate layer of 0.2 mol O_2 m^{-2} yr^{-1} with a strong interannual variability (SD= 0.8 mol O_2 m^{-2} yr^{-1}). This mean upward transfer is consistent with the general scheme of circulation (Roether and Schlitzer, 1991) or oxygen cycle (Powley et al., 2016b) and with previous observations (Tanhua et al., 2013; Mavropoulou et al., 2020) describing a gradual upwelling of deep water originating from the Adriatic Sea or Aegean Sea.

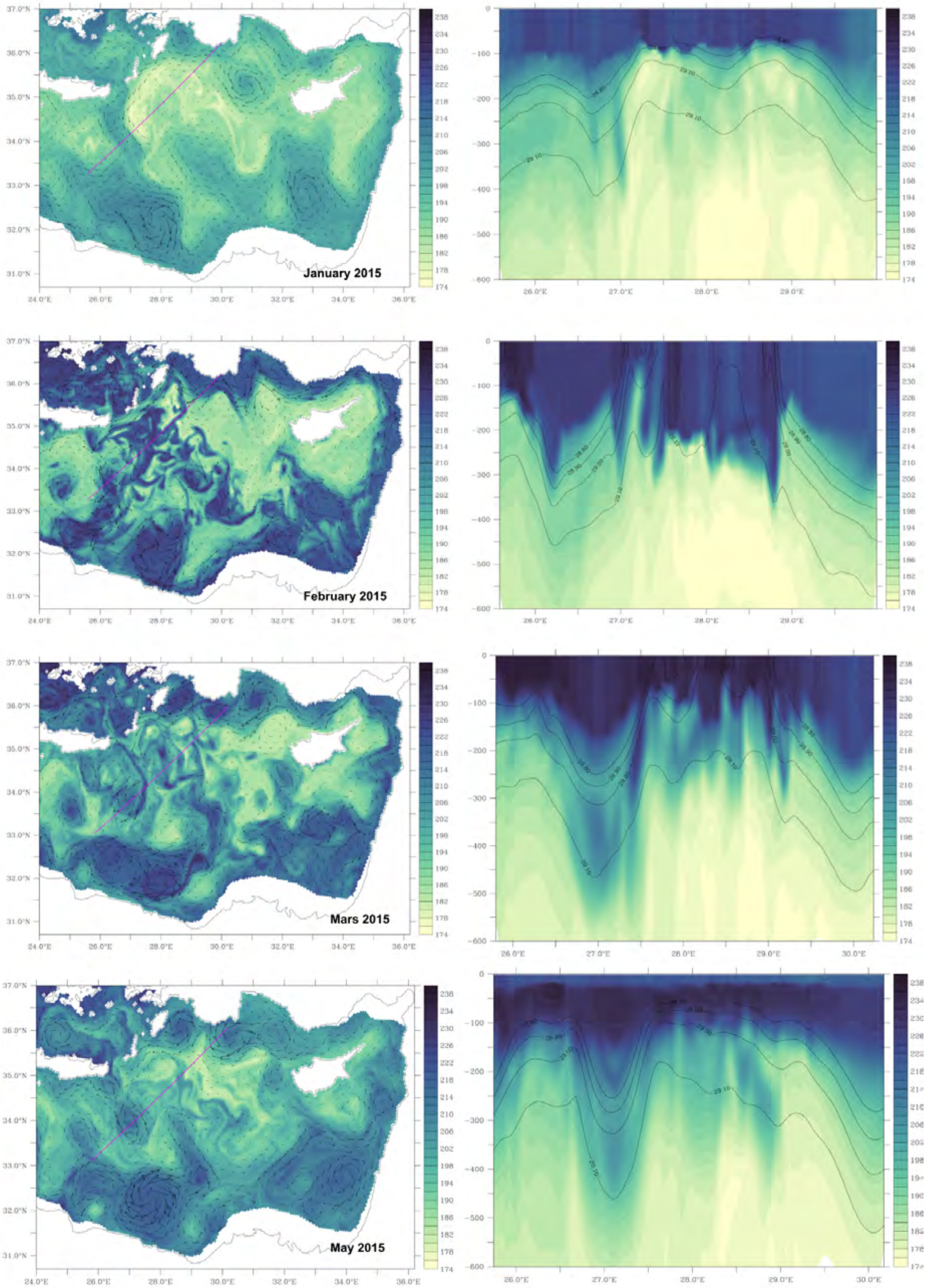

Figure 5.14: Horizontal maps of oxygen concentration at 200 m depth (left panels; expressed in µmol kg^{-1}) and vertical section across the Rhodes Gyre between January 2015 and May 2015. The potential density anomaly (kg m^{-3}) is overlaid with contours. The position of the section is indicated on the horizontal maps.

Our results show a dissolved oxygen annual inflow in the surface and intermediate layers from the Ionian and an outflow in both layers towards the Aegean Sea. The horizontal oxygen transfers also show a strengthening of these lateral fluxes in winter and a progressive decrease until fall in the surface layer and a reverse in fall in the intermediate layer (Fig. 5.7b and 5.7d). The higher intensity of the exchanges in winter compared to fall could be explained by both higher water mass transport (Estournel et al., 2021) and higher concentration of dissolved oxygen near the surface, the latter due to important net biological production and/or air-to-sea flux in winter. As regards the interannual variability, we found generally higher fluxes than average during the cold years 2014-15, 2016-17 and 2018-19 and the lateral exchanges are very low during the warm year 2013-14 (Fig. 5.11b and 5.11d), with exports to the Aegean 1.5 and 2.4 times higher during cold years in the surface and intermediate layers, respectively. However, we only obtain a significant correlation between W-HL and the annual lateral exchanges with the Aegean Sea (R=0.74, *p-value* < 0.01 in the surface layer, R=0.82, *p-value* < 0.05 in the intermediate layer). The correlation between W-HL and the lateral exchanges with the Ionian Sea (R=0.69, *p-value* < 0.08) is relatively low and not significant, maybe due to the opposite exchanges along the Egyptian coast and south of Crete.

Our results are consistent with previous studies describing the general circulation in the eastern Mediterranean Sea. Regarding the exchanges with the Aegean Sea, a net outflow of LSW and LIW by the Asia Minor Current through the Cretan Straits was documented in several observational and modeling studies (Zodiatis, 1993; Theocharis et al., 1993; Millot and Taupier-Letage, 2005; Velaoras et al., 2014; Estournel et al., 2021). The inflow of oxygen modeled in fall could be explained by the transport from the Aegean Sea to the Levantine Sea documented in the Kasos Strait (Souvermezoglou et al., 1992; Malanotte-Rizzoli et al., 1999; Kontoyiannis et al., 1999; Velaoras et al., 2014; Estournel et al., 2021). As regards the exchanges with the Ionian Sea, the general cyclonic circulation displays in the surface layer (1) an eastward inflow along the Libyo-Egyptian coast enhanced in winter (Fig. S2a, Supplementary material) and (2) an eastward outflow south of Crete (Fig. S2b, Supplementary material) enhanced in summer (Estournel et al., 2021). At intermediate depths, the flux along the Libyo Egyptian coast reverses seasonally with an inflow from the Ionian in winter (Fig. S2c, Supplementary material) and an outflow in summer (Fig. S2d, Supplementary material) while the flow south of Crete exports all year round to the Ionian. The annual balance is a weak inflow of oxygen from the Ionian to the Levantine with for some mild years a reversal of this balance probably related to a weaker transport along the Libyo Egyptian coast.

Finally, our oxygen budget shows the following general scheme for the Levantine Sea over the 2013-2020 period: a net oxygen lateral inflow from the surrounding seas in the surface layer which accounts for 2.5 ± 0.6 mol O_2 m^{-2} yr^{-1}, a net oxygen downward export from the surface layer to the intermediate layer of 4.2 ± 1.1 mol O_2 m^{-2} yr^{-1}, a low net oxygen upward supply from the deep layer to the intermediate layer of 0.2 ± 0.8 mol O_2 m^{-2} yr^{-1} and a net outflow of oxygen from the intermediate layer of 2.2 ± 0.7 mol O_2 m^{-2} yr^{-1} to the surrounding regions with an important export to the Aegean (3.3 ± 1.6 mol O2 m-2 yr-1). Thus, considering the surface of the basin (540 000 km^2), the Levantine Basin absorbs 1361 Gmol yr^{-1} of oxygen in the upper layer and releases 1197 Gmol yr^{-1} of oxygen in the surrounding intermediate depths areas.

5.5 Conclusion

In this study, a high resolution 3D coupled hydrodynamic-biogeochemical model was used to investigate the seasonal and interannual variabilities of the oxygen in the Levantine Basin and to estimate its budget over the whole basin over the period of 2013-2020. The study period was marked by contrasted atmospheric and hydrodynamic winter conditions. The confrontation of the model results with cruise and BGC-Argo float observations shows the capacity of the model to capture the general seasonal and spatial dissolved oxygen variability and the main oxygen features across the water column in the basin. The following conclusions can be drawn:

- The model results show a clear seasonal cycle for the oxygen air-sea flux. During winter, with the decrease of temperature, the heat loss and mixing events, the surface layer is undersaturated in oxygen and thus absorbs atmospheric oxygen at the surface. The undersaturation averaged over the whole basin reaches 2 % during winter. During the stratified period, the surface layer is oversaturated in oxygen, the over-saturation reaches a maximum of 0.62 % during summer.

- The Levantine Basin acts as a sink for the atmospheric oxygen at an annual scale, capturing 1.5 ± 0.6 mol O_2 m^{-2} yr^{-1} of oxygen . Most of the oxygen uptake occurs during winter when it accounts for 10.7 ± 2.8 mol O_2 m^{-2} yr^{-1}. The Rhodes Gyre absorbs atmospheric oxygen at a 2-fold higher rate than the whole Levantine Basin.

- Our budget shows that the surface layer of the Levantine Basin is a source of dissolved oxygen for the intermediate depths, with winter vertical export of oxygen influenced by the winter heat loss intensity. Regarding the exchanges with the surrounding seas, we found that oxygen is laterally transported from the Ionian Sea into the basin , and from the basin towards the Aegean Sea. The lateral annual oxygen outflow to the Aegean is strongly enhanced by the heat loss intensity with exports 1.5 and 2.4 times higher during cold years in the surface and intermediate layer respectively compared to mild years.

- The Levantine Basin is found to act as a weak autotrophic ecosystem on an annual level, with a net community production in the surface layer alternating between auto- and heterotrophic status influenced by the magnitude of the winter heat loss. In deeper depths, respiration and nitrification resulted in an oxygen consumption of 2.0 ± 0.3 mol O_2 m^{-2} yr^{-1}. Spatially, the Rhodes Gyre appears to be a major oxygen production area across the basin contributing to 41 % of the oxygen production of the whole surface layer.

This work represents a first step in our modelling of the dissolved oxygen dynamics in the Levantine Basin. Further investigations on the role of the various cyclonic and anticyclonic eddies will be conducted in the future. Besides, several studies suggest a decadal variability of dissolved oxygen across the whole water column linked to the dense water formations in the south Adriatic and Aegean seas and to the general eastern Mediterranean circulation, notably the reversal of the North Ionian Gyre (Ozer et al., 2019, 2022). A time extended simulation of the coupled model could contribute to examining this longer variability in the Levantine Basin and the connections between the sub-basins of the eastern Mediterranean.

Conclusion and perspectives

Conclusion

This thesis, based on a high-resolution 3D coupled physical-biogeochemical model, made it possible to focus on the scientific objectives mentioned in the introduction of this manuscript: The impact of Levantine Intermediate Water (LIW) formation on the annual cycle of nutrients and plankton, and the processes driving the dissolved oxygen dynamics in the eastern basin of the Mediterranean. It also contributed to the estimate of the organic carbon and dissolved oxygen budget in the Rhodes Gyre and across the Levantine Basin.

In order to address these scientific goals, we implemented the coupled model in the whole Mediterranean with a focus on the Levantine Basin over the period from December 2013 to May 2021. The study period was marked by contrasted winters differentiated by the sea heat loss and wind-stress intensity.

We assessed the model using various datasets: satellite (chlorophyll), cruise (PERLE program and CARIMED), and BGC-Argo floats data.

Overall, despite some biases, the model reproduces well the seasonal variability of the biogeochemical parameters (oxygen, nutrients, and chlorophyll) in the surface and intermediate layers. The comparisons with the BGC-Argo floats show an underestimation of chlorophyll and oxygen concentrations in the subsurface, in addition to a bias of oxygen in winter. We discussed potential uncertainties for the model and observations.

The influence of the winter mixing on the organic carbon dynamics in the Rhodes Gyre

The study of the organic carbon dynamics in the Levantine Basin was focused on the LIW formation site: the Rhodes Gyre. This persistent cyclonic gyre is considered as presenting the higher planktonic production rate in the oligotrophic Levantine Basin due to a relatively strong winter nutrient supply by vertical mixing.

With our model results, we described the seasonal variability of the planktonic ecosystem. During fall, the mixed layer begins deepening and the nutriclines shallow. In winter, when the mixed layer reaches the nutriclines, the vertical mixing events induce nutrient injections near the surface. Phytoplankton accumulation at the surface begins to increase and then after March phytoplankton concentration decreases following the depletion of nutrients near the surface. The phytoplankton growth at the surface occurs during the mixing period, with maximum rates often during the restratification periods.

An interannual variability for the phytoplanktonic ecosystem was also depicted. During cold winter years, the deep mixing leads to higher nutrient injection in the euphotic layer favoring a more intense phytoplankton growth.

The annual budget of the surface layer of the Rhodes Gyre acts as a source of organic carbon for the intermediate layer and its surrounding through downward and lateral export. Convection in the gyre, resulting from the cooling/densification of the surface waters in winter, leads to the subduction of dense waters and their organic carbon content towards the surrounding

Levantine Basin and then further dispersion by meso and submesoscale structures.
Finally, the Rhodes Gyre acts as an autotrophic system, 50 % of the organic carbon exported below 150 m depth in the Rhodes Gyre is respired at intermediate levels inside the Gyre and 45 % of the carbon produced in the surface is exported towards the surrounding Levantine Basin. The intensity of the sea heat loss and vertical mixing influences the net community production, with an enhanced autotrophic metabolism during cold years, as well as the export.

The dissolved oxygen dynamics in the Levantine Basin

We also used the model to analyze the spatial and temporal evolution of dissolved oxygen in the surface and intermediate layers of the Levantine Basin.The model results show that during winter, spring and summer, the Levantine Basin planktonic ecosystem produces oxygen in the surface layer whereas it consumes oxygen during fall. The surface layer acts, on average, as a weak autotrophic system, alternating between heterotrophic and autotrophic status based on the sea heat loss intensity. The intermediate layer is dominated by respiration, with an oxygen consumption governed by the heat loss intensity. Globally, our results suggest the possible heterotrophic status of the Levantine Basin and its recycling role for the Mediterranean Sea. Spatially, the Levantine Basin possesses an heterogeneous distribution of NCP, with productive areas in the center of the basin including the Rhodes Gyre, 41 % of the total oxygen production for a surface of 5 % of the Levantine Basin.
The Levantine possesses a clear seasonal cycle for the air-sea oxygen flux; the basin alternates between an oxygen undersaturated surface layer during winter and an oversaturated surface layer during stratified periods. The basin is a sink for atmospheric oxygen, especially in the Rhodes Gyre that shows a rate of uptake twice as high as the Levantine Basin. The annual atmospheric oxygen uptake in the Levantine Basin is higher during years classified as cold.
The surface layer of the Levantine Basin is a source of dissolved oxygen for the intermediate layer. The winter sea heat loss magnitude influences the winter vertical export of oxygen. The basin receives oxygen from the Ionian and exports oxygen to the Aegean Sea. The annual oxygen outflow to the Aegean is strongly enhanced during years with a cold winters.

Perspectives

Despite gaining insight into the planktonic ecosystem dynamics in the Levantine Basin, this work showed some limitations, associated with the data and tools that were available for the region and the choices for the initialization and the biogeochemical parameters in the model. Further work and studies are therefore still necessary to better understand the functioning and the variability of the hydrodynamic and biological processes governing the Levantine Basin.

Observations

As was mentioned before, the PERLE program provided a rich database of nutrients and oxygen for the western part of the Levantine Basin. CARIMED database, which aims to group and qualify the different observational data collected from cruises and subsequently inter-calibrate them, covered a transect in the center of the Levantine. Some gaps were filled using float data which provided detailed insights of the chlorophyll and oxygen variation across the water column in most of the basin. Satellite data were also used in order to qualify the model's spatial ability in reproducing the chlorophyll gradient at a basin scale. It is noteworthy to mention that some of the cruises variables (chlorophyll, bacteria growth, primary production processes, ...) were still being processed and therefore were not included in this study. The model validation using satellite data was challenging due to the differences between satellite and cruise data. However, even with the combination of all these various data, the description of our region remains limited by the number of observations. Most parts of the Levantine are, to our knowledge, undersampled and some are not sampled, for example, no data were available for nutrients in the Cilician basin. All these limitations have made the validation exercise difficult. Thus, an intensive fieldwork activity (satellite correction, floats, cruises) should be done for key physical and biogeochemical parameters including long-term observations.

Model improvements

Despite showing good results in terms of representation of hydrodynamical-biogeochemical processes compared to observations, further developments in our model configuration could be made to improve the realism of its outputs.

In this study, the river configuration is set up to be as realistic as possible, however, the water discharges of the rivers for the eastern basin should be prescribed more accurately. This might be challenging due to the low availability of hydrological data.

Suggestions for future modelling works

Dense water formation regions

Although the Rhodes Gyre region was established as the LIW formation area, other observations indicate the presence of additional dense water formation sites such as the Turkish coast (Fach et al., 2021). Fach et al. (2021) suggested that 10 % of the total LIW produced in the Rhodes Gyre, may be formed in the Cilician basin. Therefore the process of water mass formation in this site (and other potential sites) might be important. A complete description of the LIW formation in coastal and off-shore areas of the eastern Mediterranean and its impact on biological processes deserves further work.

Impact of mesoscale structures on the biogeochemistry of the basin

The hydrologic regime of the eastern Mediterranean is modulated by sub-basin gyres and mesoscale features. These structures may result in contrasted properties of the water column biogeochemical properties, through a horizontal and vertical transfer of nutrient, carbon, and oxygen (Siokou-Frangou et al., 2010). Understanding the processes that control the quantity and quality of POC flux export to the deep Eastern Mediterranean Sea is needed to better characterize the strength and efficiency of the biological pump. Pedrosa-Pamies et al. (2021) examined the POC export to deep layers of the Levantine basin in the Ierapetra anticyclone. They found the export of organic matter to the deep Eastern Mediterranean Sea is crucial for the food supply and the export of atmospheric CO2. This thesis work focused on the Levantine

Basin and on a smaller scale, the cyclonic Rhodes Gyre where we were able to quantify the organic carbon and dissolved oxygen export into deeper layers and to the surrounding areas. In Chapter 5, we presented a non-detailed comparison of the vertical oxygen dynamic in an anticyclone and a cyclone in the Levantine Basin. However, it is necessary to complete our work with a more extensive comparison of different mesoscale structures, for example, Ierapetra which could interact with the neighboring Rhodes Gyre or anticyclones developing at the periphery of the basin interacting with the inflow of Atlantic Water. Such structures store large amounts of oxygen and organic matter for periods of several months/years. The fate of these constituents when the physical structures are destroyed is a subject that also deserves attention.

Implications for the future evolution of the carbon cycle in the eastern basin

This study has allowed a better understanding of the organic carbon cycle in the Levantine Basin. We only described the cycle of the organic carbon and partially the cycle of DIC through its consumption by plankton and production by living organisms. Other terms of the budget such as air-sea flux, and the vertical and lateral transport terms were not analyzed. This limits the understanding of the role of the sink or source of the Rhodes Gyre relative to the atmospheric CO_2 and the influence of winter mixing intensity on the air-sea exchanges. Previous studies have identified the Levantine Basin and the Rhodes Gyre as a source of CO_2 for the atmosphere (D'Ortenzio et al., 2008; Taillandier et al., 2012), while Cossarini et al. (2021) found that the Rhodes Gyre acts as a small sink of atmospheric carbon whereas the surrounding Levantine Basin is a source for the atmosphere. The latter study also found a shift from source to sink for the whole Levantine Basin in recent years, in response to the increasing CO2 atmospheric content. The atmospheric CO_2 absorption and dissolved inorganic carbon content in the Mediterranean Sea have been predicted to increase with the increase of temperature and stratification (Somot et al., 2006; Soto-Navarro et al., 2020) as reported by by Solidoro et al. (2022) and Reale et al. (2022). The impact of the sea surface temperature increase can either lead to more stratified upper layers, reducing deep nutrients availability and new primary production and thus affecting the organic carbon budget (Behrenfeld et al., 2006) or might enhance the rate of primary production providing an efficient carbon export to the deep layers (Taillandier et al., 2012). The Levantine Basin seems to be an ideal natural laboratory for understanding the current and future functioning of low nutrient, low chlorophyll regions with respect to CO2 fluxes (sink or source). Future works should be carried out in order to investigate more into details the dynamics of dissolved inorganic carbon and the impact of global warming on the carbon cycle of the Levantine Basin and more particularly the Rhodes Gyre .

Link between the basins

The Mediterranean Sea presents short renewal periods of water masses (LIW: 10-20 years, Stratford and Williams (1997)), and thus has fast responses to external forcings and to internal processes (convection, advection,...) in the system Napolitano et al. (2000). The Levantine Intermediate Water disperses throughout the eastern basin before being exported to the western basin through the Sicily Strait. Its physical and chemical properties change along its path suggesting both internal processes (mixing and remineralization) and perhaps further ventilation. More advanced research would make it possible to investigate the influence of LIW on the processes driving the ecosystem and biogeochemistry in different regions and elucidate processes involved in the west-east nutrient, oxygen, chlorophyll gradient, the stoichiometry and evaluate the fate of the oxygen and carbon produced within the eastern basin and exported to the western basin.

Conclusion et perspectives

Conclusion

Ce travail de thèse, basé sur un modèle 3D couplé physique-biogéochimie à haute résolution, a permis de se focaliser sur les objectifs scientifiques mentionnés dans l'introduction de ce manuscrit: L'impact de la formation des Eaux Levantines Intermédiaires (LIW) sur le cycle annuel des nutriments et du plancton, ainsi que des processus à l'origine de la dynamique de l'oxygène dissous dans le bassin oriental de la Méditerranée. Il a également contribué à l'estimation du bilan de carbone organique et d'oxygène dissous dans le Gyre de Rhodes et dans l'ensemble du Bassin Levantin.

Pour pouvoir répondre à ces objectifs scientifiques, nous avons mis en place le modèle couplé sur l'ensemble de la Méditerranée avec un focus sur le Bassin Levantin, puis validé notre modèle à l'aide de différents jeux de données : les données satellitaires (chlorophylle), de campagnes à la mer (programme PERLE et CARIMED) et les données des flotteurs BGC-Argo.

Globalement, malgré quelques biais, le modèle reproduit bien la variabilité saisonnière des paramètres biogéochimiques (oxygène, nutriments et chlorophylle) dans les couches superficielles et intermédiaires. Les comparaisons avec les flotteurs BGC-Argo montrent une sous-estimation de la concentration en chlorophylle et oxygène en subsurface. Nous avons également discuté des incertitudes potentielles pour le modèle et les observations.

L'influence du mélange hivernal sur la dynamique du carbone organique dans le gyre de Rhodes

Pour étudier le carbone organique dans le Bassin Levantin, nous nous sommes concentrés sur le principal site de formation des LIW : le Gyre de Rhodes. Ce gyre cyclonique, persistant, est considéré comme la région présentant le taux de production primaire le plus élévé dans le Bassin Levantin, fortement oligotrophe; ceci en raison de l' apport hivernal en nutriments par le mélange vertical.

Sur la base de nos résultats de modèle, nous avons décrit la variabilité saisonnière de l'écosystème planctonique. Au cours de l'automne, la couche de mélange commence à s'approfondir tandis que les nutriclines remontent. En hiver, lorsque la couche de mélange atteint les nutriclines, les événements de mélange vertical induisent une injection de nutriments en surface. L'accumulation de phytoplancton commence à augmenter puis la concentration phytoplanctonique diminue au mois de mars suite à l'appauvrissement en nutriments près de la surface. La croissance phytoplanctonique a lieu pendant la période mélange et le pic de concentration phytoplanctonique à la surface se produit généralement quand la colonne d'eau à la fin de la période de mélange quand la colonne d'eau se restratifie.

La variabilité interannuelle de l'écosystème phytoplanctonique a également été décrite. Pendant les années d'hiver froid, le mélange en profondeur conduit à une injection plus importante de nutriments dans la couche euphotique favorisant une croissance plus intense du phytoplancton.

Le bilan annuel de carbone organique permet de montrer que la couche de surface du Gyre de Rhodes agit comme une source de carbone organique pour la couche intermédiaire et les régions avoisinantes, à travers un export vers le fond et latéral. La convection dans le gyre résultant du refroidissement/densification des eaux de surface en hiver est associé à la subduction des eaux denses et de leur contenu en carbone organique vers les régions avoisinantes du Bassin Levantin puis à leur dispersion à travers la dynamique de méso et sub-mésoéchelles.

Enfin, le Gyre de Rhodes agit comme un système autotrophe. 50 % du carbone organique exporté en dessous de 150 m de profondeur est respiré à des niveaux intermédiaires et 45 % du carbone organique produit en surface est exporté vers le Bassin Levantin environnant. L'intensité de la perte de chaleur et le mélange vertical influencent la production communautaire nette, avec une augmentation du métabolisme autotrophe pendant les années froides.

La dynamique de l'oxygène dans le Bassin Levantin

Nous avons également utilisé le modèle couplé pour analyser l'évolution spatiale et temporelle de l'oxygène dissous dans les couches superficielles et intermédiaires du Bassin Levantin. La période d'étude a été marquée par des hivers contrastés par l'intensité des pertes de chaleur. Les résultats du modèle montrent qu'en hiver, au printemps et en été, l'écosystème planctonique du Bassin Levantin produit de l'oxygène dissous dans la couche de surface alors qu'il en consomme à l'automne. La couche de surface agit en moyenne comme un système faiblement autotrophe, alternant entre statut hétérotrophe et autotrophe en fonction de l'intensité de la perte de chaleur en surface hivernale. La couche intermédiaire est dominée par le processus de respiration communautaire, avec une intensité de la consommation d'oxygène dissous également liée à celle des pertes de chaleur en surface en hiver. Nos résultats confirment le statut globalement hétérotrophe du Bassin Levantin et son rôle de recyclage pour la mer Méditerranée.

Le Bassin Levantin possède une distribution spatiale hétérogène de la production communautaire nette, avec des zones productives au centre du bassin comprenant le Gyre de Rhodes;la production d'oxygène dans le Gyre de Rhodes, qui couvre 5 % de la surface du Bassin Levantin, représente 41 % de la production totale d'oxygène du bassin.

Le Bassin Levantin possède un cycle saisonnier clair pour le flux d'oxygène air-mer, et alterne entre une situation à la surface de sous-saturation en oxygène par rapport à l'atmosphère pendant l'hiver et de sur-saturation pendant les périodes stratifiées. Nos résultats montrent qu'à l'échelle annuelle le bassin est un puits d'oxygène atmosphérique, en particulier dans le Gyre de Rhodes qui présente des taux d'absorbtion 2 fois plus élevés que le Bassin Levantin. Le Bassin Levantin tend à posséder des flux air-mer plus élevés durant les années qualifiées de froides.

La couche superficielle du Bassin Levantin est une source d'oxygène dissous pour la couche intermédiaire. L'intensité de la perte de chaleur hivernale influence l'export vertical hivernal d'oxygène. Le bassin reçoit de l'oxygène de la Mer Ionienne et en exporte vers la mer Égée. L'écoulement annuel d'oxygène vers la Mer Égée dans les couche de surface et intermédiaire est fortement renforcé pendant les années dont les hivers sont froids.

Perspectives

Malgré l'amélioration des connaissances générales sur la dynamique des écosystèmes planctoniques dans le Bassin Levantin que ce travail de thèse apporte, il a été montré certaines limitations, liées aux données et outils disponibles pour la région et aux choix concernant l'initialisation et les valeurs des paramètres biogéochimiques dans le modèle. Des travaux et études complémentaires sont donc encore nécessaires pour mieux comprendre le fonctionnement et la variabilité des processus hydrodynamiques et biologiques régissant le Bassin Levantin.

Observations

Comme mentionné précédemment, le programme PERLE nous a fourni une riche base de données sur les nutriments et l'oxygène pour la partie ouest du Bassin Levantin. La base de données CARIMED, qui vise à regrouper et qualifier les différentes données d'observation recueillies lors des campagnes et à les inter-calibrer ultérieurement, a couvert un transect au centre du Levantin. Certaines lacunes ont été comblées à l'aide de données de flotteurs qui ont fourni des informations détaillées sur la variation de la chlorophylle et de l'oxygène dans la colonne d'eau dans la majeure partie du bassin. Des données satellitaires ont également été utilisées afin de qualifier la capacité du modèle à reproduire les gradients spatiaux de chlorophylle à l'échelle du bassin. Cependant, même avec la combinaison de toutes ces différentes données, notre région reste limitée en nombre d'observations dans le temps et l'espace. La plupart des parties du Levantin, à notre connaissance, sont sous-échantillonnées et certaines ne sont pas échantillonnées, par exemple aucune donnée n'était disponible pour les nutriments dans le Bassin Cilicien. Toutes ces limitations ont rendu l'exercice de validation difficile. Ainsi, une activité intensive de travail de terrain (correction satellite, flotteurs, campagnes à la mer) devrait être menée pour les paramètres physiques et biogéochimiques clés incluant de l'observation à plus long terme pour pouvoir suivre leur variabilité interannuelle.

Améliorations du modèle

Malgré de bons résultats en termes de représentation des processus hydrodynamiques et biogéochimiques par rapport aux observations, des développements supplémentaires dans la configuration de notre modèle pourraient être faits pour améliorer le réalisme de ses sorties. Dans cette étude, la configuration des rivières a été établie pour être la plus réaliste possible, cependant, les débits d'eau et les concentrations des variables biogéochimiques des rivières pour le bassin oriental devraient être prescrits avec plus de précision, ce qui est complexe en raison de la limitation des données hydrologiques.

Suggestions pour de futures études couplées

Régions de formation d'eau dense

Bien que la région du Gyre de Rhodes ait été établie comme zone majeure de formation des LIW, des observations indiquent la présence de sites de formation supplémentaires tels que la côte Turque (Fach et al., 2021). Fach et al. (2021) ont suggéré que l'équivalent de 10 % du volume de LIW produit dans la principale région de formation, le Gyre de Rhodes, pourrait être formé dans le Bassin Cilicien. Une description complète de la formation de LIW dans les zones côtières et au large et de son impact sur les processus biologiques mérite d'être approfondie.

Impact des structures méso-échelle sur la biogéochimie du bassin

Le régime hydrologique de la Méditerranée orientale est modulé par des gyres et des structures de méso-échelle. Ces structures peuvent entraîner une variabilité des propriétés biogéochimiques de la colonne d'eau, par des transferts horizontaux et verticaux des nutriments, du carbone et de l'oxygène (Siokou-Frangou et al., 2010). Comprendre les processus qui contrôlent la quantité et la qualité de l'exportation du POC vers le bassin oriental profond est nécessaire pour mieux caractériser la puissance et l'efficacité de la pompe biologique. Pedrosa-Pamies et al. (2021) ont examiné l'export de POC vers les couches profondes du Bassin Levantin dans l'anticyclone Ierapetra. Ils ont découvert que le flux de matière organique marine vers les eaux profondes du bassin oriental constitue une source de nourriture et de CO2 atmosphérique. Ce travail de thèse s'est concentré sur le Bassin Levantin et à plus petite échelle, le gyre cyclonique de Rhodes où nous avons pu quantifier l'exportation de carbone organique et d'oxygène dissous vers les couches plus profondes et vers les zones environnantes. Dans le chapitre 5, nous avons présenté une comparaison non détaillée des flux verticaux d'oxygène dissous dans un anticyclone et un cyclone dans le Bassin Levantin. Il serait intéressant de compléter notre travail par une comparaison plus approfondie de différentes structures de mésoéchelle, par exemple Ierapetra qui est susceptible d'interagir avec le Gyre de Rhodes situé à proximité, ou bien les anticyclones se développant à la périphérie est du bassin et qui interagissent avec les Eaux Atlantiques entrantes. De telles structures stockent de grandes quantités d'oxygène et de matière organique pendant des périodes de plusieurs mois à plusieurs années. Le devenir de ces constituants quand ces structures physiques sont détruites est aussi un sujet qui mérite d'être étudié.

Implications pour l'évolution future du cycle du carbone dans le bassin oriental

Cette étude a permis de mieux comprendre le cycle du carbone organique dans le Bassin Levantin. Nous n'avons décrit que le cycle du carbone organique et partiellement le cycle du DIC à travers sa consommation par le plancton et sa production par les organismes vivants. D'autres termes du budget, i.e. les flux air-mer, les termes de transport vertical et latéral, n'ont pas été analysés. Cela limite notre compréhension du rôle du Gyre de Rhodes en termes de source ou puits de CO2 atmosphérique et l'influence de l'intensité du mélange hivernal sur ces échanges. Des études antérieures ont identifié le Bassin Levantin, dont le Gyre de Rhodes, comme source de CO2 pour l'atmosphère (D'Ortenzio et al., 2008; Taillandier et al., 2012), tandis que d'après Cossarini et al. (2021) le Gyre de Rhodes agit comme un puits (faible) de carbone atmosphérique alors que le Bassin Levantin environnant est une source pour l'atmosphère. Ces études ont souligné tune tendance d'augmentation de l'absorption de CO2 atmosphérique en Méditerranée et le passage d'un rôle de source à celui de puits pour le Bassin Levantin au cours des années récentes. Il a été prédit également par Solidoro et al. (2022) et Reale et al. (2022) une augmentation de l'absorption de CO2 atmosphérique et de la teneur en carbone dans la mer Méditerranée avec l'augmentation de la température et de la stratification au cours du 21ème siècle (Somot et al., 2006; Soto-Navarro et al., 2020). L'augmentation de la température de surface de la mer conduit à des couches supérieures plus stratifiées, réduisant la disponibilité des nutriments profonds et la production primaire nouvelle et affecte ainsi le bilan du carbone organique (Behrenfeld et al., 2006). Elle pourrait aussi augmenter l'activité biologique, en particulier la production primaire, alimentant ainsi l'export de carbone organique vers les couches profondes (Taillandier et al., 2012). Le Bassin Levantin apparaît comme un laboratoire naturel idéal pour comprendre le fonctionnement actuel et futur des régions pauvres en nutriments et en chlorophylle vis-à-vis des flux de CO2 (rôle de puits ou sources). Des travaux devraient être menés afin d'étudier la dynamique du carbone inorganique dissous et l'impact du réchauffement climatique sur le cycle du carbone dans le Bassin Levantin, en particulier le Gyre de Rhodes.

Lien entre les bassins de la Méditerranée

Le renouvellement des masses d'eau est rapide en Méditerranée (LIW : 10-20 ans, Stratford and Williams (1997)), et donc cette mer présente des réponses rapides aux forçages externes et aux processus internes (mélange, convection, advection, . . .) au système ((Napolitano et al., 2000)). Les Eaux Levantines Intermédiaires se dispersent à travers le bassin est avant d'être exportées vers le bassin ouest par le détroit de Sicile. Leurs propriétés physiques et chimiques changent le long de leur trajet suggérant à la fois des processus internes de mélange et peut-être de nouvelles ventilations. Des recherches plus avancées permettraient d'étudier les principaux forçages des écosystèmes et de la biogéochimie dans différentes régions et de continuer à améliorer notre compréhension des processus à l'origine du gradient ouest-est de nutriments, d'oxygène, de chlorophylle, des valeurs de la stoechiométrie et d'évaluer le devenir de l'oxygène et du carbone produits dans le bassin oriental et exportés vers le bassin occidental.

Supplementary material

Supplement Material

Text S1: Equation of dissolved oxygen balance

The variation of the dissolved oxygen inventory in the upper layer between times t_1 and t_2 ($\Delta\, DOx\, I_{upper}$), in mol O_2 m^{-2}, is equal to the sum of all DOx fluxes within the Levantine Basin between t_1 and t_2:

$$\Delta\, DOx\, I_{upper} = DOx\, I_{upper,\,t1} - DOx\, I_{upper,t2} = \int_{t_1}^{t_2} \left(F_{DOx,air-sea} + F_{DOx,lat} + F_{DOx,vert} + F_{DOx,bgc} \right) dt \tag{S1}$$

where $F_{DOx,lat}$ and $F_{DOx,vert}$ are the lateral and vertical exchange fluxes at the boundaries of the Levantine Basin area, $F_{DOx,air-sea}$ the air-sea flux and $F_{DOx,bgc}$ is the biogeochemical flux.

$DOx\ I_{upper,t}$ was computed from:

$$DOx\, I_{upper,t} = \iint\limits_{(x,y)\in RG/z\in upper\ layer} \int DOx(x,y,z,t)\, dx\, dy\, dz \tag{S2}$$

where (x,y) belongs to the upper layer (150 m to the surface) of the Levantine Basin.

The lateral exchange flux was computed from:

$$F_{DOx,lat} = \iint\limits_{A} DOx(x,y,z,t)\, v_t(x,y,z,t)\, dA \tag{S3}$$

where v_t is the current velocity normal to the limits of the Levantine Basin (in m^3 s^{-1}), A is the area of the section from the base of the upper layer (150 m) to the surface. We distinguished the limit with the Ionian Sea and the one with the Aegean Sea (indicated on Fig. 1)

$F_{DOx,bgc}$ was computed from:

$$F_{DOx,bgc} = \int \int\limits_{(x,y)\in RG\,/\,z\,\in\, upper\ layer} \int BGCflux(x,y,z,t)\, dx\, dy\, dz \tag{S4}$$

where *BGCflux* is the biogeochemical flux, i.e. $\gamma_{C/DOx}$ GPP - $\gamma_{C/DOx}$ CR - $\gamma_{N/DOx}$ Nitrification.
Finally, the vertical transport flux, $F_{DOx,vert}$, was derived from all other terms of Eq. (S1).

The computation of DOx balance in the intermediate layer is computed in a similar way, with the inventory variation as the sum of the lateral and vertical exchanges flux at the boundaries, and biogeochemical flux.

Table S1: Metrics computed for MLD and heat flux for the Levantine basin over the period of 2013-2020 winter (December-January-February)

	Units	2013-14	2014-15	2015-16	2016-17	2017-18	2018-19	2019-20	2020-21	Mean (SD)
Mean winter heat flux	W m^{-2}	-121	-169	-137	-177	-124	-182	-168	-132	-152 (25)
Maximum MLD	m	95	123	107	121	107	112	105	92	108 (11)
Date of maximum MLD	-	4 Feb	20 Feb	25 Jan	28 Jan	26 Jan	16 Jan	9 Feb	18 Feb	-
Mean MLD	m	70	76	67	83	71	83	69	59	72 (8)

Table S2: Annual air-sea oxygen flux, biogeochemical oxygen flux, vertical flux of oxygen at 150 and 400 m for the different years and averaged over the 7-year period, estimated from the model in the Levantine basin. Positive values correspond to an input for the study area. The annual budget is calculated from December.

		Units	2013-14	2014-15	2015-16	2016-17	2017-18	2018-19	2019-20	Mean
Surface layer (0 -150 m)	Internal variation	Mol m^{-2}	-0.23	0.31	-0.22	0.06	-0.22	0.36	-0.32	-0.03 (0.28)
	Air -sea flux	Mol m^{-2}	0.7	2.11	0.96	2.11	0.89	2.15	1.26	1.45 (0.6)
	BGC	Mol m^{-2}	-0.17	0.34	0.11	0.4	-0.06	0.46	0.08	0.2 (0.2)
	NCP	Mol m^{-2}	0.82	1.39	1.15	1.5	1.06	1.6	1.2	1.23 (2.95)
	Physical transfer	Mol m^{-2}	-0.76	-2.15	-1.29	-2.46	-1.05	-2.25	-1.67	-1.66 (0.65)
	Downward flux at 150 m	Mol m^{-2}	-3.89	-6.18	-3.91	-3.94	-2.91	-4.98	-3.46	-4.2 (1.1)
	Lat Ionian flux	Mol m^{-2}	9.13	14.0	9.92	11.78	11.2	14.38	10.07	11.5 (2)
	Lat Aegean flux	Mol m^{-2}	-6.00	-9.98	-7.31	-10.31	-9.34	-11.65	-8.29	-9 (1.9)
Intermediate layer (150 - 400 m)	Internal variation	Mol m^{-2}	-0.19	0.80	-0.06	0.24	-0.03	0.72	-0.08	0.22 (0.4)
	BGC	Mol m^{-2}	-1.62	-2.24	-1.89	-2.23	-1.65	-2.33	-1.95	-2 (0.3)
	Physical transfer	Mol m^{-2}	1.45	3.04	1.84	2.48	1.62	3.05	1.86	2.19 (0.66)
	vertical flux at 400 m	Mol m^{-2}	0.58	-0.95	0.37	1.22	-0.58	-0.04	0.99	0.22 (0.79)
	Vertical flux net	Mol m^{-2}	4.47	5.24	4.28	5.16	2.33	4.94	4.45	4.4 (0.99)
	Lat Ionian flux	Mol m^{-2}	-1.41	1.4	-1.01	2.46	2.18	3.76	0.2	1.1 (1.9)
	Lat Aegean flux	Mol m^{-2}	-1.61	-3.60	-1.43	-5.14	-2.89	-5.65	-2.79	-3.3 (1.6)

Table S3 Annual air-sea oxygen flux, biogeochemical oxygen flux, vertical oxygen flux at 150 and 400 m and lateral oxygen flux averaged over the 7-year period, estimated from the model in the Rhodes Gyre. Positive values correspond to an input for the study area. The annual budget is calculated from December.

		Surface (0-150m)	Intermediate (150-400m)		Surface (0-150m)	Intermediate (150-400m)
Internal variation	Mol $m^{-2} yr^{-1}$	0.01 (0.3)	0.26 (0.39)	Gmol yr^{-1}	0.3 (8)	7 (10.8)
Air -sea flux	Mol $m^{-2} yr^{-1}$	3.92 (1.7)	-	Gmol yr^{-1}	108 (49)	-
BGC	Mol $m^{-2} yr^{-1}$	1.34 (0.56)	-1.08 (0.33)	Gmol yr^{-1}	37 (15)	-30 (9)
Physical transfer	Mol $m^{-2} yr^{-1}$	-5.25 (2)	1.35 (0.7)	Gmol yr^{-1}	-144 (57)	37 (19)
Vertical flux	Mol $m^{-2} yr^{-1}$	4.15 (4.3)	6.98 (2.7)	Gmol yr^{-1}	114 (119)	192 (75)
Lateral flux	Mol $m^{-2} yr^{-1}$	-9.4 (3.11)	-5.63 (2.3)	Gmol yr^{-1}	-258 (85)	-155 (63)

Table S4 Annual biogeochemical carbon flux, vertical flux of organic carbon at 150 and 400 m, and lateral flux towards the Aegean and Ionian seas, averaged over the 7-year period, estimated from the model for the Levantine Basin. Positive values correspond to an input for the study area.

Organic carbon for the Levantine Basin		Units	Annual mean
Surface	BGC	Gg yr^{-1}	7886 ± 1763
	Vertical Flux at 150 m	Gg yr^{-1}	-9225 ± 1642
	Aegean lateral flux	Gg yr^{-1}	-2921 ± 675
	Ionian lateral flux	Gg yr^{-1}	4777 ± 722
Intermediate	NCP	Gg yr^{-1}	-8397 ± 1583
	Aegean lateral flux	Gg yr^{-1}	-393 ± 191
	Ionian lateral flux	Gg yr^{-1}	88 ± 200
	Vertical export at 400 m	Gg yr^{-1}	531 ± 126

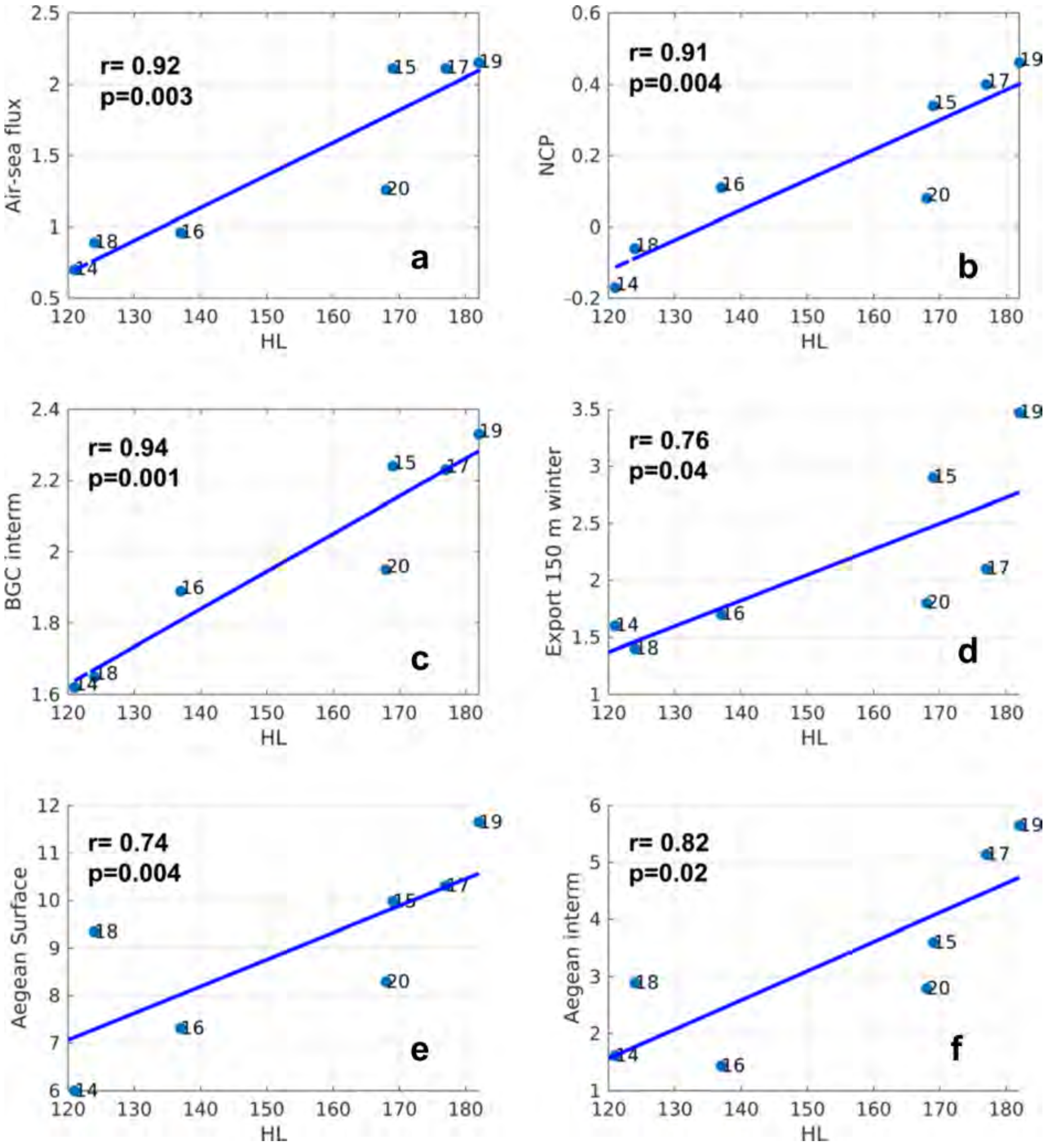

Fig S1: Scatter-plot of winter heat loss (W m^{-2}) vs. mean annual values of : (a) Air-sea oxygen flux (mol m^{-2}) into surface layer (b) NCP (mol m^{-2}), (c) biogeochemical consumption in the intermediate layer, (d) winter downward export of oxygen at 150 m, (e) lateral oxygen export towards the Aegean in the surface layer, and (f) in the intermediate layer. The years are identified by the numbers in black e.g. 14 stands for 2013-14. The blue line shows the linear regression with the 7 years.The corresponding correlations and p values are shown for each variable.

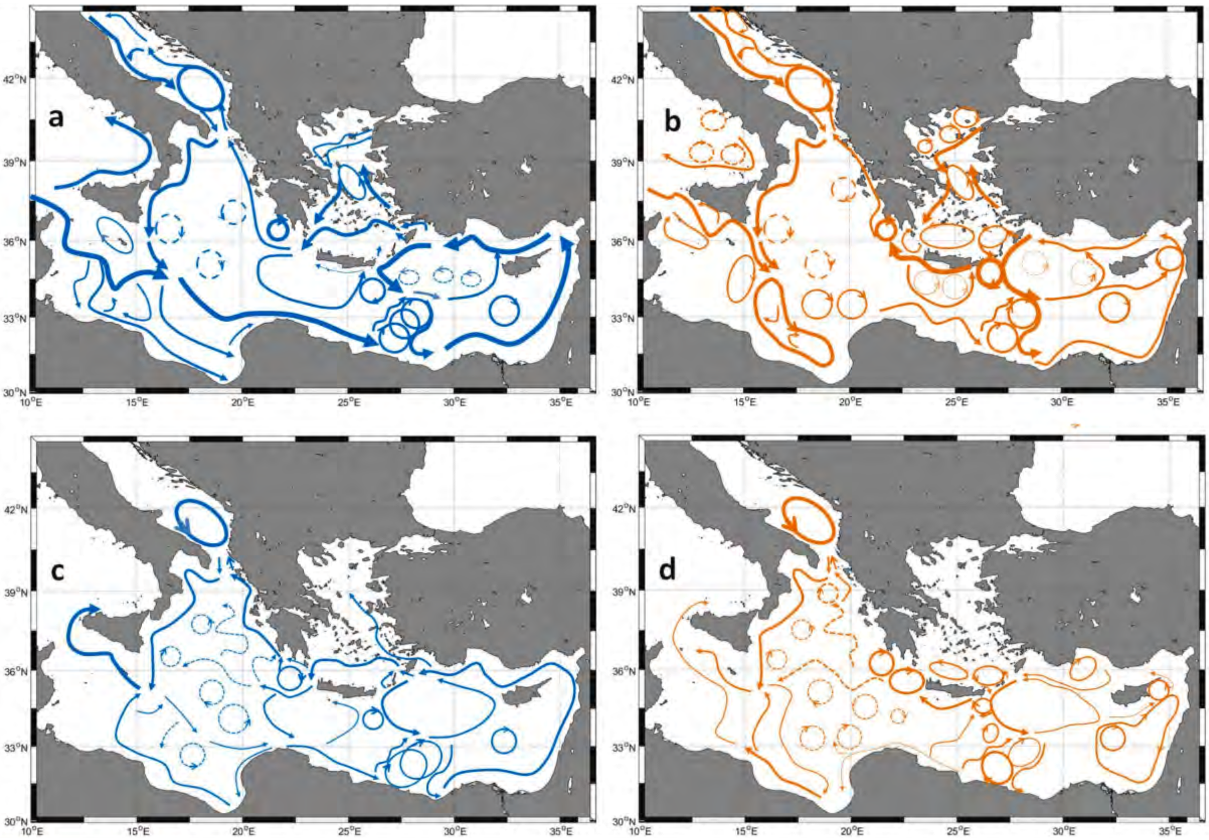

Fig S2: Seasonal simulated circulation of the surface water (a) for winter, (b) for summer, the intermediate layer (c) for winter and (d) for summer extracted from (Estournel et al., 2021).

Appendix A

Appendix A: The biogeochemical model and its initialization

A- Model description

Table 1. Name and units of the state variables of the biogeochemical model

State Variables	Description	Unit
Nut_1 (NO_3), Nut_2 (NH_4), Nut_3 (PO_4), Nut_4 (SiO_4)	Nitrate, ammonium, phosphate, silicate, with X = C (carbon), N (nitrogen), P (phosphorus) or Si (silica)	mmol X m^{-3}
$XPhy_1$, $XPhy_2$, $XPhy_3$	Pico-, nano-, micro- phytoplankton in X, X = C, N, P or Si	mmol X m^{-3}
$ChlPhy_1$, $ChlPhy_2$, $ChlPhy_3$	Pico-, nano- micro- phytoplankton in chlorophyll	mg Chl m^{-3}
$CZoo_1$, $CZoo_2$, $CZoo_3$	Nano-, micro- and meso-zooplankton	mmol C m^{-3}
CBac	Bacteria	mmol C m^{-3}
DOX	Dissolved organic X, X=carbon, nitrogen and phosphorus	mmol X m^{-3}
$XDet_Y$	Heavy (Y=H) and light (Y=L) particulate organic X, X= carbon, nitrogen, phosphorus, silica and chlorophyll	mmol X m^{-3}
DOx	Dissolved oxygen	mmol O_2 m^{-3}

Table 2. List of biogeochemical fluxes and functions

Symbol	Definition	Unit
GPP_i	Phytoplankton i gross primary production	mmol C m^{-3} d^{-1}
$\mu^{NR}_{Phy_i}$	Phytoplankton i maximal growth rate in nutrient-replete (NR) conditions	d^{-1}
μ_{Phy_i}	Phytoplankton i growth rate	d^{-1}
gml_i	Growth multi-nutrient limitation function for phytoplankton i	-
$f^{Q}_{Phy_i,Xlim}$	Phytoplankton i growth quota function, Xlim = N, P, Si	-
$f^{Q_{Phy_i,X}}_{Upt}$	Phytoplankton i quota function for uptake of nutrient XNut, X = N, P, Si	-
$RespPhy_i$	Phytoplankton i respiration rate	mmol C m^{-3} d^{-1}
$UptPhy_{i,Nut_j}$	Phytoplankton i uptake rate of nutrient Nut_j, where $Nut_1 = NO_3$, $Nut_2 = NH_4$, $Nut_3 = PO_4$, $Nut_4 = SiO_4$	mmol m^{-3} d^{-1}
$V^{max}_{Phy_i,X}$	Phytoplankton i maximum carbon specific gross uptake rate of XNut, where X = N, P, Si	mol X mol C^{-1} m^{-3} d^{-1}
$(X/C)_{Phy_i}$	Phytoplankton I internal X/C quota, X = C, N, P, Si, Chl	mol X mol C^{-1}
$Exu_{i,X}$	Phytoplankton i exudation rate of DOX, where X = C, N, P, or SiO_4	mmol X m^{-3} d^{-1}
$SynthChl_i$	Phytoplankton i chlorophyll synthesis rate	mg Chl m^{-3} d^{-1}
$\rho_{Phy_i,Chl}$	Phytoplankton i chlorophyll synthesis regulation term	g Chl mol N^{-1}

$MortPhy_{i,X}$	Phytoplankton i mortality rate in X, where X = C, N, P, Si or Chl	mmol X m^{-3} d^{-1} or mg Chl m^{-3} d^{-1}
$Graz_{i,XPrey}$	Zooplankton i grazing rate on XPrey, where Prey = Phy_i, Zoo_i, Bac, $Det_{L,H}$ and X = C, N, P, Si or Chl	mmol X m^{-3} d^{-1} or mg Chl m^{-3} d^{-1}
$(X/C)_{Prey}$	X/C quota in zooplankton prey, where Prey = Phy_i, Zoo_i, Bac, $Det_{L,H}$	mol X mol C^{-1}
$MessyFeed_{i,X}$	Zooplankton i messy feeding rate, X = C, N, P	mmol X m^{-3} d^{-1}
$Eges_{i,X}$	Zooplankton i egestion rate in X, X = C, N, P, Si or Chl	mmol X m^{-3} d^{-1}
$GrowthZoo_{i,C}$	Zooplankton i net growth rate in carbon	mmol C m^{-3} d^{-1}
$RespZoo_{i}$	Zooplankton i respiration rate	mmol C m^{-3} d^{-1}
$FoodZoo_{i,X}$	Zooplankton i food flux in X, where X = C, N, P	mmol X m^{-3} d^{-1}
$(X/C)_{FoodZoo_i}$	Zooplankton i food X/C quota, where X = C, N, P	mol X mol C^{-1}
$ExcZoo_{i,XNut}$	Zooplankton i excretion of dissolved inorganic nutrient XNut, where XNut = NH_4, PO_4	mmol X m^{-3} d^{-1}
$RespZoo_{i}^{add}$	Zooplankton i additional respiration rate	mmol C m^{-3} d^{-1}
$MortZoo_{i,X}$	Zooplankton i mortality rate in X, X = C, N, P	mmol X m^{-3} d^{-1}
$PredZoo_{3,X}$	Mortality of zooplankton 3 through predation by higher trophic level rate in X, X = C, N, P	mmol X m^{-3} d^{-1}
$UptBac_{DOX}$	Bacteria uptake of dissolved organic X, where X = C, N, P	mmol X m^{-3} d^{-1}
$UptBac_{XNut}$	Bacteria uptake of dissolved inorganic nutrient XNut, XNut = NH_4, PO_4	mmol X m^{-3} d^{-1}
$UptBac_{XNut}^{max}$	Bacteria maximal uptake of dissolved inorganic nutrient XNut, XNut = NH_4, PO_4	mmol X m^{-3} d^{-1}
$GrowthBac$	Net bacterial production	mmol C m^{-3} d^{-1}
$GrowthBac$	Potential net bacterial production	mmol C m^{-3} d^{-1}
$(X/C)_{FoodBac}$	Bacteria food X/C quota, where X = C, N, P	mol X mo C^{-1}
$(X/C)_{DOM}$	Dissolved organic matter X/C quota, where X = C, N, P	mol X mol C^{-1}
$FoodBac_{X}$	Bacteria food flux in X, X = C, N, P	mmol X m^{-3} d^{-1}
$ExcBac_{XNut}$	Bacteria excretion of dissolved inorganic nutrient XNut, XNut = NH_4, PO_4	mmol X m^{-3} d^{-1}
$RespBac$	Bacteria respiration rate	mmol C m^{-3} d^{-1}
$MortBac_{X}$	Bacteria mortality rate in X, X = C, N, P	mmol X m^{-3} d^{-1}
NBP	Nitrification flux	mmol N m^{-3} d^{-1}
Rem_{XDet_Y}	Remineralisation of XDetY, X = C, N, P, Si, Chl and Y= L (light), H (heavy)	mmol X m^{-3} d^{-1}
f^{T}	Temperature function for phytoplankton growth, zooplankton grazing, bacterial growth, remineralization and nitrification processes	-
PAR(z)	Photosynthetically active radiation at the depth z	J m^{-2} d^{-1}
PAR_{surf}	Photosynthetically active radiation at the surface: PARsurf = PAR(z=0)	J m^{-2} d^{-1}

Table 3. Equations of the biogeochemical processes

1. Phytoplankton:	
Gross primary production and growth rates	$GPP_i = \frac{a_{Chl,Phy_i} \varphi_{max,Phy_i} PAR(z) f^T_{Phy} ChlPhy_i}{1+\tau_{Phy_i}\sigma_{Phy_i}PAR(z)+\tau_{Phy_i}\frac{k_d}{k_r}\left(\sigma_{Phy_i}PAR(z)\right)^2}$ (A1) $\mu^{NR}_{Phy_i} = \frac{1}{CPhy_i}GPP_i$ (A2) $\mu_{Phy_i} = gml_i \mu^{NR}_{Phy_i}$ (A3) with {{ (A4) where Xlim such as $\frac{(X_{lim}/C)_{Phy_i}}{(X_{lim}/C)^{max}_{Phy_i}} = min\left(\frac{(X_{lim}/C)_{Phy_i}}{(X_{lim}/C)^{max}_{Phy_i}}\right) \quad with \quad X \in [N, P, Si]$ and {{ (A5)
Nutrient uptake	$UptPhy_{i,NO_3} = V^{max}_{Phy_i,N} \frac{NO_3}{NO_3+k_{Phy_i,NO_3}}\left(1 - (\delta_{i,1} + \delta_{i,2})\, Inhib\,.\, \frac{NH_4}{NH_4+k_{inhib}}\right) CPhy_i$ (A6) $UptPhy_{i,NH_4} = V^{max}_{Phy_i,N} \frac{NH_4}{NH_4+k_{Phy_i,NH_4}} CPhy_i$ (A7) $UptPhy_{i,XO_4} = V^{max}_{Phy_i,X} \frac{XO_4}{XO_s+k_{Phy_i,XO_4}}\, CPhy_i, \quad X \in [P, Si]$ (S25) with $V^{max}_{Phy_i,X} = \mu^{NR}_{Phy_i}(X/C)^{max}_{Phy_i}, X \in [N, P, Si]$ (A8)
Exudation of dissolved organic carbon	$Exu_{i,C} = \left(1 - gml_i\right) \cdot GPP_i$ (A9)
Exudation of dissolved organic X ($X \in [N, P]$) or SiO$_4$ resulting from nutrient uptake	$Exu_{i,N} = \sum_{j=1}^{2}\left(1 - f_{Upt}^{Q_{Phy_i,X}}\right)UptPhy_{i,Nut_j}$ (S28) $\mathrm{Exu}_{\mathrm{i,X}} = \left(1 - \mathrm{f}^{\mathrm{Q}}_{\mathrm{upt}_{\mathrm{X,Phyi}}}\right) \cdot \mathrm{UptPhy}_{\mathrm{i,Nut}_\mathrm{j}}, \quad j = 3,4 \quad X \in [P, Si]$ (A10)

	where $f_{Upt}^{Q_{Phy_i,X}} = \left(\frac{(X/C)_{Phy_i}^{max} - (X/C)_{Phy_i}}{(X/C)_{Phy_i}^{max} - (X/C)_{Phy_i}^{min}}\right)^2, X \in [N, P, Si]$ (A11)
Respiration	$RespPhy_i = k_{resp,Phy_i} \cdot gml_i GPP_i + \sum_j r_{Phy_i,Nut_j} UptPhy_{i,Nut_j}$ (A12)
Chlorophyll synthesis	$SynthChl_i = \rho_{Phy_i,Chl} \cdot \sum_{j=1}^{2} UptPhy_{i,Nut_j}$ (A13) $\rho_{Phy_i,Chl} = \frac{(Chl/N)_{Phy_i}^{max} \mu_{Phy_i}}{a_{Chl,Phy_i} \phi_{max,Phy_i} PAR(z) \cdot (Chl/C)_{Phy_i}} \frac{1 - \frac{(Chl/N)_{Phy_i}}{(Chl/N)_{Phy_i}^{max}}}{1.05 - \frac{(Chl/N)_{Phy_i}}{(Chl/N)_{Phy_i}^{max}}}$ (A14)
Mortality	$MortPhy_{i,X} = \tau_{mort,Phy_i} \cdot f_{Phy_i}^{T} XPhy_i,\ X \in [C, N, P, Si, Chl]$ (A15)
<u>2. Zooplankton</u>	
Grazing	$Graz_{i,XPrey} = \frac{f_{Zoo}^{T} . g_{Zoo_i} \cdot pref_{i,Prey} (CPrey)^2 (X/C)_{Prey} CZoo_i}{k_{g,Zoo_i}\left(\sum_{Prey} pref_{i,Prey} CPrey\right) + \sum_{Prey} pref_{i,Prey} (CPrey)^2},\ X \in [C, N, P, Si, Chl]$ (A16)
Messy feeding	$MessyFeed_{i,X} = \psi_{Zoo_i} \sum_{Prey} Graz_{i,XPrey},\ X \in [C, N, P]$ (A17)
Egestion	$Eges_{i,X} = \left(1 - \beta_{Zoo_i}\right) \cdot \left(1 - \psi_{Zoo_i}\right) \sum_{Prey} Graz_{i,XPrey},\ X \in [C, N, P]$ (S37) $and\ \ Eges_{i,Y} = \sum_{Prey} Graz_{i,YPrey},\ Y \in [Si, Chl]$ (A18)
Zooplankton growth	$GrowthZoo_{i,C} = k_{c,Zoo_i} \cdot \left(Graz_{i,CPrey} - Eges_{i,C} - MessyFeed_{i,C}\right)$ (A19)
Basal respiration	$RespZoo_i = \left(1 - k_{c,Zoo_i}\right) \cdot \left(Graz_{i,CPrey} - Eges_{i,C} - MessyFeed_{i,C}\right)$ (A20)
Dissolved inorganic matter excretion and additional respiration	$FoodZoo_{i,C} = GrowthZoo_{i,C}$ (A21) $FoodZoo_{i,X} = \left(Graz_{i,XPrey} - Eges_{i,X} - MessyFeed_{i,X}\right) X \in [N, P]$ (A22) $(X/C)_{FoodZoo_i} = \frac{FoodZoo_{i,X}}{FoodZoo_{i,C}},\ X \in [N, P]$

	● If the most limiting element is carbon, that is $(N/C)_{FoodZoo_i} > (N/C)_{Zoo_i}$ and $(P/C)_{FoodZoo_i} > (P/C)_{Zoo_i}$: $ExcZoo_{i,XNut} = FoodZoo_{i,X} - (X/C)_{Zoo_i} \cdot FoodZoo_{i,C} \quad , X \in [N, P]\ and\ XNut \in$ (S43) ● If the food is carbon-enriched and the most limiting element is X_1= [N or P] found by the following conditions $min_{X \in [N,P]}\left(\frac{(X/C)_{FoodZoo_i}}{(X/C)_{Zoo_i}}\right)$ and $\left(\frac{(X_1/X_2)_{FoodZoo_i}}{(X_1/X_2)_{Zoo_i}}\right)1$ (X_2= [N or P] being in excess relative to X_1) then: (A23) $ExZoo_{i,X2\ nut} = FoodZoo_{i,X2} - \frac{(X2/C)_{zoo\ i}}{(X1/C)zoo\ i} . FoodZoo_{i,x1}$ $RespZoo_i^{add} = FoodZoo_{i,C} - \frac{1}{(X1/C)zoo\ i} . FoodZoo_{i,x1}$
Mortality and predation by higher trophic level	For $i \in [1, 2]\{$ $MortZoo_{i,C} = \tau_{mort,\,Zooi} . f^T_{Zoo} . CZoo_i$ $MortZoo_{i,X} = (X/C)_{Zooi} . MortZoo_{i,\,C}$ (A24) For $Zoo_3\{$ $PredZoo_{3,C} = \tau_{pred\ i} . f^T_{Zoo} . CZoo_3^2$ $PredZoo_{3,X} = (X/C)_{Zoo3} . PredZoo_{3,\,C}$ (A25)
3. Bacteria	
Uptake of dissolved organic matter	$UptBac_{DOX} = \mu_{Bac} \cdot \left(\frac{DOC}{DOC+k_{DOC}}\right) \cdot (X/C)_{DOM} \cdot CBac$ (A26)
Uptake and release of nutrients, and net bacterial growth	$GrowthBac = \omega_{Bac} \cdot UptBac_{DOC}$ (S48) $(X/C)_{FoodBac} = \frac{1}{\omega_{Bac}}(X/C)_{DOM}\ X \in [N, P]$ $UptBac^{max}_{XNut} = \mu_{Bac} \cdot (X/C)_{Bac} \cdot \frac{XNut}{XNut+k_{XNut,Bac}} \cdot CBac,\ X \in [N, P]$ (A27) ● If the most limiting element is carbon, *i.e.* $(N/C)_{FoodBac} > (N/C)_{Bac}$and $(P/C)_{FoodBac} > (P/C)_{Bac}$: $UptBac_{x\,Nut} = 0$ with X ϵ [N, P]

$$ExcBac_{x\ Nut} = UptBac_{DOX} - GrowthBac^{*} \ . \ (X/C)_{bac}$$

with X ϵ [N, P]

$$GrowthBac = GrowthBac^{*} \qquad \text{(A28)}$$

- If the food has a deficit in element X_1 with X_1=P or N, and the element X_2 with $X_2 \neq X_1$=N or P is in excess relative to carbon. That is, $\left(X_1/C\right)_{FoodBac} \leq \left(X_1/C\right)_{Bac}$ and $\left(X_2/C\right)_{FoodBac} > \left(X_2/C\right)_{Bac}$

$$UptBac_{X1\ Nut} = min\left[\,UptBac^{max}_{X1\ Nut},\ GrowthBac^{*}.\ (X1/C)_{bac} - UptBac_{DOX}\right.$$

$$UptBac_{DOX2} = 0$$

$$ExcBac_{X1\ Nut} = 0$$

$$ExcBac_{X2\ Nut} = UptBac_{DOX2} - GrowthBac^{*} \ . \ (X2/C)_{bac}$$

$$GrowthBac = \frac{UptBac_{DOX_1} + UptBac_{X_1Nut}}{\left(X_1/C\right)_{Bac}} \qquad \text{(A29)}$$

- If the food has both deficit in nitrogen and phosphorus and X_1 is the most limiting element with X_1=P or N, that is $\left(X_1/C\right)_{FoodBac} \leq \left(X_2/C\right)_{Bac}$ and $\left(X_2/C\right)_{FoodBac} \leq \left(X_2/C\right)_{Bac}$ with $\left(X_2/X_1\right)_{FoodBac} \leq \left(X_2/X_1\right)_{Bac}$.

$$UptBac_{X_1Nut} = min\left[UptBac^{max}_{X_1Nut},\ GrowthBac\ \cdot\ \left(X_1/C\right)_{Bac} - UptBac_{DOX_1}\right.$$

If $UptBac_{DOX_2} \leq \left(UptBac_{DOX_1} + UptBac_{X_1Nut}\right)\left(X_2X_1\right)_{Bac}$

$$UptBac_{X_2Nut} = \min\left[UptBac^{max}_{X_2Nut}, \left(UptBac_{DOX_1} + UptBac^{*}_{X_1Nut}\right)\cdot\left(X_2/X_1\right)_{Bac} - UptBac\right.$$

$$ExcBac_{X_2Nut} = 0$$

$$UptBac_{X_1Nut} = \min\left[UptBac^{*}_{X_1Nut}, \left(UptBac^{max}_{X_2Nut} + UptBac_{DOX_2}\right)\cdot\left(X_1/X_2\right)_{Bac} - UptBa\right.$$

$$ExcBac_{X_1Nut} = 0$$

$$GrowthBac = \frac{UptBac_{DOX_1} + UptBac_{X_1Nut}}{\left(X_1/C\right)_{Bac}}$$

(A30)

Else

	(A31) $\text{UptBac}_{X_2\text{Nut}} = 0$ $\text{ExcBac}_{X_2\text{Nut}} = UptBac_{DOX_2} - \left(UptBac_{DOX_1} + UptBac_{X_1Nut}\right) \cdot (X_2 / X_1$ $\text{UptBac}_{X_1\text{Nut}} = UptBac^{*}_{X_1Nut}$ $\text{ExcBac}_{X_1\text{Nut}} = 0$ $\text{GrowthBac} = \frac{\text{UptBac}_{\text{DOX}_1} + \text{UptBac}_{X_1\text{Nut}}}{(X_1/C)_{\text{Bac}}}$
Respiration	$RespBac = GrowthBac \cdot \left(\frac{1}{\omega_{Bac}} - 1\right)$ (A32)
Mortality 4. Other process	$MortBac_X = \tau_{mort,Bac} \cdot f^T_{Bac} \cdot (X/C)_{Bac} \cdot CBac,\ X \in [C, N, P]$ (A33)
Remineralisation	$Rem_{XDet_{L,H}} = \tau_{rem,XDet} XDet_{L,H}$ (A34)
Nitrification	$Nitrif = \tau_{nitrif} \cdot NH_4 \cdot f^T_{Nitrif} \cdot \left(1 - \frac{PAR(z)}{PAR_{surf}}\right)$ (A35)
Temperature function for phytoplankton, zooplankton and bacterial growth, and nitrification	$f^T(T) = Q^{10^{\left(\frac{T-T^{REF}}{10}\right)}}$, Q^{10} and T^{REF} empirical constants (A36)

$\delta_{i,j}$ is the Kronecker symbol, equals to 1 if i=j, to 0 else

Table 4. List of parameters of the biogeochemical model and references.

Symbol	Description	Unit	Value			Reference
Phytoplankton			**Phy_1**	**Phy_2**	**Phy_3**	
φ_{max,Phy_i}	Maximum quantum yield	mmolC J^{-1}	2.2e-4	2.6e-4	3.6e-4	1,2,C
a_{Chl,Phy_i}	Chl-specific absorption coeff.	m^2 $mgChl^{-1}$	0.032	0.016	0.013	2,C
τ_{Phy_i}	Renewal time of photosystems	s	2.e-3	3.e-3	4.1e-3	3,C
σ_{Phy_i}	Cross-section of photosystems	m^2 J^{-1}	18	12	9	4,5,C
k_d	Dimensionless photoinhibition rate	-	2.6e-8	2.6e-8	2.6e-8	6
k_{rep}	Rate of repair of photoinhibition damaged PSII	d	2.e-4	2e-4	2e-4	6

$(N/C)_{min,Phy_i}$	Minimal internal N/C quota	molN molC^{-1}	0.05	0.05	0.05	7,8,9
$(N/C)_{max,Phy_i}$	Maximal internal N/C quota	molN molC^{-1}	0.2	0.2	0.2	7,8,9
$(P/C)_{min,Phy_i}$	Minimal internal P/C quota	molP molC^{-1}	0.004	0.002	0.002	8,10,11
$(P/C)_{max,Phy_i}$	Maximal internal P/C quota	molP molC^{-1}	0.019	0.019	0.019	8,10,11
$(Si/C)_{min,Phy_i}$	Minimal internal Si/C quota	molSi molC^{-1}	-	-	0.05	9,11
$(Si/C)_{max,Phy_i}$	Maximal internal Si/C quota	molSi molC^{-1}	-	-	0.19	9,11
$(Chl/N)_{max,Phy_i}$	Maximal internal Chl/N quota	molChl molN^{-1}	2.3	2.3	2.3	12,13,C
Q^{10}_{Phy}	Temperature coefficient	-	2.0	2.0	2.0	14
T^{REF}_{Phy}	Reference temperature	°C	14	14	14	15, C
k_{resp,Phy_i}	Respiration cost for growth	-	0.3	0.25	0.2	13,14,16,C
$\beta_{Phy_i,N}$	Nitrogen parameter for growth rate limitation	molN molC^{-1}	-	0.0072	0.002	C
$\beta_{Phy_i,P}$	Phosphorus parameter for growth rate limitation	molP molC^{-1}	-	0.0002	0.0005	C
$\beta_{Phy_i,Si}$	Silica parameter for growth rate limitation	molSi molC^{-1}	-	-	0.004	C
k_{Si}	Nitrogen parameter for growth rate limitation by silica	molN molC^{-1}	-	-	0.1	C
k_{Phy_i,NO_3}	Half saturation constant for NO$_3$	mmolN m^{-3}	0.5	0.7	1	11,15,17,18, C
k_{Phy_i,NH_4}	Half saturation constant for NH$_4$	mmolN m^{-3}	0.1	0.3	0.7	15,17,18,C
k_{inhib}	Inhibition coefficient by NH$_4$	mmolN m^{-3}	0.578	0.578	-	17
$Inhib$	Inhibition parameter by NH$_4$	-	0.82	0.82	-	17
k_{Phy_i,PO_4}	Half saturation constant for PO$_4$	mmolP m^{-3}	0.005	0.015	0.05	11,18,19,C
k_{Phy_i,SiO_4}	Half saturation constant for SiO$_4$	mmolSi m^{-3}	-	-	1.2	11,C
r_{Phy_i,NO_3}	Respiration cost for NO$_3$ uptake	molC molN^{-1}	0.397	0.397	0.397	16
r_{Phy_i,NH_4}	Respiration cost for NH$_4$ uptake	molC molN^{-1}	0.198	0.198	0.198	16
r_{Phy_i,PO_4}	Respiration cost for PO$_4$ uptake	molC molP^{-1}	0.155	0.155	0.155	16
r_{Phy_i,SiO_4}	Respiration cost for SiO$_4$ uptake	molC molSi^{-1}	-	-	0.14	16
τ_{mort,Phy_i}	Natural mortality rate	s^{-1}	3.15e-6	2.25e-6	2e-6	7,20,C
w_{s,Phy_i}	Sinking rate	m d^{-1}	-	-	0.7	7,15,C
Zooplankton			**Zoo$_1$**	**Zoo$_2$**	**Zoo$_3$**	
g_{Zoo_i}	Maximum grazing rate	d^{-1}	5.83	3.9	1.9	7,21,22, C
k_{g,Zoo_i}	Half saturation constant	mmolC m^{-3}	5	8.5	20	23,C
Ψ_{Zoo_i}	Messy feeding fraction	-	0.23	0.23	0.23	7,24

β_{Zoo_i}	Assimilation efficiency	-	0.6	0.6	0.6	7,24
k_{c,Zoo_i}	Net growth efficiency	-	0.8	0.8	0.8	7,24
$(N/C)_{Zoo_i}$	Internal N/C quota	molN molC^{-1}	0.18	0.18	0.18	7,10,25
$(P/C)_{Zoo_i}$	Internal P/C quota	molP molC^{-1}	0.013	0.013	0.013	10,25,C
τ_{mort,Zoo_i}	Natural mortality rate	d^{-1}	0.09	0.03	-	20,C
τ_{pred}	Predation mortality rate	m^3 (mmolC d)$^{-1}$	-	-	0.05	20,C
$fr_{Det_L}^{Eges_{Si}}$	Ratio light/heavy Si detritus in residu of egestion		-	-	0.8	C
$fr_{Det_L}^{MortZoo_i}$	Ratio light/heavy detritus in zooplankton loss term	-	1	1	0.95	C
Q_{Zoo}^{10}	Temperature coefficient	-	2.0	2.0	2.0	7
T_{Zoo}^{REF}	Reference temperature	°C	18	18	18	C
$pref_{i,Prey}$	Preference of Zooplankton i for Prey	-				

Zooi/Prey	Bacteria	Phy_1	Phy_2	Phy_3	Zoo_1	Zoo_2	Det_L
Zoo_1	0.35	0.65	0	0	0	0	0
Zoo_2	0.08	0.06	0.25	0.2	0.25	0.2	0.05
Zoo_3	0	0	0	0.5	0	0.45	0.05

Bacteria				
μ_{Bac}	Maximum DOC uptake	d^{-1}	3.672	15,24,C
k_{DOC}	Half-saturation for DOC uptake	mmolC m^{-3}	25	24
ω_{Bac}	Bacteria gross growth efficiency	-	0.17	24,C
$(N/C)_{Bac}$	Bacteria internal N/C quota	molN molC^{-1}	0.232	10
$(P/C)_{Bac}$	Bacteria internal P/C quota	molP molC^{-1}	0.022	10,28
$k_{NH_4,Bac}$	Half-saturation for NH_4 uptake	mmolN m^{-3}	0.2	24,C
$k_{PO_4,Bac}$	Half-saturation for PO_4 uptake	mmolP m^{-3}	0.007	25,C
$\tau_{mort,Bac}$	Bacteria natural mortality rate	d^{-1}	0.60	20
Q_{Bac}^{10}	Temperature coefficient	-	2.95	10
T_{Bac}^{REF}	Reference temperature	°C	20	C
Non-living matter				
$\tau_{rem,CDet}$	Detritus remineralisation rate, C	d^{-1}	0.04	24,C
$\tau_{rem,NDet}$	Detritus remineralisation rate, N	d^{-1}	0.05	24,C
$\tau_{rem,PDet}$	Detritus remineralisation rate, P	d^{-1}	0.06	28,C
$\tau_{rem,ChlDet}$	Detritus remineralisation rate, Chl	d^{-1}	0.1	C
$\tau_{rem,SiDet}$	Detritus remineralisation rate, Si	d^{-1}	0.005	20

w_{s,Det_L}	Light detritus sinking rate	m d^{-1}	0.7	15,C
w_{s,Det_H}	Heavy detritus sinking rate	m d^{-1}	90	15,C
Q^{10}_{rem}	Temperature coefficient for remineralization	-	2.95	10
T^{REF}_{rem}	Reference temperature for remineralization	°C	20	c
τ_{nitrif}	Nitrification rate	d^{-1}	0.05	15,C
Q^{10}_{nitrif}	Temperature coefficient for nitrification	-	2.37	10
T^{REF}_{nitrif}	Reference temperature for nitrification	°C	10	C
Chemical model				
$\gamma_{C/DOx}$	Mole of DOx used per mole of C in oxic respiration	mol O2 (mol C)	1	29
$\gamma_{NH_4/DOx}$	Mole of DOx used per mole of NH4 in nitrification	mol O2 (mol NH4) $^{-1}$	2	29

C: carbon ; N: nitrogen ; P: phosphorus ; Si: silicate ; NO3 : nitrate ; NH4 : ammonium ; PO4 : phosphate ; SiO4 : silica ; Phy1 : pico-phytoplankton ; Phy2: nano-phytoplankton ; Phy3: micro-zooplankton ; Zoo1 : nano-zooplankton ; Zoo2: micro-zooplankton ; Zoo3: meso-zooplankton ; DOC: Dissolved organic carbon ; (c) Calibration ; (1) (Babin et al., 1996) ; (2) (Claustre et al., 2005) ; (3) (Laney et al., 2005) ; (4) (Moore et al., 2003) ; (5) (Gorbunov et al., 1999) ; (6) (Oliver et al., 2003) ; (7) (Raick et al., 2005) ; (8) (Riegman et al., 2000) ; (9) (Geider et al., 1998) ; (10) (Vichi et al., 2007) ; (11) (Sarthou et al., 2005) ; (12) (van den Meersche et al., 2004) ; (13) (Sondergaard et Theil-Nielsen, 1997) ; (14) (Soetaert et al, 2001) ; (15) (Lacroix et Grégoire, 2002) ; (16) (Cannell et Thornley, 2000) ; (17) (Harrison et al., 1996) ; (18) (Tyrrell et Taylor, 1996) ; (19) (Timmermans et al., 2005) ; (20) (Fasham et al., 2006) ; (21) (Christaki et al., 2002) ; (22) (Nejstgaard et al., 1997) ; (23) (Hansen et al., 1997); (24) (Anderson et Pondaven, 2003); (25) (Goldman et al., 1987) ; (26) (Liu et Dagg, 2003) ; (27) (Thingstad et al., 1993) ; (28) (Thingstad, 2005) (29) Grégoire et al. (2008)

B- Initialization of the model

The Mediterranean Sea was divided into 10 sub-regions to initialize the biogeochemical model as in Lazzari et al. (2012) and Kesouri (2015). We imposed specific profiles of nutrients and oxygen in each of the subregions for the initialization (Figure A.1). The eastern basin was divided into 4 sub-basins: the Levantine, Aegean, Ionian and Adriatic seas. The western basin was composed of 6 sub-basins: the Gulf of Lion shelf, Ligurian Sea and Balearic and the deep Gulf of Lion to the north, Tyrrhenian, Algerian and Alboran Sea to the south.

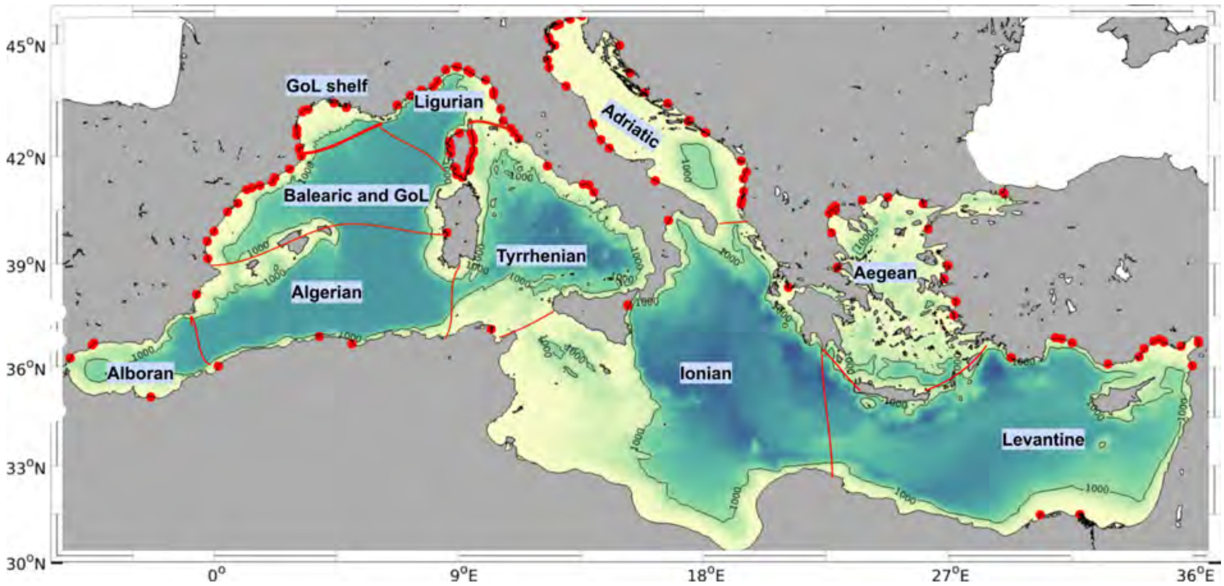

Figure A.1 Subregions of the modeled Mediterranean Sea.

The observations of nutrients, chlorophyll, dissolved oxygen concentrations from BOUM (Moutin, 2008) and Meteor (2011) cruises, as well as those included in the CARIMED database (Alvarez et al., 2019), over the summer period, before 2012, were averaged in each sub-region. The spatially averaged profiles were then imposed as initial profiles for each sub-region, by interpolating them on the model grid (Fig. A.2). These vertical profiles imposed at the initialization can have a significant influence on future simulation results, that is why it is important to correctly represent the horizontal and vertical gradient of the different variables for the more or less stratified regions. The importance of this exercise also lies in allowing the model to find in a short period of time its equilibrium with correct nutricline depths. The same protocol was also applied for the chlorophyll based on biogeochemical (BGC) Argo floats and the dissolved oxygen from cruise data and BGC Argo floats. When no chlorophyll Argo data was available, the MEDAR database was used (Fichaud et al., 2003). The initialization profiles for the eastern and western Mediterranean are represented in Figure A.2

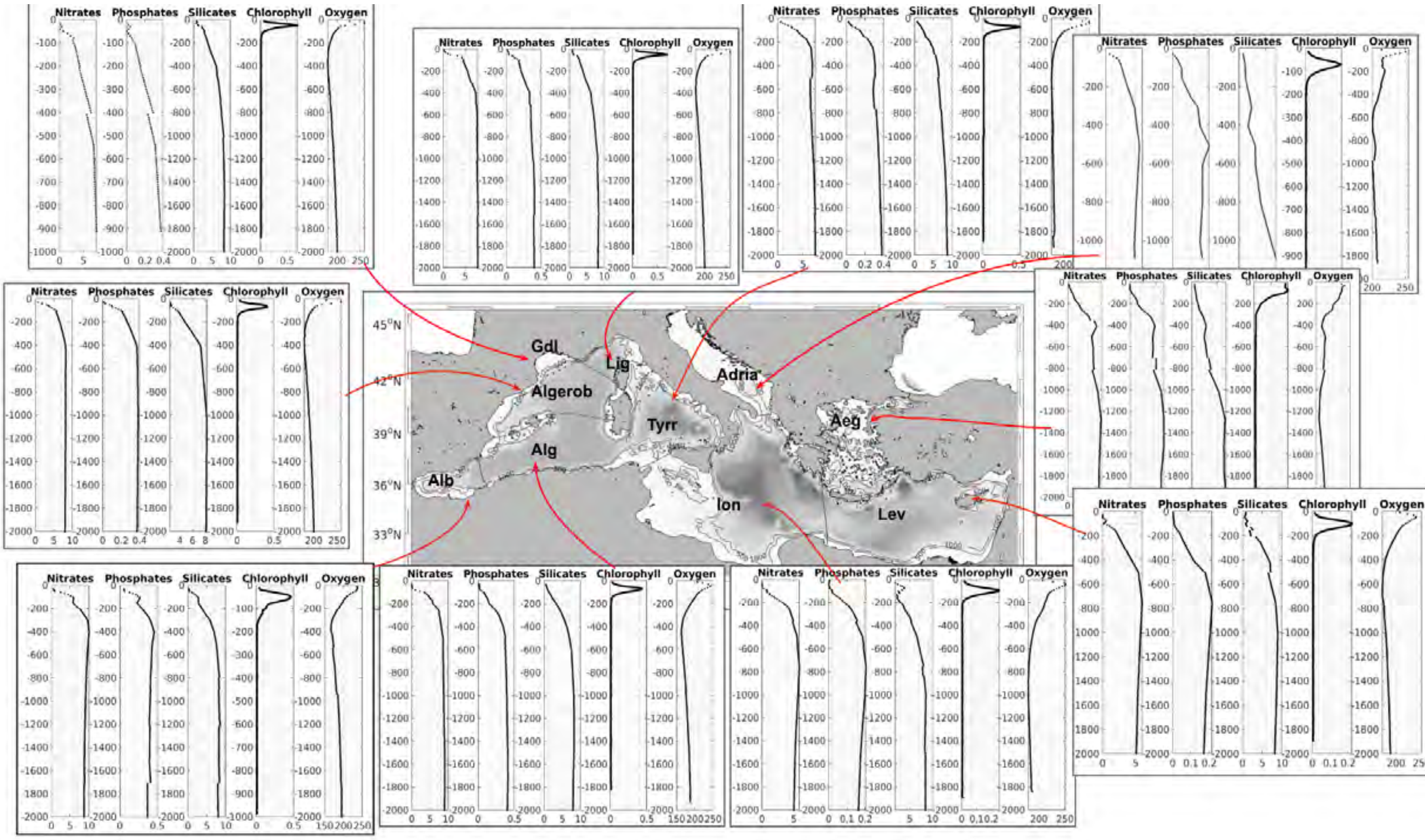

Figure A.2 profiles from the climatology of nitrates, phosphates, silicates, chlorophyll and oxygen, which will serve as the initial fields of the basin model.

Appendix B

Appendix B

1. Cruises and model comparisons

Table B.1: Statistical metrics of modeled and observed nitrate from cruises (CARIMED, PERLE-1 and PERLE-2 respectively) for the different water layers. $Mean^o$ and $Mean^m$ are the means of the observations and the model, respectively, R is the correlation coefficient and RMSD is the Root Mean Square Difference.

Nitrate		$Mean^o$	$Mean^m$	Bias	R	RMSD
CARIMED	Surface (0-150m)	0.57	0.46	-0.11	0.96	0.15
	Intermediate (150-400m)	2.39	3.23	0.83	0.96	0.92
	Transition (400-1000)	4.09	5	1.09	0.94	1.1
	Deep (1000-2000)	3.81	5.38	1.57	0.74	1.57
PERLE-1	Surface (0-150m)	0.18	0.23	0.053	0.98	0.12
	Intermediate (150-400m)	3.04	3.6	0.55	0.96	0.69
	Transition (400-1000)	5.55	5.2	0.34	0.75	0.38
	Deep (1000-2000)	5.09	5.38	0.28	0.97	0.3
PERLE-2	Surface (0-150m)	1.26	1.05	-0.21	0.93	0.29
	Intermediate (150-400m)	3.73	3.71	-0.02	0.94	0.58
	Transition (400-1000)	5.71	5.24	-0.46	Non sig	0.55
	Deep (1000-2000)	5.22	5.36	0.13	0.98	0.17

Table B.2: Statistical metrics of modeled and observed phosphate from cruises (CARIMED, PERLE-1 and PERLE-2 respectively) for the different water layers. Mean^o and Mean^m are the means of the observations and the model, respectively, R is the correlation coefficient and RMSD is the Root Mean Square Difference.

Phosphate		Mean^o	Mean^m	Bias	R	RMSD
CARIMED	Surface (0-150m)	0.024	0.011	-0.012	0.97	0.01
	Intermediate (150-400m)	0.09	0.11	0.02	0.95	0.02
	Transition (400-1000)	0.18	0.18	-0.0001	0.94	0.004
	Deep (1000-2000)	0.17	0.18	0.0096	0.97	0.0097
PERLE-1	Surface (0-150m)	0.01	0.006	-0.0046	0.84	0.01
	Intermediate (150-400m)	0.08	0.13	0.05	0.84	0.05
	Transition (400-1000)	0.22	0.18	-0.03	0.85	0.03
	Deep (1000-2000)	0.19	0.18	-0.01	0.97	0.01
PERLE-2	Surface (0-150m)	0.03	0.03	-0.0004	0.97	0.01
	Intermediate (150-400m)	0.12	0.13	0.01	0.91	0.03
	Transition (400-1000)	0.24	0.18	-0.05	0.52	0.06
	Deep (1000-2000)	0.21	0.18	-0.03	0.97	0.03

2. The float and model comparison

A- Float trajectories

We conducted an assessment of the model outputs using float data in order to validate the coupled model. In Fig. B.1 , we represent the trajectories of 11 floats in the eastern basin, covering different parts of the Levantine basin and different periods. Float 6901897 was discarded due to the bad values under the surface layer. In this section, we will focus on the comparison of the biogeochemical variables only, as the validation of the hydrodynamic variables was conducted by Estournel et al. (2021). The first step was a visual analysis of the modeled and observed chlorophyll and oxygen. This step was completed by a statistical analysis (check the results in chapter 3). It should be noted that BGC argo floats sometimes showed very high chlorophyll concentrations (>0.5mg m^{-3}) during their life cycle.

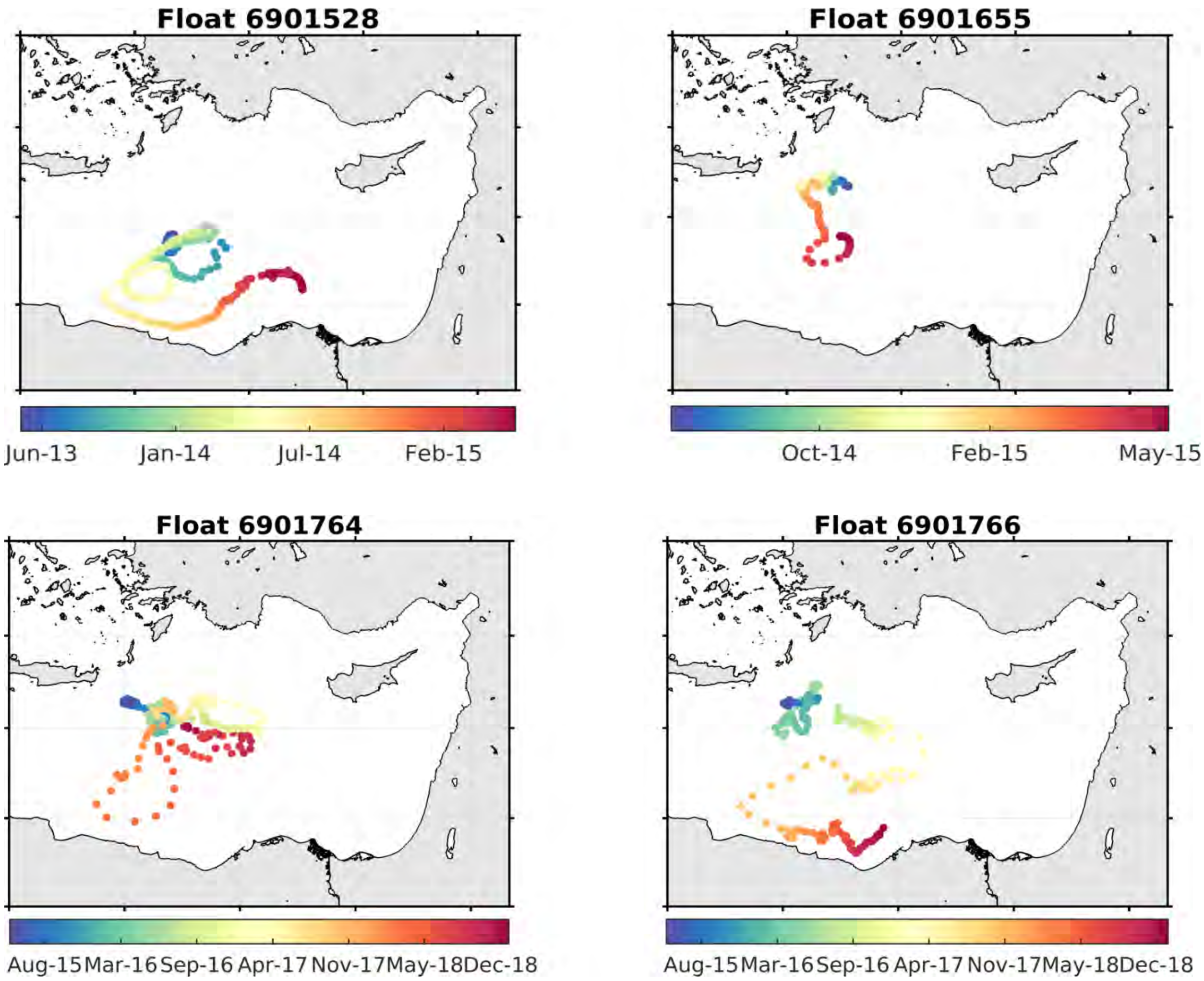

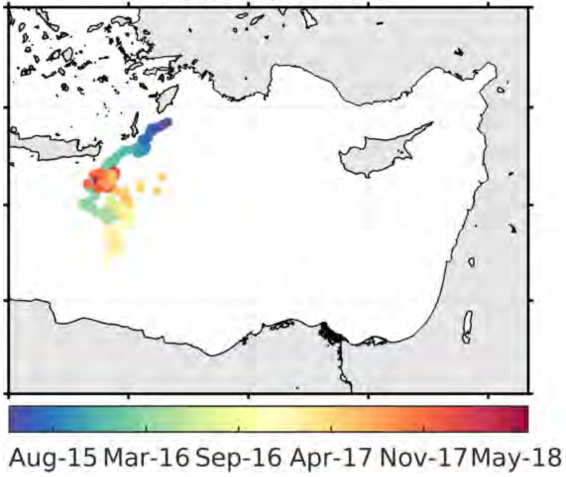

Float 6901770

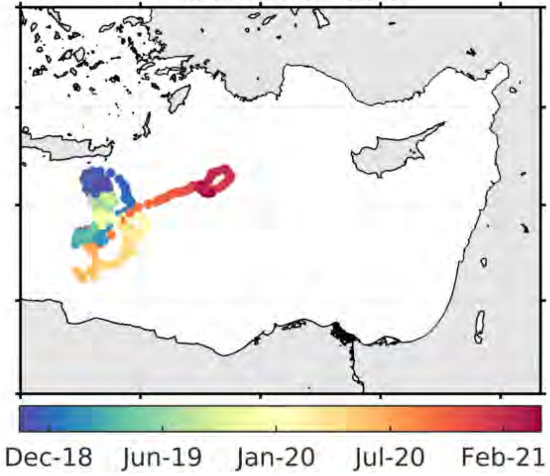

Float 6902898

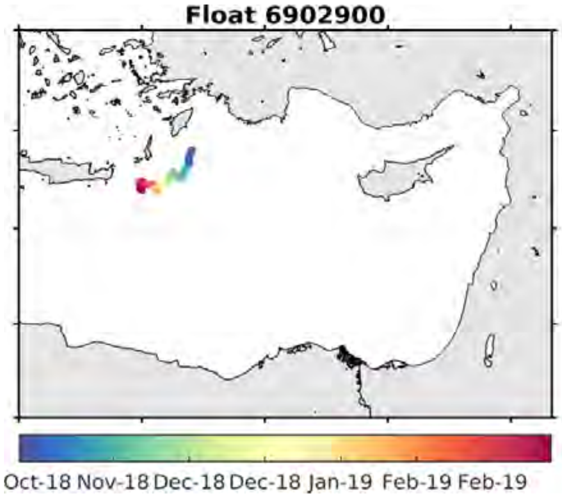

Float 6902900

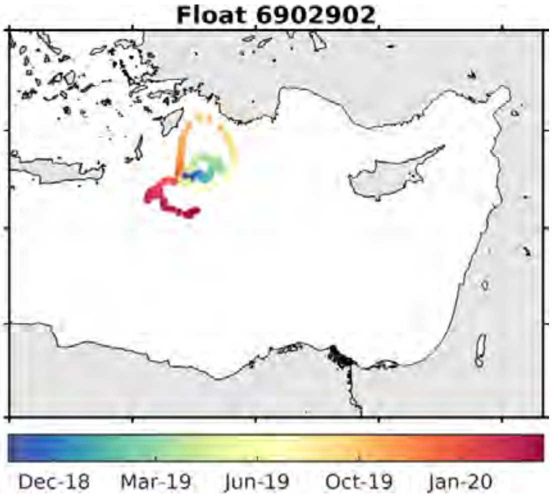

Float 6902902

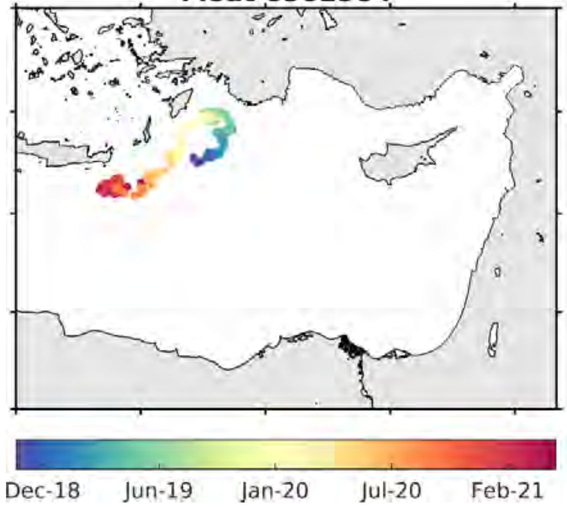

Float 6902904

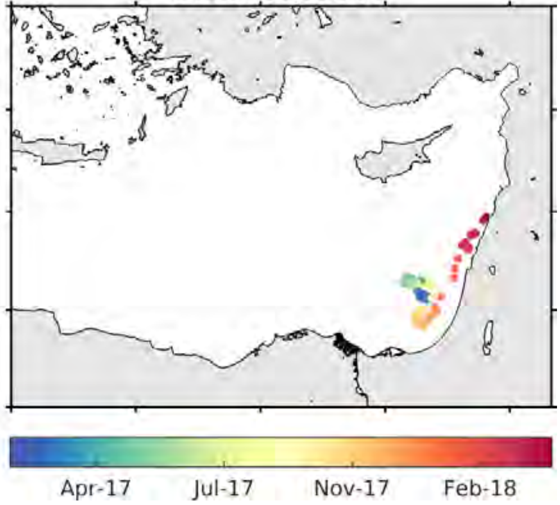

Float 6903222

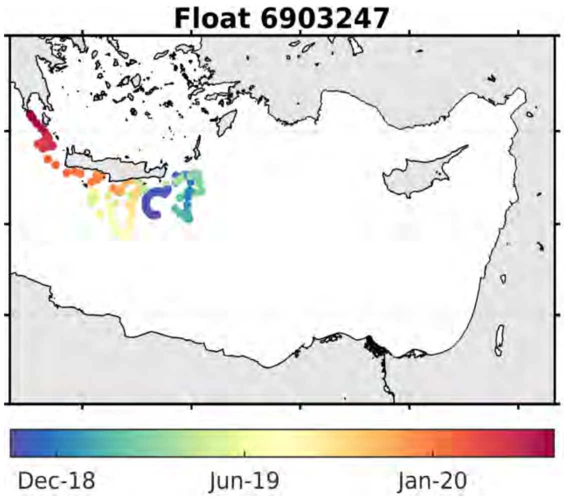

Figure B.1 The trajectories of the floats used for validation.

B- Hovmoller Chlorophyll model vs. float

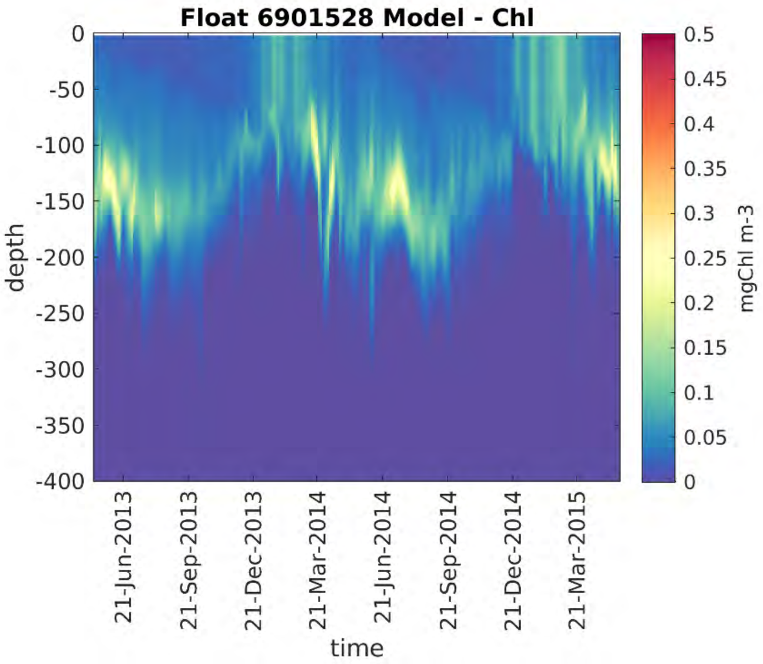

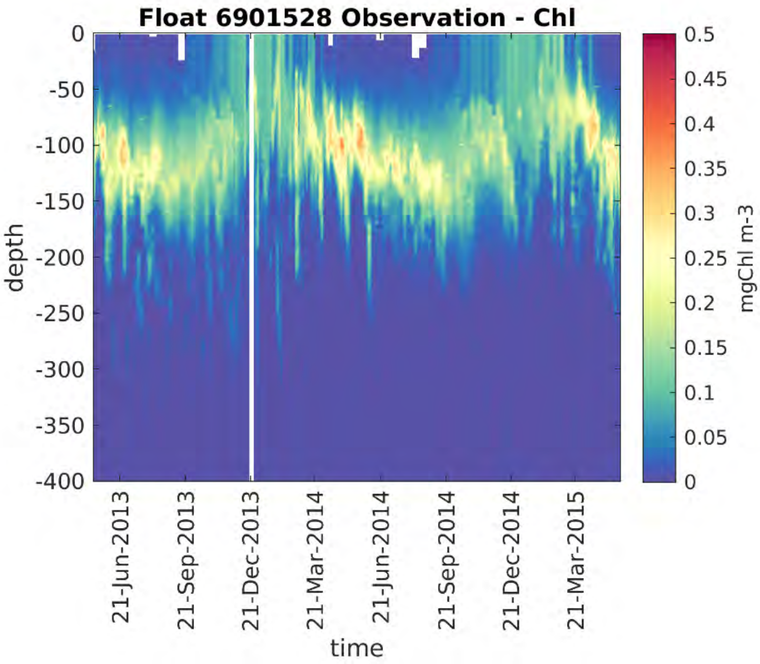

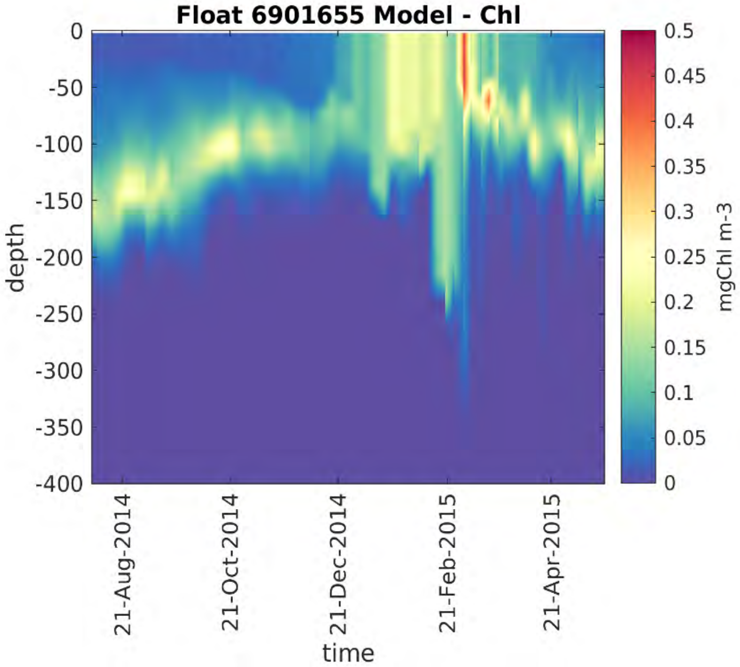
Float 6901655 Model - Chl
depth
0
-50
-100
-150
-200
-250
-300
-350
-400
21-Aug-2014
21-Oct-2014
21-Dec-2014
21-Feb-2015
21-Apr-2015
time
mgChl m-3
0.5
0.45
0.4
0.35
0.3
0.25
0.2
0.15
0.1
0.05
0

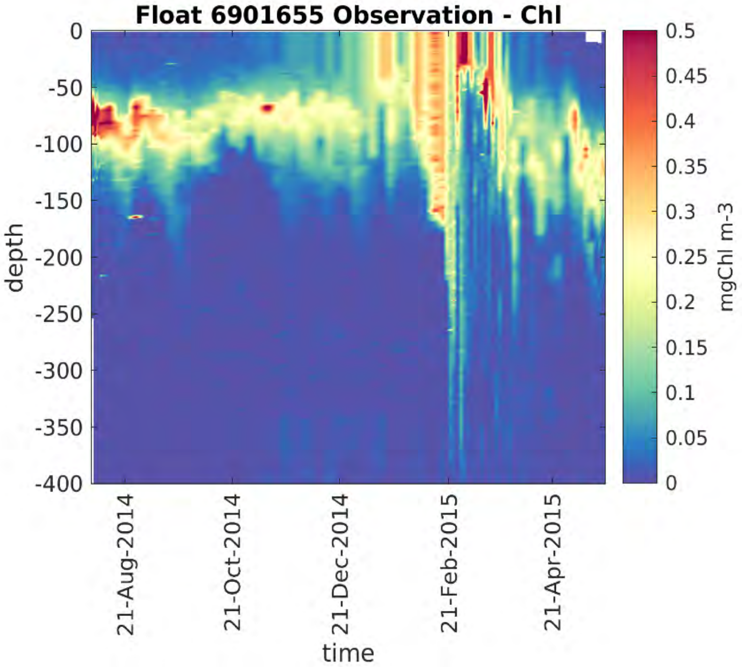
Float 6901655 Observation - Chl
depth
0
-50
-100
-150
-200
-250
-300
-350
-400
21-Aug-2014
21-Oct-2014
21-Dec-2014
21-Feb-2015
21-Apr-2015
time
mgChl m-3
0.5
0.45
0.4
0.35
0.3
0.25
0.2
0.15
0.1
0.05
0

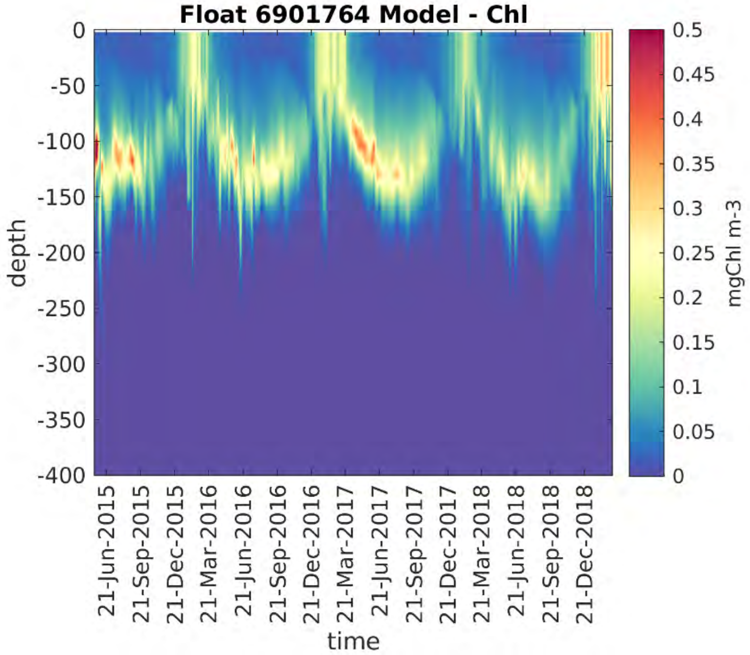
Float 6901764 Model - Chl
depth
0
-50
-100
-150
-200
-250
-300
-350
-400
21-Jun-2015
21-Sep-2015
21-Dec-2015
21-Mar-2016
21-Jun-2016
21-Sep-2016
21-Dec-2016
21-Mar-2017
21-Jun-2017
21-Sep-2017
21-Dec-2017
21-Mar-2018
21-Jun-2018
21-Sep-2018
21-Dec-2018
time
mgChl m-3
0.5
0.45
0.4
0.35
0.3
0.25
0.2
0.15
0.1
0.05
0

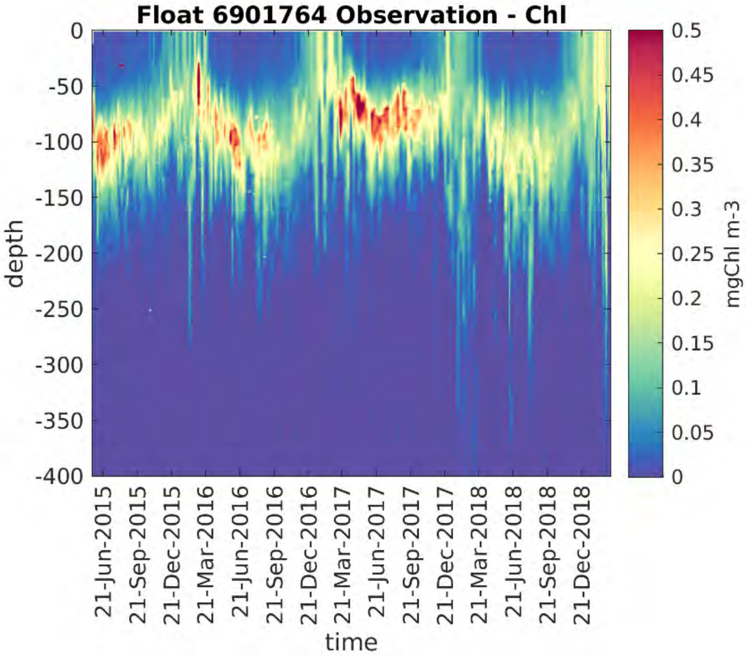
Float 6901764 Observation - Chl
depth
0
-50
-100
-150
-200
-250
-300
-350
-400
21-Jun-2015
21-Sep-2015
21-Dec-2015
21-Mar-2016
21-Jun-2016
21-Sep-2016
21-Dec-2016
21-Mar-2017
21-Jun-2017
21-Sep-2017
21-Dec-2017
21-Mar-2018
21-Jun-2018
21-Sep-2018
21-Dec-2018
time
mgChl m-3
0.5
0.45
0.4
0.35
0.3
0.25
0.2
0.15
0.1
0.05
0

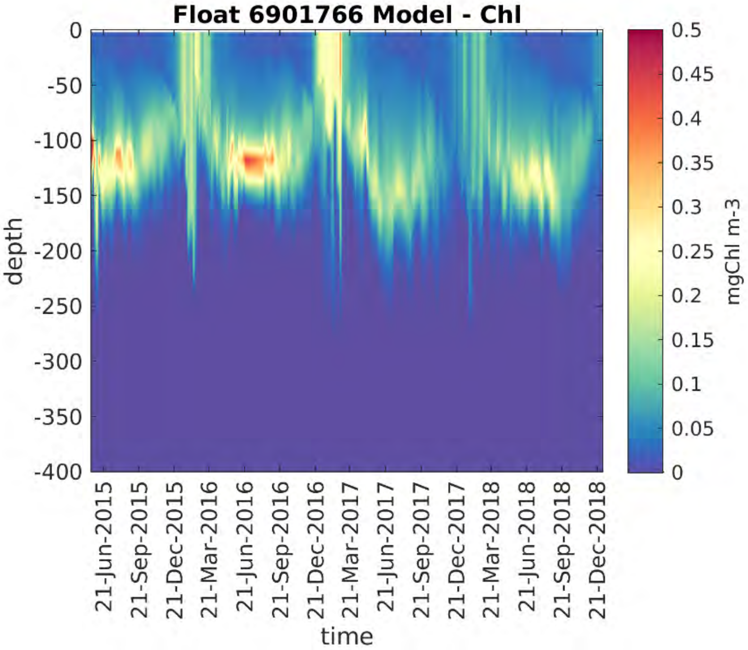
Float 6901766 Model - Chl

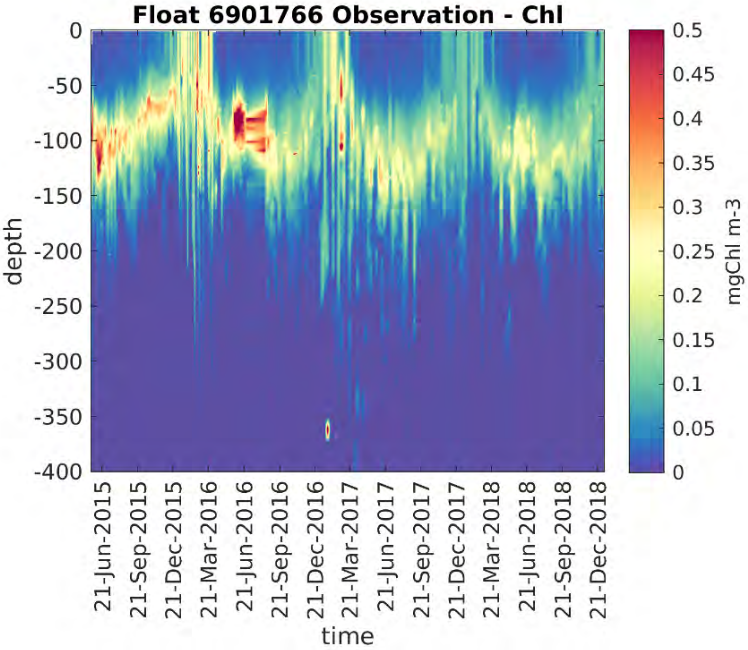
Float 6901766 Observation - Chl

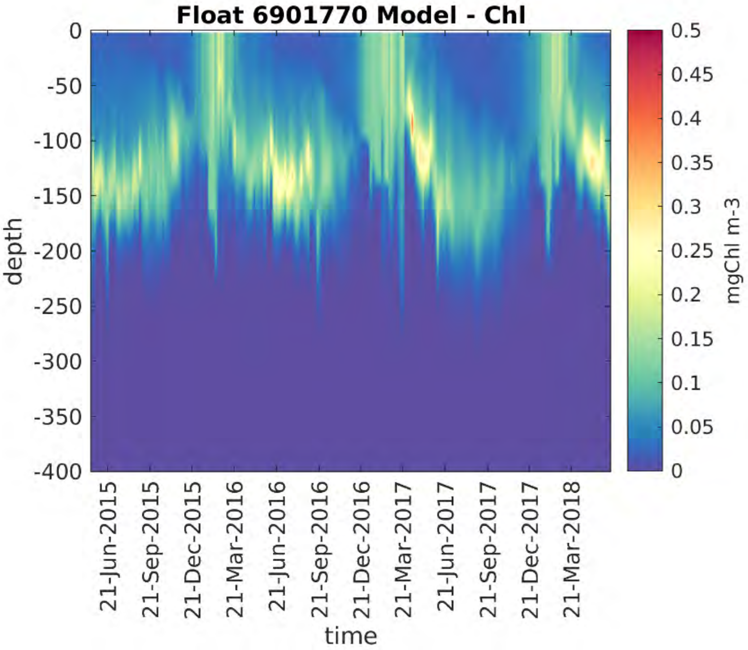
Float 6901770 Model - Chl

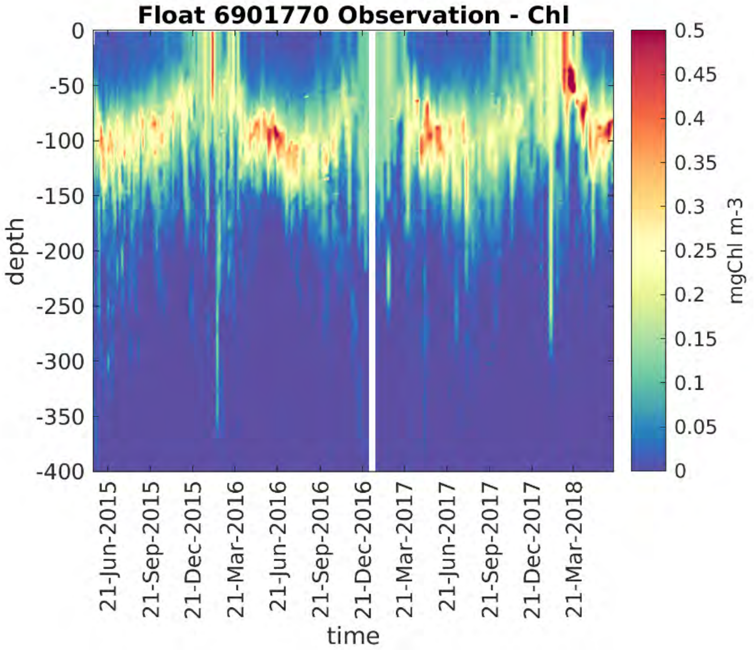
Float 6901770 Observation - Chl

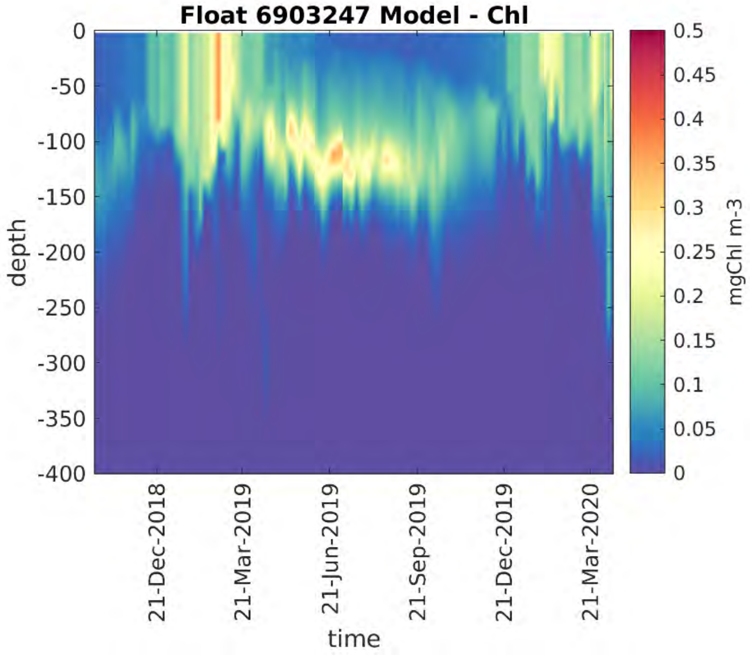

Float 6903247 Model - Chl

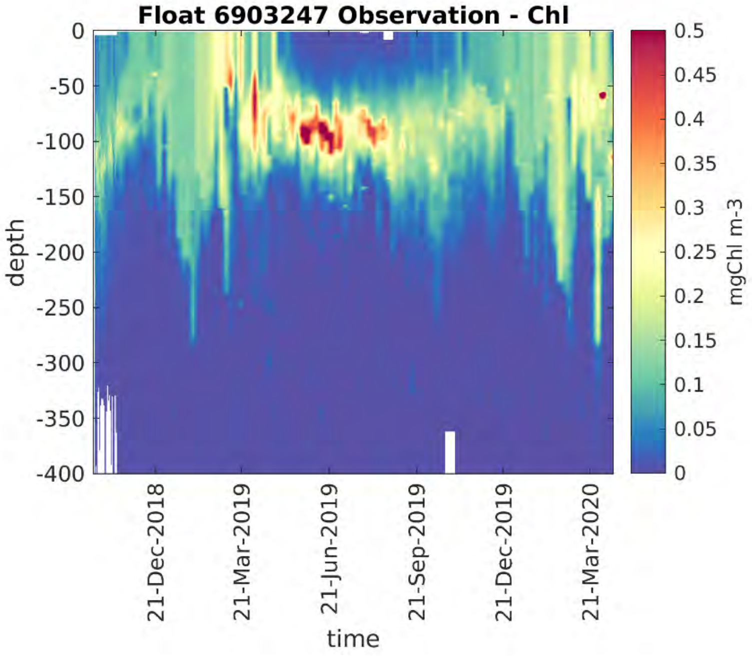

Float 6903247 Observation - Chl

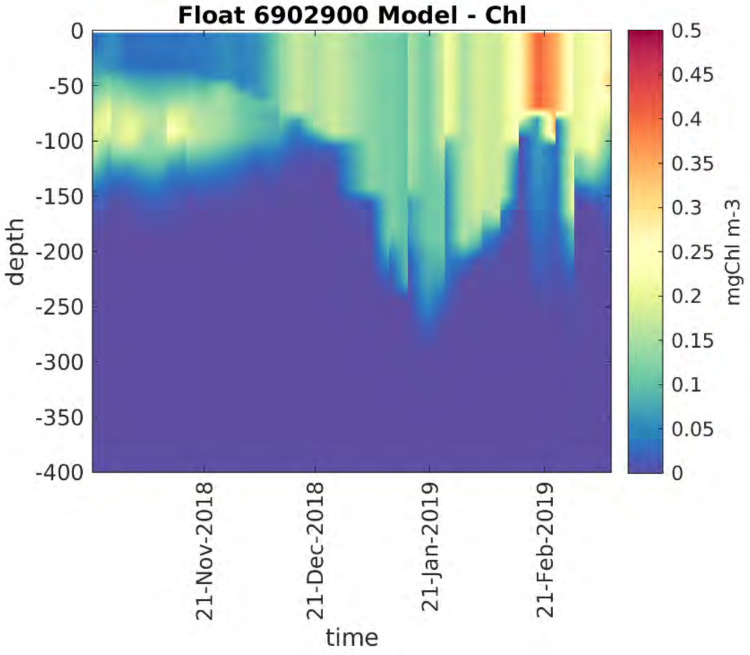

Float 6902900 Model - Chl

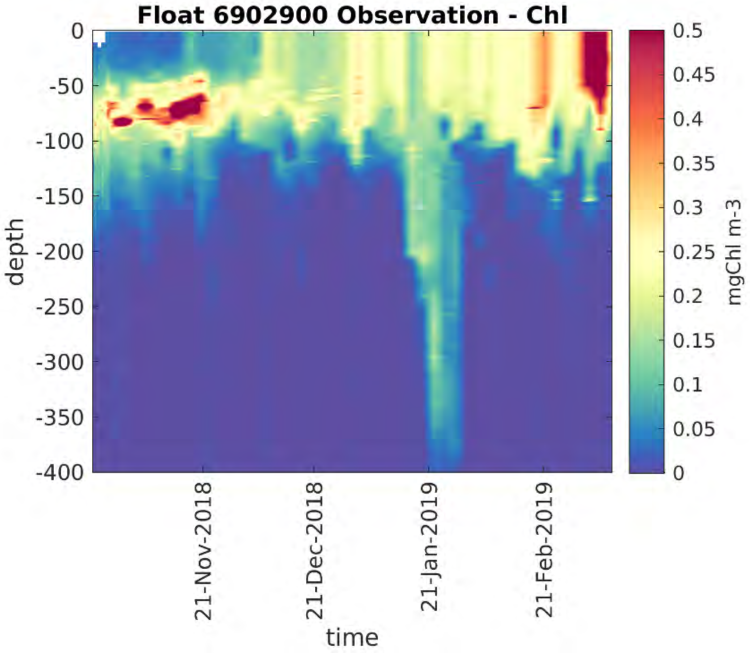

Float 6902900 Observation - Chl

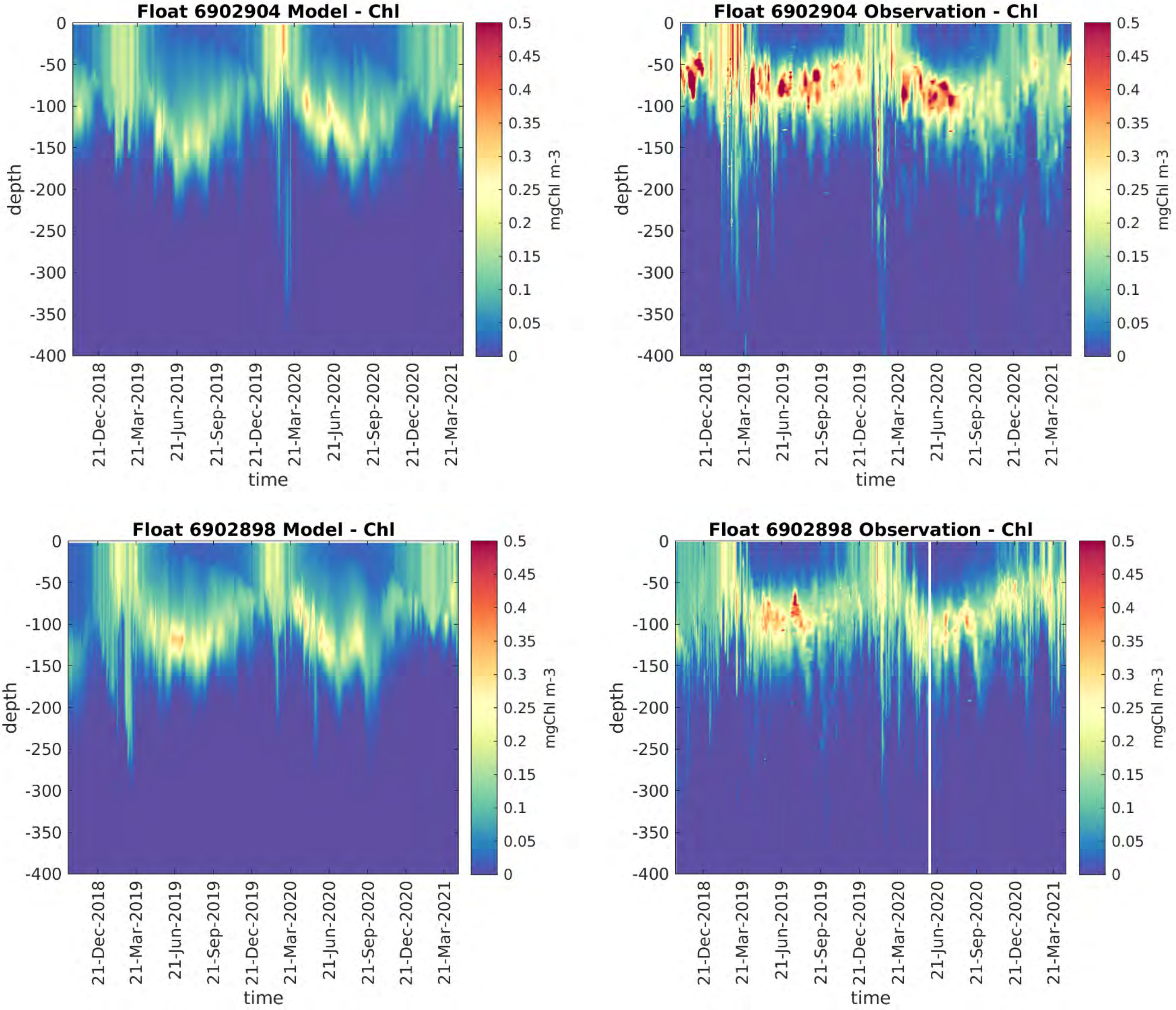

Figure B.2 Hovmoller diagrams of observed and modeled chlorophyll (mg m^{-3}) used for the model validation.

C- Hovmoller oxygen model vs. float

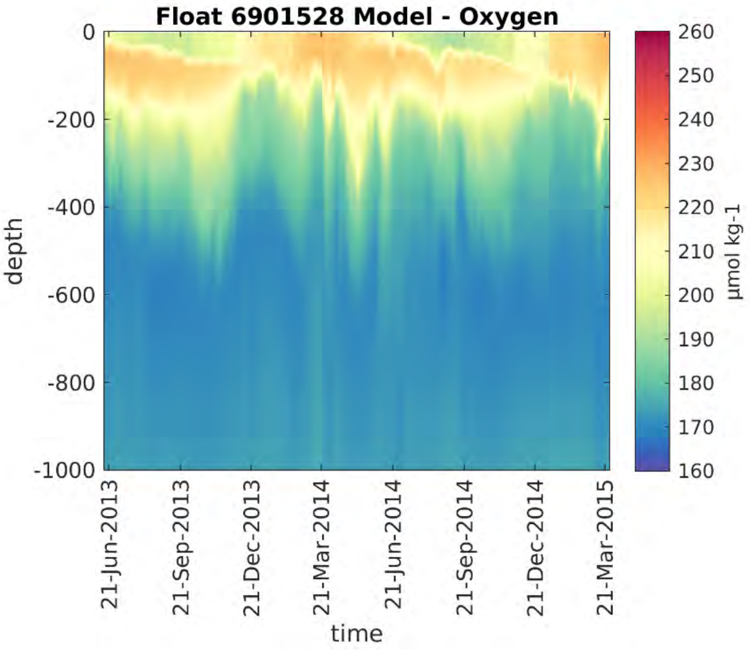
Float 6901528 Model - Oxygen

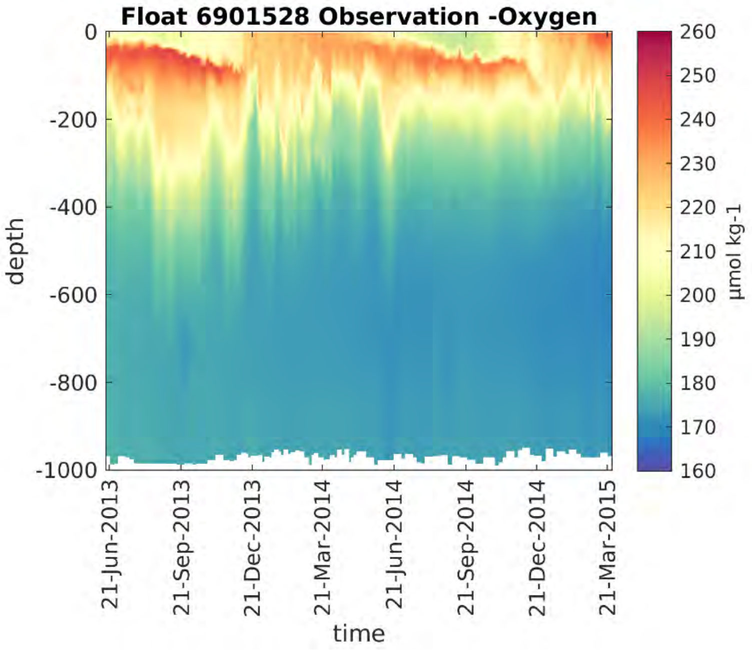
Float 6901528 Observation -Oxygen

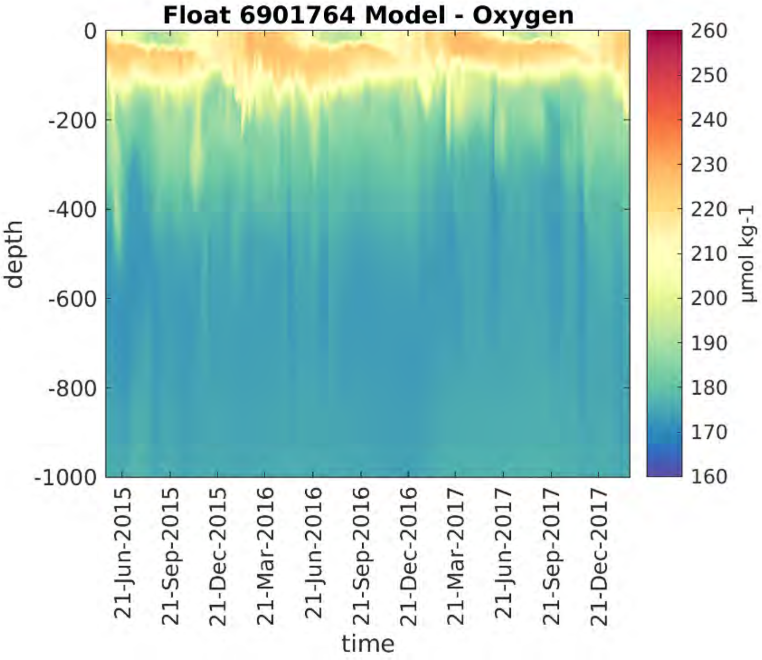
Float 6901764 Model - Oxygen

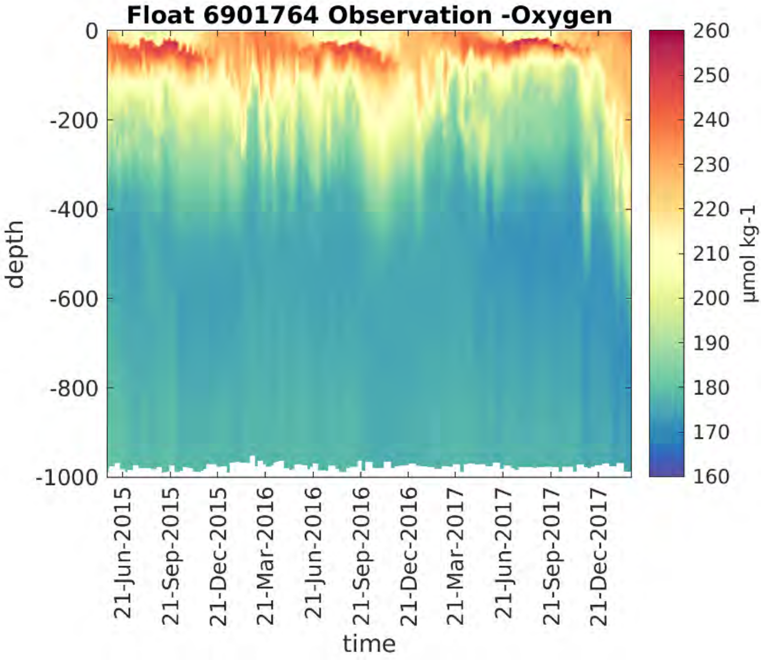
Float 6901764 Observation -Oxygen

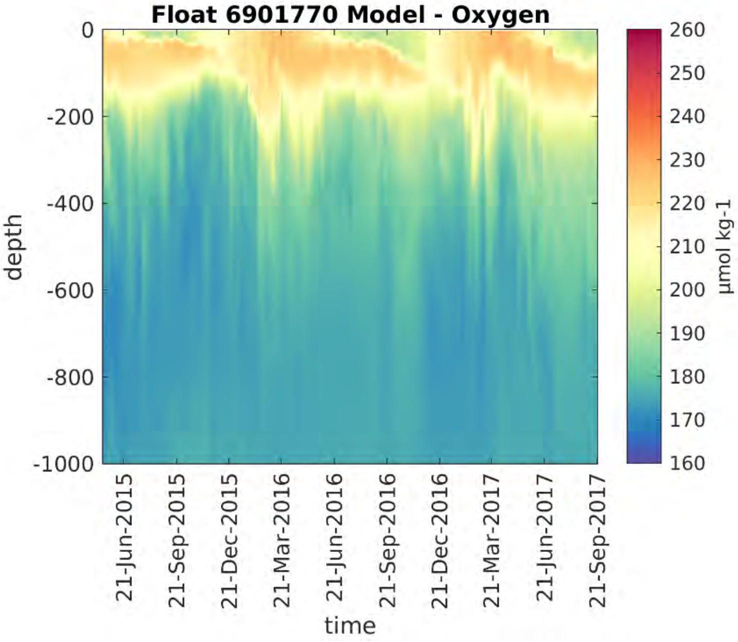
Float 6901770 Model - Oxygen

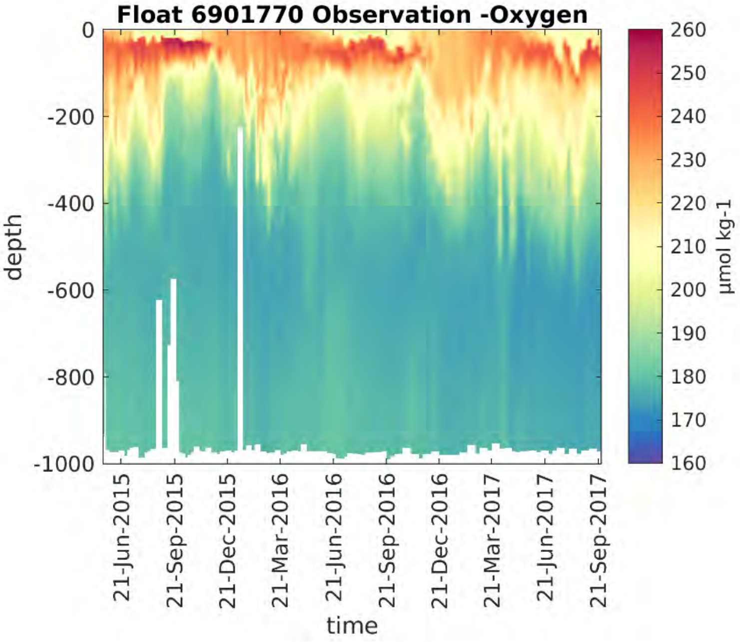
Float 6901770 Observation -Oxygen

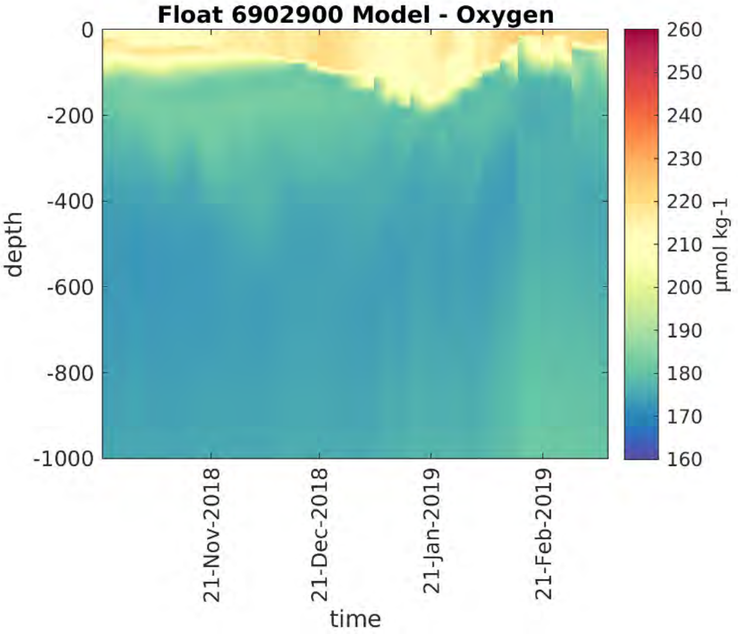
Float 6902900 Model - Oxygen

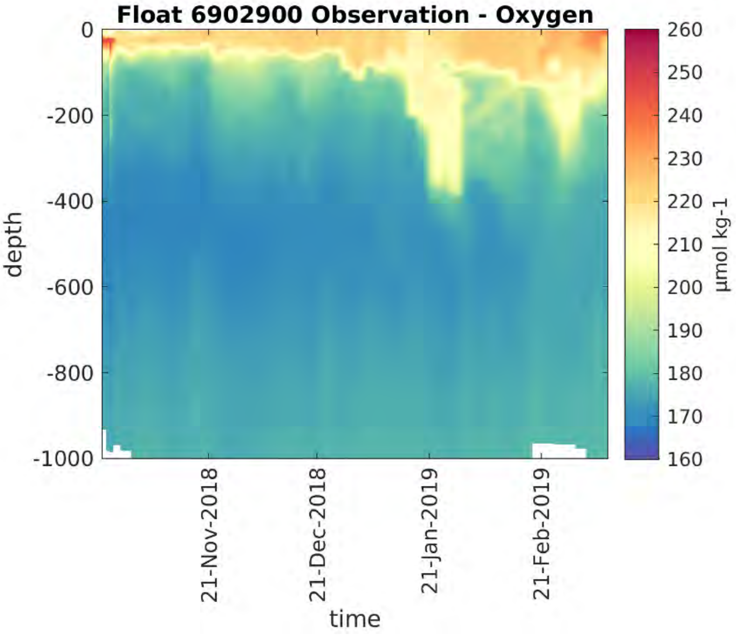
Float 6902900 Observation - Oxygen

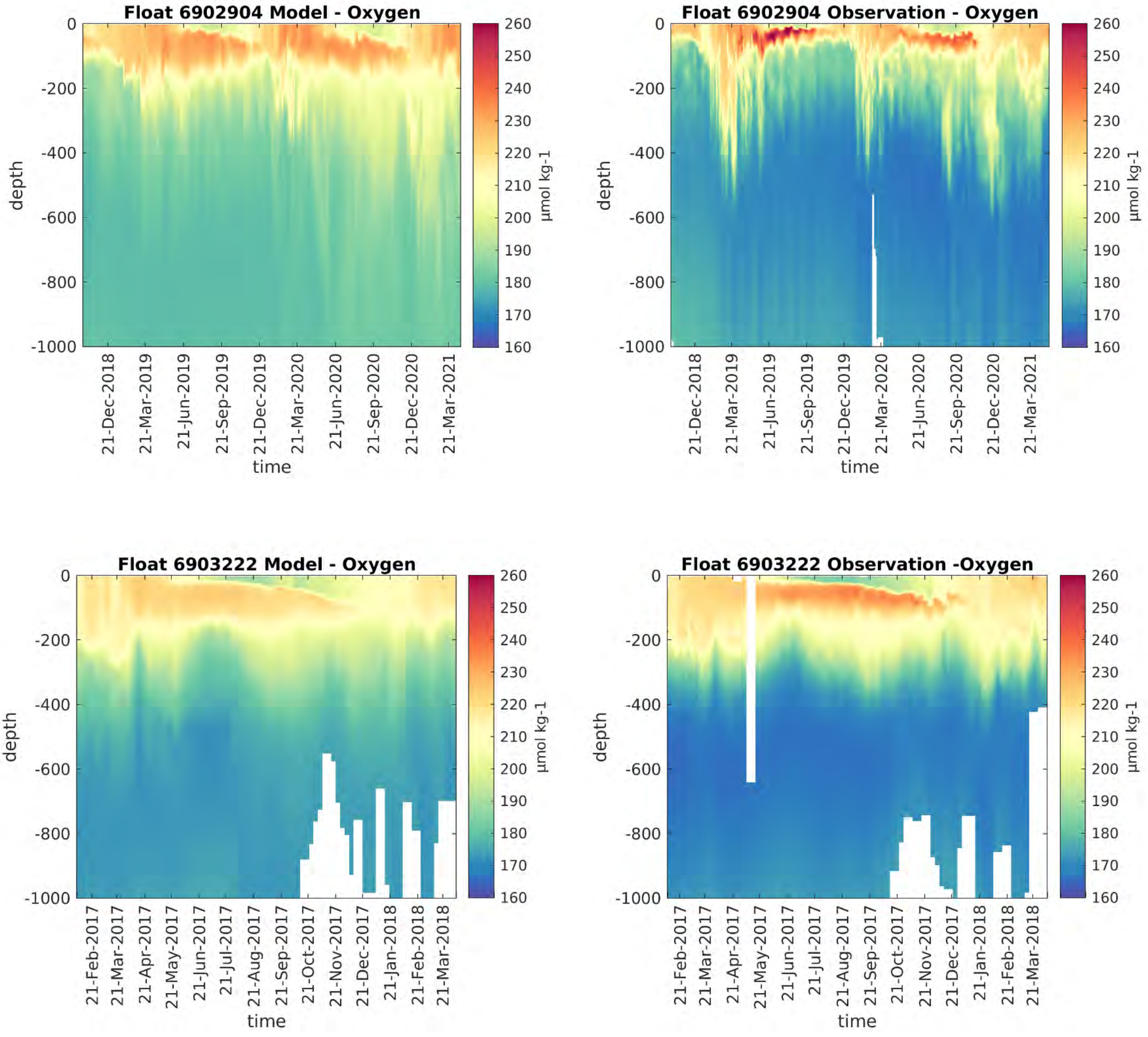

Figure B.3 Hovmoller diagrams of observed and modeled oxygen (μmol kg^{-1}) used for the model validation.

Bibliography

Akpinar, A., Yilmaz, E., Salihoglu, B., Fach, B.A., 2016. Physical oceanography of the eastern Weddell Sea. February.

Allen, J.I., Somerfield, P.J., Gilbert, F.J., 2007. Quantifying uncertainty in high-resolution coupled hydrodynamic-ecosystem models. Journal of Marine Systems 64, 3–14. doi:`10.1016/j.jmarsys.2006.02.010`.

Allen, J.I., Somerfield, P.J., Siddorn, J., 2002. Primary and bacterial production in the Mediterranean Sea: A modelling study. Journal of Marine Systems 33-34, 473–495. doi:`10.1016/S0924-7963(02)00072-6`.

Álvarez, M., Sanleón-Bartolomé, H., Tanhua, T., Mintrop, L., Luchetta, A., Cantoni, C., Schroeder, K., Civitarese, G., 2014. The CO2 system in the Mediterranean Sea: A basin wide perspective. Ocean Science 10, 69–92. doi:`10.5194/os-10-69-2014`.

Álvarez, M., Velo, A., Tanhua, T., Key, R., Heuven, S.V., Español, I., Ieo, D.O., Coruña, A., Marinas, I.D.I., 2019. Carbon, tracer and ancillary data in the MEDSEA, CARIMED: an internally consistent data product for the Mediterranean Sea. Technical Report 2019. Instituto Español de Oceanografía.

Anati, D.A., 1984. A dome of cold water in the Levantine Basin. Deep-Sea Research 31.

Anderson, T.R., Pondaven, P., 2003. Non-redfield carbon and nitrogen cycling in the Sargasso Sea: Pelagic imbalances and export flux. Deep-Sea Research Part I: Oceanographic Research Papers 50, 573–591. doi:`10.1016/S0967-0637(03)00034-7`.

Antoine, D., Andrt, J.M., Morel, A., 1996. Oceanic primary production: 2. Estimation at global scale from satellite (Coastal Zone Color Scanner) chlorophyll. Global Biogeochemical Cycles 10, 57–69. doi:`10.1029/95GB02832`.

Antoine, D., Morel, A., Andre, J.M., 1995. Algal pigment distribution and primary production in the eastern Mediterranean as derived from coastal zone color scanner observations. Journal of Geophysical Research 100. doi:`10.1029/95jc00466`.

Argo, 2022. Argo: Argo float data and metadata from Global Data Assembly Centre (Argo GDAC), SEANOE. Technical Report. ARGO GDAC. doi:`https://doi.org/https://doi.org/10.17882/42182`.

Auger, P.A., Diaz, F., Ulses, C., Estournel, C., Neveux, J., Joux, F., Pujo-Pay, M., Naudin, J.J., 2011. Functioning of the planktonic ecosystem on the Gulf of Lions shelf (NW Mediterranean) during spring and its impact on the carbon deposition: A field data and 3-D modelling combined approach. Biogeosciences 8, 3231–3261. doi:`10.5194/bg-8-3231-2011`.

Auger, P.A., Ulses, C., Estournel, C., Stemmann, L., Somot, S., Diaz, F., 2014. Interannual control of plankton communities by deep winter mixing and prey/predator interactions in the NW Mediterranean: Results from a 30-year 3D modeling study. Progress in Oceanography 124, 12–27. doi:`10.1016/j.pocean.2014.04.004`.

Avril, B., 2002. DOC dynamics in the northwestern Mediterranean sea (DYFAMED site). Deep-Sea Research Part II: Topical Studies in Oceanography 49, 2163–2182. doi:`10.1016/S0967-0645(02)00033-4`.

Baklouti, M., Faure, V., Pawlowski, L., Sciandra, A., 2006. Investigation and sensitivity analysis of a mechanistic phytoplankton model implemented in a new modular numerical tool (Eco3M) dedicated to biogeochemical modelling. Progress in Oceanography 71, 34–58. doi:`10.1016/j.pocean.2006.05.003`.

Barbieux, M., Uitz, J., Gentili, B., Pasqueron De Fommervault, O., Mignot, A., Poteau, A., Schmechtig, C., Taillandier, V., Leymarie, E., Penkerc'H, C., D'Ortenzio, F., Claustre, H., Bricaud, A., 2019. Bio-optical characterization of subsurface chlorophyll maxima in the Mediterranean Sea from a Biogeochemical-Argo float database. Biogeosciences 16, 1321–1342. doi:`10.5194/bg-16-1321-2019`.

Behrenfeld, M.J., O'Malley, R.T., Siegel, D.A., McClain, C.R., Sarmiento, J.L., Feldman, G.C., Milligan, A.J., Falkowski, P.G., Letelier, R.M., Boss, E.S., 2006. Climate-driven trends in contemporary ocean productivity. Nature 444, 752–755. doi:`10.1038/nature05317`.

Bergametti, G., Remoudaki, E., Losno, R., Steiner, E., Chatenet, B., Buat-Menard, P., 1992. Source, transport and deposition of atmospheric phosphorus over the Northwestern Mediterranean. Journal of Atmospheric Chemistry 14, 501–513. doi:`10.1007/BF00115254`.

Berman, T., TOWNSEND, D., EL SAYED, S., TREES, C., AZOV, Y., 1984. Optical transparency, chlorophyll and primary productivity in the eastern Mediterranean near the Israeli coast. Oceanologica acta 7, 367–372.

Bethoux, J.P., Copin-Montégut, G., 1986. Biological fixation of atmospheric nitrogen in the Mediterranean Sea. Limnology and Oceanography 31, 1353–1358. doi:`10.4319/lo.1986.31.6.1353`.

Bethoux, J.P., El Boukhary, M.S., Ruiz-Pino, D., Morin, P., Copin-Montégut, C., 2005. Nutrient, Oxygen and Carbon Ratios, CO2 Sequestrationand Anthropogenic Forcing in the Mediterranean Sea, in: The Mediterranean Sea. July, pp. 67–86. doi:`10.1007/b107144`.

Bethoux, J.P., Gentili, B., Morin, P., Nicolas, E., Pierre, C., Ruiz-Pino, D., 1999. The Mediterranean Sea: A miniature ocean for climatic and environmental studies and a key for the climatic functioning of the North Atlantic. Progress in Oceanography 44, 131–146. doi:`10.1016/S0079-6611(99)00023-3`.

Bethoux, J.P., de Madron, X., Nyffeler, F., Tailliez, D., Durieu de Madron, X., Nyffeler, F., Tailliez, D., 2002. Deep water in the western Mediterranean: Peculiar 1999 and 2000 characteristics, shelf formation hypothesis, variability since 1970 and geochemical inferences. Journal of Marine Systems 33-34, 117–131. doi:`10.1016/S0924-7963(02)00055-6`.

Bethoux, J.P., Morin, P., Chaumery, C., Connan, O., Gentili, B., Ruiz-Pino, D., 1998. Nutrients in the Mediterranean Sea, mass balance and statistical analysis of concentrations with respect to environmental change. Marine Chemistry 63, 155–169. doi:`10.1016/S0304-4203(98)00059-0`.

Bethoux, J.P., Morin, P., Madec, C., Gentili, B., 1992. Phosphorus and nitrogen behaviour in the Mediterranean Sea. Deep Sea Research Part A, Oceanographic Research Papers 39, 1641–1654. doi:`10.1016/0198-0149(92)90053-V`.

Béthoux, J.P., Morin, P., Ruiz-Pino, D.P., 2002. Temporal trends in nutrient ratios: Chemical evidence of Mediterranean ecosystem changes driven by human activity. Deep-Sea Research Part II: Topical Studies in Oceanography 49, 2007–2016. doi:`10.1016/S0967-0645(02)00024-3`.

Bittig, H.C., Maurer, T.L., Plant, J.N., Wong, A.P., Schmechtig, C., Claustre, H., Trull, T.W., Bhaskar, T.V., Boss, E., Dall'Olmo, G., Organelli, E., Poteau, A., Johnson, K.S., Hanstein, C., Leymarie, E., Le Reste, S.L., Riser, S.C., Rupan, A.R., Taillandier, V., Thierry, V., Xing, X., 2019. A BGC-Argo guide: Planning, deployment, data handling and usage. Frontiers in Marine Science 6. doi:`10.3389/fmars.2019.00502`.

Boldrin, A., Miserocchi, S., Rabitti, S., Turchetto, M.M., Balboni, V., Socal, G., 2002. Particulate matter in the southern Adriatic and Ionian Sea: Characterisation and downward fluxes. Journal of Marine Systems 33-34, 389–410. doi:`10.1016/S0924-7963(02)00068-4`.

Bosc, E., Bricaud, A., Antoine, D., 2004. Seasonal and interannual variability in algal biomass and primary production in the Mediterranean Sea, as derived from 4 years of SeaWiFS observations. Global Biogeochemical Cycles 18, n/a–n/a. doi:`10.1029/2003gb002034`.

Brasseur, P., Beckers, J.M., Brankart, J.M., Schoenauen, R., 1996. Seasonal temperature and salinity fields in the Mediterranean Sea: Climatological analyses of a historical data set. Deep-Sea Research Part I: Oceanographic Research Papers 43, 159–192. doi:`10.1016/0967-0637(96)00012-X`.

Bricaud, A., Bosc, E., Antoine, D., 2002. Algal biomass and sea surface temperature in the Mediterranean Basin Intercomparison of data from various satellite sensors, and implications for primary production estimates. Remote Sensing of Environment 81, 163–178. URL: `http://qualis.capes.gov.br/webqualis/principal.seam%0Ainternal-pdf://0.0.4.1/principal.html`.

Bricaud, A., Claustre, H., Ras, J., Oubelkheir, K., 2004. Natural variability of phytoplanktonic absorption in oceanic waters: Influence of the size structure of algal populations. Journal of Geophysical Research: Oceans 109, 1–12. doi:`10.1029/2004JC002419`.

Bryden, H.L., Candela, J., Kinder, T.H., 1994. Exchange through the Strait of Gibraltar. Progress in Oceanography 33, 201–248. doi:`10.1016/0079-6611(94)90028-0`.

Butenschön, M., Zavatarelli, M., Vichi, M., 2012. Sensitivity of a marine coupled physical biogeochemical model to time resolution, integration scheme and time splitting method. Ocean Modelling 52-53, 36–53. doi:`10.1016/j.ocemod.2012.04.008`.

Cardin, V., Civitarese, G., Hainbucher, D., Bensi, M., Rubino, A., 2015. Thermohaline properties in the Eastern Mediterranean in the last three decades: Is the basin returning to the pre-EMT situation? Ocean Science 11, 53–66. doi:`10.5194/os-11-53-2015`.

Christaki, U., Van Wambeke, F., Lefevre, D., Lagaria, A., Prieur, L., Pujo-Pay, M., Grattepanche, J.D., Colombet, J., Psarra, S., Dolan, J.R., Sime-Ngando, T., Conan, P., Weinbauer, M.G., Moutin, T., 2011. Microbial food webs and metabolic state across oligotrophic waters of the Mediterranean Sea during summer. Biogeosciences 8, 1839–1852. doi:`10.5194/bg-8-1839-2011`.

Christodoulaki, S., Petihakis, G., Kanakidou, M., Mihalopoulos, N., Tsiaras, K., Triantafyllou, G., 2013. Atmospheric deposition in the Eastern Mediterranean. A driving force for ecosystem dynamics. Journal of Marine Systems 109-110, 78–93. URL: `http://dx.doi.org/10.1016/j.jmarsys.2012.07.007`, doi:`10.1016/j.jmarsys.2012.07.007`.

Civitarese, G., Gačić, M., Lipizer, M., Eusebi Borzelli, G.L., 2010. On the impact of the Bimodal Oscillating System (BiOS) on the biogeochemistry and biology of the Adriatic and Ionian Seas (Eastern Mediterranean). Biogeosciences 7, 3987–3997. doi:`10.5194/bg-7-3987-2010`.

Claustre, H., Morel, A., Hooker, S.B., Babin, M., Antoine, D., Oubelkheir, K., Bricaud, A., Leblanc, K., Quéguiner, B., Maritorena, S., 2002. Is desert dust making oligotrophic waters greener? Geophysical Research Letters 29, 101–107. doi:`10.1029/2001gl014056`.

Conan, P., Testor, P., Estournel, C., D'Ortenzio, F., Pujo-Pay, M., Durrieu de Madron, X., 2018. Preface to the Special Section: Dense Water Formations in the Northwestern Mediterranean: From the Physical Forcings to the Biogeochemical Consequences. Journal of Geophysical Research: Oceans 123, 6983–6995. doi:`10.1029/2018JC014301`.

Copin-Montegut, C., Begovic, M., 2002. Distributions of carbonate properties and oxygen along the water column (0 – 2000 m) in the central part of the NW Mediterranean Sea (Dyfamed site): influence of winter vertical mixing on air – sea CO 2 and O 2 exchanges. Deep Sea Research Part II 49, 2049–2066.

Coppola, L., Legendre, L., Lefevre, D., Prieur, L., Taillandier, V., Diamond Riquier, E., 2018. Seasonal and inter-annual variations of dissolved oxygen in the northwestern Mediterranean Sea (DYFAMED site). Progress in Oceanography 162, 187–201. URL: `https://doi.org/10.1016/j.pocean.2018.03.001`, doi:`10.1016/j.pocean.2018.03.001`.

Coppola, L., Prieur, L., Taupier-Letage, I., Estournel, C., Testor, P., Lefevre, D., Belamari, S., LeReste, S., Taillandier, V., 2017. Observation of oxygen ventilation into deep waters through targeted deployment of multiple Argo-O2 floats in the north-western Mediterranean Sea in 2013. Journal of Geophysical Research: Oceans 122, 6325–6341. doi:`10.1002/2016JC012594`.

Cossarini, G., Feudale, L., Teruzzi, A., Bolzon, G., Coidessa, G., Solidoro, C., Di Biagio, V., Amadio, C., Lazzari, P., Brosich, A., Salon, S., 2021. High-Resolution Reanalysis of the Mediterranean Sea Biogeochemistry (1999–2019). Frontiers in Marine Science 8, 1–21. doi:`10.3389/fmars.2021.741486`.

Coste, B., Corre, P.L., Minas, H.J., 1988. Re-evaluation of the nutrient exchanges in the strait of gibraltar. Deep Sea Research Part A, Oceanographic Research Papers 35, 767–775. doi:`10.1016/0198-0149(88)90029-5`.

Crise, A., Allen, J.I., Baretta, J., Crispi, G., Mosetti, R., Solidoro, C., 1999. The Mediterranean pelagic ecosystem response to physical forcing. Progress in Oceanography 44, 219–243. doi:`10.1016/S0079-6611(99)00027-0`.

Crise, A., Crispi, G., Mauri, E., 1998. A seasonal three-dimensional study of the nitrogen cycle in the Mediterranean Sea Part I. Model implementation and numerical results. Journal of Marine Systems 18, 287–312. doi:`10.1016/S0924-7963(98)00016-5`.

Crispi, G., Crise, A., Solidoro, C., 2002. Coupled Mediterranean ecomodel of the phosphorus and nitrogen cycles. Journal of Marine Systems 33-34, 497–521. doi:`10.1016/S0924-7963(02)00073-8`.

Crispi, G., Mosetti, R., Solidoro, C., Crise, A., 2001. Nutrients cycling in Mediterranean basins: The role of the biological pump in the trophic regime. Ecological Modelling 138, 101–114. doi:`10.1016/S0304-3800(00)00396-3`.

Damien, P., Bosse, A., Testor, P., Marsaleix, P., Estournel, C., 2017. Modeling Postconvective Submesoscale Coherent Vortices in the Northwestern Mediterranean Sea. Journal of Geophysical Research: Oceans 122, 9937–9961. doi:`10.1002/2016JC012114`.

Di Biagio, V., Salon, S., Feudale, L., Cossarini, G., 2022. Subsurface oxygen maximum in oligotrophic marine ecosystems: mapping the interaction between physical and biogeochemical processes. Biogeosciences 2018, 1–33. doi:`10.5194/bg-2022-70`.

Diaz, P., Raimbault, F., Boudjellal, B., Garcia, N., Moutin, T., 2001. Early spring phosphorus limitation of primary productivity in a NW Mediterranean coastal zone (Gulf of Lions). Marine Ecology Progress Series 211, 51–62. doi:`10.3354/meps211051`.

Diffenbaugh, N.S., Scherer, M., 2011. Observational and model evidence of global emergence of permanent, unprecedented heat in the 20th and 21st centuries. Climatic Change 107, 615–624. doi:`10.1007/s10584-011-0112-y`.

D'Ortenzio, F., Antoine, D., Marullo, S., 2008. Satellite-driven modeling of the upper ocean mixed layer and air-sea CO2 flux in the Mediterranean Sea. Deep-Sea Research Part I: Oceanographic Research Papers 55, 405–434. doi:`10.1016/j.dsr.2007.12.008`.

D'Ortenzio, F., Lavigne, H., Besson, F., Claustre, H., Coppola, L., Garcia, N., Laës-huon, A., Reste, S.L., Malardé, D., Migon, C., Morin, P., Mortier, L., Poteau, A., Prieur, L., Raimbault, P., Testor, P., 2014. Observing mixed layer depth, nitrate and chlorophyll concentrations in the northwestern Mediterranean: A combined satellite and NO3 profiling floats experiment Fabrizio. AGU. global biogeochemical cycles , 6443–6451doi:`10.1002/2014GL061020.Received`.

D'Ortenzio, F., Marullo, S., Ragni, M., D'Alcalà, M.R., Santoleri, R., 2002. Validation of empirical SeaWiFS algorithms for chlorophyll-a retrieval in the Mediterranean Sea: A case study for oligotrophic seas. Remote Sensing of Environment 82, 79–94. doi:`10.1016/S0034-4257(02)00026-3`.

D'Ortenzio, F., Ragni, M., Marullo, S., Ribera d'Alcalà, M., 2003. Did biological activity in the Ionian Sea change after the Eastern Mediterranean Transient? Results from the analysis of remote sensing observations. Journal of Geophysical Research: Oceans 108. doi:`10.1029/2002jc001556`.

D'Ortenzio, F., Ribera d'Alcalà, M., 2009. On the trophic regimes of the Mediterranean Sea: a satellite analysis. Biogeosciences Discussions 5, 2959–2983. doi:`10.5194/bgd-5-2959-2008`.

D'Ortenzio, F., Taillandier, V., Claustre, H., Coppola, L., Conan, P., Dumas, F., Durrieu du Madron, X., Fourrier, M., Gogou, A., Karageorgis, A., Lefevre, D., Leymarie, E., Oviedo, A., Pavlidou, A., Poteau, A., Poulain, P.M., Prieur, L., Psarra, S., Puyo-Pay, M., Ribera d'Alcalà, M., Schmechtig, C., Terrats, L., Velaoras, D., Wagener, T., Wimart-Rousseau, C., du Madron, X., Fourrier, M., Gogou, A., Karageorgis, A., Lefevre, D., Leymarie, E., Oviedo, A., Pavlidou, A., Poteau, A., Poulain, P.M., Prieur, L., Psarra, S., Puyo-Pay, M., Ribera d'Alcalà, M., Schmechtig, C., Terrats, L., Velaoras, D., Wagener, T., Wimart-Rousseau, C., 2021. BGC-Argo Floats Observe Nitrate Injection and Spring Phytoplankton Increase in the Surface Layer of Levantine Sea (Eastern Mediterranean). Geophysical Research Letters 48, 1–11. doi:`10.1029/2020GL091649`.

Doval, M.D., Pérez, F.F., Berdalet, E., 1999. Dissolved and particulate organic carbon and nitrogen in the Northwestern Mediterranean. Deep-Sea Research Part I: Oceanographic Research Papers 46, 511–527. doi:`10.1016/S0967-0637(98)00072-7`.

Drobinski, P., Ducrocq, V., Alpert, P., Anagnostou, E., Béranger, K., Borga, M., Braud, I., Chanzy, A., Davolio, S., Delrieu, G., Estournel, C., Filali Boubrahmi, N., Font, J., Grubišić, V., Gualdi, S., Homar, V., Ivančan-Picek, B., Kottmeier, C., Kotroni, V., Lagouvardos, K., Lionello, P., Llasat, M.C., Ludwig, W., Lutoff, C., Mariotti, A., Richard, E., Romero, R., Rotunno, R., Roussot, O., Ruin, I., Somot, S., Taupier-Letage, I., Tintor, J., Uijlenhoet, R., Wernli, H., 2014. HYMEX: A 10-year multidisciplinary program on the mediterranean water cycle. Bulletin of the American Meteorological Society 95, 1063–1082. doi:`10.1175/BAMS-D-12-00242.1`.

Duce, R.A., LaRoche, J., Altieri, K., Arrigo, K.R., Baker, A.R., Capone, D.G., Cornell, S., Dentener, F., Galloway, J., Ganeshram, R.S., Geider, R.J., Jickells, T., Kuypers, M.M., Langlois, R., Liss, P.S., Liu, S.M., Middelburg, J.J., Moore, C.M., Nickovic, S., Oschlies, A., Pedersen, T., Prospero, J., Schlitzer, R., Seitzinger, S., Sorensen, L.L., Uematsu, M., Ulloa, O., Voss, M., Ward, B., Zamora, L., 2008. Impacts of atmospheric anthropogenic nitrogen on the open ocean. Science 320, 893–897. doi:`10.1126/science.1150369`.

Ducklow, H.W., Steinberg, D.K., Buesseler, K.O., 2001. Upper ocean carbon export and the biological pump. Oceanography 14, 50–58. doi:`10.5670/oceanog.2001.06`.

Dukhovskoy, D.S., Morey, S.L., Martin, P.J., O'Brien, J.J., Cooper, C., 2009. Application of a vanishing, quasi-sigma, vertical coordinate for simulation of high-speed, deep currents over the Sigsbee Escarpment in the Gulf of Mexico. Ocean Modelling 28, 250–265. URL: `http://dx.doi.org/10.1016/j.ocemod.2009.02.009`, doi:`10.1016/j.ocemod.2009.02.009`.

Ediger, D., Tugrul, S., Yilmaz, A., 2005. Vertical profiles of particulate organic matter and its relationship with chlorophyll-a in the upper layer of the NE Mediterranean Sea. Journal of Marine Systems 55, 311–326. doi:`10.1016/j.jmarsys.2004.09.003`.

Ediger, D., Yilmaz, A., 1996. Characteristics of deep chlorophyll maximum in the Northeastern Mediterranean with respect to environmental conditions. Journal of Marine Systems 7963.

Escudier, R., Clementi, E., Cipollone, A., Pistoia, J., Drudi, M., Grandi, A., Lyubartsev, V., Lecci, R., Aydogdu, A., Delrosso, D., Omar, M., Masina, S., Coppini, G., Pinardi, N., 2021. A High Resolution Reanalysis for the Mediterranean Sea. Frontiers in Earth Science 9, 1–20. doi:`10.3389/feart.2021.702285`.

Estournel, C., Broche, P., Marsaleix, P., Devenon, J.L., Auclair, F., Vehil, R., 2001. The rhone river plume in unsteady conditions: Numerical and experimental results. Estuarine, Coastal and Shelf Science 53, 25–38. doi:`10.1006/ecss.2000.0685`.

Estournel, C., De Madron, X.D., Marsaleix, P., Auclair, F., Julliand, C., Vehil, R., 2003. Observation and modeling of the winter coastal oceanic circulation in the Gulf of Lion under wind conditions influenced by the continental orography (FETCH experiment). Journal of Geophysical Research: Oceans 108, 1–19. doi:`10.1029/2001jc000825`.

Estournel, C., Kondrachoff, V., Marsaleix, P., Vehil, R., 1997. The plume of the Rhone: Numerical simulation and remote sensing. Continental Shelf Research 17, 899–924. doi:`10.1016/S0278-4343(96)00064-7`.

Estournel, C., Marsaleix, P., Ulses, C., 2021. A new assessment of the circulation of Atlantic and Intermediate Waters in the Eastern Mediterranean. Progress in Oceanography 198, 102673. doi:`10.1016/j.pocean.2021.102673`.

Estournel, C., Testor, P., Taupier-Letage, I., Bouin, M.N., Coppola, L., Durand, P., Conan, P., Bosse, A., Brilouet, P.E., Beguery, L., Belamari, S., Béranger, K., Beuvier, J., Bourras, D., Canut, G., Doerenbecher, A., de Madron, X.D., D'Ortenzio, F., Drobinski, P., Ducrocq, V., Fourrié, N., Giordani, H., Houpert, L., Labatut, L., Brossier, C.L., Nuret, M., Prieur, L., Roussot, O., Seyfried, L., Somot, S., 2016. HyMeX-SOP2: The field campaign dedicated to dense water formation in the northwestern Mediterranean. Oceanography 29, 196–206. doi:`10.5670/oceanog.2016.94`.

Estournel, C., Zervakis, V., Marsaleix, P., Papadopoulos, A., Auclair, F., Perivoliotis, L., Tragou, E., 2005. Dense water formation and cascading in the Gulf of Thermaikos (North Aegean), from observations and modelling. Continental Shelf Research 25, 2366–2386. doi:`10.1016/j.csr.2005.08.014`.

Fach, B.A., Orek, H., Yilmaz, E., Tezcan, D., Salihoglu, I., Salihoglu, B., Latif, M.A., 2021. Water Mass Variability and Levantine Intermediate Water Formation in the Eastern Mediterranean between 2015-2017. Journal of Geophysical Research: Oceans 2. doi:`10.1029/2020jc016472`.

Fourrier, M., 2020. Dataset used for CANYON-MED training and validation. Technical Report. figshare. doi:`https://doi.org/10.6084/m9.figshare.12452795.v2`.

Fourrier, M., 2021. Impact des forçages physiques sur la dynamique des éléments biogéochimiques en mer Méditerranée Approche couplée observations in situ et réseaux. Ph.D. thesis. Sorbonne Université. URL: `https://tel.archives-ouvertes.fr/tel-03533028`.

Fourrier, M., Coppola, L., Claustre, H., D'Ortenzio, F., Sauzède, R., Gattuso, J.P., 2020. A Regional Neural Network Approach to Estimate Water-Column Nutrient Concentrations and Carbonate System Variables in the Mediterranean Sea: CANYON-MED. Frontiers in Marine Science 7. doi:`10.3389/fmars.2020.00620`.

Fourrier, M., Coppola, L., D'Ortenzio, F., Migon, C., Gattuso, J., 2022. Impact of intermittent Convection in the northwestern Mediterranean Sea on Oxygen content, Nutrients and the Carbonate system. Journal of Geophysical Research: Oceans , 1–18doi:`10.1029/2022jc018615`.

Fusco, G., Manzella, G.M.R., Cruzado, A., Gačić, M., Gasparini, G.P., Kovačević, V., Millot, C., Tziavos, C., Velasquez, Z.R., Walne, A., Zervakis, V., Zodiatis, G., 2003. Variability of mesoscale features in the Mediterranean Sea from XBT data analysis. Annales Geophysicae 21, 21–32. doi:`10.5194/angeo-21-21-2003`.

Gačić, M., Civitarese, G., Eusebi Borzelli, G.L., Kovačević, V., Poulain, P.M., Theocharis, A., Menna, M., Catucci, A., Zarokanellos, N., 2011. On the relationship between the decadal oscillations of the northern Ionian Sea and the salinity distributions in the eastern Mediterranean. Journal of Geophysical Research: Oceans 116, 1–9. doi:`10.1029/2011JC007280`.

Gačić, M., Eusebi Borzelli, G.L., Civitarese, G., Cardin, V., Yari, S., 2010. Can internal processes sustain reversals of the ocean upper circulation? The Ionian Sea example. Geophysical Research Letters 37, 1–5. doi:`10.1029/2010GL043216`.

Garcia, H.E., Gordon, L.I., 1992. Oxygen solubility in seawater: Better fitting equations. Limnology and Oceanography 37, 1307–1312. doi:`10.4319/lo.1992.37.6.1307`.

Gaspar, P., Grégoris, Y., Lefevre, J.M., 1990. A simple eddy kinetic energy model for simulations of the oceanic vertical mixing: Tests at station Papa and long-term upper ocean study site. Journal of Geophysical Research 95, 16179. doi:`10.1029/jc095ic09p16179`.

Gemayel, E., Hassoun, A.E., Benallal, M.A., Goyet, C., Rivaro, P., Abboud-Abi Saab, M., Krasakopoulou, E., Touratier, F., Ziveri, P., 2015. Climatological variations of total alkalinity and total dissolved inorganic carbon in the Mediterranean Sea surface waters. Earth System Dynamics 6, 789–800. doi:`10.5194/esd-6-789-2015`.

Gerin, R., Poulain, P.M., Taupier-Letage, I., Millot, C., S. Ben Ismail, 2009. Surface circulation in the Eastern Mediterranean using drifters (2005–2007). Ocean Science Discussions (OSD) 6, 525–555. doi:`10.5194/osd-6-525-2009`.

Giorgi, F., Lionello, P., 2008. Climate change projections for the Mediterranean region. Global and Planetary Change 63, 90–104. doi:`10.1016/j.gloplacha.2007.09.005`.

Gogou, A., Sanchez-Vidal, A., Durrieu de Madron, X., Stavrakakis, S., Calafat, A.M., Stabholz, M., Psarra, S., Canals, M., Heussner, S., Stavrakaki, I., Papathanassiou, E., de Madron, X., Stavrakakis, S., Calafat, A.M., Stabholz, M., Psarra, S., Canals, M., Heussner, S., Stavrakaki, I., Papathanassiou, E., 2014. Reprint of: Carbon flux to the deep in three open sites of the Southern European Seas (SES). Journal of Marine Systems 135, 170–179. doi:`10.1016/j.jmarsys.2014.04.012`.

Graham, J.A., O'Dea, E., Holt, J., Polton, J., Hewitt, H.T., Furner, R., Guihou, K., Brereton, A., Arnold, A., Wakelin, S., Sanchez, J.M.C., Adame, C.G.M., 2018. AMM15: A new high-resolution NEMO configuration for operational simulation of the European north-west shelf. Geoscientific Model Development 11, 681–696. doi:`10.5194/gmd-11-681-2018`.

Grégoire, M., Garçon, V., Garcia, H., Breitburg, D., Isensee, K., Oschlies, A., Telszewski, M., Barth, A., Bittig, H.C., Carstensen, J., Carval, T., Chai, F., Chavez, F., Conley, D., Coppola, L., Crowe, S., Currie, K., Dai, M., Deflandre, B., Dewitte, B., Diaz, R., Garcia-Robledo, E., Gilbert, D., Giorgetti, A., Glud, R., Gutierrez, D., Hosoda, S., Ishii, M., Jacinto, G., Langdon, C., Lauvset, S.K., Levin, L.A., Limburg, K.E., Mehrtens, H., Montes, I., Naqvi, W., Paulmier, A., Pfeil, B., Pitcher, G., Pouliquen, S., Rabalais, N., Rabouille, C., Recape, V., Roman, M., Rose, K., Rudnick, D., Rummer, J., Schmechtig, C., Schmidtko, S., Seibel, B., Slomp, C., Sumalia, U.R., Tanhua, T., Thierry, V., Uchida, H., Wanninkhof, R., Yasuhara, M., 2021. A Global Ocean Oxygen Database and Atlas for Assessing and Predicting Deoxygenation and Ocean Health in the Open and Coastal Ocean. Frontiers in Marine Science 8, 1–29. doi:`10.3389/fmars.2021.724913`.

Grégoire, M., Raick, C., Soetaert, K., 2008. Numerical modeling of the central Black Sea ecosystem functioning during the eutrophication phase. Progress in Oceanography 76, 286–333. doi:`10.1016/j.pocean.2008.01.002`.

Guerzoni, S., Chester, R., Dulac, F., Herut, B., Loÿe-Pilot, M.D., Measures, C., Migon, C., Molinaroli, E., Moulin, C., Rossini, P., Saydam, C., Soudine, A., Ziveri, P., 1999. The role of atmospheric deposition in the biogeochemistry of the Mediterranean Sea. Progress in Oceanography 44, 147–190. doi:`10.1016/S0079-6611(99)00024-5`.

Guyennon, A., Baklouti, M., Diaz, F., Palmieri, J., Beuvier, J., Lebaupin-Brossier, C., Arsouze, T., Beranger, K., Dutay, J.C., Moutin, T., 2015. New insights into the organic carbon export in the Mediterranean Sea from 3-D modeling. Biogeosciences 12, 7025–7046. doi:`10.5194/bg-12-7025-2015`.

Hainbucher, D., Álvarez, M., Astray, B., Bachi, G., Cardin, V., Celentano, P., Montero, M.C., Civitarese, G., Rahman, A.E., Fajar, N.M., Fripiat, F., Gerke, L., Gogou, A., Guallart, E., Gülk, B., Lange, N., Rochner, A., Santinelli, C., Schroeder, K., Tanhua, T., Urbini, L., Velaoras, D., Wolf, F., Welsch, A., 2019. Variability and Trends in Physical and Biogeochemical Parameters of the Mediterranean Sea. Technical Report. MSM72. doi:`10.2312/cr{\{}{\textbackslash}{\_}{\}}msm72`.

Hamad, N., Millot, C., Taupier-Letage, I., 2005. A new hypothesis about the surface circulation in the eastern basin of the mediterranean sea. Progress in Oceanography 66, 287–298. doi:`10.1016/j.pocean.2005.04.002`.

Hamad, N., Millot, C., Taupier-Letage, I., 2006. The surface circulation in the eastern basin ot the Mediterranean Sea. Scientia Marina 70, 457–503. doi:`10.3989/scimar.2006.70n3457`.

Hassoun, A.E.R., Gemayel, E., Krasakopoulou, E., Goyet, C., Abboud-Abi Saab, M., Guglielmi, V., Touratier, F., Falco, C., 2015a. Acidification of the Mediterranean Sea from anthropogenic carbon penetration. Deep-Sea Research Part I: Oceanographic Research Papers 102, 1–15. doi:`10.1016/j.dsr.2015.04.005`.

Hassoun, A.E.R., Gemayel, E., Krasakopoulou, E., Goyet, C., Abi-saab, M.A., Ziveri, P., Touratier, F., Guglielmi, V., Falco, C., 2015b. Modeling of the Total Alkalinity and the Total Inorganic Carbon in the Mediterranean Sea. Journal of Water Resources and Ocean Science 4, 24. doi:`10.11648/j.wros.20150401.14`.

Hecht, A., Robinson, A.R., Pinardi, N., 1988. Currents, water masses, eddies and jets in the Mediterranean Levantine Basin.

Helm, K.P., Bindoff, N.L., Church, J.A., 2011. Observed decreases in oxygen content of the global ocean. Geophysical Research Letters 38, 1–6. doi:`10.1029/2011GL049513`.

Herrmann, M., 2008. Formation et devenir des masses d ’ eau en Méditerranée nord-occidentale - Influence sur l ’ écosystème planctonique pélagique - Variabilité interannuelle et changement climatique Marine Herrmann To cite this version : HAL Id : tel-00329937 DOCTEUR DE L ’. Ph.D. thesis. Paul Sabatier.

Herrmann, M., Diaz, F., Estournel, C., Marsaleix, P., Ulses, C., 2013. Impact of atmospheric and oceanic interannual variability on the Northwestern Mediterranean Sea pelagic planktonic ecosystem and associated carbon cycle. Journal of Geophysical Research: Oceans 118, 5792–5813. doi:`10.1002/jgrc.20405`.

Herrmann, M., Somot, S., Sevault, F., Estournel, C., Déqué, M., 2008. Modeling the deep convection in the northwestern Mediterranean sea using an eddy-permitting and an eddy-resolving model: Case study of winter 1986-1987. Journal of Geophysical Research: Oceans 113, 1–25. doi:`10.1029/2006JC003991`.

Herut, B., Krom, M., 1996. Atmospheric Input of Nutrients and Dust to the SE Mediterranean, in: Guerzoni, S., Chester, R. (eds) The Impact of Desert Dust Across the Mediterranean.. springe,dordrecht, pp. 349–358. doi:`10.1007/978-94-017-3354-0{\{}{\textbackslash}{\_}{\}}35`.

Huertas, I.E., Ríos, A.F., García-Lafuente, J., Makaoui, A., Rodríguez-Gálvez, S., Sánchez-Román, A., Orbi, A., Ruíz, J., Pérez, F.F., 2009. Anthropogenic and natural CO2 exchange through the strait of gibraltar. Biogeosciences 6, 647–662. doi:`10.5194/bg-6-647-2009`.

Huertas, I.E., Ríos, A.F., Navarro, G., Makaoui, A., Orbi, A., Ruíz, J., Pérez, F.F., 2012. Atlantic forcing of the Mediterranean oligotrophy. Global Biogeochemical Cycles 26, 1–9. doi:`10.1029/2011GB004167`.

Kalaroni, S., Tsiaras, K., Petihakis, G., Economou-Amilli, A., Triantafyllou, G., 2020. Modelling the mediterranean pelagic ecosystem using the POSEIDON ecological model. Part II: Biological dynamics. Deep-Sea Research Part II: Topical Studies in Oceanography 171, 104711. doi:`10.1016/j.dsr2.2019.104711`.

Kanakidou, M., Duce, R.A., Prospero, J.M., Baker, A.R., Benitez-Nelson, C., Dentener, F.J., Hunter, K.A., Liss, P.S., Mahowald, N., Okin, G.S., Sarin, M., Tsigaridis, K., Uematsu, M., Zamora, L.M., Zhu, T., 2012. Atmospheric fluxes of organic N and P to the global ocean. Global Biogeochemical Cycles 26, 1–12. doi:`10.1029/2011GB004277`.

Kessouri, F., Mer, D., Processus, M., 2015. Cycles biogéochimiques de la Mer Méditerranée : Processus et bilans. Ph.D. thesis. Paul Sabatier.

Kessouri, F., Ulses, C., Estournel, C., Marsaleix, P., D'Ortenzio, F., Severin, T., Taillandier, V., Conan, P., 2018. Vertical Mixing Effects on Phytoplankton Dynamics and Organic Carbon Export in the Western Mediterranean Sea. Journal of Geophysical Research: Oceans 123, 1647–1669. doi:`10.1002/2016JC012669`.

Kessouri, F., Ulses, C., Estournel, C., Marsaleix, P., Severin, T., Pujo-Pay, M., Caparros, J., Raimbault, P., Pasqueron de Fommervault, O., D'Ortenzio, F., Taillandier, V., Testor, P., Conan, P., de Fommervault, O., D'Ortenzio, F., Taillandier, V., Testor, P., Conan, P., 2017. Nitrogen and Phosphorus Budgets in the Northwestern Mediterranean Deep Convection Region. Journal of Geophysical Research: Oceans 122, 9429–9454. doi:`10.1002/2016JC012665`.

Klein, B., Roether, W., Kress, N., Manca, B.B., Ribera d'Alcala, M., Souvermezoglou, E., Theocharis, A., Civitarese, G., Luchetta, A., 2003. Accelerated oxygen consumption in eastern Mediterranean deep waters following the recent changes in thermohaline circulation. Journal of Geophysical Research: Oceans 108. doi:`10.1029/2002jc001454`.

Kontoyiannis, H., Theocharis, A., Balopoulos, E., Kioroglou, S., Papadopoulos, V., Collins, M., Velegrakis, A.F., Iona, A., 1999. Water fluxes through the Cretan Arc Straits, Eastern Mediterranean Sea: March 1994 to June 1995. Progress in Oceanography 44, 511–529. doi:`10.1016/S0079-6611(99)00044-0`.

Körtzinger, A., Schimanski, J., Send, U., Wallace, D., 2004. The ocean takes a deep breath. Science 306, 1337. doi:`10.1126/science.1102557`.

Körtzinger, A., Send, U., Lampitt, R.S., Hartman, S., Wallace, D.W.R., Karstensen, J., Villagarcia, M.G., Llinás, O., DeGrandpre, M.D., 2008. The seasonal pCO2 cycle at 49{\${}^\circ\$}N/16.5{\${}^\circ\$}W in the northeastern Atlantic Ocean and what it tells us about biological productivity. Journal of Geophysical Research: Oceans 113, 1–15. doi:`10.1029/2007JC004347`.

Kress, N., Gertman, I., Herut, B., 2014. Temporal evolution of physical and chemical characteristics of the water column in the Easternmost Levantine basin (Eastern Mediterranean Sea) from 2002 to 2010. Journal of Marine Systems 135, 6–13. URL: `http://dx.doi.org/10.1016/j.jmarsys.2013.11.016`, doi:`10.1016/j.jmarsys.2013.11.016`.

Kress, N., Herut, B., 2001. Spatial and seasonal evolution of dissolved oxygen and nutrients in the Southern Levantine Basin (Eastern Mediterranean Sea): Chemical characterization of the water masses and inferences on the N : P ratios. Deep-Sea Research Part I: Oceanographic Research Papers 48, 2347–2372. doi:`10.1016/S0967-0637(01)00022-X`.

Kress, N., Manca, B.B., Klein, B., Deponte, D., 2003. Continuing influence of the changed thermohaline circulation in the eastern Mediterranean on the distribution of dissolved oxygen and nutrients: Physical and chemical characterization of the water masses. Journal of Geophysical Research: Oceans 108, 1–20. doi:`10.1029/2002jc001397`.

Krom, Brenner, S., Kress, N., Neori, A., Gordon, L.I., 1991. Nutrient dynamics and new production in a warm core eddy from the eastern Mediterranean Sea. Deep-Sea Research Part I 39, 467–480.

Krom, M., Groom, S., Zohary, T., 2003. The Eastern Mediterranean. oxford. doi:`https://doi.org/10.1201/9780367812423`.

Krom, M.D., Herut, B., Mantoura, R.F.C., 2004. Nutrient budget for the Eastern Mediterranean: Implications for phosphorus limitation. Limnology and Oceanography 49, 1582–1592. doi:`10.4319/lo.2004.49.5.1582`.

Krom, M.D., Kress, N., Brenner, S., Gordon, L.I., 1991. Phosphorus limitation of primary productivity in the eastern Mediterranean Sea. Limnology and Oceanography 36, 424–432. doi:`10.4319/lo.1991.36.3.0424`.

Krom, M.D., Woodward, E.M.S., Herut, B., Kress, N., Carbo, P., Mantoura, R.F.C., Spyres, G., Thingsted, T.F., Wassmann, P., Wexels-Riser, C., Kitidis, V., Law, C., Zodiatis, G., 2005. Nutrient cycling in the south east Levantine basin of the eastern Mediterranean: Results from a phosphorus starved system. Deep-Sea Research Part II: Topical Studies in Oceanography 52, 2879–2896. doi:`10.1016/j.dsr2.2005.08.009`.

Kubin, E., Poulain, P.M., Mauri, E., Menna, M., Notarstefano, G., 2019. Levantine intermediate and levantine deep water formation: An Argo float study from 2001 to 2017. Water (Switzerland) 11. doi:`10.3390/w11091781`.

Lacombe, H., 1972. Caractères hydrologiques et circulation des eaux en Méditerranée.The Mediterranean Sea: A natural sedimentation laboratory. Elsevier oceanography series .

Lagaria, A., Psarra, S., Lefèvre, D., Van Wambeke, F., Courties, C., Pujo-Pay, M., Oriol, L., Tanaka, T., Christaki, U., 2011. The effects of nutrient additions on particulate and dissolved primary production and metabolic state in surface waters of three Mediterranean eddies. Biogeosciences 8, 2595–2607. doi:`10.5194/bg-8-2595-2011`.

Lascaratos, A., Nittis, K., 1998. A high-resolution three-dimensional numerical study of intermediate water formation in the Levantine Sea. Journal of Geophysical Research: Oceans 103, 18497–18511. doi:`10.1029/98JC01196`.

Lascaratos, A., Roether, W., Nittis, K., Klein, B., 1999. Recent changes in deep water formation and spreading in the Eastern Mediterranean Sea: A review. Progress in Oceanography 44, 5–36. doi:`10.1016/S0079-6611(99)00019-1`.

Lascaratos, A., Williams, R.G., Tragou, E., 1993. A mixed-layer study of the formation of Levantine Intermediate Water. Journal of Geophysical Research 98.

Lavigne, H., D'Ortenzio, F., Migon, C., Claustre, H., Testor, P., D'Alcalà, M.R., Lavezza, R., Houpert, L., Prieur, L., 2013. Enhancing the comprehension of mixed layer depth control on the Mediterranean phytoplankton phenology. Journal of Geophysical Research: Oceans 118, 3416–3430. doi:`10.1002/jgrc.20251`.

Lavigne, H., D'Ortenzio, F., D'Alcalà, M.R., Claustre, H., Sauzède, R., Gacic, M., 2015. On the vertical distribution of the chlorophyll a concentration in the Mediterranean Sea : a basin-scale and seasonal approach. Biogeosciences , 5021–5039doi:`10.5194/bg-12-5021-2015`.

Lazzari, P., Mattia, G., Solidoro, C., Salon, S., Crise, A., Zavatarelli, M., Oddo, P., Vichi, M., 2013. The impacts of climate change and environmental management policies on the trophic regimes in the Mediterranean Sea: Scenario analyses. Journal of Marine Systems 135, 137–149. URL: `http://dx.doi.org/10.1016/j.jmarsys.2013.06.005`, doi:`10.1016/j.jmarsys.2013.06.005`.

Lazzari, P., Solidoro, C., Ibello, V., Salon, S., Teruzzi, A., Béranger, K., Colella, S., Crise, A., 2012. Seasonal and inter-annual variability of plankton chlorophyll and primary production in the Mediterranean Sea: A modelling approach. Biogeosciences 9, 217–233. doi:`10.5194/bg-9-217-2012`.

Lazzari, P., Solidoro, C., Salon, S., Bolzon, G., 2016. Spatial variability of phosphate and nitrate in the Mediterranean Sea: A modeling approach. Deep-Sea Research Part I: Oceanographic Research Papers 108, 39–52. URL: `http://dx.doi.org/10.1016/j.dsr.2015.12.006`, doi:`10.1016/j.dsr.2015.12.006`.

Lellouche, J.M., Le Galloudec, O., Drévillon, M., Régnier, C., Greiner, E., Garric, G., Ferry, N., Desportes, C., Testut, C.E., Bricaud, C., Bourdallé-Badie, R., Tranchant, B., Benkiran, M., Drillet, Y., Daudin, A., De Nicola, C., 2013. Evaluation of global monitoring and forecasting systems at Mercator Océan. Ocean Science 9, 57–81. doi:`10.5194/os-9-57-2013`.

Lévy, M., Mémery, L., Madec, G., 1998. The onset of a bloom after deep winter convection in the northwestern Mediterranean sea: Mesoscale process study with a primitive equation model. Journal of Marine Systems 16, 7–21. doi:`10.1016/S0924-7963(97)00097-3`.

Longhurst, A., Sathyendranath, S., Platt, T., Caverhill, C., 1995. An estimate of global primary production in the ocean from satellite radiometer data. Journal of Plankton Research 17, 1245–1271. doi:`10.1093/plankt/17.6.1245`.

Loÿe-Pilot, M.D., Martin, J.M., Morelli, J., 1990. Atmospheric input of inorganic nitrogen to the Western Mediterranean. Biogeochemistry 9, 117–134. doi:`10.1007/BF00692168`.

Ludwig, W., Bouwman, A.F., Dumont, E., Lespinas, F., 2010. Water and nutrient fluxes from major Mediterranean and Black Sea rivers: Past and future trends and their implications for the basin-scale budgets. Global Biogeochemical Cycles 24, 1–14. doi:`10.1029/2009GB003594`.

Ludwig, W., Dumont, E., Meybeck, M., Heussner, S., 2009. River discharges of water and nutrients to the Mediterranean and Black Sea: Major drivers for ecosystem changes during past and future decades? Progress in Oceanography 80, 199–217. URL: `http://dx.doi.org/10.1016/j.pocean.2009.02.001`, doi:`10.1016/j.pocean.2009.02.001`.

Lyard, F.H., Allain, D.J., Cancet, M., Carrère, L., Picot, N., 2021. FES2014 global ocean tide atlas: Design and performance. Ocean Science 17, 615–649. doi:`10.5194/os-17-615-2021`.

Macías, D., Guerranti, C., Prieto, L., Peliz, A., Ruiz, J., 2014a. A high-resolution hydrodynamic-biogeochemical coupled model of the Gulf of Cadiz – Alboran Sea region. Mediterranean Marine Science 22, 739–752.

Macías, D., Stips, A., Garcia-Gorriz, E., 2014b. The relevance of deep chlorophyll maximum in the open Mediterranean Sea evaluated through 3D hydrodynamic-biogeochemical coupled simulations. Ecological Modelling 281, 26–37. doi:`10.1016/j.ecolmodel.2014.03.002`.

Durrieu de Madron, X., Conan, P., 2019. PERLE2 cruise, RV Pourquoi pas ? Technical Report. PERLE2. doi:`10.17600/18000865`.

Mahowald, N., Jickells, T.D., Baker, A.R., Artaxo, P., Benitez-Nelson, C.R., Bergametti, G., Bond, T.C., Chen, Y., Cohen, D.D., Herut, B., Kubilay, N., Losno, R., Luo, C., Maenhaut, W., McGee, K.A., Okin, G.S., Siefert, R.L., Tsukuda, S., 2008. Global distribution of atmospheric phosphorus sources, concentrations and deposition rates, and anthropogenic impacts. Global Biogeochemical Cycles 22, 1–19. doi:`10.1029/2008GB003240`.

Malanotte-Rizzoli, P., Artale, V., Borzelli-Eusebi, G.L., Brenner, S., Crise, A., Gacic, M., Kress, N., Marullo, S., Ribera D'Alcalà, M., Sofianos, S., Tanhua, T., Theocharis, A., Alvarez, M., Ashkenazy, Y., Bergamasco, A., Cardin, V., Carniel, S., Civitarese, G., D'Ortenzio, F., Font, J., Garcia-Ladona, E., Garcia-Lafuente, J.M., Gogou, A., Gregoire, M., Hainbucher, D., Kontoyannis, H., Kovacevic, V., Kraskapoulou, E., Kroskos, G., Incarbona, A., Mazzocchi, M.G., Orlic, M., Ozsoy, E., Pascual, A., Poulain, P.M., Roether, W., Rubino, A., Schroeder, K., Siokou-Frangou, J., Souvermezoglou, E., Sprovieri, M., Tintoré, J., Triantafyllou, G., 2014. Physical forcing and physical/biochemical variability of the Mediterranean Sea: A review of unresolved issues and directions for future research. Ocean Science 10, 281–322. doi:`10.5194/os-10-281-2014`.

Malanotte-rizzoli, P., Charnock, H., Hecht, A., Roether, W., Muench, E.R.D., Theocharis, A., Ocean, R.M., 1988. POEM: Physical Oceanography of the Eastern Mediterranean. Eos 69.

Malanotte-Rizzoli, P., Eremeev, V., 1999. The Eastern Mediterranean as a Laboratory Basin for the Assessment of Contrasting Ecosystems. January 1999. doi:`10.1007/978-94-011-4796-5`.

Malanotte-Rizzoli, P., Manca, B.B., D'Alcalà, M.R., Theocharis, A., Bergamasco, A., Bregant, D., Budillon, G., Clvitarese, G., Georgopoulos, D., Mlchelato, A., Sansone, E., Scarazzato, P., Souvermezoglou, E., 1997. A synthesis of the Ionian Sea hydrography, circulation and water mass pathways during POEM-phase I. Progress in Oceanography 39, 153–204. doi:`10.1016/S0079-6611(97)00013-X`.

Malanotte-Rizzoli, P., Manca, B.B., D'Alcala, M.R., Theocharis, A., Brenner, S., Budillon, G., Ozsoy, E., 1999. The Eastern Mediterranean in the 80s and in the 90s: The big transition in the intermediate and deep circulations. Dynamics of Atmospheres and Oceans 29, 365–395. doi:`10.1016/S0377-0265(99)00011-1`.

Malanotte-Rizzoli, P., Manca, B.B., Marullo, S., D'Alcala, R., Roether, W., Theocharis, A., Bergamasco, A., Budillon, G., Sansone, E., Civitarese, G., Conversano, F., Gertman, I., Herut, B., Kress, N., Kioroglou, S., Kontoyannis, H., Nittis, K., Klein, B., Lascaratos, A., Latif, M.A., Ozsoy, E., Robinson, A.R., Santoleri, R., Viezzoli, D., Kovacevic, V., 2003. The Levantine Intermediate Water Experiment (LIWEX) Group: Levantine basin - A laboratory for multiple water mass formation processes. Journal of Geophysical Research C: Oceans 108. doi:`10.1029/2002jc001643`.

Manca, B., Burca, M., Giorgetti, A., Coatanoan, C., Garcia, M.J., Iona, A., 2004. Physical and biochemical averaged vertical profiles in the Mediterranean regions: An important tool to trace the climatology of water masses and to validate incoming data from operational oceanography. Journal of Marine Systems 48, 83–116. doi:`10.1016/j.jmarsys.2003.11.025`.

Many, G., Ulses, C., Estournel, C., Marsaleix, P., 2021. Particulate organic carbon budget of the Gulf of Lion shelf (NW Mediterranean) using a coupled hydrodynamic-biogeochemical model. Biogeosciences Discussions , 1–41doi:`10.5194/bg-2021-82`.

Margirier, F., Testor, P., Heslop, E., Mallil, K., Bosse, A., Houpert, L., Mortier, L., Bouin, M.N., Coppola, L., D'Ortenzio, F., Durrieu de Madron, X., Mourre, B., Prieur, L., Raimbault, P., Taillandier, V., de Madron, X., Mourre, B., Prieur, L., Raimbault, P., Taillandier, V., 2020. Abrupt warming and salinification of intermediate waters interplays with decline of deep convection in the Northwestern Mediterranean Sea. Scientific Reports 10, 1–11. doi:`10.1038/s41598-020-77859-5`.

Markaki, Z., Loÿe-Pilot, M.D., Violaki, K., Benyahya, L., Mihalopoulos, N., 2010. Variability of atmospheric deposition of dissolved nitrogen and phosphorus in the Mediterranean and possible link to the anomalous seawater N/P ratio. Marine Chemistry 120, 187–194. URL: `http://dx.doi.org/10.1016/j.marchem.2008.10.005`, doi:`10.1016/j.marchem.2008.10.005`.

Marsaleix, P., Auclair, F., Estournel, C., 2006. Considerations on open boundary conditions for regional and coastal ocean models. Journal of Atmospheric and Oceanic Technology 23, 1604–1613. doi:`10.1175/JTECH1930.1`.

Marsaleix, P., Auclair, F., Floor, J.W., Herrmann, M.J., Estournel, C., Pairaud, I., Ulses, C., 2008. Energy conservation issues in sigma-coordinate free-surface ocean models. Ocean Modelling 20, 61–89. doi:`10.1016/j.ocemod.2007.07.005`.

Marsaleix, P., Estournel, C., Kondrachoff, V., Vehil, R., 1998. A numerical study of the formation of the Rhone River plume. Journal of Marine Systems 14, 99–115. doi:`10.1016/S0924-7963(97)00011-0`.

Marshall, J., Schott, F., 1999. Open-Ocean Convection ' Theory , and Models Observations ,. Reviews of Geophysics 37, 1–64.

Martínez-Pérez, A.M., Álvarez-Salgado, X.A., Arístegui, J., Nieto-Cid, M., 2017. Deep-ocean dissolved organic matter reactivity along the Mediterranean Sea: Does size matter. Scientific Reports 7. doi:`10.1038/s41598-017-05941-6`.

Marty, J.C., Chiavérini, J., Pizay, M.D., Avril, B., 2002. Seasonal and interannual dynamics of nutrients and phytoplankton pigments in the western Mediterranean Sea at the DYFAMED time-series station (1991-1999). Deep-Sea Research Part II: Topical Studies in Oceanography 49, 1965–1985. doi:`10.1016/S0967-0645(02)00022-X`.

Marullo, S., Napolitano, E., Santoleri, R., Manca, B., Evans, R., 2003. Variability of Rhodes and Ierapetra Gyres during Levantine Intermediate Water Experiment: Observations and model results. Journal of Geophysical Research: Oceans 108, 1–18. doi:`10.1029/2002jc001393`.

Mattia, G., Zavatarelli, M., Vichi, M., Oddo, P., 2013. The Eastern Mediterranean Sea biogeochemical dynamics in the 1990s: A numerical study. Journal of Geophysical Research: Oceans 118, 2231–2248. doi:`10.1002/jgrc.20160`.

Mauri, E., Sitz, L., Gerin, R., Poulain, P.M., Hayes, D., Gildor, H., 2019. On the variability of the circulation and water mass properties in the eastern Levantine Sea between September 2016-August 2017. Water (Switzerland) 11, 17–19. doi:`10.3390/w11091741`.

Mavropoulou, A.M., Vervatis, V., Sofianos, S., 2020. Dissolved oxygen variability in the Mediterranean Sea. Journal of Marine Systems 208. doi:`10.1016/j.jmarsys.2020.103348`.

Mayot, N., D'Ortenzio, F., D'Alcalà, M.R., Lavigne, H., Claustre, H., 2016. Interannual variability of the Mediterranean trophic regimes from ocean color satellites. Biogeosciences 13, 1901–1917. doi:`10.5194/bg-13-1901-2016`.

McClain, C.R., Hooker, S., Feldman, G., Bontempi, P., 2006. Satellite data for ocean biology, biogeochemistry, and climate research. Eos 87, 340–342. doi:`10.1029/2006eo340002`.

Medoc group, 1970. Observation of Formation of Deep Water in the Mediterranean Sea, 1969. Nature 227, 10–13.

Mendez, J., 2010. Atmospheric input of manganese and iron to the ocean: Seawater dissolution experiments with Saharan and North American dusts. Marine Chemistry 120, 34–43. URL: `http://dx.doi.org/10.1016/j.marchem.2008.08.006`, doi:`10.1016/j.marchem.2008.08.006`.

Menna, M., Gačić, M., Martellucci, R., Notarstefano, G., Fedele, G., Mauri, E., Gerin, R., Poulain, P.M., 2022. Climatic, Decadal, and Interannual Variability in the Upper Layer of the Mediterranean Sea Using Remotely Sensed and In-Situ Data. Remote Sensing 14. doi:`10.3390/rs14061322`.

Menna, M., Notarstefano, G., Poulain, P.M., Mauri, E., Falco, P., Zambianchi, E., 2020. Section 3 . 5 : Surface picture of the Levantine Basin as derived by drifter and satellite data. Technical Report. Copernicus Marine Service Ocean State Report, Issue 4.

Menna, M., Poulain, P.M., Zodiatis, G., Gertman, I., 2012. On the surface circulation of the Levantine sub-basin derived from Lagrangian drifters and satellite altimetry data. Deep-Sea Research Part I: Oceanographic Research Papers 65, 46–58. URL: `http://dx.doi.org/10.1016/j.dsr.2012.02.008`, doi:`10.1016/j.dsr.2012.02.008`.

Mignot, A., Claustre, H., D'Ortenzio, F., Xing, X., Poteau, A., Ras, J., 2011. From the shape of the vertical profile of in vivo fluorescence to Chlorophyll-a concentration. Biogeosciences 8, 2391–2406. doi:`10.5194/bg-8-2391-2011`.

Mignot, A., Claustre, H., Uitz, J., Poteau, A., Ortenzio, F.D., Xing, X., 2014. Understanding the seasonal dynamics and the deep chlorophyll maximum in oligotrophic. AGU. global biogeochemical cycles , 856–876doi:`10.1002/2013GB004781.Received`.

Mignot, A., Ortenzio, F.D., Taillandier, V., Cossarini, G., Salon, S., 2019. Quantifying observational errors in Biogeochemical-Argo oxygen , nitrate and chlorophyll a concentrations. AGU. global biogeochemical cycles , 0–3doi:`10.1029/2018GL080541`.

Migon, C., Sandroni, V., Marty, J.C., Gasser, B., Miquel, J.C., 2002. Transfer of atmospheric matter through the euphotic layer in the northwestern Mediterranean: Seasonal pattern and driving forces. Deep-Sea Research Part II: Topical Studies in Oceanography 49, 2125–2141. doi:`10.1016/S0967-0645(02)00031-0`.

Mikolajczak, G., Estournel, C., Ulses, C., Marsaleix, P., Bourrin, F., Martín, J., Pairaud, I., Puig, P., Leredde, Y., Many, G., Seyfried, L., Durrieu de Madron, X., de Madron, X., 2020. Impact of storms on residence times and export of coastal waters during a mild autumn/winter period in the Gulf of Lion. Continental Shelf Research 207. doi:`10.1016/j.csr.2020.104192`.

Millot, C., Taupier-Letage, I., 2005. Circulation in the Mediterranean Sea. Life in the Mediterranean Sea: A Look at Habitat Changes 5, 99–125. doi:`10.1007/b107143`.

Minas, H.J., Bonin, M.C., 1988. Oxygenation physique et biologique de la Méditerranée nord-occidentale en hiver et au printemps. Oceanologica Acta sn , 123–132.

Moutin, T., Prieur, L., 2012. Influence of anticyclonic eddies on the Biogeochemistry from the Oligotrophic to the Ultraoligotrophic Mediterranean (BOUM cruise). Biogeosciences , 3827–3855doi:`10.5194/bg-9-3827-2012`.

Moutin, T., Raimbault, P., 2002. Primary production, carbon export and nutrients availability in western and eastern Mediterranean Sea in early summer 1996 (MINOS cruise). Journal of Marine Systems 33-34, 273–288. doi:`10.1016/S0924-7963(02)00062-3`.

Mueller, J.L., Austin, R.W., 1995. SeaWiFS Technical Report Series Volume 25 , Ocean Optics Protocols for SeaWiFS Validation , Revision 1. Nasa Technical Memorandum 104566 25.

Nabat, P., Somot, S., Mallet, M., Michou, M., Sevault, F., Driouech, F., Meloni, D., Di Sarra, A., Di Biagio, C., Formenti, P., Sicard, M., Léon, J.F., Bouin, M.N., 2015. Dust aerosol radiative effects during summer 2012 simulated with a coupled regional aerosol-atmosphere-ocean model over the Mediterranean. Atmospheric Chemistry and Physics 15, 3303–3326. doi:`10.5194/acp-15-3303-2015`.

Napolitano, E., Oguz, T., Malanotte-Rizzoli, P., Yilmaz, A., Sansone, E., 2000. Simulations of biological production in the Rhodes and Ionian basins of the eastern Mediterranean. Journal of Marine Systems 24, 277–298. doi:`10.1016/S0924-7963(99)00090-1`.

Nielsen, R.L., 1912. Hydrography of the Mediterranean Sea. Oceanol Acta 10 2, 143–149.

Nittis, K., Lascaratos, A., 1998. Diagnostic and prognostic numerical studies of LIW formation. Journal of Marine Systems , 179–195.

Nittis, K., Tziavos, C., Bozzano, R., Cardin, V., Thanos, Y., Petihakis, G., Zanon, F., Nittis, K., Tziavos, C., Bozzano, R., Cardin, V., Thanos, Y., Ma, T., 2006. The M3A multi-sensor buoy network of the Mediterranean Sea To cite this version : HAL Id : hal-00298416 The M3A multi-sensor buoy network of the Mediterranean Sea. Ocean Science Discussions .

Nixon, S.W., 2003. Replacing the Nile: Are anthropogenic nutrients providing the fertility once brought to the Mediterranean by a great river? Ambio 32, 30–39. doi:`10.1579/0044-7447-32.1.30`.

O'Reilly, J., Maritorena, S., 2000. Ocean color chlorophyll a algorithms for SeaWiFS, OC2, and OC4: Version 4. SeaWiFS postlaunch … , 8–22URL: `http://www.spg.ucsd.edu/People/Mati/2000_OReilly_et_al_OC4v4_11-Chapt2.pdf`.

Ovchinnikov, 1966. CIRCULATION IN SURFACE AND INTERMEDIATE LAYERSOF MEDITERRANEAN. Oceanology-USSR 6.1.

Ovchinnikov, 1984. The formation of intermediate water in the Mediterranean. Oceanology 24, 262.

Ozer, T., Gertman, I., Gildor, H., Goldman, R., Herut, B., 2019. Evidence for recent thermohaline variability and processes in the deep water of the Southeastern Levantine Basin, Mediterranean Sea. Deep-Sea Research Part II: Topical Studies in Oceanography 171, 104651. URL: `https://doi.org/10.1016/j.dsr2.2019.104651`, doi:`10.1016/j.dsr2.2019.104651`.

Ozer, T., Gertman, I., Kress, N., Silverman, J., Herut, B., 2016. Interannual thermohaline (1979–2014) and nutrient (2002–2014) dynamics in the Levantine surface and intermediate water masses, SE Mediterranean Sea. Global and Planetary Change 151, 60–67. URL: `http://dx.doi.org/10.1016/j.gloplacha.2016.04.001`, doi:`10.1016/j.gloplacha.2016.04.001`.

Ozer, T., Rahav, E., Gertman, I., Sisma-Ventura, G., Silverman, J., Herut, B., 2022. Relationship between thermohaline and biochemical patterns in the levantine upper and intermediate water masses, Southeastern Mediterranean Sea (2013–2021). Frontiers in Marine Science 9, 1–11. doi:`10.3389/fmars.2022.958924`.

Özsoy, E., Hecht, A., Unluata, U., 1989. Circulation and hydrography of the Levantine Basin. Results of POEM coordinated experiments 1985-1986. Progress in Oceanography 22, 125–170. doi:`10.1016/0079-6611(89)90004-9`.

Özsoy, E., Hecht, A., Unluata, U., Brenner, S., Oguz, T., Bishop, J., Latif, M.A., Rozentraub, Z., 1991. A review of the Levantine Basin circulation and its variability during 1985-1988. Dynamics of Atmospheres and Oceans 15, 421–456. doi:`10.1016/0377-0265(91)90027-D`.

Özsoy, E., Hecht, A., Unluata, U., Brenner, S., Sur, H.I., Bishop, J., Latif, M.A., Rozentraub, Z., Oguz, T., 1993. A synthesis of the Levantine Basin circulation and hydrography, 1985-1990. Deep-Sea Research Part II 40, 1075–1119. doi:`10.1016/0967-0645(93)90063-S`.

Pagès, R., Baklouti, M., Barrier, N., Ayache, M., Sevault, F., Somot, S., Moutin, T., 2020a. Projected Effects of Climate-Induced Changes in Hydrodynamics on the Biogeochemistry of the Mediterranean Sea Under the RCP 8.5 Regional Climate Scenario. Frontiers in Marine Science 7, 1–17. doi:`10.3389/fmars.2020.563615`.

Pagès, R., Baklouti, M., Barrier, N., Richon, C., Dutay, J.C., Moutin, T., 2020b. Changes in rivers inputs during the last decades significantly impacted the biogeochemistry of the eastern Mediterranean basin: A modelling study. Progress in Oceanography 181, 102242. URL: `https://doi.org/10.1016/j.pocean.2019.102242`, doi:`10.1016/j.pocean.2019.102242`.

Pairaud, I.L., Lyard, F., Auclair, F., Letellier, T., Marsaleix, P., 2008. Dynamics of the semi-diurnal and quarter-diurnal internal tides in the Bay of Biscay. Part 1: Barotropic tides. Continental Shelf Research 28, 1294–1315. doi:`10.1016/j.csr.2008.03.004`.

Pasqueron, O., Dynamique, D.F., 2016. Dynamique des nutriments en Méditerranée : des campagnes océanographiques aux flotteurs Bio-Argo To cite this version : HAL Id : tel-01332478 Université Pierre et Marie Curie Dynamique des nutriments en Méditerranée : des campagnes océanographiques aux fl. Ph.D. thesis. Université Pierre et Marie Curie.

Paulson, C.A., Simpson, J.J., 1386. Irradiance measurements in the upper ocean. Journal of Physical Oceanography 7.

Pedrosa-Pamies, R., Parinos, C., Sanchez-Vidal, A., Calafat, A., Canals, M., Velaoras, D., Mihalopoulos, N., Kanakidou, M., Lampadariou, N., Gogou, A., 2021. Atmospheric and Oceanographic Forcing Impact Particle Flux Composition and Carbon Sequestration in the Eastern Mediterranean Sea: A Three-Year Time-Series Study in the Deep Ierapetra Basin. Frontiers in Earth Science 9. doi:`10.3389/feart.2021.591948`.

Pedrosa-Pàmies, R., Sanchez-Vidal, A., Canals, M., Lampadariou, N., Velaoras, D., Gogou, A., Parinos, C., Calafat, A., 2016. Enhanced carbon export to the abyssal depths driven by atmosphere dynamics. Geophysical Research Letters 43, 8626–8636. doi:`10.1002/2016GL069781`.

Petihakis, G., Triantafyllou, G., Tsiaras, K., Korres, G., Pollani, A., Hoteit, I., 2009. Eastern Mediterranean biogeochemical flux model - Simulations of the pelagic ecosystem. Ocean Science 5, 29–46. doi:`10.5194/os-5-29-2009`.

Petrenko, A., Dufau, C., Estournel, C., 2008. Barotropic eastward currents in the western Gulf of Lion, north-western Mediterranean Sea, during stratified conditions. Journal of Marine Systems 74, 406–428. doi:`10.1016/j.jmarsys.2008.03.004`.

Picotti, V., Go, S., Dubinsky, Z., Krom, M.D., Kress, N., Berman-Frank, I., Rahav, E., Picotti, V., Go, S., Dubinsky, Z., 2014. The Mediterranean Sea: it's history and present challenges. doi:`10.1007/978-94-007-6704-1`.

Pinardi, N., Korres, G., Lascaratos, A., Roussenov, V., Stanev, E., 1997. Numerical simulation of the interannual variability of the Mediterranean Sea upper ocean circulation. Geophysical Research Letters 24, 425–428. doi:`10.1029/96GL03952`.

Pinardi, N., Zavatarelli, M., Adani, M., Coppini, G., Fratianni, C., Oddo, P., Simoncelli, S., Tonani, M., Lyubartsev, V., Dobricic, S., Bonaduce, A., 2015. Mediterranean Sea large-scale low-frequency ocean variability and water mass formation rates from 1987 to 2007: A retrospective analysis. Progress in Oceanography 132, 318–332. URL: `http://dx.doi.org/10.1016/j.pocean.2013.11.003`, doi:`10.1016/j.pocean.2013.11.003`.

Pinazo, C., Marsaleix, P., Millet, B., Estournel, C., Véhil, R., 1996. Spatial and temporal variability of phytoplankton biomass in upwelling areas of the northwestern Mediterranean: A coupled physical and biogeochemical modelling approach. Journal of Marine Systems 7, 161–191. doi:`10.1016/0924-7963(95)00028-3`.

Polimene, L., Pinardi, N., Zavatarelli, M., Colella, S., 2007. The Adriatic Sea ecosystem seasonal cycle: Validation of a three-dimensional numerical model. Journal of Geophysical Research: Oceans 112. doi:`10.1029/2005JC003260`.

Pope, R.M., Fry, E.S., 1997. Absorption spectrum (380-700 nm) of pure water . {II} . Integrating cavity measurements. Applied Optics 36, 8710–8723. URL: `http://www.opticsinfobase.org/abstract.cfm?URI=ao-36-33-8710OP-Ja%5Cnhttp://www.opticsinfobase.org/abstract.cfm?URI=ao-36-33-8710`.

Potter, R.A., Lozier, M.S., 2004. On the warming and salinification of the Mediterranean outflow waters in the North Atlantic. Geophysical Research Letters 31, 1–4. doi:`10.1029/2003GL018161`.

Poulain, P.M., Menna, M., Mauri, E., 2012. Surface geostrophic circulation of the mediterranean sea derived from drifter and satellite altimeter data. Journal of Physical Oceanography 42, 973–990. doi:`10.1175/JPO-D-11-0159.1`.

Poulos, S.E., Drakopoulos, P.G., Collins, M.B., 1997. Seasonal variability in sea surface oceanographic conditions in the Aegean Sea (Eastern Mediterranean). Journal of Marine Systems 13, 225–244.

Powley, H., Van Cappelen, P., Krom, M.D., 2016a. Nutrient Cycling in the Mediterranean Sea: The Key to Understanding How the Unique Marine Ecosystem Functions and Responds to Anthropogenic Pressures1. Intech i, 13. doi:`http://dx.doi.org/10.5772/57353`.

Powley, H.R., Krom, M.D., Emeis, K.C., Van Cappellen, P., 2014. A biogeochemical model for phosphorus and nitrogen cycling in the Eastern Mediterranean Sea: Part 2: Response of nutrient cycles and primary production to anthropogenic forcing: 1950-2000. Journal of Marine Systems 139, 420–432. URL: `http://dx.doi.org/10.1016/j.jmarsys.2014.08.017`, doi:`10.1016/j.jmarsys.2014.08.017`.

Powley, H.R., Krom, M.D., Van Cappelen, P., Becker, J. M., M.A.M., H.Yoon, Becker J. M., M.A.M., H.Yoon, 2016b. Circulation and oxygen cycling in the Mediterranean Sea: Sensitivity to future climate change. Journal of Geophysical Research: Oceans 121, 3010–3028. doi:`10.1002/2015JC011516`.

Powley, H.R., Krom, M.D., Van Cappellen, P., 2017. Understanding the unique biogeochemistry of the Mediterranean Sea: Insights from a coupled phosphorus and nitrogen model. Global Biogeochemical Cycles 31, 1010–1031. doi:`10.1002/2017GB005648`.

Pujo-Pay, M., Conan, P., Oriol, L., Cornet-Barthaux, V., Falco, C., Ghiglione, J.F., Goyet, C., Moutin, T., Prieur, L., 2011. Integrated survey of elemental stoichiometry (C, N, P) from the western to eastern Mediterranean Sea. Biogeosciences 8, 883–899. doi:`10.5194/bg-8-883-2011`.

Raick, C., Delhez, E.J., Soetaert, K., Grégoire, M., 2005. Study of the seasonal cycle of the biogeochemical processes in the Ligurian Sea using a 1D interdisciplinary model. Journal of Marine Systems 55, 177–203. doi:`10.1016/j.jmarsys.2004.09.005`.

Randone, M., Di Carlo, G., Costantini, M., 2017. Reviving the Economy of the Mediterranean Sea: Actions for a Sustainable Future. Technical Report. WWF. Rome, Italy. URL: `http://www.wwf.gr/images/pdfs/reviving_mediterranean_sea_economy_full_rep_lowres.pdf%0Ahttps://www.ansa.it/documents/1506517281253_wwf_REVIVING-MED-ECO_web_embargoed.pdf`.

Reale, M., Cossarini, G., Lazzari, P., Lovato, T., Bolzon, G., Masina, S., Solidoro, C., Salon, S., 2022. Acidification, deoxygenation, and nutrient and biomass declines in a warming Mediterranean Sea. Biogeosciences 19, 4035–4065. doi:`10.5194/bg-19-4035-2022`.

Redfield, A.C., 1934. On the Proportions of Organic Derivatives in Sea Water and Their Relation to the Composition of Plankton. University Press of Liverpool, James Johnstone Memorial Volume , 1192–1767URL: `http://scholar.google.com/scholar?hl=en&btnG=Search&q=intitle:On+the+proportions+of+organic+derivatives+in+sea+water+and+their+relation+to+the+composition+of+plankton#0`.

Regaudie-De-Gioux, A., Vaquer-Sunyer, R., Duarte, C.M., 2009. Patterns in planktonic metabolism in the Mediterranean Sea. Biogeosciences 6, 3081–3089. doi:`10.5194/bg-6-3081-2009`.

Reiter, E., 1975. Handbook for Forecasters in the Mediterranean; Weather Phenomena of the Mediterranean Basin; Part 1. General Description of the Meteorological Processes. EPRFNPS, Monterey , 334URL: `http://oai.dtic.mil/oai/oai?verb=getRecord&metadataPrefix=html&identifier=ADA024271`.

Ribera d'Alcalà, M., Civitarese, G., Conversano, F., Lavezza, R., 2003. Nutrient ratios and fluxes hint at overlooked processes in the Mediterranean Sea. Journal of Geophysical Research: Oceans 108. doi:`10.1029/2002jc001650`.

Richon, C., Dutay, J.C., Dulac, F., Wang, R., Balkanski, Y., 2018. Modeling the biogeochemical impact of atmospheric phosphate deposition from desert dust and combustion sources to the Mediterranean Sea. Biogeosciences 15, 2499–2524. doi:`10.5194/bg-15-2499-2018`.

Richon, C., Dutay, J.C., Dulac, F., Wang, R., Balkanski, Y., Nabat, P., Aumont, O., Desboeufs, K., Laurent, B., Guieu, C., Raimbault, P., Beuvier, J., 2017. Modeling the impacts of atmospheric deposition of nitrogen and desert dust-derived phosphorus on nutrients and biological budgets of the Mediterranean Sea. Progress in Oceanography 163, 21–39. doi:`10.1016/j.pocean.2017.04.009`.

Ridame, C., Guieu, C., 2002. Saharan input of phosphate to the oligotrophic water of the open western Mediterranean sea. Limnology and Oceanography 47, 856–869. doi:`10.4319/lo.2002.47.3.0856`.

Ridame, C., Moutin, T., Guieu, C., 2003. Does phosphate adsorption onto Saharan dust explain the unusual N/P ratio in the Mediterranean Sea? Oceanologica Acta 26, 629–634. doi:`10.1016/S0399-1784(03)00061-6`.

Robinson, A.R., Golnaraghi, M., 1993a. Circulation and dynamics of the Eastern Mediterranean Sea; quasi-synoptic data-driven simulations. Deep-Sea Research Part II 40, 1207–1246. doi:`10.1016/0967-0645(93)90068-X`.

Robinson, A.R., Golnaraghi, M., 1993b. The physical and dynamical oceanography of the Mediterranean sea.

Robinson, A.R., Golnaraghi, M., Leslie, W.G., Artegiani, A., Hecht, A., Lazzoni, E., Michelato, A., Sansone, E., Theocharis, A., Unluata, U., 1991. The eastern Mediterranean general circulation: features, structure and variability. Dynamics of Atmospheres and Oceans 15, 215–240. doi:`10.1016/0377-0265(91)90021-7`.

Robinson, A.R., Leslie, W.G., Theocharis, A., Lascaratos, A., 2001. Mediterranean Sea Circulation. Encyclopedia of Ocean Sciences , 1689–1705doi:`10.1006/rwos.2001.0376`.

Roesler, C., Uitz, J., Claustre, H., Boss, E., Xing, X., Organelli, E., Briggs, N., Bricaud, A., Schmechtig, C., Poteau, A., D'Ortenzio, F., Ras, J., Drapeau, S., Haëntjens, N., Barbieux, M., 2017. Recommendations for obtaining unbiased chlorophyll estimates from in situ chlorophyll fluorometers: A global analysis of WET Labs ECO sensors. Limnology and Oceanography: Methods 15, 572–585. doi:`10.1002/lom3.10185`.

Roether, W., Manca, B.B., Klein, B., Bregant, D., Georgopoulos, D., Bietzel, V., Kovačević, V., Luchetta, A., 1996. Recent Changes in Eastern Mediterranean Deep Waters. Technical Report 5247. Science. URL: `http://www.jstor.org/stable/2890461`.

Roether, W., Schlitzer, R., 1991. Eastern Mediterranean deep water renewal on the basis of chlorofluoromethane and tritium data. Dynamics of Atmospheres and Oceans 15, 333–354. doi:`10.1016/0377-0265(91)90025-B`.

Sanchez-Gomez, E., Somot, S., Josey, S.A., Dubois, C., Elguindi, N., Déqué, M., 2011. Evaluation of Mediterranean Sea water and heat budgets simulated by an ensemble of high resolution regional climate models. Climate Dynamics 37, 2067–2086. doi:`10.1007/s00382-011-1012-6`.

Santinelli, Nannicini, L., Seritti, A., 2010. DOC dynamics in the meso and bathypelagic layers of the Mediterranean Sea. Deep-Sea Research Part II: Topical Studies in Oceanography 57, 1446–1459. URL: `http://dx.doi.org/10.1016/j.dsr2.2010.02.014`, doi:`10.1016/j.dsr2.2010.02.014`.

Santinelli, C., Hansell, D.A., Ribera d'Alcalà, M., 2013. Influence of stratification on marine dissolved organic carbon (DOC) dynamics: The Mediterranean Sea case. Progress in Oceanography 119, 68–77. URL: `http://dx.doi.org/10.1016/j.pocean.2013.06.001`, doi:`10.1016/j.pocean.2013.06.001`.

Santinelli, C., Santinelli, Santinelli, C., Santinelli, Santinelli, C., Santinelli, 2015. DOC in the Mediterranean Sea. Biogeochemistry of Marine Dissolved Organic Matter: Second Edition , 579–608doi:`10.1016/B978-0-12-405940-5.00013-3`.

Sarmiento, J.L., Herbert, T., 1988. Mediterranean nutrient balance and episodes of anoxia. Global Biogeochemical Cycles 2, 427–444.

Sauzède, R., Claustre, H., Jamet, C., Uitz, J., Mignot, A., D'Ortenzio, F., Ras, J., 2015. Retrieving the vertical distribution of chlorophyll a concentration and phytoplankton community composition from in situ fluorescence profiles: A method based on a neural network with potential for global-scale applications. Journal of Geophysical Research: Oceans , 2813–2825doi:`10.1002/2014JC010387.Received`.

Schlitzer, R., Roether, W., Oster, H., Hausmann, M., Johannsen, I.H., 1991. Chlorofluoromethane and oxygen in the Eastern Mediterranean. Deep-Sea Research 3.

Schmidtko, S., Stramma, L., Visbeck, M., 2017. Decline in global oceanic oxygen content during the past five decades. Nature 542, 335–339. URL: `http://www.nature.com/articles/nature21399`, doi:`10.1038/nature21399`.

Schneider, A., Tanhua, T., Roether, W., Steinfeldt, R., 2014. Changes in ventilation of the mediterranean Sea during the past 25 year. Ocean Science 10, 1–16. doi:`10.5194/os-10-1-2014`.

Schroeder, K., Chiggiato, J., Josey, S.A., Borghini, M., Aracri, S., Sparnocchia, S., 2017. Rapid response to climate change in a marginal sea. Scientific Reports 7, 1–7. doi:`10.1038/s41598-017-04455-5`.

Schroeder, K., Cozzi, S., Belgacem, M., Borghini, M., Cantoni, C., Durante, S., Petrizzo, A., Poiana, A., Chiggiato, J., 2020. Along-Path Evolution of Biogeochemical and Carbonate System Properties in the Intermediate Water of the Western Mediterranean. Frontiers in Marine Science 7, 1–19. doi:`10.3389/fmars.2020.00375`.

Schroeder, K., Gasparini, G.P., Tangherlini, M., Astraldi, M., 2006. Deep and intermediate water in the western Mediterranean under the influence of the Eastern Mediterranean Transient. Geophysical Research Letters 33, 1–6. doi:`10.1029/2006GL027121`.

SHOM, 2018. PROTEVSMED_PERLE_2018 cruise, RV L'Atalante. Division Plans de DMI .

Siddorn, J.R., Furner, R., 2013. An analytical stretching function that combines the best attributes of geopotential and terrain-following vertical coordinates. Ocean Modelling 66, 1–13. URL: `http://dx.doi.org/10.1016/j.ocemod.2013.02.001`, doi:`10.1016/j.ocemod.2013.02.001`.

Siokou-Frangou, I., Christaki, U., Mazzocchi, M.G., Montresor, M., Ribera D'Alcala, M., Vaque, D., Zingone, A., 2010. Plankton in the open mediterranean Sea: A review. Biogeosciences 7, 1543–1586. doi:`10.5194/bg-7-1543-2010`.

Sisma-Ventura, G., Kress, N., Silverman, J., Gertner, Y., Ozer, T., Biton, E., Lazar, A., Gertman, I., Rahav, E., Herut, B., 2021. Post-eastern Mediterranean Transient Oxygen Decline in the Deep Waters of the Southeast Mediterranean Sea Supports Weakening of Ventilation Rates. Frontiers in Marine Science 7, 1–10. doi:`10.3389/fmars.2020.598686`.

Sisma-Ventura, G., Yam, R., Kress, N., Shemesh, A., 2016. Water column distribution of stable isotopes and carbonate properties in the South-eastern Levantine basin (Eastern Mediterranean): Vertical and temporal change. Journal of Marine Systems 158, 13–25. doi:`10.1016/j.jmarsys.2016.01.012`.

Skliris, N., Lascaratos, A., 2004. Impacts of the Nile River damming on the thermohaline circulation and water mass characteristics of the Mediterranean Sea. Journal of Marine Systems 52, 121–143. doi:`10.1016/j.jmarsys.2004.02.005`.

Soetaert, K., Herman, P.M.J., Middelburg, J.J., Heip, C., Smith, C.L., Tett, P., Wild-Allen, K., 2001. Numerical modelling of the shelf break ecosystem: Reproducing benthic and pelagic measurements. Deep-Sea Research Part II: Topical Studies in Oceanography 48, 3141–3177. doi:`10.1016/S0967-0645(01)00035-2`.

Soetaert, K., Middelburg, J.J., Herman, P.M.J., Buis, K., 2000. On the coupling of benthic and pelagic biogeochemical models. Earth Science Reviews 51, 173–201. doi:`10.1016/S0012-8252(00)00004-0`.

Solidoro, C., Cossarini, G., Lazzari, P., Galli, G., Bolzon, G., Somot, S., Salon, S., 2022. Modeling Carbon Budgets and Acidification in the Mediterranean Sea Ecosystem Under Contemporary and Future Climate. Frontiers in Marine Science 8, 1–15. doi:`10.3389/fmars.2021.781522`.

Somot, S., 2005. Modélisation climatique du bassin méditerranéen: variabilité et scénarios de changement climatique. Ph.D. thesis. Université Paul Sabatier-Toulouse III.

Somot, S., Sevault, F., Déqué, M., Somot, S., Sevault, F., Déqué, M., 2006. Transient climate change scenario simulation of the Mediterranean Sea for the 21st century using a high-resolution ocean circulation model To cite this version : HAL Id : hal-00195045 Transient climate change scenario simulation of the Mediterranean Sea f. Climate Dynamics 27, 851–879.

Soto-Navarro, J., Jordá, G., Amores, A., Cabos, W., Somot, S., Sevault, F., Macías, D., Djurdjevic, V., Sannino, G., Li, L., Sein, D., 2020. Evolution of Mediterranean Sea water properties under climate change scenarios in the Med-CORDEX ensemble. Climate Dynamics 54, 2135–2165. doi:`10.1007/s00382-019-05105-4`.

Souvermezoglou, E., Hatzigeorgiou, E., Pampidis, I., Siapsali, K., 1992. Distribution and seasonal variability of nutrients and dissolved oxygen in the northeastern Ionian Sea. Oceanologica Acta 15, 585–594.

Speicher, E.A., Moran, S.B., Burd, A.B., Delfanti, R., Kaberi, H., Kelly, R.P., Papucci, C., Smith, J.N., Stavrakakis, S., Torricelli, L., Zervakis, V., 2006. Particulate organic carbon export fluxes and size-fractionated POC/234Th ratios in the Ligurian, Tyrrhenian and Aegean Seas. Deep-Sea Research Part I: Oceanographic Research Papers 53, 1810–1830. doi:`10.1016/j.dsr.2006.08.005`.

Stratford, K., Williams, R.G., 1997. A tracer study of the formation, dispersal, and renewal of Levantine Intermediate Water. Journal of Geophysical Research: Oceans 102, 12539–12549. doi:`10.1029/97JC00019`.

Struglia, M.V., Mariotti, A., Filograsso, A., 2004. River discharge into the Mediterranean sea: Climatology and aspects of the observed variability. Journal of Climate 17, 4740–4751. doi:`10.1175/JCLI-3225.1`.

Sur, H., Ozsoy, E., Unluata, U., 1993. Simultaneous deep and intermediate depth convection in the Northem Levantine Sea ,. oceanologica 16, 33–43.

Taillandier, V., D'Ortenzio, F., Antoine, D., 2012. Carbon fluxes in the mixed layer of the Mediterranean Sea in the 1980s and the 2000s. Deep-Sea Research Part I: Oceanographic Research Papers 65, 73–84. URL: `http://dx.doi.org/10.1016/j.dsr.2012.03.004`, doi:`10.1016/j.dsr.2012.03.004`.

Taillandier, V., D'Ortenzio, F., Prieur, L., Conan, P., Coppola, L., Cornec, M., Dumas, F., Durrieu de Madron, X., Fach, B., Fourrier, M., Gentil, M., Hayes, D., Husrevoglu, S., Legoff, H., Le Ster, L., Örek, H., Ozer, T., Poulain, P.M., Pujo-Pay, M., Ribera d'Alcalà, M., Salihoglu, B., Testor, P., Velaoras, D., Wagener, T., Wimart-Rousseau, C., de Madron, X., Fach, B., Fourrier, M., Gentil, M., Hayes, D., Husrevoglu, S., Legoff, H., Le Ster, L., Örek, H., Ozer, T., Poulain, P.M., Pujo-Pay, M., Ribera d'Alcalà, M., Salihoglu, B., Testor, P., Velaoras, D., Wagener, T., Wimart-Rousseau, C., 2022. Sources of the Levantine Intermediate Water in Winter 2019. Journal of Geophysical Research: Oceans 127, 1–19. doi:`10.1029/2021JC017506`.

Tanhua, T., 2013. Repeat hydrography in the Mediterranean Sea - Cruise No. M84/3 - April 5 - April 28, 2011, Istanbul (Turkey) - Vigo (Spain). METEOR-Berichte , 48 ppdoi:`10.2312/cr`.

Tanhua, T., Hainbucher, D., Schroeder, K., Cardin, V., Álvarez, M., Civitarese, G., 2013. The Mediterranean Sea system: A review and an introduction to the special issue. Ocean Science 9, 789–803. doi:`10.5194/os-9-789-2013`.

The MerMex Group, 2011. Marine ecosystems responses to climatic and anthropogenic forcings in the Mediterranean. Progress in Oceanography 91, 97–166. doi:`10.1016/j.pocean.2011.02.003`.

The POEM group, 1992. General circulation of the Eastern Mediterranean. Earth Science Reviews 32, 285–309. doi:`10.1016/0012-8252(92)90002-B`.

Theocharis, A., Georgopoulos, D., Lascaratos, A., Nittis, K., 1993. Water masses and circulation in the central region of the Eastern Mediterranean. Deep-Sea Research II 40, 1121–1142.

Theocharis, A., Krokos, G., Velaoras, D., Korres, G., 2014. An Internal Mechanism Driving the Alternation of the Eastern Mediterranean Dense/Deep Water Sources. The Mediterranean Sea: Temporal Variability and Spatial Patterns 9781118847, 1–167. doi:`10.1002/9781118847572`.

Thierry, V., Bittig, H., Team, A.B.., 2021. Argo quality control manual for dissolved oxygen concentration, v2.1. Argo Data Management , 1–33doi:`10.13155/46542`.

Thingstad, T.F., Hagstrom, A., Rassoulzadegan, F., 1997. Accumulation of degradable DOC in surface waters: Is it caused by a malfunctioning microbial loop? Limnology and Oceanography 42, 398–404. doi:`10.4319/lo.1997.42.2.0398`.

Thingstad, T.F., Rassoulzadegan, F., 1995. Nutrient limitations, microbial food webs, and biological C-pumps”: Suggested interactions in a P-limited Mediterranean. Marine Ecology Progress Series 117, 299–306. doi:`10.3354/meps117299`.

Tugrul, S., Besiktepe, S.T., Salihoglu, I., Becsiktepe, S.T., Salihoglu, I., 2002. Nutrient exchange fluxes between the Aegean and Black Seas through the marmara sea. Mediterranean Marine Science 3, 33–42. doi:`10.12681/mms.256`.

Tusseau, M.H., Lancelot, C., Martin, J.M., Tassin, B., 1997. 1-D coupled physical-biological model of the northwestern Mediterranean Sea. Deep-Sea Research Part II: Topical Studies in Oceanography 44, 851–880. doi:`10.1016/S0967-0645(96)00087-2`.

Uitz, J., Stramski, D., Gentili, B., D’Ortenzio, F., Claustre, H., 2012. Estimates of phytoplankton class-specific and total primary production in the Mediterranean Sea from satellite ocean color observations. Global Biogeochemical Cycles 26, 1–10. doi:`10.1029/2011GB004055`.

Ulses, C., Estournel, C., Bonnin, J., de Madron, X., Marsalei, P., Durrieu de Madron, X., Marsalei, P., 2008. Impact of storms and dense water cascading on shelf-slope exchanges in the Gulf of Lion (NW Mediterranean). Journal of Geophysical Research: Oceans 113. doi:`10.1029/2006JC003795`.

Ulses, C., Estournel, C., Fourrier, M., Coppola, L., Kessouri, F., Lefèvre, D., Marsaleix, P., 2021. Oxygen budget of the north-western Mediterranean deep- convection region. Biogeosciences 18, 937–960. doi:`10.5194/bg-18-937-2021`.

Ulses, C., Estournel, C., Kessouri, F., Hermann, M.J., Marsaleix, P., 2016. Modeling, Budget of organic carbon in the North-Western Mediterranean open sea over the period 2004–2008 using 3-D coupled physical Modeling. Journal of Geophysical Research : Oceans 121, 7026–7055. doi:`10.1002/2016JC011818`.

UNEP, 2020. State of the environment. Environmental Science {\&} Technology 16, 445–446. doi:`10.1021/es00102a607`.

Unlulata, U., Oguz, T., Latif, M.A., Özsoy, E., 1990. On the Physical Oceanography of the Turkish Straits. The Physical Oceanography of Sea Straits , 25–60doi:`10.1007/978-94-009-0677-8{\_}2`.

Van Cappellen, P., Powley, H.R., Emeis, K.C., Krom, M.D., 2014. A biogeochemical model for phosphorus and nitrogen cycling in the Eastern Mediterranean Sea: Part 1: Model development, initialization and sensitivity. Journal of Marine Systems 139, 460–471. doi:`10.1016/j.jmarsys.2014.08.016`.

Velaoras, D., Krokos, G., Nittis, K., Theocharis, A., 2014. Dense intermediate water outflow from the Cretan Sea: A salinity driven, recurrent phenomenon, connected to thermohaline circulation changes. Journal of Geophysical Research: Oceans , 3868–3882URL: `http://onlinelibrary.wiley.com/doi/10.1002/jgrc.20353/abstract`, doi:`10.1002/2014JC009937.Received`.

Velaoras, D., Krokos, G., Theocharis, A., 2015. Recurrent intrusions of transitional waters of Eastern Mediterranean origin in the Cretan Sea as a tracer of Aegean Sea dense water formation events. Progress in Oceanography 135, 113–124. URL: `http://dx.doi.org/10.1016/j.pocean.2015.04.010`, doi:`10.1016/j.pocean.2015.04.010`.

Vichi, M., Pinardi, N., Masina, S., 2007. A generalized model of pelagic biogeochemistry for the global ocean ecosystem. Part I: Theory. Journal of Marine Systems 64, 89–109. doi:`10.1016/j.jmarsys.2006.03.006`.

Vidussi, F., Claustre, H., Manca, B.B., Luchetta, A., Jean-Claude, M., 2001. Phytoplankton pigment distribution in relation to upper thermocline circulation in the eastern Mediterranean Sea during winter. Journal of Geophysical Research 106, 939–956.

Violaki, K., Bourrin, F., Aubert, D., Kouvarakis, G., Delsaut, N., Mihalopoulos, N., 2018. Organic phosphorus in atmospheric deposition over the Mediterranean Sea: An important missing piece of the phosphorus cycle. Progress in Oceanography 163, 50–58. URL: `https://doi.org/10.1016/j.pocean.2017.07.009`, doi:`10.1016/j.pocean.2017.07.009`.

Violaki, K., Zarbas, P., Mihalopoulos, N., 2010. Long-term measurements of dissolved organic nitrogen (DON) in atmospheric deposition in the Eastern Mediterranean: Fluxes, origin and biogeochemical implications. Marine Chemistry 120, 179–186. URL: `http://dx.doi.org/10.1016/j.marchem.2009.08.004`, doi:`10.1016/j.marchem.2009.08.004`.

Volpe, G., Colella, S., Forneris, V., Tronconi, C., Santoleri, R., 2012. The Mediterranean Ocean Colour Observing System – System development and product validation. Ocean Science 8, 869–883. doi:`10.5194/os-8-869-2012`.

Volpe, G., Santoleri, R., Vellucci, V., Ribera d'Alcalà, M., Marullo, S., D'Ortenzio, F., 2007. The colour of the Mediterranean Sea: Global versus regional bio-optical algorithms evaluation and implication for satellite chlorophyll estimates. Remote Sensing of Environment 107, 625–638. doi:`10.1016/j.rse.2006.10.017`.

Wangersky, P.J., 1978. Methods of seawater analysis. Marine Chemistry 7, 86–87. doi:`10.1016/0304-4203(78)90045-2`.

Wanninkhof, R., McGillis, W.R., 1999. A cubic relationship between air-sea CO2 exchange and wind speed. Geophysical Research Letters 26, 1889–1892. doi:`10.1029/1999GL900363`.

Williams, N., 1998. The Mediterranean beckons to Europe's oceanographers. Science 279, 483–484. doi:`10.1126/science.279.5350.483`.

Wimart-Rousseau, C., Wagener, T., Álvarez, M., Moutin, T., Fourrier, M., Coppola, L., Niclas-Chirurgien, L., Raimbault, P., D'Ortenzio, F., de Madron, X., Taillandier, V., Dumas, F., Conan, P., Pujo-Pay, M., Lefèvre, D., Durrieu de Madron, X., Taillandier, V., Dumas, F., Conan, P., Pujo-Pay, M., Lefèvre, D., 2021. Seasonal and Interannual Variability of the CO2 System in the Eastern Mediterranean Sea: A Case Study in the North Western Levantine Basin. Frontiers in Marine Science 8, 1–18. doi:`10.3389/fmars.2021.649246`.

Winkler, L.W., 1888. Die Bestimmung des im Wasser gelösten Sauerstoffes. Berichte der deutschen chemischen Gesellschaft 21, 2843–2854. doi:`10.1002/cber.188802102122`.

Wolf, M.K., Hamme, R.C., Gilbert, D., Yashayaev, I., Thierry, V., 2018. Oxygen Saturation Surrounding Deep Water Formation Events in the Labrador Sea From Argo-O2 Data. Global Biogeochemical Cycles 32, 635–653. URL: `https://doi.org/10.1002/2017GB005829`, doi:`10.1002/2017GB005829`.

Wüst, G., 1961. On the Vertical Circulation of the Mediterranean influenced depths between. Journal of Geophysical Research 66, 3261–3271.

Yilmaz, A., Ediger, D., Basturk, O., Tugrul, S., 1994. Phytoplankton fluorescence and deep chlorophyll maxima in the northeastern Mediterranean. Oceanologica Acta 17, 69–77.

Yilmaz, A., Tugrul, S., 1998. The effect of cold- and warm-core eddies on the distribution and stoichiometry of dissolved nutrients in the northeastern Mediterranean. Journal of Marine Systems 16, 253–268. doi:`10.1016/S0924-7963(97)00022-5`.

Yogev, T., Rahav, E., Bar-Zeev, E., Man-Aharonovich, D., Stambler, N., Kress, N., Béjà, O., Mulholland, M.R., Herut, B., Berman-Frank, I., 2011. Is dinitrogen fixation significant in the Levantine Basin, East Mediterranean Sea? Environmental Microbiology 13, 854–871. doi:`10.1111/j.1462-2920.2010.02402.x`.

Zavatarelli, M., Baretta, J.W., Baretta-Bekker, J.G., Pinardi, N., 2000. The dynamics of the Adriatic Sea ecosystem. An idealized model study. Deep-Sea Research Part I: Oceanographic Research Papers 47, 937–970. doi:`10.1016/S0967-0637(99)00086-2`.

Ziveri, P., Grelaud, M., 2015. Physical oceanography during Ángeles Alvariño cruise MedSeA2013. doi:`10.1594/PANGAEA.846067`.

Zodiatis, G., 1993. Circulation of the Cretan Sea water masses (eastern Mediterranean Sea). Oceanologica Acta 16, 107–114.

Zohary, T., Herut, B., Krom, M.D., Fauzi, R., Pitta, P., Psarra, S., Rassoulzadegan, F., Stambler, N., Tanaka, T., Frede Thingstad, T., Malcolm, E., 2005. P-limited bacteria but N and P co-limited phytoplankton in the Eastern Mediterranean - A microcosm experiment. Deep-Sea Research Part II: Topical Studies in Oceanography 52, 3011–3023. doi:`10.1016/j.dsr2.2005.08.011`.